Title

Spectrally efficient underwater acoustic communications : channel characterization and design aspects for OFDM

Permalink

https://escholarship.org/uc/item/3v09150v

Author

Radošević, Andreja

Publication Date

2012

Peer reviewed|Thesis/dissertation

UNIVERSITY OF CALIFORNIA, SAN DIEGO

Spectrally Efficient Underwater Acoustic Communications: Channel Characterization and Design Aspects for OFDM

A dissertation submitted in partial satisfaction of the
requirements for the degree
Doctor of Philosophy

in

Electrical Engineering (Communication Theory and Systems)

by

Andreja Radošević

Committee in charge:

Professor John G. Proakis, Chair
Professor Laurence B. Milstein, Co-Chair
Professor William S. Hodgkiss
Professor Ryan Kastner
Professor William Kuperman
Professor Milica Stojanovic

2012

The dissertation of Andreja Radošević is approved, and it is acceptable in quality and form for publication on microfilm and electronically:

Co-Chair

Chair

University of California, San Diego

2012

DEDICATION

To my parents and brother

TABLE OF CONTENTS

LIST OF FIGURES

LIST OF TABLES

ACKNOWLEDGEMENTS

Chapter 2, in part, is a reprint of the material as it appears in "Statistical characterization and capacity of shallow water acoustic channels," by A. Radosevic, J. G. Proakis, and M. Stojanovic, IEEE Oceans'09 Conference, Bremen, Germany, May 2009. The dissertation author was the primary investigator and author of this paper.

Sections 3.1 and 3.2, in part, are a reprint of the material as it appears in "Statistical characterization and capacity of shallow water acoustic channels," by A. Radosevic, J. G. Proakis, and M. Stojanovic, IEEE Oceans'09 Conference, Bremen, Germany, May 2009. The dissertation author was the primary investigator and author of this paper.

Section 3.2, in part, is a reprint of the material as it appears in "Capacity of MIMO systems in shallow water acoustic channels," by A. Radosevic, D. Fertonani, T. M. Duman, J. G. Proakis, and M. Stojanovic, IEEE 43rd Asilomar Conference on Signals, Systems and Computers, Nov. 2009. The dissertation author was the primary investigator and author of this paper.

Section 3.3, in part, is a reprint of the material as it appears in "Bounds on the information rate for sparse channels with long memory and i.u.d. inputs," by A. Radosevic, D. Fertonani, T. M. Duman, J. G. Proakis, and M. Stojanovic, IEEE Transactions on Communications, vol. 59, no. 12, pp. 3343 – 3352, December 2011. The dissertation author was the primary investigator and author of this paper.

Sections 4.1, 4.2 and 4.4, in part, are a reprint of the material as it appears in "Channel prediction for adaptive modulation in underwater acoustic communications," by A. Radosevic, T. M. Duman, J. G. Proakis, and M. Stojanovic, IEEE Oceans'11 Conference, Santander, Spain, June 2011. The dissertation author was the primary investigator and author of this paper.

Sections 4.3 and 4.4, in part, are a reprint of the material as it appears in "Adaptive OFDM for underwater acoustic channels with limited feedback," by A. Radosevic, T. M. Duman, J. G. Proakis, and M. Stojanovic, 45rd Asilomar Conference on Signals, Systems and Computers, Nov. 2011. The dissertation author was the primary investigator and author of this paper.

Sections 4.1 through 4.4, in part, are also a reprint of the material as it appears in "Adaptive OFDM modulation for underwater acoustic communications: design considerations and experimental study," by A. Radosevic, R. Ahmed, T. M. Duman, J. G. Proakis, and M. Stojanovic, submitted for publication in IEEE Journal of Oceanic Engineering. The dissertation author was the primary investigator and author of this paper.

Sections 5.1 and 5.2, in part, are a reprint of the material as it appears in "Selective decision directed channel estimation for UWA OFDM systems," by A. Radosevic, T. M. Duman, J. G. Proakis, and M. Stojanovic, 49th Allerton Conference on Communication, Control, and Computing, Sept. 2011. The dissertation author was the primary investigator and author of this paper.

Sections 5.3 and 5.4, in part, are a reprint of the material as it appears in "Selective decision directed channel estimation for OFDM communications over multipath Rician fading channels," by A. Radosevic, T. M. Duman, J. G. Proakis, and M. Stojanovic, International Workshop on Signal Processing Advances in Wireless Communications (SPAWC), accepted. The dissertation author was the primary investigator and author of this paper.

VITA

2012	Ph. D. in Electrical Engineering (Communication Theory and Systems), University of California, San Diego
2009	M. S. in Electrical Engineering (Communication Theory and Systems), University of California, San Diego
2007	B. S. in Electrical Engineering, University of Belgrade, Serbia

PUBLICATIONS

A. Radosevic, J. G. Proakis, and M. Stojanovic, "Statistical characterization and capacity of shallow water acoustic channels," *in Proc. IEEE Oceans'09 Conference*, Bremen, Germany, May 2009.

A. Radosevic, D. Fertonani, T. M. Duman, J. G. Proakis, and M. Stojanovic, "Capacity of MIMO systems in shallow water acoustic channels," *in Proc. IEEE 43rd Asilomar Conference on Signals, Systems and Computers*, Nov. 2009.

A. Radosevic, D. Fertonani, T. M. Duman, J. G. Proakis, and M. Stojanovic, "Bounds on the information rate for sparse channels with long memory and i.u.d. inputs," *IEEE Transactions on Communications*, vol. 59, no. 12, pp. 3343 – 3352, December 2011.

A. Radosevic, T. M. Duman, J. G. Proakis, and M. Stojanovic, "Channel prediction for adaptive modulation in underwater acoustic communications," *in Proc. IEEE Oceans'11 Conference*, Santander, Spain, June 2011.

A. Radosevic, T. M. Duman, J. G. Proakis, and M. Stojanovic, "Selective decision directed channel estimation for UWA OFDM systems," *in Proc. 49th Allerton Conference on Communication, Control, and Computing*, Sept. 2011.

A. Radosevic, T. M. Duman, J. G. Proakis, and M. Stojanovic, "Adaptive OFDM for underwater acoustic channels with limited feedback," *in Proc. IEEE 45rd Asilomar Conference on Signals, Systems and Computers*, Nov. 2011.

A. Radosevic, T. M. Duman, J. G. Proakis, and M. Stojanovic, "Selective decision directed channel estimation for OFDM communications over multipath Rician fading channels," *International Workshop on Signal Processing Advances in Wireless Communications* (SPAWC), accepted.

A. Radosevic, R. Ahmed, T. M. Duman, J. G. Proakis, and M. Stojanovic, "Adaptive OFDM modulation for underwater acoustic communications: design considerations and experimental study," *IEEE Journal of Oceanic Engineering*, submitted.

ABSTRACT OF THE DISSERTATION

Spectrally Efficient Underwater Acoustic Communications: Channel Characterization and Design Aspects for OFDM

by

Andreja Radošević

Doctor of Philosophy in Electrical Engineering (Communication Theory and Systems)

University of California, San Diego, 2012

Professor John G. Proakis, Chair
Professor Laurence B. Milstein, Co-Chair

In this dissertation, we consider design aspects of spectrally efficient underwater acoustic (UWA) communications. In particular, we first focus on statistical characterization and capacity evaluation of shallow water acoustic communications channels. Wideband single-carrier and multi-carrier probe signals are employed during the Kauai Acoustic Communications MURI 2008 (KAM08) and 2011 (KAM11) experiments, to measure the time-varying channel response, and to estimate its statistical properties and capacity that play an important role in the design of spectrally efficient communication systems. Besides the capacity analysis for unconstrained inputs, we determine new bounds on the achievable information rate for discrete-time Gaussian channels with inter-symbol interference and independent and uniformly distributed channel input symbols drawn from finite-order modulation alphabets. Specifically, we derived new bounds on the achievable rates for sparse channels with long memory. Furthermore, we explore design aspects of adaptive modulation based on orthogonal frequency division multiplexing (OFDM) for UWA communications, and study its performance using real-time at-sea experiments. Lastly, we investigate a channel estimation (CE) method for improving the spectral efficiency of UWA communications. Specifically, we determine the performance of a selective decision directed (DD) CE method for UWA OFDM-based communications.

Chapter 1

Introduction

This chapter gives a general overview of design challenges for underwater acoustic communication systems and our contributions that address some of the challenges in the rest of the thesis. In particular, Section 1.1 presents the objective of the work that is presented in the thesis, Section 1.2 gives an overview of experiments during which data measurements used in the thesis were recorded, and Section 1.3 gives an overview of the major contributions that are addressed in the thesis.

1.1 Objective of the Research

In the past decade, there has been an increased interest in underwater acoustic (UWA) communications due to a variety of applications such as marine research, oceanography, and offshore oil exploration. Ongoing research has been focused on the design of communication systems that provide improved performance and robustness, in the presence of channel distortion. In the design of such systems, relatively accurate models of the channel characteristics are required. This is a challenging problem because the UWA channel is characterized by frequency-dependent path loss, time-varying multipath propagation, and low propagation speed (i.e., about 1500 m/s) [1]. Time variations of the propagation paths, induced by the system motion as well as by changes in the medium, result in Doppler spreading and shifting of the signal. Also, since acoustic propagation is best supported at low frequencies, the system is inherently wideband. This fact is of particular importance because of the large delay spreads that typically affect UWA channels, which cause inter-symbol interference (ISI) spanning tens or even hundreds of symbol intervals in the case of wideband single-carrier systems. However, the channel impulse response is typically sparse, i.e., very few propagation paths carry significant energy [1]. A complete model must take into account the frequency-dependent path loss, channel sparseness, and Doppler shifting and spreading effects.

Design and simulation of UWA communication systems requires accurate channel modeling. Ray theory [2] can be used to provide a deterministic description of the (average) multipath propagation. However, in order to explore the communication limits of this complex medium, a statistical description of the random time variations of the channel is needed. Due to the non-stationarity of the channel, analysis should be constrained to short-term statistical characterization only. Hence, the statistical properties of the channel fading, as well as the parameters of the underlying statistical model are subject to the evolution in time. This is an important observation since the assessment of the channel capacity, depends on how well the fading statistics can be estimated. Moreover, because of the non-stationarity, design of the capacity-achieving adaptive coding/modulation is of particular interest, and it is based on the ability of the communication system to track the channel model parameters. Based on statistical characterization of the fading process, a time-varying channel model can be developed which can be used for the information-theoretical analysis of the capacity of the UWA channels.

The objectives of the research were as follows:

1. Statistical characterization of the UWA channel based on channel measurements, which were made during the experiments, introduced in the next section.

2. Evaluation of the capacity of the shallow water UWA channel by employing the channel characteristics extracted from the experimental data.

3. Design and implementation of spectrally efficient orthogonal frequency divi-

sion multiplexing (OFDM) signals for UWA communications.

4. Introduction of a selective decision directed channel estimation method for spectrally efficient OFDM communications.

1.2 Channel Measurement Experiments

In this section, we give an overview of experiments during which data measurements used in the thesis were recorded. Specifically, we will provide general information regarding the Kauai Acoustic Communications MURI 2008 (KAM08) experiment [3], conducted in shallow water off the western coast of Kauai, Hawaii, in June 2008, and the Kauai Acoustic Communications MURI 2011 (KAM11) experiment [4], conducted at the same location in July 2011.

1.2.1 KAM08 Experiment

The Kauai Acoustic Communications MURI 2008 experiment was conducted off the western side of Kauai, Hawaii, at the Pacific Missile Range Facility (PMRF) over the period 16 June – 2 July 2008. In particular, the experiment was performed in shallow water (20 – 400 m deep) in the region northwest of Barking Sands (see Figure 1.1). All equipment was deployed (and recovered) from a University-National Oceanographic Laboratory System (UNOLS) research vessel R/V Melville, operated by the Scripps Institution of Oceanography.

The objective of the KAM08 experiment was to collect acoustic and environmental data appropriate for studying the coupling of oceanography, acoustics, and underwater communications. Specifically, the goal was to obtain data which will relate the impact of a fluctuating oceanographic environment and source/receiver motion to fluctuations in the waveguide acoustic impulse response between multiple sources and receivers and ultimately to the design and performance characterization of underwater acoustic digital data communication systems in shallow water. The focus was on fluctuations over scales of a few seconds to a few tens of seconds that directly affect the reception of a data packet and packet-to-packet variability.

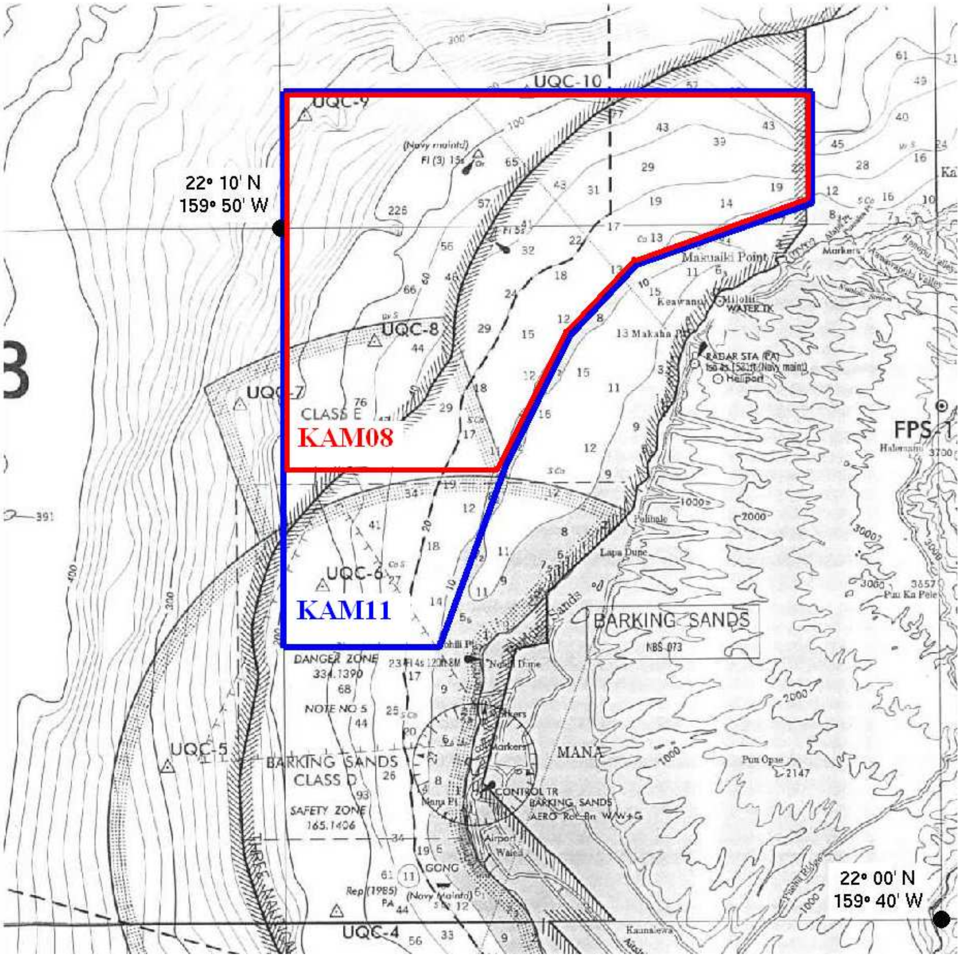

Figure 1.1: The KAM08 and KAM11 operational areas are outlined by the red and blue solid lines, respectively.

Sources and Receivers

A number of acoustic sources and receivers as well as environmental moorings were deployed. The characteristics of each are summarized below.

1. *Source Array.* An array of 8 ITC-1001 transducers (provided by the Marine Physical Laboratory (MPL)) was deployed over the side while the R/V Melville was in dynamic positioning mode for extended periods of time (on the order of hours). The sampling frequency at the transmitter was $f_{s,Tx} = 100$ kHz per element with 7.5 m element separation (52.5 m aperture). The array dimensions are shown in Figure 1.2. Note that Transducer 1 is closest to the sea surface and had a nominal depth of 30 m. The nominal bandwidth of each source was $12 - 32$ kHz with a maximum source level of 185 dB $+/-$ 4 dB across this band. The measured source level characteristics of one channel of the source array are in Figure 1.3 (6 dB below full power). Continuous transmissions from all channels simultaneously or a single channel at a time (e.g. round-robin fashion for channel impulse response measurement purposes or single channel transmissions at a selected depth) were feasible.

2. *Towed Sources.* In addition, source tows in the operational area were carried out with R/V Melville underway. During source tow operations, a pair of transducers (ITC-1001 and ITC-2015) were towed in at nominal depths of 50 m and 20 m. In all cases, the maximum source level from these transducers was approximately 185 dB re μPa. The source tow transducers were driven by separate power amplifiers and both transducers could be operated simultaneously. A depth sensor was included. The TVR characteristics of the ITC-1001 and ITC-2015 transducers are shown in Figure 1.4. The ITC-1001 has a resonant peak at 17.5 kHz and is approximately 8 dB down at 12 kHz and 24 kHz. The ITC-2015 is roughly flat within approximately 6 dB down over $1.6 - 4.2$ kHz and $6.1 - 8.7$ kHz.

3. *Vertical Line Array.* Two autonomous MPL 16-element vertical line arrays (VLAs) were deployed. The VLAs had a sampling rate of $f_{s,Rx} = 50$ kHz per

element with 3.75 m interelement spacing (total aperture of 56.25 m). The array dimensions are shown in Figure 1.5. The hydrophones used were HTI-94-SSQ. A tilt/heading/depth sensor was placed 0.5 m above Element 16. The frequency response was flat in the range 20 Hz -20 kHz (antialiasing filter with -3 dB at 20 kHz, -15 dB at 25 kHz). The moorings incorporated a sacrificial weight (900 lbs, surplus train wheels). Total maximum continuous record duration of each array was 96 hours.

A set of preapproved mooring locations were defined with PMRF which were at least 250 m from any PMRF instrumentation or seafloor cable. These are shown in Figure 1.6 along with the coordinates that bound the operational area. The acoustic data collected during the KAM08 experiment include transmissions from the source array located at Sta00, and the receiving arrays located at Sta08 and Sta16.

1.2.2 KAM11 Experiment

The Kauai Acoustic Communications MURI 2011 experiment was conducted at the PMRF, the location of the previous KAM08 experiment (see Figure 1.1) over the period 24 June $-$ 15 July 2011. All equipment was deployed (and recovered) from a UNOLS research vessel R/V Kilo Moana, operated by the University of Hawaii.

Similarly as for the KAM08 experiment, the objective of KAM11 was to obtain acoustic and environmental data appropriate for studying the coupling of oceanography, acoustics, and underwater communications. Specifically, interest was coastal shallow water recording of various predefined transmit waveforms in single-source and multiple-source transducer configurations. Transmissions over a wide variety of source/receiver configurations (ranges on the order of $1-15$ km, shallow and deep sources and receivers, along-slope and upslope/downslope propagation), fixed and mobile sources, and a variety of sea surface and water column conditions. Also, interest was to demonstrate and test techniques for adapting modulation and coding parameters based on feedback from the receiver to the transmitter over a variety of ranges and environmental conditions.

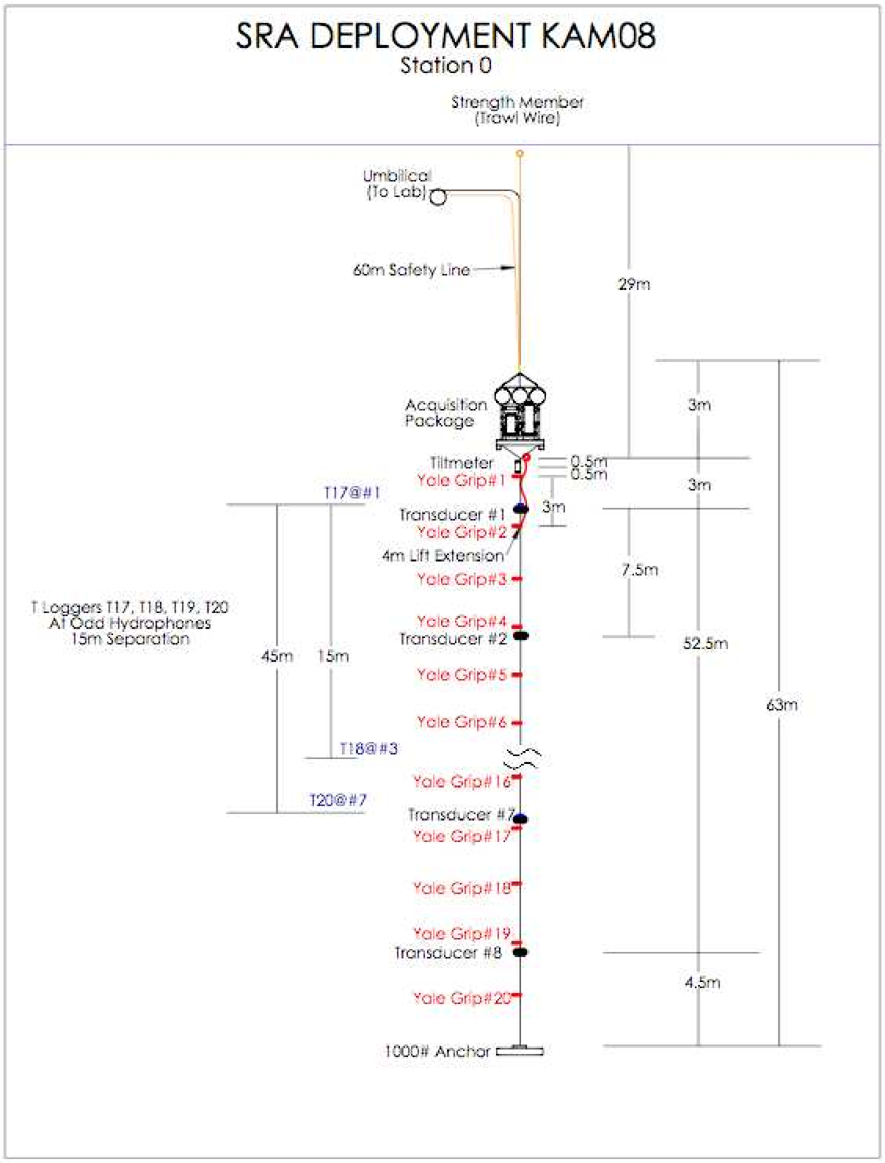

Figure 1.2: Source array deployment.

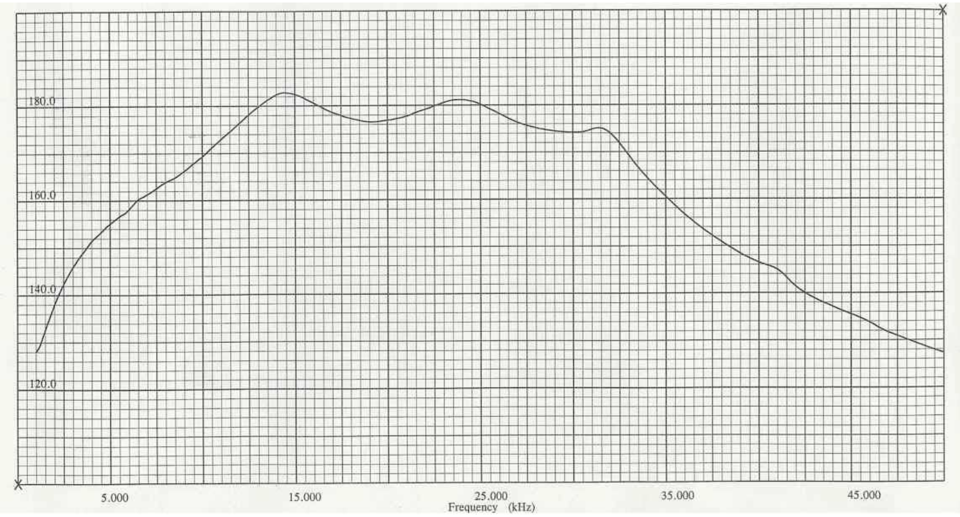

Figure 1.3: Source array single channel calibration (6dB below full power).

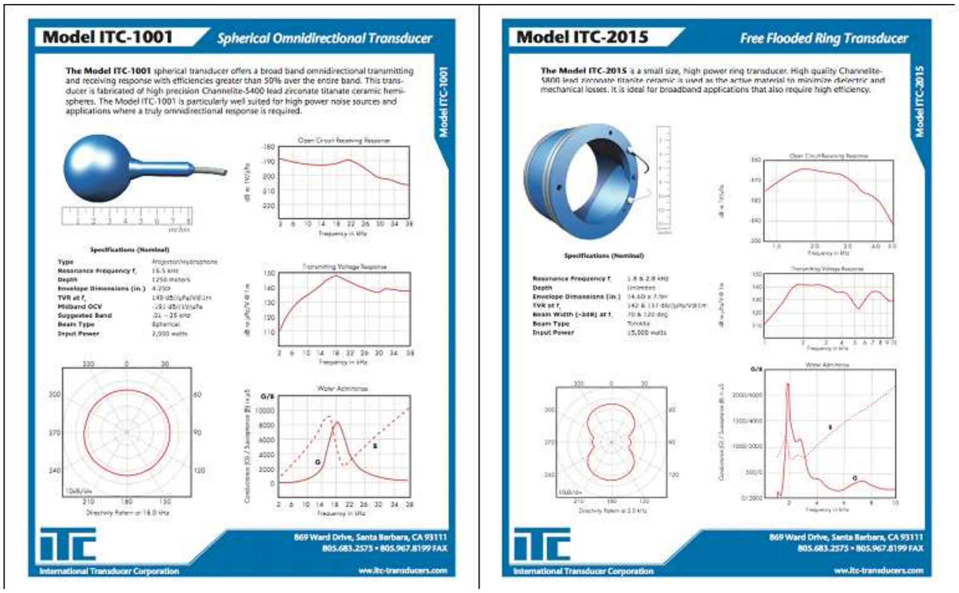

Model ITC-1001 *Spherical Omnidirectional Transducer*

The Model ITC-1001 spherical transducer offers a broad band omnidirectional transmitting and receiving response with efficiencies greater than 50% over the entire band. This transducer is fabricated of high precision Channelite-5400 lead zirconate titanate ceramic hemispheres. The Model ITC-1001 is particularly well suited for high power noise sources and applications where a truly omnidirectional response is required.

Specifications (Nominal)

Type	Projector/Hydrophone
Resonance Frequency f_r	15.5 kHz
Depth	1250 meters
Envelope Dimensions (in.)	4.250
TVR at f_r	149 dB//µPa/V@1m
Midband OCV	-193 dB//1V/µPa
Suggested Band	.01 – 25 kHz
Beam Type	Spherical
Input Power	2,000 watts

869 Ward Drive, Santa Barbara, CA 93111
805.683.2575 • 805.967.8199 FAX
International Transducer Corporation
www.itc-transducers.com

Model ITC-2015 *Free Flooded Ring Transducer*

The Model ITC-2015 is a small size, high power ring transducer. High quality Channelite-5800 lead zirconate titanite ceramic is used as the active material to minimize dielectric and mechanical losses. It is ideal for broadband applications that also require high efficiency.

Specifications (Nominal)

Resonance Frequency f_r	1.8 & 2.8 kHz
Depth	Unlimited
Envelope Dimensions (in.)	14.60 x 7.9H
TVR at f_r	142 & 137 dB//µPa/V@1m
Beam Width (-3dB) at f_r	70 & 120 deg
Beam Type	Toroidal
Input Power	15,000 watts

869 Ward Drive, Santa Barbara, CA 93111
805.683.2575 • 805.967.8199 FAX
International Transducer Corporation
www.itc-transducers.com

Figure 1.4: TVR characteristics of the ITC-1001 and ITC-2015 towed source transducers.

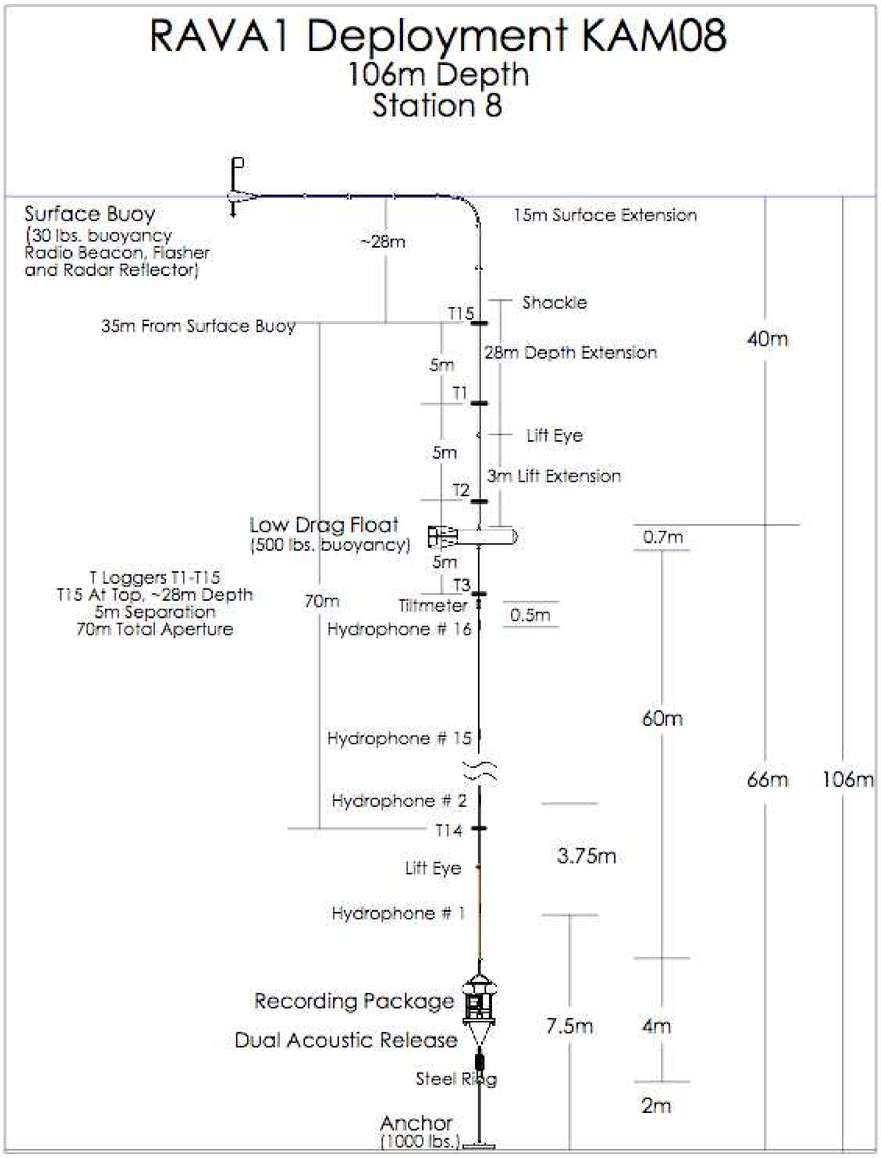

Figure 1.5: Receive array deployment.

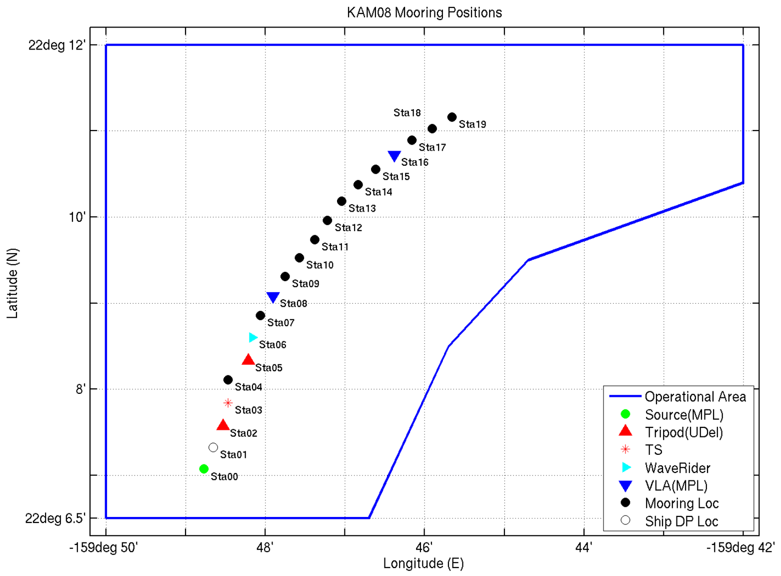

24-Jun-2008 10:20:53

Figure 1.6: Mooring deployment positions during the KAM08 in latitude and longitude. The acoustic source array was located at Sta00, while the VLAs were located at Sta08 and Sta16.

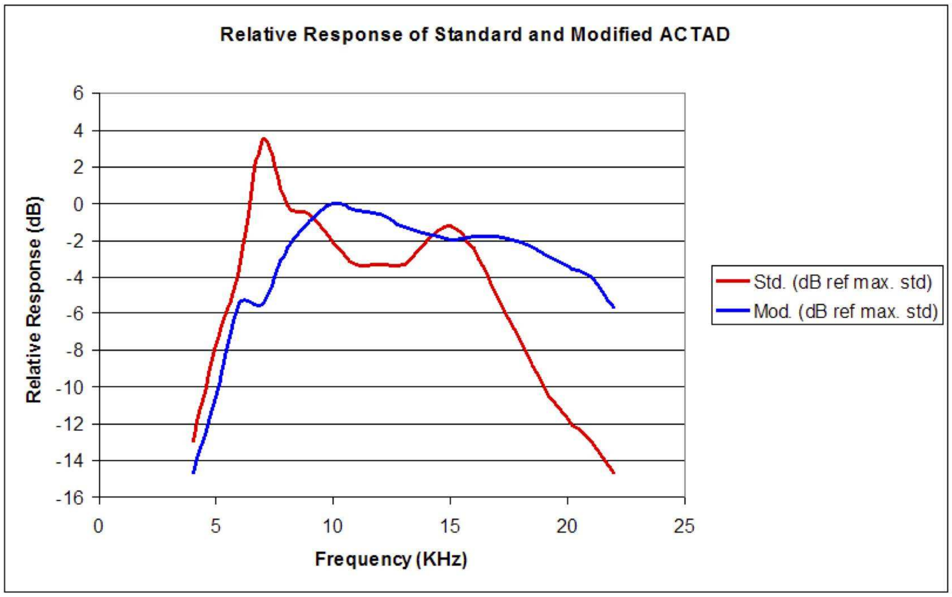

Figure 1.7: Frequency response of the compensated ITC-1007 sources in the transmit array (blue curve).

Sources and Receivers

The KAM11 experiment employed the same sources and receivers as for the KAM08 experiment, with addition of hardware that was provided by the Woods Hole Oceanographic Institution (WHOI). In particular, the following arrays were used.

1. *Autonomous Source Array.* Autonomous 4-channel transmit system configured as a vertical line array with 0.5 m transducer spacing. Transmit band $8.5-17.5$ kHz flat within 2 dB (ITC-1007) and sampling rate of 39062.5 samples/sec. The measured source level characteristics of one channel of the source array are in Figure 1.7. This system could transmit arbitrary waveforms and had a duration of approximately 6 days. Timing was provided by a rubidium clock.

2. *Ship-Based RF Coupled Source Array.* One 4-channel source array that was tied into the same disk sharing RF data link as the buoy-based systems. This source array was the primary source for the adaptive modulation and coding tests and allowed for rapid semi-autonomous adaptation. The source array used ITC-1032 transducers with a 25 to 35 kHz operating band and element spacing of 0.5 m. The array was deployed to 50 m depth. This hardware was used for adaptive modulation and coding.

3. *Autonomous Receive Arrays.* Two 24-channel autonomous receive systems. One system (WHOI-Rx1) had a 5 cm spacing ($\lambda/2$ at 15 kHz), and the other system (WHOI-Rx2) had a 20 cm spacing ($\lambda/2$ at 3.75 kHz). Sample rate was 39062.5 samples/sec. The arrays could operate autonomously for extended periods. Deployment duration 6 days.

4. *Buoy-Based Receive Array Systems.* Two 4-channel acoustic receive systems in buoys with in-situ data processing capability (Matlab), data storage, and a modest speed RF data link back to ship with range approximately 5 km. Data files were stored on board buoy for later retrieval. Hardware was set up with a sampling rate of 100 kHz per channel. The array hydrophones were

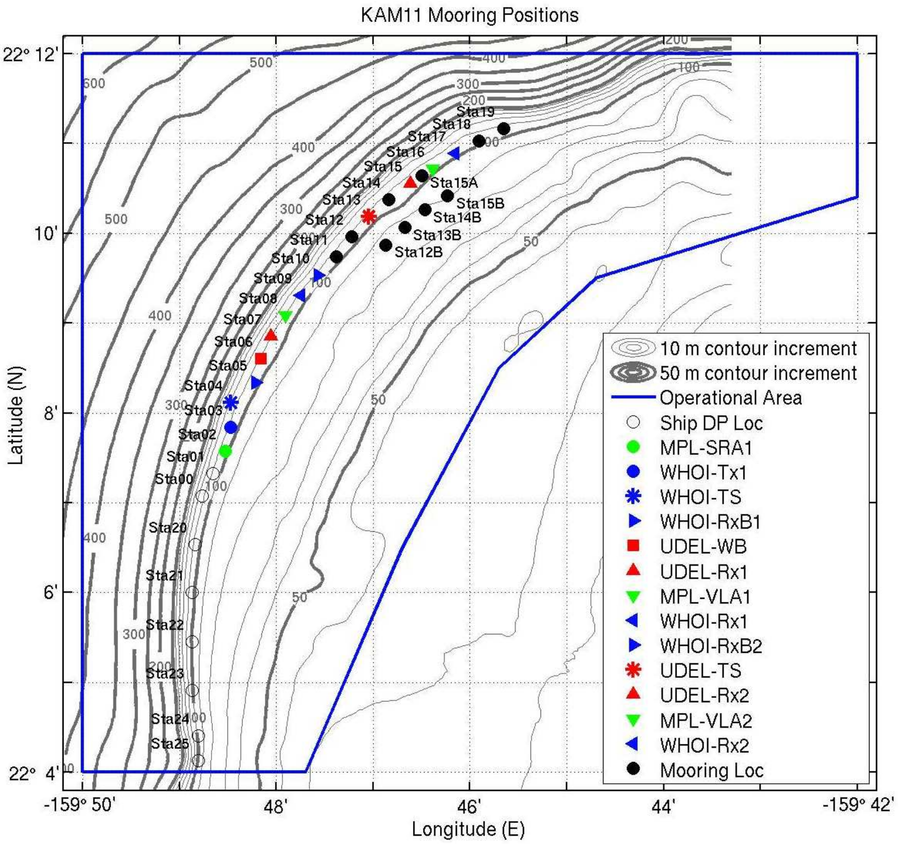

Figure 1.8: Mooring deployment positions during the KAM11 in latitude and longitude. The acoustic source array was located at Sta00, while the VLAs were located at Sta08 and Sta16.

HTI-96-MIN and the data channels were numbered surface-to-seafloor. The array was cut for an inter-element spacing of 20 cm deployed to 50 m depth. This hardware was used for adaptive modulation and coding.

As in the KAM08 experiment, a set of preapproved mooring locations were defined with PMRF for KAM11 which were at least 250 m from any PMRF instrumentation or seafloor cable. These are shown in Figure 1.8 along with the bathymetry in the operational area. Also indicated are the coordinates that bound the operational area. Due to PMRF cables in the southern part of the operational area, there were no seafloor moorings. Source tows were carried out in this region.

1.3 Major Contributions

In this section, we present the major contributions of the thesis. First, in Chapter 2 we focus on statistical characterization of shallow water acoustic communications channels. Based on the channel measurements from the KAM08 and KAM11 experiments, we obtain the channel impulse and frequency responses, and channel correlation functions in time and frequency, and from this data we determine the important channel parameters such as the channel coherence time and coherence bandwidth. The measurement data was also used to model the probability density functions that characterize the signal fading. We show that Rician fading provides a good match for the experimental data collected in the Pacific Ocean during the KAM08 and KAM11 experiments. This statistical model for the fading is used to evaluate the ergodic channel capacity and the related bandwidth efficiency for both single-input single-output (SISO) and multiple-input multiple-output (MIMO) systems in Chapter 3.

In Chapter 3 we determine the ergodic capacity of MIMO system. We first evaluate the ergodic capacity of the UWA channel with rank-1 channel matrix and no individual path dispersion. We then extend these results to more realistic channel models with full-rank matrix and individual path dispersion. We consider two different scenarios: in one the transmitter has partial channel state information (CSI) and knows the statistics of the channel, while in the other it has no CSI at all. In both scenarios, perfect CSI at the receiver is assumed.

We also determined new bounds on the achievable information rate for discrete-time Gaussian channels with ISI and independent and uniformly distributed (i.u.d.) channel input symbols drawn from finite-order modulation alphabets. Specifically, we derived new bounds on the achievable rates for sparse channels with long memory. We obtained a lower bound which can be achieved by practical receivers. An upper bound is also derived in the form of a semi-analytical solution obtained by using basic information theoretic inequalities, by a grouping of the channel taps into several clusters resulting in a newly defined single-input multiple-output (SIMO) channel. We show that the so obtained time-dispersive SIMO channel can be represented by an equivalent SISO channel with a significantly shorter channel memory. The reduced computational complexity allows the use of the Bahl-Cocke-Jelinek-Raviv (BCJR) algorithm for the newly defined channel. The proposed bounds are illustrated through several sparse channel examples and i.u.d. input symbols, showing that the upper bound significantly outperforms existing bounds. Performance of our lower bound strongly depends on the channel structure, showing best results for minimum-phase and maximum-phase systems.

In Chapter 4 we explore design aspects of adaptive modulation based on OFDM for UWA communications, and study its performance using real-time at-sea experiments. Our design criterion is to maximize the system throughput under a target average bit error rate (BER). We consider two different schemes based on the level of adaptivity: in the first scheme only the modulation levels are adjusted while the power is allocated uniformly across the sub-carriers, whereas in the second scheme, both the modulation levels and the power are adjusted adaptively. For both schemes we linearly predict the channel one travel time ahead so as to improve the performance in the presence of a long propagation delay. The effectiveness of the proposed adaptive schemes is demonstrated using computer simulations, real channel measurements recorded in shallow water during the KAM08 experiment, and real-time at-sea trials conducted during the KAM11 experiment. We note that this is the first work that presents adaptive modulation results for UWA links with real-time at-sea experiments.

In Chapter 5 we investigate a channel estimation (CE) method for improving the spectral efficiency of UWA communications. Specifically, we determine the performance of a selective decision directed (DD) CE method for UWA OFDM-based communications. The method is based on hard or soft selection of data sub-carriers that are used in the decision directed mode. Particularly, in the process of hard selection we choose those sub-carriers that have high signal-to-noise ratios (SNR), while in the process of soft selection we weight the data sub-carriers for reliable channel estimation. The latter approach is shown to be advantageous since the CSI from all data sub-carriers is exploited. We explore the trade-offs resulting from using a varying number of pilots and/or decision directed data sub-carriers in terms of the overall system throughput and BER. Experimental results are obtained using real data measurements from the Mobile Acoustic Communication Experiment 2010 (MACE10), conducted off the coast of Martha's Vineyard. Moreover, we explore the performance of the proposed DD CE method over multipath Rician fading channels, where fading is modeled as an auto-regressive (AR) random process.

In Chapter 6 concluding remarks and future work discussion are provided.

Chapter 2

Statistical Channel Characterization

In this chapter we focus on statistical characterization of shallow water acoustic communication channels based on a set of measured channel responses, obtained from signals recorded during the KAM08 and KAM11 experiments. Wideband single-carrier and multi-carrier probe signals are employed to measure the time-varying channel response, and to estimate its statistical properties that play an important role in the design of bandwidth-efficient and power-efficient communication systems. In particular, by examining the channel impulse and frequency responses, and channel correlation functions in time and frequency, important channel parameters were extracted; namely, the channel coherence time and coherence bandwidth [5]. Because the channel is not stationary, we will focus on short-term characterization (order of seconds) that will be employed later in Chapter 3 to assess the capacity of quasi-stationary channels.

This chapter is organized as follows. We begin in Section 2.1 by reviewing major properties of UWA channels, and introduce continuous and discrete-time channel models that are used in this chapter for statistical channel characterization, and in the rest of the thesis; in Section 2.2 we describe the single-carrier and multi-carrier signals used for channel probing during the experiments, and the channel estimation methods used to process experimentally recorded data; in Section 2.3 we present time and frequency-domain channel measurements, and discuss time-varying properties of the channel; in Section 2.4 we address statistical modeling of the UWA channels, and examine their time and frequency-domain correlation properties. Finally, we give our concluding remarks in the Summary section.

2.1 Channel Modeling

An underwater acoustic channel is considered as one of the most challenging media for wireless communications. It is characterized by frequency-dependent path loss, multipath propagation and low speed of sound propagation (approx. 1500 m/s). Moreover, the channel impulse response is sparse and each channel path acts as a time-varying low-pass filter with additional Doppler shifting and spreading [1]. Due to the large delay spreads ($10 - 100$ ms) an UWA channel exhibits frequency selectivity which affects wideband acoustic communications signals. Because of the extreme channel complexity, design and simulation of UWA communication systems requires accurate channel modeling. In this section we address all of these characteristics, and derive continuous and discrete-time baseband channel models.

2.1.1 Attenuation

We start this section by discussing the attenuation or path loss of general acoustic channels given by the following expression [1]

$$A(l, f) = l^k a(f)^l, \tag{2.1}$$

where l is the length of a communication link, f is the signal frequency, and k is the spreading factor which is typically between 1 and 2 (for cylindrical and spherical spreading, respectively). As for the general case of open-space communications, we note that acoustic signals suffer from a spreading loss which increases with distance. However, the path loss also depends on frequency as a result of absorption, a thermal process which transfers the energy of the acoustic pressure waves into heat. In fact, this is one of the major properties of acoustic channels which distinguishes them from the other wireless communication media in use today (e.g.

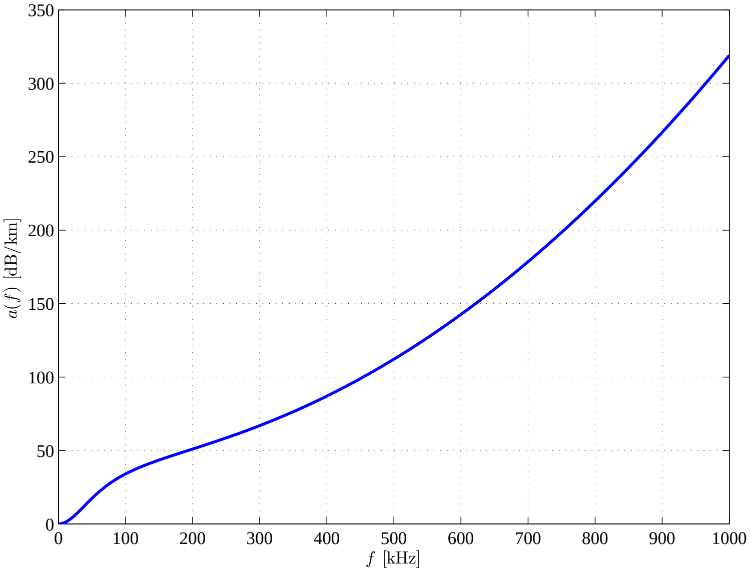

Figure 2.1: Absorption coefficient as a function of frequency.

mobile terrestrial radio and satellite channels). The absorption coefficient $a(f)$ is an increasing function of frequency which is modeled by an empirical formula [6]

$$10 \log a(f) = 0.11 \frac{f^2}{1+f^2} + 44 \frac{f^2}{4100+f^2} + 2.75 \cdot 10^{-4} f^2 + 0.003, \tag{2.2}$$

for frequencies higher than a few hundred Hz, and by the expression

$$10 \log a(f) = 0.11 \frac{f^2}{1+f^2} + 0.011 f^2 + 0.002, \tag{2.3}$$

for low frequencies. The absorption coefficient (2.2) is illustrated in the Figure 2.1 in dB/km for f in kHz.

2.1.2 Ambient Noise

Another characteristic of underwater channels is the ocean ambient noise which is typically modeled as a non-white Gaussian process, and given as a linear combination of four independent noise sources: turbulence, shipping, waves and thermal noise [7]. The power spectral density (PSD) of the four noise components in dB re μ Pa per Hz is given by the following empirical formulas [8]

$$\begin{aligned}10\log N_t(f) &= 17-30\log f,\\ 10\log N_s(f) &= 40+20(s-0.5)+26\log f-60\log(f+0.03),\\ 10\log N_w(f) &= 50+7.5w^{1/2}+20\log f-40\log(f+0.4),\\ 10\log N_{th}(f) &= -15+20\log f\end{aligned}\tag{2.4}$$

where f is in kHz. The PSD of the ambient noise is given as

$$N(f)=N_t(f)+N_s(f)+N_w(f)+N_{th}(f).\tag{2.5}$$

The turbulence and distant shipping noise are dominant at very low frequencies, $f < 100$ Hz, where the latter is modeled by the shipping activity factor $s \in [0,1]$; wind-generated waves or ocean surface waves, where w is the wind speed in m/s, induce surface resulting in the most dominant noise source in the frequency region $0.1-100$ kHz which represents the operational region for most of the UWA communication systems; finally, the thermal noise has a significant impact only at high frequencies, $f > 100$ kHz. Figure 2.2 illustrates the PSD of the ambient noise $N(f)$ for various values of the wind speed w, and the log-scale linear approximation given by the following formula:

$$10\log N(f) \approx n_0-18\log f,\tag{2.6}$$

where the level $n_0(=50$ dB) is a site-specific constant that is subject to adjustment for a particular UWA channel of interest.

2.1.3 Signal-to-noise Ratio

Using the expressions (2.1) and (2.6), the SNR for a small bandwidth Δf around a frequency f can be defined as

$$SNR(l,f)=\frac{S(f)}{A(l,f)N(f)},\tag{2.7}$$

where $S(f)$ is the PSD of the transmitted signal. This frequency and distance dependence of SNR is shown in Figure 2.3. Note that the available bandwidth of

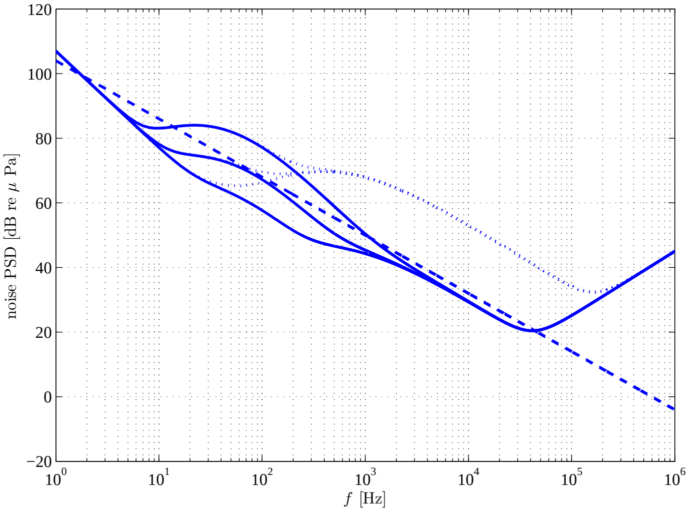

Figure 2.2: Power spectral density of the ambient noise. The solid and dotted lines correspond to wind speed of 0 and 10 m/s, respectively, for shipping activity 0, 0.5 and 1 (from bottom to top). The dashed line corresponds to the noise PSD approximation from Eq. (2.6).

the channel is centered at low frequencies, and severely limited for higher distances. Also, note that the effective acoustic bandwidth B is on the order of its center frequency f_c, which makes acoustic communication systems inherently wideband. This observation will have a significant impact on the receiver design, since the narrowband assumption ($B << f_c$) (which is used to ease the design of radio communication systems) is not valid anymore. The wideband nature of UWA systems is of particular importance for multi-channel (array) processing [9], time synchronization for mobile systems [10], and multi-carrier systems [11].

2.1.4 Propagation Delay

Sound waves propagate in water at a very low speed of 1500 m/s, which is $4-5$ times higher than the speed of sound in dry air at 68 °F (20 °C), and $2 \cdot 10^5$ lower than the speed of electromagnetic waves in vacuum. The sound speed depends on pressure (hence depth), temperature (a change of 4 m/s per 1 °C), and salinity (a change of 1 m/s per 1 ppt). A typical sound speed profile is shown in Figure 2.4, where we note that the speed reaches its minimum at the depth of

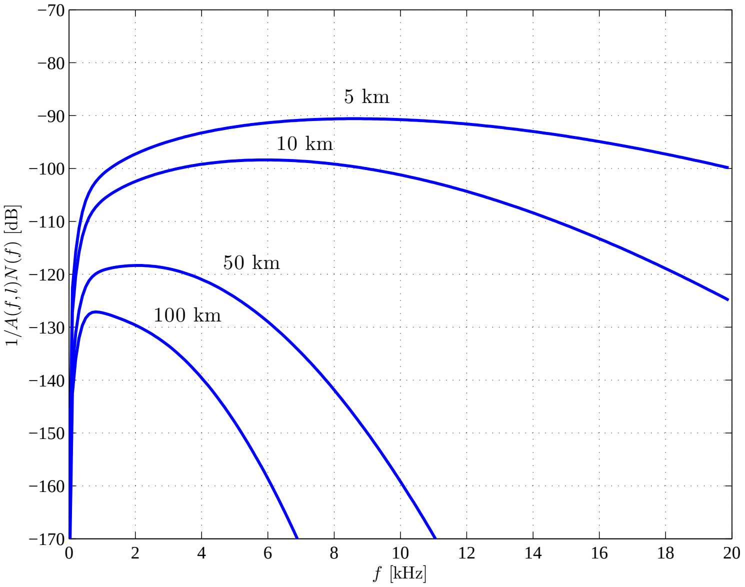

Figure 2.3: Signal-to-noise ratio in acoustic channels as the function of frequency and distance given in (2.7).

several hundred meters, and then increases again with increasing depth.

The low propagation speed puts significant constraints on the design of adaptive UWA systems that utilize a feedback link from the receiver to the transmitter. For example, mid-range UWA systems (with a communication distance of several kilometers), experience a propagation delay on the order of several seconds; if the channel coherence time is of the same order as the propagation delay, the CSI conveyed back through the feedback channel is outdated and, therefore, not reliable for current processing at the transmitter. In the case of radio communication systems, the issue of propagation delay is neglected due to a very high propagation speed of electromagnetic waves (approximately $3 \cdot 10^8$ m/s in vacuum).

2.1.5 Doppler Effects

UWA communication systems are subject to motion even without intentional moving of one or both ends of a link (e.g. autonomous underwater vehicles (AUVs) which move at speeds on the order of few m/s). In particular,

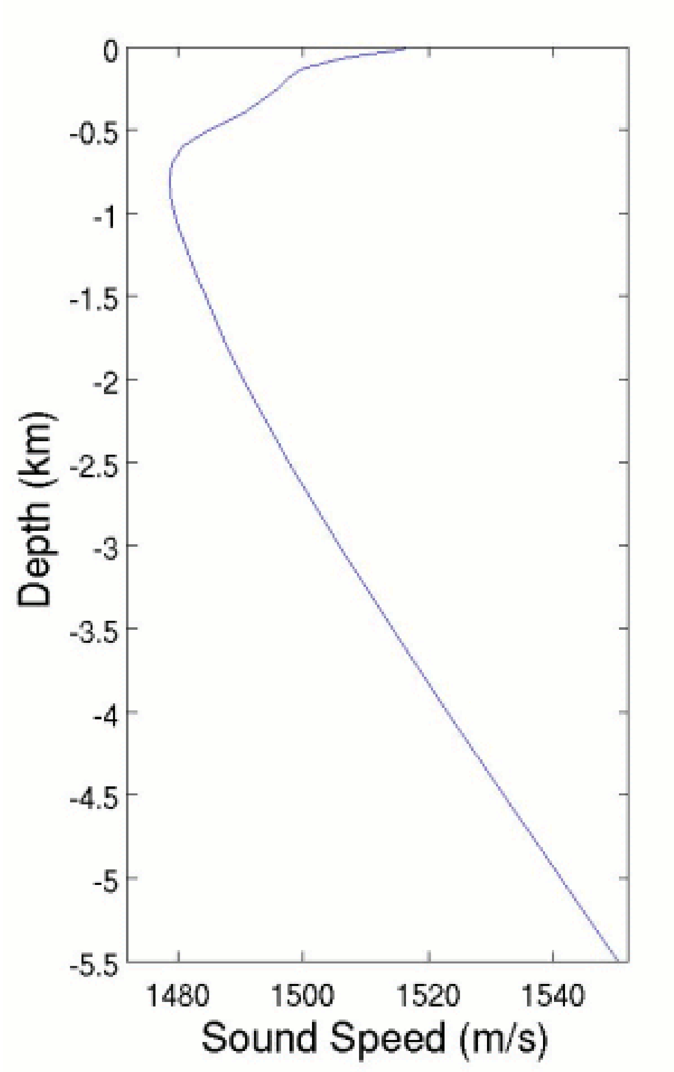

Figure 2.4: Sound speed profile.

underwater instruments are subject to drifting with waves, currents and tides; In other words, there is always some motion present in the system, and the resulting motion-induced distortion has to be taken into account for the receiver design, with particular emphasis to synchronization algorithms.

Let us consider the following scenario, where the transmitter and the receiver move relative to each other with constant velocity v, resulting in the decrease of the distance [1]. This will result in a different propagation delay of the leading and trailing edge of the signal as illustrated in Figure 2.5. We note that a transmitted pulse of duration T is observed at the receiver as having the duration

$$T' = T(1 + a), \tag{2.8}$$

where $a = v/c$, and c is the sound speed. Consequently, in the frequency domain, the operational bandwidth B is observed as $B/(1 + a)$, which is a well-known motion induced distortion, called Doppler spreading. As we will see later in the thesis, the received signal (given in a baseband representation with respect to a central frequency of the transmitted signal) is additionally effected by a motion-induced distortion called Doppler shifting, which results in non-uniform shifting of the signal spectrum.

The impact of the Doppler effects on signal detection depends on the value of the Doppler scaling factor a. For example, in the case of mobile radio systems, at the speed of 160 km/h (100 mph), the Doppler scaling factor has value of $1.5 \cdot 10^{-7}$. Such a small value can be ignored, since the resulting Doppler spreading has diminishing effect on signal detection. In contrast, a stationary UWA system can experience unintentional motion at the speed of 0.5 m/s (1 knot), which results in $a = 3 \cdot 10^{-4}$. Additionally, a mobile UWA system with an AUV moving at the speed of several m/s results in Doppler scaling factor on the order of 10^{-3} or greater, a value which cannot be ignored.

Since motion-induced Doppler effects are not diminishing, they arise as another major challenge of the UWA channel which distinguish it from the mobile radio channel. Therefore, more attention should be given in the design of synchronization algorithms. For example, in the case of single-carrier systems, an explicit synchronization scheme was proposed and demonstrated successful performance

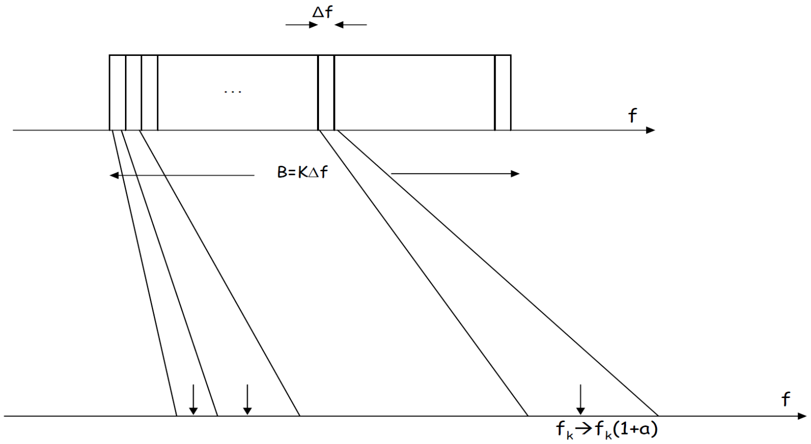

Figure 2.5: Motion induced signal distortion.

in [12]. In multi-carrier systems, Doppler effects result in a particularly severe distortion because of the inherently wideband nature of UWA systems. In particular, Doppler spreading is non-uniform across the bandwidth, forcing the design of synchronization algorithms to focus on each sub-carrier individually [11].

2.1.6 Multipath Propagation

Underwater acoustic channels are subject to multipath propagation where different arrivals experienced at the receiver correspond to multiple reflections from the bottom and the surface (typical for shallow water channels), or refraction of the sound in the water due to speed variations with depth (typical for deep water channels). The path gain of each arrival depends on the number of reflections from the bottom and surface, and their reflection properties, while the path arrival time is driven by the geometry of the channel. The number of significant channel paths is limited, since propagation paths with multiple reflections over a long communication distance attenuate the transmitted signal significantly, such that it becomes undetectable at the receiver. The propagation paths are subject to time-variations due to changing conditions in the channel (e.g. random surface motion, water fluctuations due to currents and tides, temperature variations, etc.).

We model the effect of multipath propagation as a linear time-varying system, which give us the following representation of the channel impulse response

$$c(\tau, t) = \sum_{p=0}^{P-1} c_p(t)\delta(\tau - \tau_p(t)), \tag{2.9}$$

where P is the number of distinct propagation paths, τ is the delay variable and t is the time at which the channel is observed. The coefficient $c_p(t)$ represents the real-valued gain of the p-th path, and $\tau_p(t)$ represents the corresponding delay. Assuming a high bandwidth (sufficient resolution in the delay variable τ), the set of coefficients $c_0(t), ..., c_{P-1}(t)$ offers a good representation of the actual propagation paths between the transmitter and the r-th receiver. We should emphasize again that the path loss (2.1) depends on the signal frequency, which makes each path acting as a low-pass filter. However, under the wideband assumption (earlier discussed to be valid for UWA communications), the path dispersion is significantly smaller than the multipath spread of the channel and, hence, it can be neglected.

The impulse response (2.9) links the transmitted signal $s(t)$ and the received signal $r(t)$ as

$$r(t) = \sum_{p=0}^{P-1} h_p(t)s(t - \tau_p(t)) + n(t), \tag{2.10}$$

where $n(t)$ represents additive colored Gaussian noise, as given in (2.5). We also define the equivalent baseband signals $u(t)$ and $y(t)$ with respect to a carrier frequency f_c, such that

$$s(t) = Re\left\{u(t)e^{j2\pi f_c t}\right\} \tag{2.11}$$

$$r(t) = Re\left\{y(t)e^{j2\pi f_c t}\right\}. \tag{2.12}$$

We then obtain

$$y(t) = \sum_{p=0}^{P-1} h_p(t)u(t - \tau_p(t)) + w(t), \tag{2.13}$$

where

$$h_p(t) = c_p(t)e^{-j2\pi f_c \tau_p(t)}, \tag{2.14}$$

and $w(t)$ is the equivalent baseband noise. Expression (2.13) implies the equivalent baseband channel response

$$h(\tau, t) = \sum_{p=0}^{P-1} h_p(t)\delta(\tau - \tau_p(t)). \tag{2.15}$$

From this continuous-time model we now derive a discrete-time baseband channel model which is a preferable representation in most practical applications.

2.1.7 Discrete-time Baseband Channel Model

Following an approach from [13], let us first assume that the transmitted signal $s(t)$ is bandlimited to B. The baseband equivalent $u(t)$ is then bandlimited to $B/2$, and by applying the sampling theorem [5] it can written as

$$u(t) = \sum_{m} u(m/B)\mathrm{sinc}(Bt - m), \tag{2.16}$$

where

$$\mathrm{sinc}(t) = \frac{\sin(\pi t)}{\pi t}. \tag{2.17}$$

Then, using (2.15), the received baseband signal $y(t)$ is given by

$$y(t) = \sum_{m} u(m/B) \sum_{p=0}^{P-1} h_p(t)\mathrm{sinc}(Bt - B\tau_p(n/B) - m) + w(t). \tag{2.18}$$

If we sample the received signal at time n/B, the following expression is obtained

$$y(n/B) = \sum_{m} u(m/B) \sum_{p=0}^{P-1} h_p(t)\mathrm{sinc}(n - m - B\tau_p(n/B)) + w(n/B). \tag{2.19}$$

By letting $l = n - m$, we obtain the equivalent discrete-time baseband channel model

$$y_n = \sum_{l} h_{l,n} u_{n-l} + w_n, \tag{2.20}$$

where

$$h_{l,n} = \sum_{p=0}^{P-1} h_p(n/B)\mathrm{sinc}(l - B\tau_p(n/B)), \tag{2.21}$$

$y_n = y(n/B)$, and $u_{n-l} = u((n - l)/B)$. The channel tap gains, $\{h_{m_l,n}\}$, where $m_l = [B\tau_p(n/B)]$ do not necessarily represent the actual physical propagation paths. In particular, note in (2.21) that each tap gain $h_{l,n}$ can contain in itself the contributions of *all* the physical paths; the exact relationship depends on the system bandwidth [1]. Since the UWA channel impulse response is typically sparse, these contributions are small in a wideband system, and the dominant coefficients of the uniformly spaced equivalent model (2.20) can be roughly associated with the physical propagation paths. Due to the assumption that the input signal is bandlimited, the discrete-time response (2.20) is of infinite length. However, in practice, we will limit this response to a finite number of coefficients $L = \lfloor T_m/B \rfloor + 1$, where $T_m = \tau_{P-1} - \tau_0$ is the multipath spread of the channel (2.9).

2.2 Channel Probe Signals

A shallow water communication channel is characterized by rapid phase variations, severe frequency-selectivity and long delay spread. These facts influence the proper design of channel probe signals which is a prerequisite for reliable statistical characterization of UWA channels. We designed channel probes in two forms: single-carrier (SC) and multi-carrier (MC) probes. In the case of the MC probes, we designed OFDM and OFDM-based signals where some of the sub-carriers are *nulled*, i.e. not modulated. This was done in order to reduce inter-carrier interference (ICI) effects which have a severe impact on statistical channel characterization, and result from Doppler spreading and shifting that are inherently present in UWA channels, and .

2.2.1 Single-carrier Probe (for KAM08)

In order to allow for computationally efficient coherent detection, SC probes are kept short. In particular, a 28-element long Turyn sequence [14] was chosen for channel probing. We define the Turyn sequence as

$$x_n = [x_0 x_1 \dots x_{N-1}], \tag{2.22}$$

where $N = 28$. Its auto-correlation function is given by the following expression

$$\phi_m = \frac{1}{N - |m|} \sum_{n=0}^{N-|m|-1} x_n x_{n+m}. \tag{2.23}$$

This function is shown in Figure 2.6. We observe good auto-correlation properties of the probe sequence, since the values of the correlation function for non-zero lags ($|m| > 0$) are very low when compared to ϕ_0. For the purpose of channel estimation, an ideal probe sequence would have the Dirac impulse as the auto-correlation function, i.e. $\phi_0 = 1$, while $\phi_m = 0$, $|m| > 0$ (hence, PSD should be flat). For example, an additive white Gaussian noise (AWGN) sequence of infinite length complies to the properties of the ideal probing sequence. We will address this issue later in this section.

For channel probing during the KAM08 experiment, SC probe signals were designed with the total bandwidth $B = 7812$ Hz, centered around $f_c = 16$ kHz. Square-root raised-cosine pulse shaping was applied with the roll-off factor $\alpha = 0.25$ [5]. For the chip rate of $1/T_c = 6250$ bps, the duration of the probing signal is $T = NT_c = 4.48$ ms. For such probe design, channel estimation is reliable, since the pseudo-noise properties of the modulated Turyn sequence result in a roughly flat spectrum within the operational bandwidth of the channel probe. Transmission of each probe signal is followed by a guard time interval (i.e. silence period) $T_g = 150$ ms. Therefore, we define the transmitted SC probe signal as

$$s(t) = \begin{cases} \mathrm{Re}\left\{ \sum\limits_{n=0}^{N-1} x_n g(t - nT_c) e^{j2\pi f_c t} \right\} & , 0 \le t < T \\ 0 & , T \le t < T', \end{cases} \tag{2.24}$$

where $T' = T + T_g$, and $g(t)$ is the raised-cosine pulse. Figure 2.7 illustrates the PSD of the transmitted SC probe signal. We note that the signal PSD is not perfectly flat over the operational bandwidth as a result of the finite length of the pseudo-noise sequence (2.22) (or alternatively, as the result of the imperfect auto-correlation properties of the Turyn sequence, as observed in Figure 2.6). The channel probe signal was transmitted during a 57 s long period of time, with 366 repeated transmissions. This is illustrated in Figure 2.8. The sampling frequency of the digitally generated probe signal is $f_{s,Tx} = 100$ kHz, while the receiver-end sampling rate is $f_{s,Rx} = 50$ kHz. Coherent detection at the receiver is performed via matched filtering to the transmitted probe signal, whose output gives an estimate of the channel impulse response. This channel estimation method is addressed in the following sub-section.

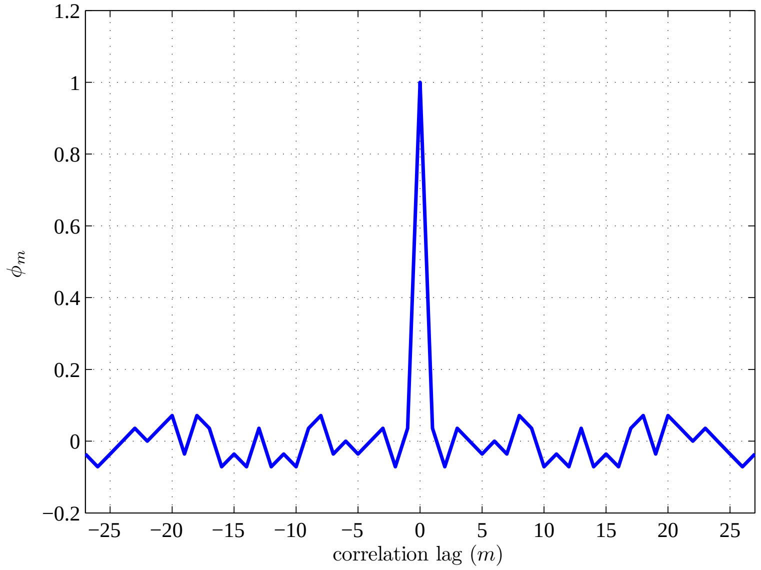

Figure 2.6: Auto-correlation function of the 28-element Turyn sequence.

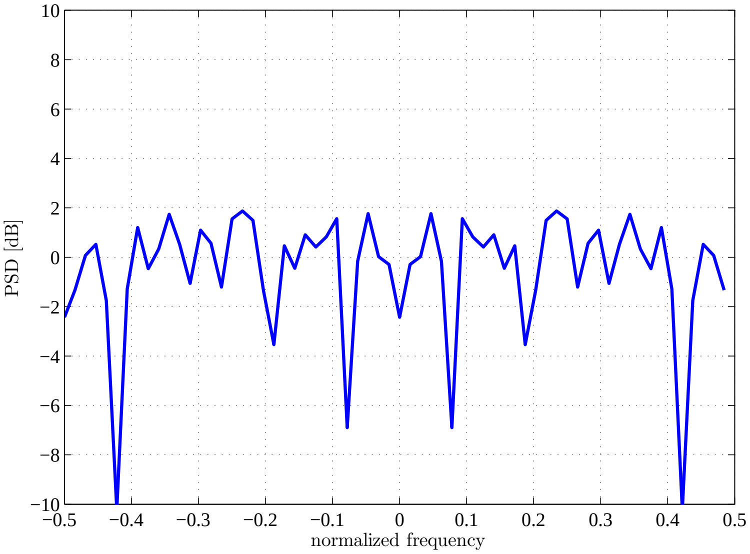

Figure 2.7: Power spectral density of the Turyn sequence.

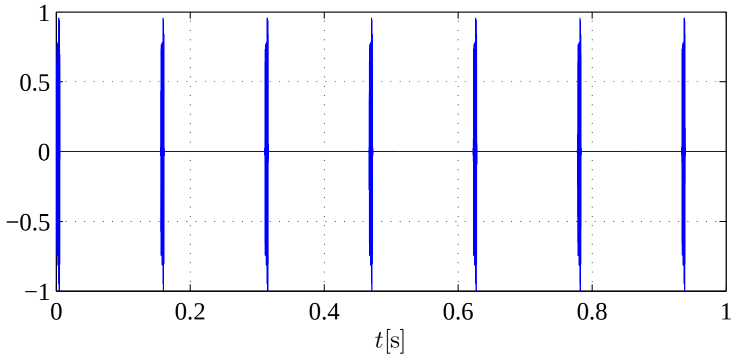

Figure 2.8: Repeated transmissions of the single-carrier probe.

2.2.2 Channel Estimation using Single-carrier Probe

We discuss now how the auto-correlation properties of the transmitted Turyn sequence (2.22) can be exploited for channel estimation.

Let us first assume that we transmit a probe signal $u(t)$ which is designed as an infinite-length Gaussian process with zero-mean and power spectral density normalized to unity. If we assume that the probe signal is transmitted over a time-invariant channel, we define the baseband received signal as

$$y(t) = \int h(\tau_0)u(t-\tau_0)d\tau_0 + w(t), \tag{2.25}$$

where $h(\tau)$ is the channel impulse response, τ_0 is the delay variable, and $w(t)$ represents a zero-mean AWGN process with unit variance. Assuming that the transmitted probe sequence is perfectly known at the receiver, we can multiply both sides of Eq. (2.25) by $u(t-\tau)$, where τ is another delay variable, and take the expectation over the transmitted probe such that

$$\begin{aligned} E\{u(t-\tau)y(t)\} &= E\left\{\int h(\tau_0)u(t-\tau)u(t-\tau_0)d\tau_0\right\} + E\{u(t-\tau)w(t)\} \\ &= \int h(\tau_0)E\{u(t-\tau)u(t-\tau_0)\}d\tau_0 \\ &= \int h(\tau_0)\phi(\tau_0-\tau)d\tau_0, \end{aligned} \tag{2.26}$$

where it is assumed that the transmitted signal and the channel noise are mutually independent, $E\{u(t)w(t)\} = 0$. Since the PSD of the random probe is flat, the auto-correlation function $\phi(\tau)$ is given as the Dirac impulse. Therefore, the estimate of the channel impulse response is given as the cross-correlation between the transmitted probe and the received signal

$$E\{u(t-\tau)y(t)\} \;=\; \int h(\tau_0)\delta(\tau_0-\tau)d\tau_0 = h(\tau). \tag{2.27}$$

Unfortunately, this idealized estimation method is not applicable in practice, since the designed probes are deterministic signals of finite duration, non-ideal auto-correlation properties (as it was shown in Figure. 2.6), and finite time resolution which is driven by the sampling frequencies at both sides of a communication link. For the purposes of practical implementation, we can estimate the channel impulse response based on the estimate of the cross-correlation function between the transmitted and received signal (2.27), which is given as

$$\hat{h}(m/f_s) = \frac{1}{Tf_s}\sum_n u((n-m)/f_s)y(n/f_s). \tag{2.28}$$

Since the UWA channels are inherently time-varying, it imposes limitations on the length of the probe sequence for the given system bandwidth B. This was the major reason to design the short probe signal (2.24) of duration $T = 4.48$ ms only. We will see later in this chapter that bandwidth limitations of the transmitter and receiver put significant constraints on the time-resolution of the channel estimate (2.28) and, therefore, on the number of resolvable propagation paths [5].

2.2.3 Multi-carrier Probe (for KAM08)

In the past two decades, systems with multi-carrier modulation have been considered as an alternative to wideband systems with single-carrier modulation for communication over channels with frequency-selective distortion [5]. By using rectangular pulse shaping in time, multi-carrier modulation and detection are efficiently implemented in the form of OFDM using the fast Fourier transform (FFT).

The design of our MC channel probe is based on modulating every 8-th sub-carrier of the OFDM signal by a pseudo-noise sequence, and leaving the remaining

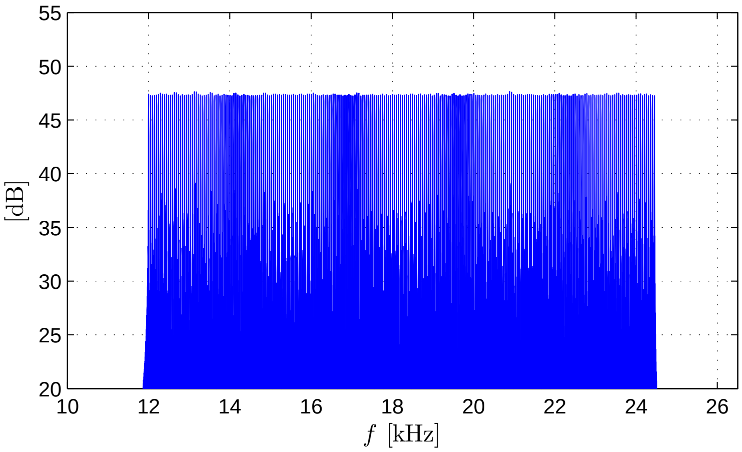

Figure 2.9: Spectrum of the multi-carrier probe.

sub-carriers empty. In this manner, the inter-carrier interference is sufficiently suppressed since it can severely degrade the performance of frequency-domain channel estimation. The operational bandwidth is $B = 12.5$ kHz, and the total number of sub-carriers is $K = 2048$ with frequency spacing of $\Delta f = B/K = 6$ Hz. The frequency of the first sub-carrier is $f_0 = 12$ kHz, while the central frequency is $f_c = f_0 + B/2 = 18.25$ kHz. The signal duration is $T = 160$ ms, with each transmission followed by the guard interval $T_g = 100$ ms. The corresponding continuous-time passband zero-padded (ZP) OFDM-based signal can be represented as

$$s(t) = \begin{cases} \mathrm{Re}\left\{ \sum_{k=0}^{K-1} x_k e^{j2\pi(f_0 + k\Delta f)t} \right\} & , 0 \leq t < T \\ 0 & , T \leq t < T', \end{cases} \tag{2.29}$$

where $T' = T + T_g$, and $\{x_k\}$, $k = 0, 7, \ldots, K-1$ are the symbols of a pseudo-noise sequence which are used as pilots.

Figure 2.9 illustrates the spectrum of the transmitted MC probe. Similarly to the case of the SC probe, the overall probing duration is 57 s with 216 transmission blocks as is partially shown in Figure 2.10. The sampling frequency of the digitally generated probe signal is $f_{s,Tx} = 100$ kHz, while the receiver-end sampling rate is $f_{s,Rx} = 50$ kHz.

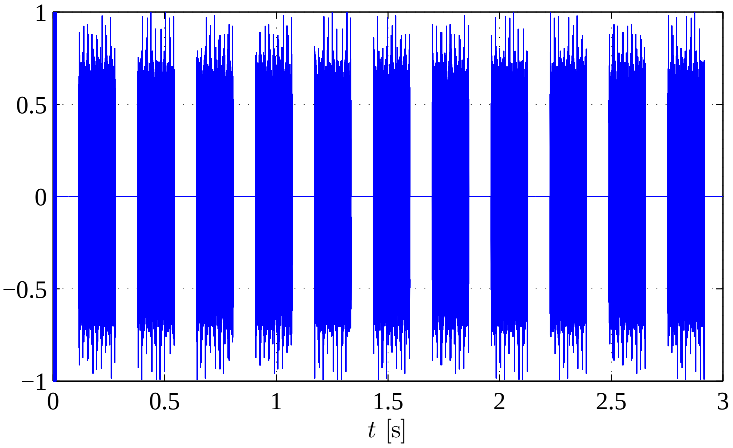

Figure 2.10: Repeated transmissions of the multi-carrier probe.

2.2.4 Channel Estimation using Multi-carrier Probe

Since every 8-th sub-carrier is modulated, the impact of ICI is significantly reduced and any residual distortion is considered as an additional noise. Equivalently, we assume that the channel is constant over the signal duration T. Then, the valid model of the received signal at the k-th sub-carrier is given as

$$Y_k = H_k x_k + W_k, \tag{2.30}$$

where $k = 0, 7, \ldots, K-1$,

$$H_k = \sum_l h_l e^{-j2\pi(k\Delta f - B/2)l/f_s}, \tag{2.31}$$

and W_k is the noise term which includes the residual ICI. At the nulled sub-carriers, only the information about the channel noise and residual ICI is available, i.e. $Y_k = W_k,\ k \neq 0, 7, \ldots, K-1$. Since the pilot symbols are known at the receiver, channel estimation in multi-carrier systems is conducted in the frequency domain by multiplying the received signal with the normalized conjugate of the pilot symbols, as given in the following expression

$$\begin{aligned} \widehat{H}_k &= \frac{x_k^*}{|x_k|^2} Y_k \\ &= H_k + \frac{x_k^*}{|x_k|^2} W_k. \end{aligned} \tag{2.32}$$

The time domain channel estimate is obtained by applying the inverse Fourier transform to the channel estimate (2.32)

$$\hat{h}_l = \frac{1}{K} \sum_{k=0}^{K-1} \widehat{H}_k e^{j2\pi(k\Delta f - B/2)l/f_s}. \tag{2.33}$$

Since the channel estimates (2.32) are available only at the modulated sub-carriers, the large frequency separation between the neighboring estimates ($7 \cdot \Delta f = 42$ Hz) will have an impact on the achievable time resolution of the channel estimate (2.33) and, therefore, on the number of resolvable channel paths [1].

2.2.5 OFDM Probe Signals (for KAM11)

In the case of the KAM11 experiment, the channel probe was designed in the form of an OFDM signal. In particular, the OFDM probe is based on modulating *every* sub-carrier of the OFDM signal by a pseudo-noise sequence, as opposed to the case of the MC probes (2.29). The OFDM signal bandwidth is $B = 10$ kHz, and the total number of sub-carriers is only $K = 128$. This setup results in frequency spacing of $\Delta f = B/K = 76.3$ Hz, which is considered sufficient to assume a relatively small ICI for stationary UWA communications. The frequency of the first sub-carrier is $f_0 = 8$ kHz, while the central frequency is $f_c = f_0 + B/2 = 15$ kHz. The signal duration is $T = 13.1$ ms, with each transmission followed by the guard interval $T_g = 60$ ms. Similar to the MC probes in the KAM08 experiment, we apply rectangular pulse shaping in time of the channel probe, and OFDM modulation and detection are efficiently implemented using the FFT. The corresponding continuous-time passband zero-padded (ZP) OFDM signal can be defined as the MC probe in (2.29) where all sub-carriers are modulated. The overall probe duration is 9.36 s with 128 transmission blocks. The sampling frequency of the digitally generated probe signal is $f_{s,Tx} = 39$ kHz, while the receiver-end sampling rate is $f_{s,Rx} = 39$ kHz.

Channel estimation is conducted following the same approach as in the previous subsection.

2.3 Channel Measurements

In this section we discuss the experimental results from the KAM08 and KAM11 experiments obtained by transmitting the channel probes described in the previous section. These measurements will be used later in Section 2.4 for statistical channel characterization that has a major impact on the design of bandwidth and power-efficient UWA communication systems. We start this section by presenting recorded data from the KAM08 experiment for the stationary communication scenario, where both the transmitter and the receiver are assumed to be fixed. In particular, we present time and frequency-domain channel measurements, and discuss time-varying properties of the channel. We conduct a similar study for the mobile scenario, where the source is towed at the speed of 1.5 m/s (3 knots), while the receiver remains fixed. Finally, the experimental results from the KAM11 experiment are presented for stationary UWA communications.

2.3.1 KAM08 Experiment: Single-carrier Probe (Fixed Source)

The analyzed data set from the KAM08 experiment is for the transmissions from the aperture array source 1 (AAS1) (4 km of communication distance) recorded on June 22, 2008 at 08 am coordinated universal time (UTC). In particular, the SC probe signal was transmitted during the time slot $40 - 41$ min. The transmitter was implemented as a 8-element acoustic source array which was provided by the Marine Physical Laboratory (MPL) of the Scripps Institution of Oceanography. Transmission is done from the fourth transducer from the bottom, at 49.5 m depth. The receiver was implemented as a MPL vertical line array (VLA) structure having 16 hydrophones with inter-element spacing of 3.75 m, where element 1 is closest to the seafloor. Data is gathered from the fourth element at the receiver side (87.25 m depth). Element 1 is approximately 7.5 m off the sea floor. The sampling rate at the receiver side is $f_{s,Rx} = 50$ kHz. The channel geometry is given in Figure 2.11

If we recall from (2.11) and (2.12) the definition of the equivalent baseband

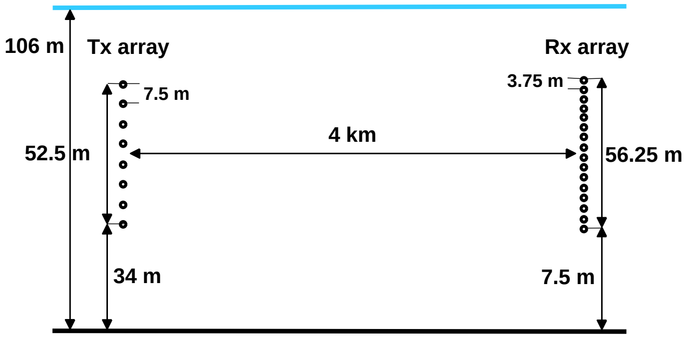

Figure 2.11: The geometry of the KAM08 experiment.

signals $u(t)$ and $y(t)$, respectively, the channel impulse response estimate (2.28), that corresponds to the i-th transmission of the channel probe (2.24), is written as

$$\hat{h}_{l,i} = \frac{1}{\Delta L} \sum_{n=0}^{\Delta L-1} u_{n+l} y_{i\Delta L+n}, \tag{2.34}$$

where $l = 0, \ldots, L$, L is the multipath delay spread, and ΔL is the discrete-time repetition interval of the transmitted probe sequence (e.g. for the single-carrier probe signal (2.24) $\Delta L = T' f_{s,Tx} = 15561$ samples).

Figure 2.12 shows the estimates of the channel impulse response (magnitude only) which are obtained by cross-correlating the baseband received and transmitted signals as in (2.34). Specifically, in the top two rows of the figure are the ensembles of 12 consecutive estimates of the channel responses. The third figure from the top in Figure 2.12 is obtained by computing the time averages given by

$$\hat{h}_l(t_\nu^*) = \frac{1}{12} \sum_{i=0}^{11} |\hat{h}_{l,12\nu\Delta L+i}|, \tag{2.35}$$

where $l = 0, \ldots, L$, and t_ν^* is the ν-th measurement interval of 12 consecutive transmissions of the probe signal (i.e., t_ν^* is discrete-time interval from $12(\nu-1)\Delta L$ to $12\nu\Delta L-1$). We emphasize here that no significant Doppler spreading is observed for the observed data set, since the observed Doppler scaling factor is $|a| < 10^{-4}$. The different peaks in the channel estimates can be associated with multiple surface and bottom reflections calculated from the geometry of the experiment. Note

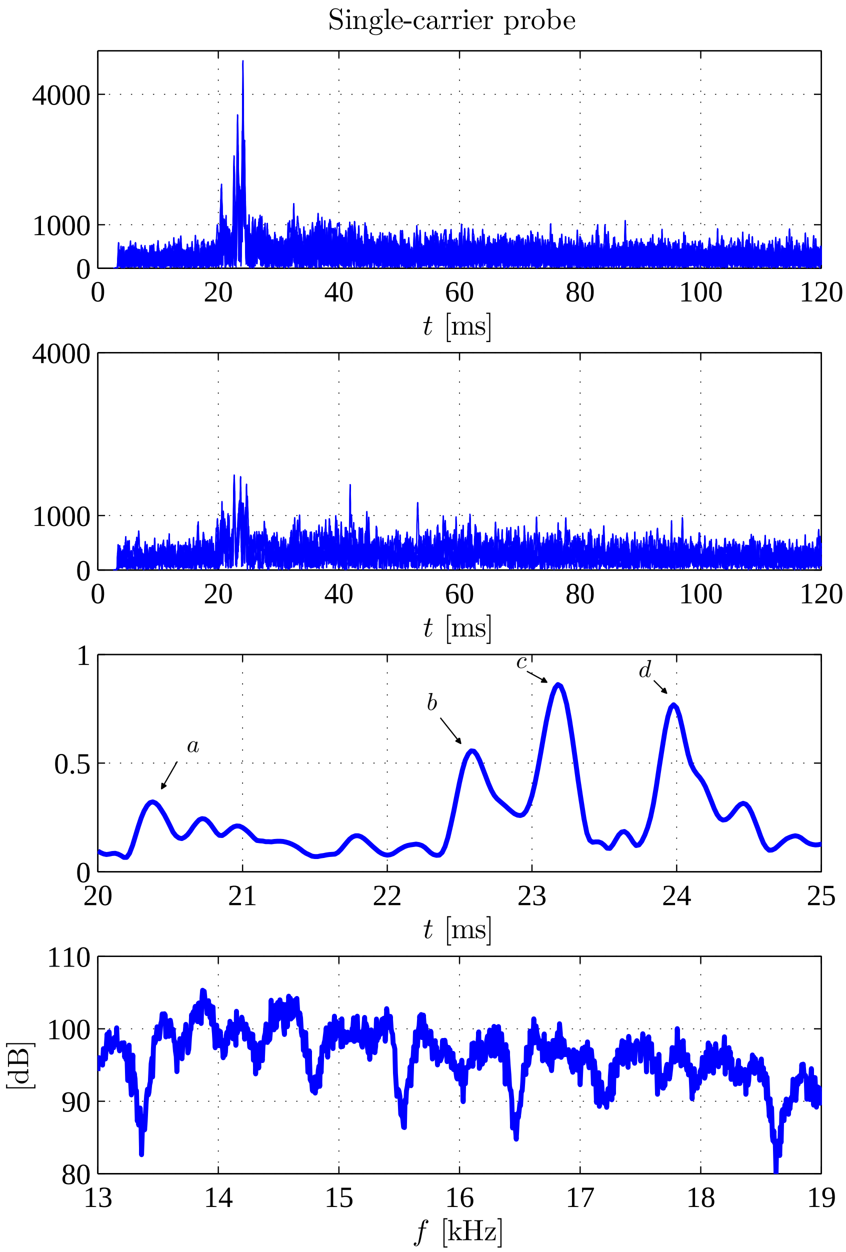

Figure 2.12: Channel estimates from the KAM08 experiment: shown in the top two rows are the ensembles of 12 consecutive channel responses in time; shown below are the top row ensemble averages in the time and frequency domains.

how these significant paths vary in time due to the changing conditions in the channel over the one minute observation interval. This fact necessitates short-term statistical characterization of the channel fading, since the energy content of the significant paths can dramatically change during longer observation intervals. The next section will focus on this problem. We note that the multipath spread T_m is on the order of 100 ms, which results in the coherence bandwidth $B_c \approx 1/T_m$ of 10 Hz [5]. The large multipath spread is the result of the appearance of occasional and unstable arrivals in the estimates of the individual channel realizations for the observation interval between 80 and 120 ms.

Each estimate of the channel frequency response is obtained as the FFT of the estimated channel impulse response. Because the FFT is an efficient algorithm for computation of discrete Fourier transform (DFT), a finite number of frequency points are obtained as

$$\widehat{H}(f_k, i) = \widehat{H}_{k,i} = \sum_{l=0}^{L} \hat{h}_{l,i} e^{-j2\pi(k\Delta f - B/2)l/f_s}, \tag{2.36}$$

where K is the number of frequency points. Therefore, the ensemble average in the frequency domain, given at the bottom of Figure 2.12, is obtained as

$$\widehat{H}_k(t_\nu^*) = \frac{1}{12} \sum_{i=0}^{11} |\widehat{H}_{k,12\nu\Delta L+i}|. \tag{2.37}$$

If f_s denotes the sampling frequency ($f_s = 50$ kHz), $\{H(f_k)\}$ are samples of the frequency response at frequencies $f_k - B/2$, where $k = 0, \ldots, K-1$. We emphasize that the channel transfer functions obtained from the SC probes are not smooth which is an artifact of the ambient noise. Further processing of the channel impulse response can provide a smoother estimate of the channel frequency response (e.g. assigning zero to channel taps with the magnitude below some prespecified threshold [10]). Note that due to the spectral characteristics of the auto-correlation function of the transmitted signal, the skirts of the estimated spectrum may be neglected. The obtained averages of 12 consecutive probe transmissions correspond to the window of stationarity of approximately 2 seconds. Note that the selection of the window of (assumed) stationarity is very important, as it has a profound impact on the analysis to follow.

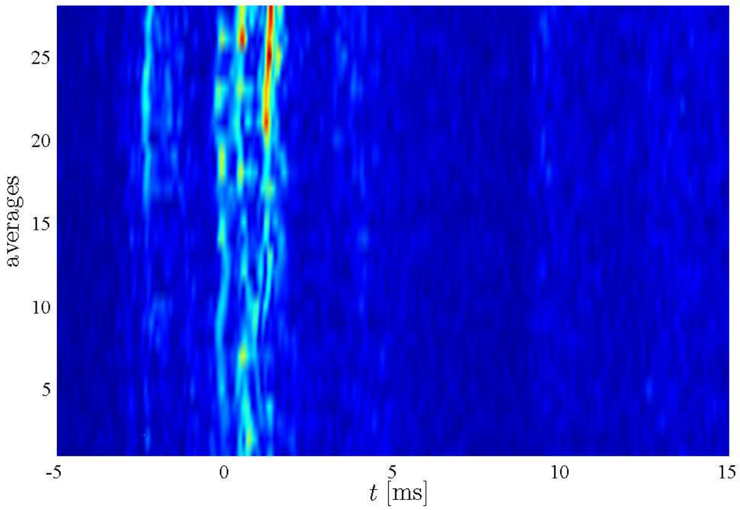

Figure 2.13: Averages of the channel impulse response.

More insight into channel impulse response fluctuations are provided in Figure 2.13, where we show 28 consecutive channel impulse response averages $\hat{h}_l(t_\nu^*)$ from (2.35), where $\nu = 0, \ldots, 27$. Because of the time-varying nature of the channel, the individual estimates (2.34) of the channel impulse response are not aligned in time. To align these estimates, the cross-correlation between consecutive channel estimates is used as an efficient tool for time-alignment. In particular, the position of the cross-correlation peak will determine the time offset between estimates. Since we are dealing with a fixed-transmitter, fixed-receiver scenario, the time offsets are on the order of several samples. By time-alignment of consecutive impulse response measurements we may average several consecutive impulse responses to suppress the measurement noise in the individual measurements. However, the phase of the individual signal samples varies significantly among consecutive impulse responses. As a consequence, the phase information is disregarded and averaging is performed by taking into consideration the magnitude of each channel estimate only. In order to take into account the phase information, fine compensation of motion-induced phase offset is needed which will be discussed later in Section 2.4.

In addition to the previous analysis, results regarding power measurements

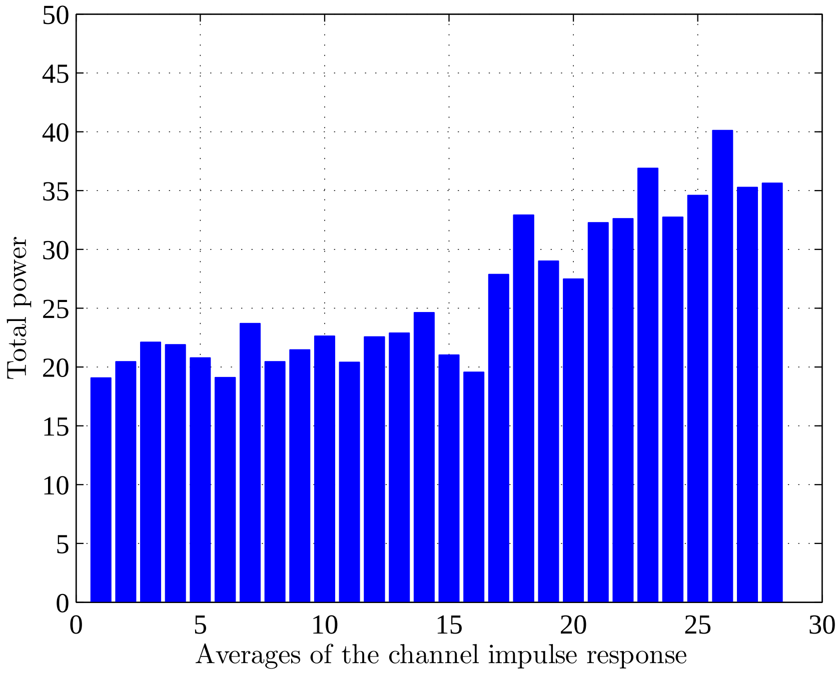

Figure 2.14: Total power of averaged impulse response.

are also provided. In particular, Figure 2.14 illustrates the total power measurements for each of 28 averaged estimates (2.35) of the channel impulse response. The total power is computed as

$$P(t_\nu^*) = \sum_{l=0}^{L} |\hat{h}_l(t_\nu^*)|^2, \tag{2.38}$$

where L is the estimated multipath delay spread of the channel. Figure 2.15 shows the corresponding total power histogram.

2.3.2 KAM08 Experiment: Single-carrier Probe (Moving Source)

The system specifications remain the same as for the previous analysis of the SC probe signal with the only difference being that the source array is not fixed anymore. We still focus on data, which was recorded on June 30, 2008 at 01 am UTC. During the one hour transmission interval, the 60 second long

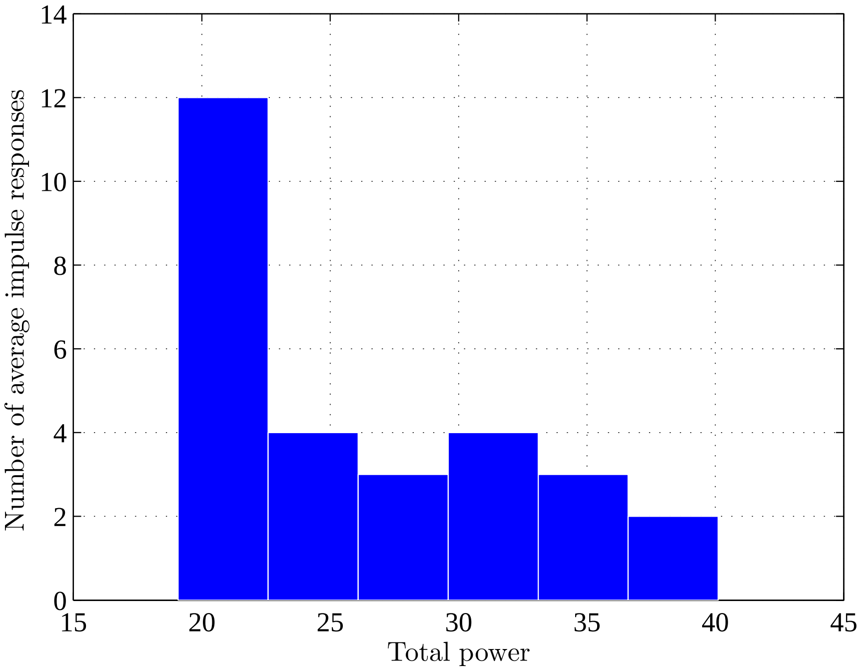

Figure 2.15: Histogram of total power.

single-carrier probe sequence is transmitted four times: $7-8$ min, $22-23$ min, $37-38$ min and $52-53$ min. The average speed of the ship is 1.5 m/s (3 knots), causing notable Doppler effects in the data. During source tow operations, a pair of transducers (ITC-1001 and ITC-2015) was towed at nominal depths of 50 m and 20 m, respectively. Presented results are based on data processing regarding transmissions from the transducer ITC-1001 and the fourth hydrophone (87.25 m depth).

Since there is a movement of the source array, Doppler shifting is present in the received signal. We should emphasize that there is no significant Doppler spreading in the channel since our probe signal is much shorter than the coherence time of the channel. Therefore, in order to remove Doppler effects, manifested through signal dilation (or compression) in time and shifting to higher (or lower) frequencies, we need to estimate the Doppler factor $a = v/c$, where v is the speed of the ship and c is the speed of sound. Preliminary measurements indicate that c can be considered as a constant value, $c = 1500$ m/s. In Ref. [1] it is shown that the transmission interval is distorted due to system movement as in expression (2.8).

There are several approaches for estimating the Doppler scaling factor a (e.g., Ref. [15]). Since the transmission interval is very short, cross-correlation of the received data and the actual probe signal can be applied to measure the effect of system motion. Measuring the time distance (in the number of samples) between two consecutive estimates of the same channel path, we are able to assess the factor a. Due to the channel fluctuations, information about the specific path used as a reference for Doppler effect mitigation should be updated periodically. This is due to the channel non-stationarity, and it could be expected that the observed path will vanish (possibly reoccurring again) during the 60 second observation interval. Our algorithm estimates the averaged factor a over 5 consecutive estimates of the channel impulse response (moving-average filtering), assuming that variations in the ship speed are on the order of a second. This assumption is confirmed by preliminary measurements conducted during the experiment with equipment for global positioning (GPS).

Once we estimate the Doppler factor, we can perform shifting of the data in the frequency domain. Since we are interested in analysis of the low-pass equivalent of the channel impulse response, our estimated carrier frequency used for down-converting will be $f_c' = f_c(1 + a)$ (Ref. [1]). After frequency compensation is done, we can perform data resampling as the last step prior to the channel analysis conducted in the similar manner as in the previous subsection. When the Doppler distortion is not too severe, one can skip performing the last step, since its effect is often negligible. In Figure 2.16 we illustrate the performance of the described approach for estimation of Doppler effects through the estimation of the ship speed v with respect to the assumed speed of sound $c = 1500\,\mathrm{m/s}$. In Figure 2.17 we have an ensemble of 29 channel impulse response averages $\hat{h}_l(t_\nu^*)$ from (2.35) based on averaging of 12 consecutive estimates of the channel impulse response realizations.

After Doppler effect compensation, the averaged estimates of the channel frequency response (magnitudes) are obtained in the same manner as in (2.37) for the fixed source array scenario.

In Figure 2.18 the total power measurements (2.38) are provided, for each

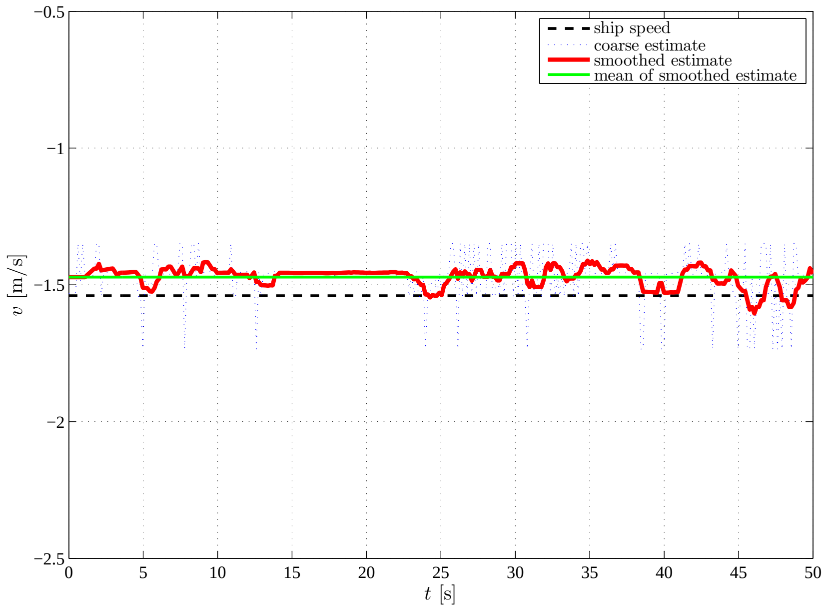

Figure 2.16: Estimation of the ship/source array movement.

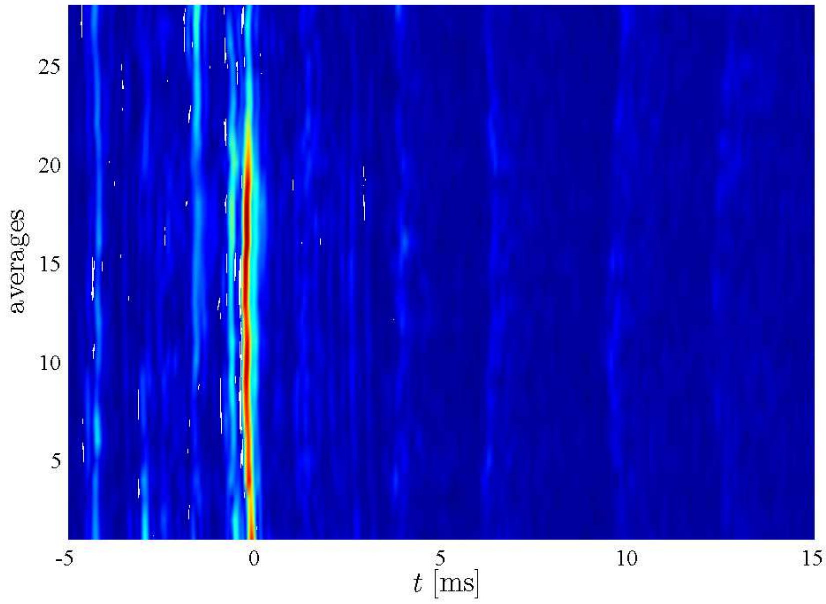

Figure 2.17: Averages of the channel impulse response.

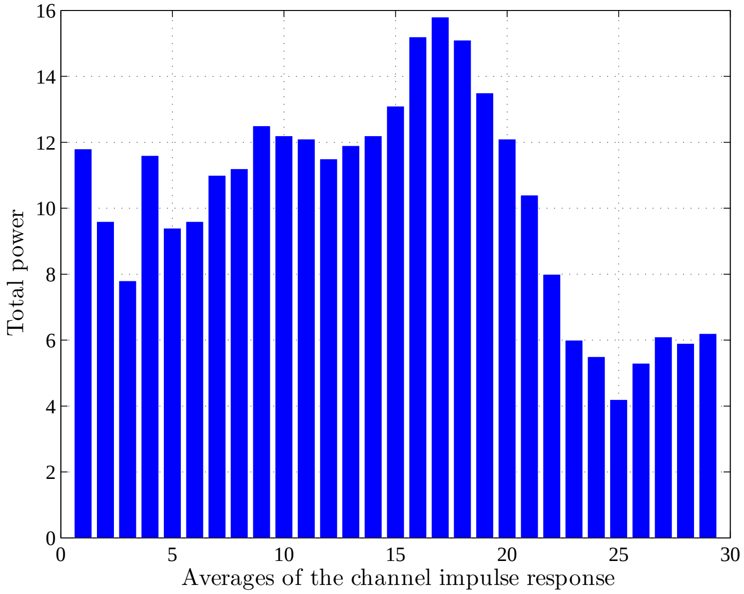

Figure 2.18: Total power of averaged impulse response.

of 29 averaged estimates of the channel impulse response. Figure 2.19 illustrates the corresponding total power histogram.

2.3.3 KAM08 Experiment: Multi-carrier Probe (Fixed Source)

The system specifications are the same as for the analysis of the SC probe signal. Moreover, we are focused once again on AAS1 (4 km) data, observing the same hour interval recorded on June 22, 2008 at 08 am UTC. To be consistent with the previous analysis, we will provide results regarding data processing from the fourth hydrophone (87.25 m depth). We emphasize that transmission is performed from different transducers depending on type of the MC probe (i.e. the number of the sub-carriers K) as opposed to single-carrier transmission. Specifically, transmission is made in the case of the multi-carrier signal $K = 512$ from the second transducer (57 m depth), $K = 1024$ from the fifth transducer (45.75 m depth) and $K = 2048$ from the eighth transducer (34.5 m depth). Therefore, the characterization of the estimated channels will be quite different with respect to the observed

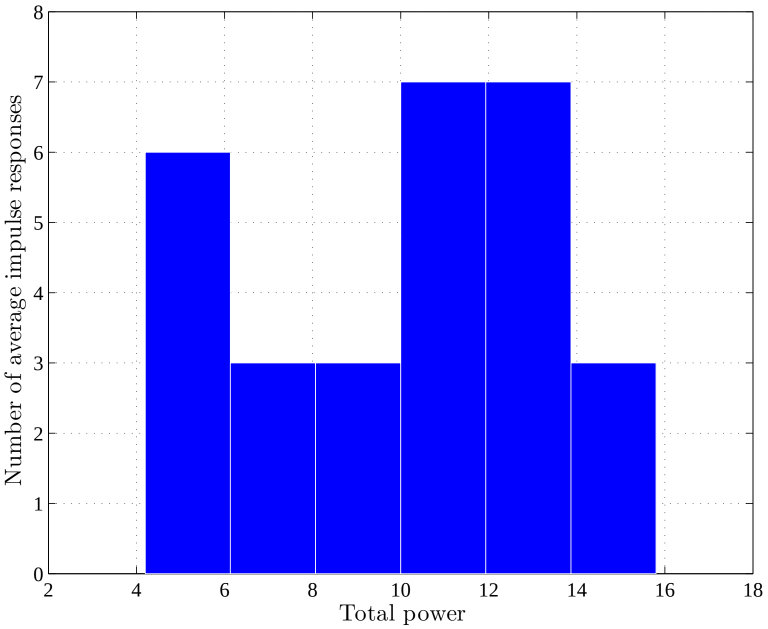

Figure 2.19: Histogram of total power.

multi-carrier signal. The time slot of 60 s, during which our multi-carrier probe signals are transmitted, are $41-42$ min, $42-43$ min and $43-44$ min for $K = 512$, $K = 1024$ and $K = 2048$, respectively. In the following study we focus on the MC probes with $K = 2048$, which were described in the previous section.

Based on the discussion from Section 2.2, channel estimation is performed through simple multiplication of the spectra of the received and transmitted signals as in (2.32). Specifically, after initial block synchronization and the FFT operation, the baseband received signal at the k-th *active* sub-carrier and the i-th transmission interval is given as

$$\begin{aligned} Y_{k,i} &= \sum_{l=0}^{L} y_{l,i} e^{-j2\pi(k\Delta f - B/2)l/f_s} \\ &= H_{k,i} x_k + W_{k,i}, \end{aligned} \tag{2.39}$$

where $y_{l,i}$ is the discrete-time baseband representation (2.20) of the received MC signal, $H_{k,i}$ is the channel frequency response (2.31), and W_k is the channel noise.

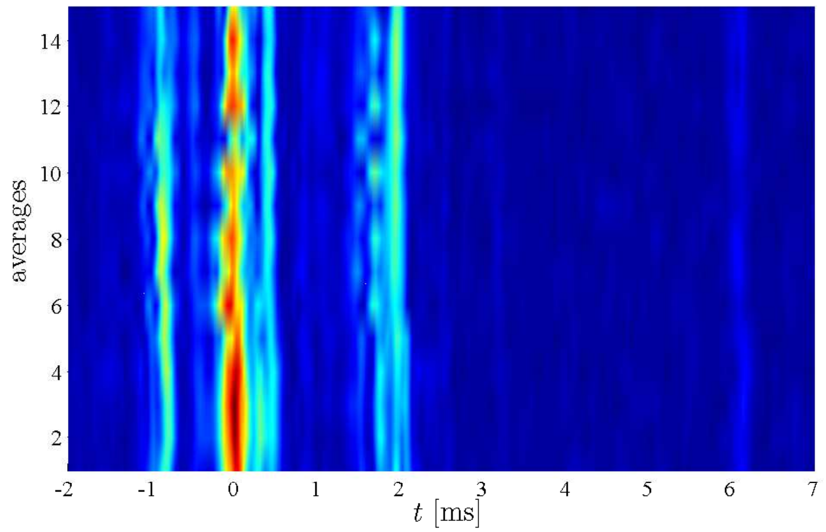

Figure 2.20: Averages of the channel impulse response.

The channel frequency response estimate is given as in (2.32)

$$\widehat{H}_{k,i} \quad = \quad H_{k,i} + \frac{x_k^*}{|x_k|^2} W_{k,i}, \tag{2.40}$$

while the corresponding time domain channel estimate is obtained by applying the inverse Fourier transform

$$\hat{h}_{l,i} = \frac{1}{K} \sum_{k=0}^{K-1} \widehat{H}_{k,i} e^{j2\pi(k\Delta f - B/2)l/f_s}. \tag{2.41}$$

At this point it is important to emphasize that the multi-carrier signal is modulated with a pseudo-noise sequence that results in a phase difference among the sub-carriers. This is done to reduce the peak-to-average power ratio. Since we have a finite number of sub-carriers, we are not able to estimate the continuous spectrum of the channel impulse response. This will directly affect the reliability of our channel impulse response estimate.

In Figures 2.20, we illustrate 15 averages of 12 consecutive estimates of the channel impulse response, which are computed in the same manner as in (2.35)

$$\hat{h}_l(t_\nu^*) = \frac{1}{12} \sum_{i=0}^{11} |\hat{h}_{l,12\nu\Delta L+i}|, \tag{2.42}$$

where $\nu = 0, \ldots, 14$, and $\Delta L = T' f_{s,Tx} = 26000$ samples. We use the same approach for time-alignment of the channel estimates as in the previous study for the SC probes. Therefore, a simple cross-correlation between consecutive estimates of the channel impulse response is a reliable approach for the determination of the time offset, because of the multipath structure of the channel as well as sufficient correlation among adjacent estimates. We disregard phase information due to the rapid phase variations and possible mutual cancelation of the channel estimates.

In Figure 2.21 we also show the channel transfer functions averages which are computed as

$$\widehat{H}_k(t_\nu^*) = \frac{1}{12} \sum_{i=0}^{11} |\widehat{H}_{k,12\nu\Delta L+i}|. \tag{2.43}$$

Note that the channel frequency response estimates obtained from the MC probes are smooth compared to those obtained from the SC probes from Figure 2.12. This is an artifact of insufficient resolution in the frequency domain of the probe signal employed. The lack of precision in the estimated frequency response is clearly seen through more spectral flatness in comparison to the estimate based on wideband SC probing. This is reflected in the time domain as the lower resolution in the impulse response, which prevents us from distinguishing adjacent propagation paths. Thus, the MC signal may not be able to capture the frequency-selectivity of the channel, and cannot be used to assess its coherence bandwidth. With 256 active sub-carriers, our MC probes are limited to a frequency resolution of 48 Hz, which corresponds to about 20 ms of multipath spread. Hence, any delay spreading longer than 20 ms will not be accurately captured. In fact, we noted from the SC probes that the multipath spread T_m for some channel examples is on the order of 100 ms (coherence bandwidth of 10 Hz). Increasing the frequency resolution of the MC probes would require an increase in the number of sub-carriers; however, the resulting increase in the signal duration would challenge the detection capability on a time-varying channel. Nonetheless, note that MC probes may be useful for assessing the time-coherence properties of the channel in each narrow sub-band.

We should emphasize that we are considering a fixed-transmitter, fixed-receiver system, and there is no need for compensation of the Doppler spreading

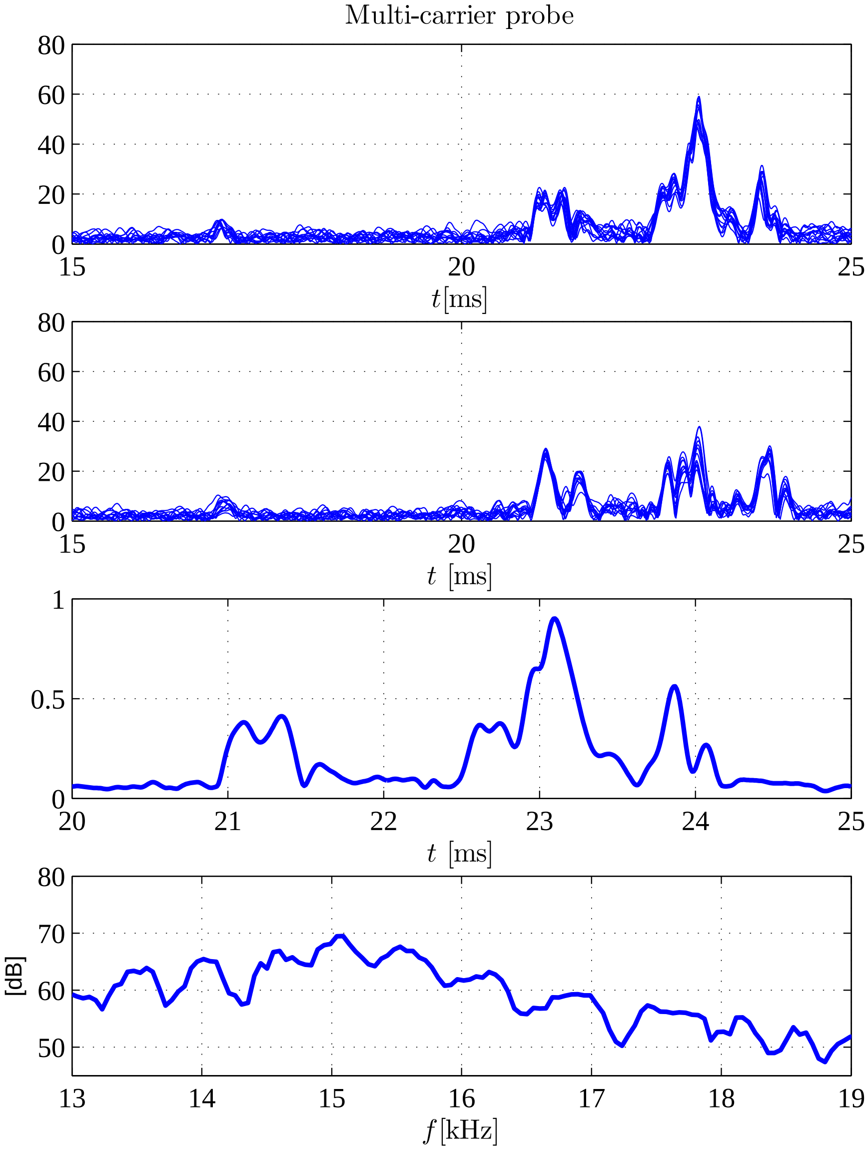

Figure 2.21: Channel estimates from the KAM08 experiment: shown in the top two rows are the ensembles of 12 consecutive channel responses in time; shown below are the top row ensemble averages in the time and frequency domains.

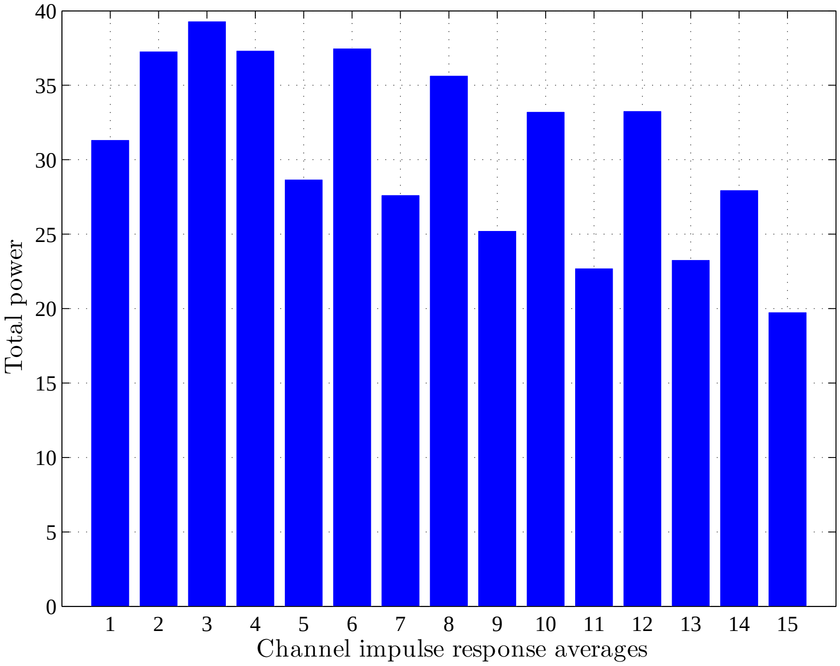

Figure 2.22: Total power of averaged impulse response.

effects. Therefore, a simple multiplication of the spectrum of the received signal and the (conjugate) spectrum of the transmitted signal, only at those frequencies where the transmitted signal has non-zero power allocation is sufficient for the channel frequency response estimation. The number of FFT points should be at least four times greater than the length of data set in order to obtain sufficient interpolation in frequency. At this point, it is important to recall our previous discussion where we stated that the multi-carrier probe signal is modulated with a PN sequence, causing phase differences among the modulated sub-carriers. Hence, the phase should be compensated prior to the spectrum multiplication. From the obtained figures, we should conclude that $K = 2048$ provides enough resolution in the frequency domain to demonstrate channel selectivity.

In addition to the previous analysis, results regarding power measurements are also provided. These results are obtained in the same manner as in (2.38). In particular, in Figure 2.22 the total power measurements are given for each of 15 averaged estimates of the channel impulse response.

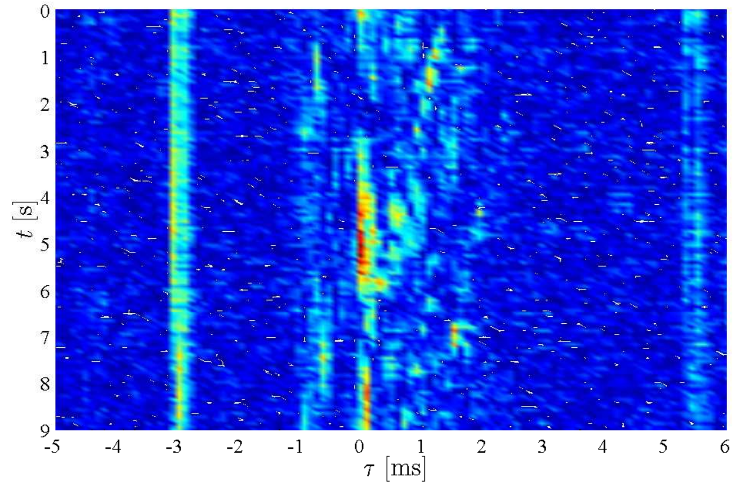

Figure 2.23: Estimates of the channel impulse response.

2.3.4 KAM11 Experiment: OFDM Probe (Fixed Source)

Results in this section are based on the data collected during KAM11 experiment. Specifically, analyzed data set is AAS2 (3km) from July 4, 2011 at 02 and 04 am. The time slot of 60 s, during which our single-carrier probe signal is transmitted, is $09 - 10$ min. The transmitter was deployed from the ship as a 4-element vertical source array consisting of ITC-1007 transducers with 0.5 m element separation (1.5 m aperture), which was provided by Woods Hole Oceanographic Institution (WHOI). The sampling rate was $f_{s,Tx} = 100$ kHz. The receiver was deployed as a MPL VLA with a sampling rate of $f_{s,Rx} = 100$ kHz per element with 3.75 m interelement spacing (total aperture of 56.25 m). Transmission is done from the first transducer at 49.5 m depth (MPL 8-element acoustic source array). Data is gathered from the last element at the receiver side (87.25 m depth).

In Figures 2.23 and 2.24, we show 128 consecutive channel estimates (2.41), for the transmissions at 02 and 04 am. We note from the results that the OFDM probe provides a good resolution in the estimate of the channel impulse response. The secondary arrival, which corresponds to the surface reflection, is significantly attenuated due to a severe Doppler effects caused by rough sea conditions. This can indicate that different propagation paths are subject to potentially different Doppler effects. Figures 2.25 and 2.26 illustrate 128 consecutive estimates (2.40) of

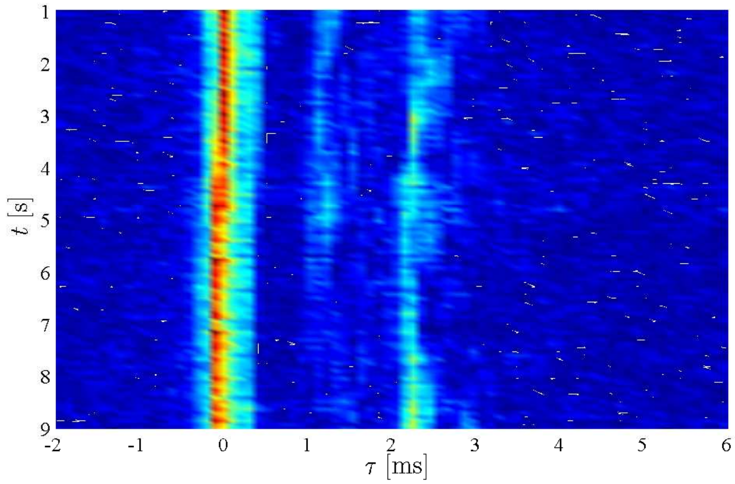

Figure 2.24: Estimates of the channel impulse response.

channel frequency response which clearly indicate that the lower parts of the operational bandwidth are imposing less attenuation to the corresponding sub-carrier frequencies.

Based on the previous discussion from this section, we favor the SC probe in statistical channel characterization, due to its advantages in both time and frequency domains, namely, short signal duration (well below the coherence time of the channel) allows simple coherent detection, while signal flatness in the frequency domain gives accurate estimates of the channel coherence bandwidth and ensures sufficient resolution in the impulse response.

2.4 Statistical Channel Characterization

Our statistical characterization focuses on three aspects: the probability density function (PDF) of the path responses, their time-correlation properties, and time and frequency-correlation properties of the channel frequency response. Because we have seen in the previous section that the channel is not stationary, we focus on short-term characterization (order of seconds). By assuming a quasi-stationary channel, and looking at its short-term characteristics, we will later in Chapter 3 assess the channel capacity.

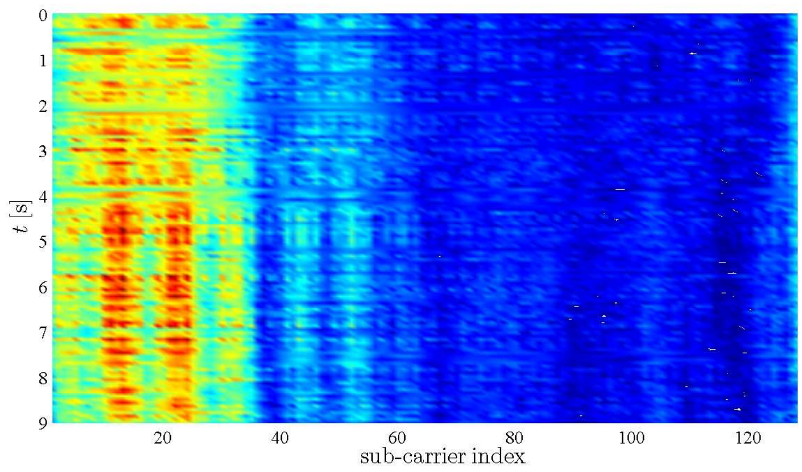

Figure 2.25: Estimates of the channel frequency response.

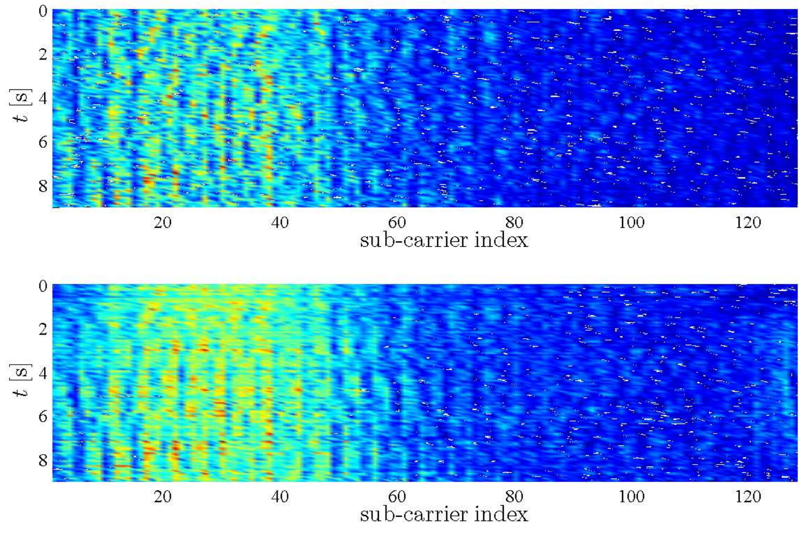

Figure 2.26: Estimates of the channel frequency response.

2.4.1 Channel Fading Distribution (KAM08)

An underwater channel is characterized by frequency-dependent path loss and random fluctuations due to motion of surface reflection points that cause variation in the path loss and, thus, signal fading. There are several possible models for the fading distribution.

Figure 2.27 illustrates the time variation of the significant paths labeled as a, b, c and d in Figure 2.12. Note that the channel tap a behaves differently in the time intervals from 0 to 30 sec and from 30 to 50 sec. The change in the local mean indicates a non-stationary random process. On the other hand, note that quasi-stationary intervals for the path b are on the order of 10 seconds for the time interval from 0 to 20 sec and on the order of seconds for the time interval from 20 to 50 sec. To account for this fact, we have chosen a window of 2 seconds to represent the quasi-stationary period for the models that we will consider. Since the behavior of different paths can be characterized using longer intervals of quasi-stationarity than the adopted window size, for the purpose of histogram presentation, we can superimpose several consecutive windows and analyze their statistical properties jointly (i.e., for tap a we can observe jointly up to 10 windows, and for tap b up to 10 windows for the time interval 0 to 20 sec). Note that the selection of the window of (assumed) stationarity is very important, as it has a profound impact on the analysis to follow.

We consider several candidate statistical models for the channel fading: Rician, Nakagami and log-normal. Figure 2.28 shows how the Rician, Nakagami and log-normal PDFs fit when superimposed on top of the measurement histograms.

The PDFs of the three distributions are given by the following expressions:

$$f_{X_{rice}}(x) \sim \frac{(1+k)}{\Omega} x e^{-\frac{(1+k)}{\Omega}x^2-k} I_0\left(2\sqrt{\frac{k(1+k)}{\Omega}}x\right), \tag{2.44}$$

$$f_{X_{naka}}(x) \sim \left(\frac{m}{\omega}\right)^m \frac{x^{2m-1}}{\Gamma(m)} e^{-\frac{mx^2}{\omega}}, x \geq 0, \tag{2.45}$$

$$f_{X_{logn}}(x) \sim \frac{1}{x\sigma\sqrt{2\pi}} e^{-\frac{(\log(x)-\mu)^2}{2\sigma^2}}, x > 0, \tag{2.46}$$

where I_0 is the zeroth-order modified Bessel function of the first kind, $E\{X_{rice}^2\} = \Omega$, and k is the Rician factor. m is the shape parameter, and ω is the spreading

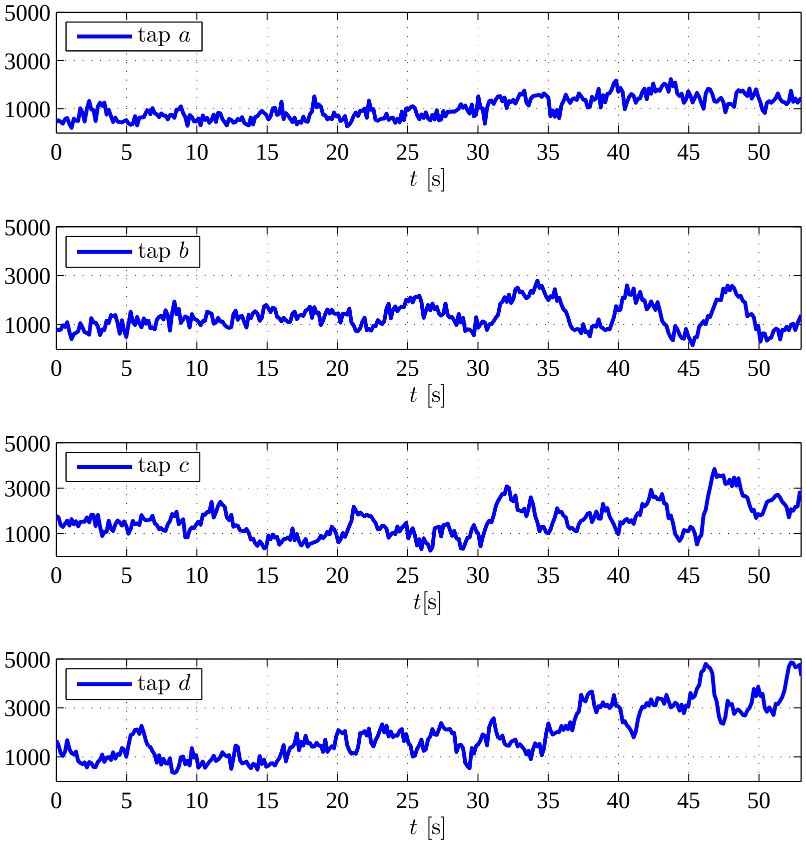

Figure 2.27: Magnitudes of the channel propagation paths (a, b, c and d from Figure 2.12) vs. time.

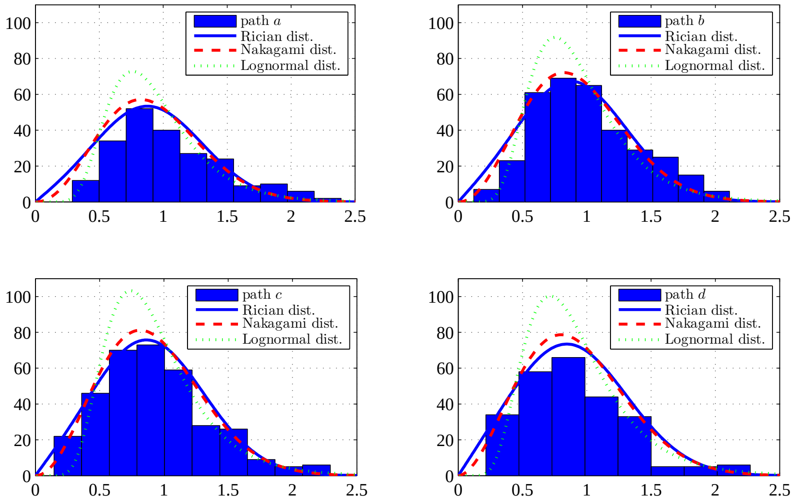

Figure 2.28: Histogram and fit of the magnitude of the channel propagation path. Each histogram is based on observations taken over 10 seconds.

factor. σ and μ are the standard deviation and the mean value of the underlying normal distribution of $\log(X_{logn})$.

The parameters of the Nakagami and log-normal PDFs have been obtained based on the estimated parameters of the fitted Rician distribution (from the data histograms in Figure 2.28). These parameters have been determined to yield equivalent second and fourth moments of the underlying random variables:

$$E\left\{X_{rice}^2\right\} = E\left\{X_{naka}^2\right\} = E\left\{X_{logn}^2\right\} = 1, \tag{2.47}$$

$$\begin{aligned} \frac{\left(E\{X_{rice}^2\}\right)^2}{E\{X_{rice}^4\} - \left(E\{X_{rice}^2\}\right)^2} &= \frac{\left(E\{X_{naka}^2\}\right)^2}{E\{X_{naka}^4\} - \left(E\{X_{naka}^2\}\right)^2} \\ &= \frac{\left(E\{X_{logn}^2\}\right)^2}{E\{X_{logn}^4\} - \left(E\{X_{logn}^2\}\right)^2}. \end{aligned} \tag{2.48}$$

This normalization is performed in order to keep the mean value of the log-normal random variable in the range of mean values of the Rician and Nakagami fading, since the conditions $E\{X_{rice}\} = E\{X_{naka}\} = E\{X_{logn}\}$ and $E\{X_{rice}^2\} = E\{X_{naka}^2\} = E\{X_{logn}^2\}$ cannot be satisfied simultaneously. It remains unanswered as to which physical process could be a possible cause of these two fading pdfs.

Let us now recall that we defined the time-varying discrete-time *equivalent* baseband channel model in (2.20) as

$$h_{m,n} = \sum_{l=0}^{L} h_{l,n}\delta((n - m_l)/B), \tag{2.49}$$

where $h_{m,n}$ is the response of the channel at time n due to an impulse applied at time $n - m$. As we have seen earlier, the channel tap gains, $h_{l,n}$, do not necessarily represent the actual physical propagation paths, since each tap gain $h_{l,n}$ can contain in itself the contributions of *all* the physical paths; However, due to a sparse structure of the channel impulse response, these contributions are small in a wideband system, and the dominant coefficients of the uniformly spaced equivalent model (2.49) can be roughly associated with the physical propagation paths.

We initially assume the Rician fading model where $\{h_l\}$ are complex Gaussian random variables with independent real and imaginary parts, distributed as $\mathcal{N}\left(\mu_l/\sqrt{2}, \sigma_l^2\right)$. The equivalent Nakagami and log-normal fading models can be derived from expressions (2.47) and (2.48). Assuming normalization to the log-normal fading, $E\{|h_l|^2\} = \Omega_l = \mu_l^2 + 2\sigma_l^2$ and $\sum\limits_l \Omega_l = 1$, each channel tap is given as

$$h_{l,n} = \sqrt{\frac{\Omega_l k_l}{k_l + 1}}\frac{(1+i)}{\sqrt{2}} + \sqrt{\frac{\Omega_l}{k_l + 1}}\frac{1}{\sqrt{2}}h_{l,n}^0, \tag{2.50}$$

where $h_{l,n}^0$ is a complex Gaussian random variable with independent real and imaginary parts, each distributed as $\mathcal{N}(0,1)$, and the Rician k-factor is defined as the ratio of the power in the mean value to the power in the diffuse component:

$$k_l = \frac{\mu_l^2}{2\sigma_l^2}. \tag{2.51}$$

2.4.2 Channel Impulse Response Correlation (KAM08)

Experimental measurements of the correlation in time of the channel impulse response give us an estimate of the channel coherence time. For a reliable estimate, the channel probe signal must be significantly shorter in duration than the channel coherence time. We also note here that Doppler shifting due to the transmitter and the receiver motion should be distinguished from Doppler spreading caused by channel motion and variation.

The normalized correlation function is defined as

$$\phi(m) = \frac{1}{|A_{n,n+m}|} \sum_{A_{n,n+m}} \frac{\left| \sum_l h^*_{l,n} h_{l,m+n} \right|}{\sqrt{\sum_l |h_{l,n}|^2 \sum_l |h_{l,n+m}|^2}}, \tag{2.52}$$

where $A_{m,m+n}$ is the set of all independent pairs of indices $(m, m+n)$ such that if $n = 1$ then $A_1 = \{(m, m+1) : (1,2), (3,4), \ldots\}$. $(m+n) = [t_{m+n}/\Delta L]$ where t_{m+n} is the observation time, and ΔL is the discrete-time repetition interval of the transmitted probe sequence (e.g., for the single-carrier probe signal $\Delta L =$ 15561 samples at $f_s = 100$ kHz). Note that the correlation coefficient will also depend on the time index m as the channel is non-stationary, but we omit this dependence with the understanding that the results will be illustrated only for a quasi-stationary interval on the order of seconds. In Figure 2.29 we see an experimental measurement of this channel parameter given as a solid blue curve. From this figure, the coherence time is estimated to be $T_c \approx 200$ ms. Since our probe signals are of duration $T = 4.5$ ms, the assumption that $T << T_c$ is justified. Additionally, the red sold curve is provided as a reference where we compute the channel correlation function (2.52) based on the magnitudes of the channel taps only, ignoring the phase variations.

In Figure 2.30 we make the comparison between the channel correlation time functions for the stationary and mobile UWA communication scenario. As we can see from the figure, the mobile channel exhibits a shorter coherence time than the stationary channel. For example, for the fixed source scenario, the correlation value drops to 0.5 in approximately 330 ms, whereas for the mobile scenario, it drops to the same value in $120 - 250$ ms, depending on the recorded data sample.

Due to the non-stationarity of the channel, we constrained the analysis to short-term statistical characterization. We note that the statistical properties of the channel fading, as well as the parameters of the underlying statistical model are subject to the evolution in time (i.e., for the Rician fading scenario, the Rician k-factor, the mean and the standard deviation of the underlying complex normal

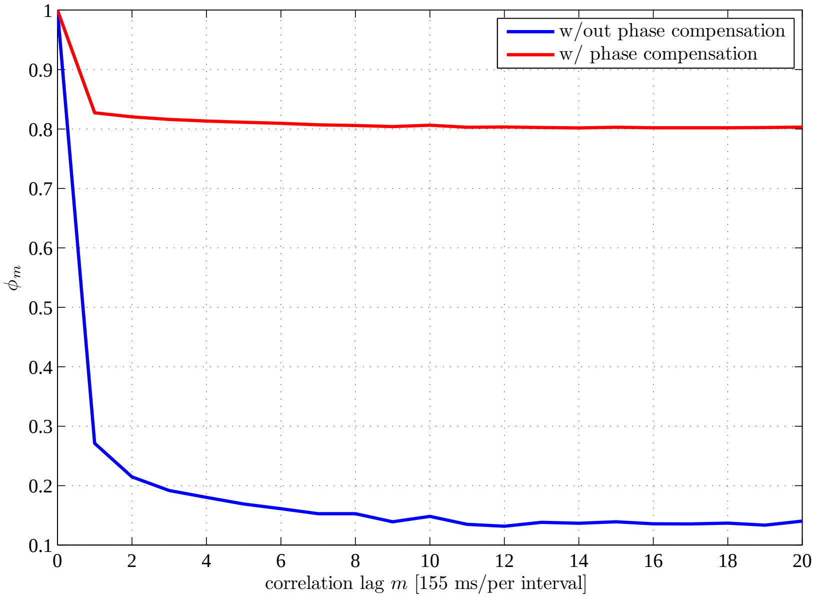

Figure 2.29: Time-correlation factor.

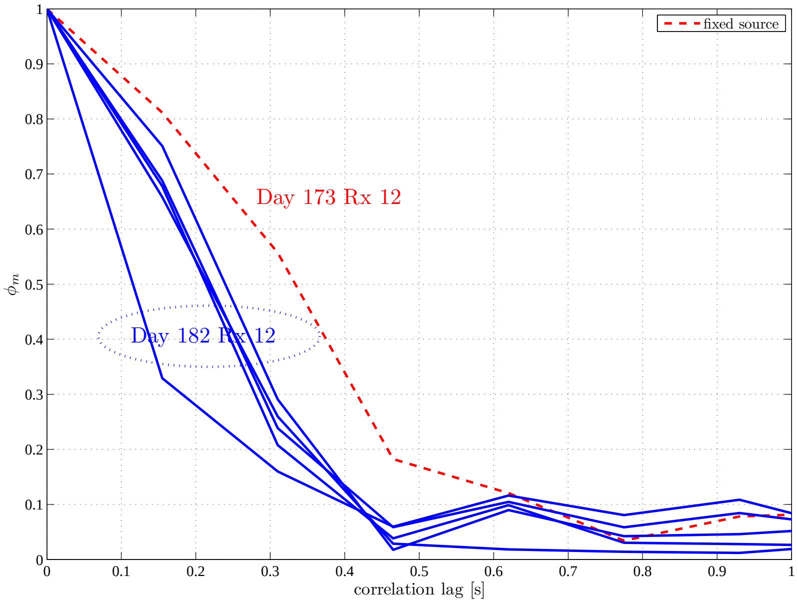

Figure 2.30: Time-correlation function for mobile UWA channels.

distribution can change in time). This is also an important observation since the assessment of the channel capacity, especially for MIMO systems, depends on how well the fading statistics can be estimated. Moreover, because of the non-stationarity, design of the capacity-achieving adaptive coding/modulation is of particular interest, and it is based on the ability of the communication system to track the channel model parameters.

2.4.3 Channel Frequency Response Time and Frequency Correlation (KAM08)

Here we define the normalized time-correlation function of the channel frequency response (2.31) as

$$\Phi_t(m,k) = \frac{1}{|A_{n,n+m}|} \sum_{A_{n,n+m}} \frac{H^*_{k,n} H_{k,m+n}}{\sqrt{\sum_k |H_{k,n}|^2 \sum_k |H_{k,n+m}|^2}}, \tag{2.53}$$

and frequency-correlation function as

$$\Phi_f(m,k) = \frac{1}{|A_{k+m,n}|} \sum_{A_{k+m,n}} \frac{H^*_{k,n} H_{k+m,n}}{\sqrt{\sum_k |H_{k,n}|^2 \sum_k |H_{k+m,n}|^2}}, \tag{2.54}$$

These time and frequency correlation estimates of the channel frequency response are illustrated in Figure 2.31. As we can see from the figure, different frequency bands exhibit significantly different values of $\Phi_t(0,k)$. For example, at the baseband frequencies $f_1 = -1.5$ kHz and $f_2 = 1.5$ kHz, we observe the correlation $\Phi_t(0,f_1) = 5.5$ and $\Phi_t(0,f_2) = 1.1$, respectively. In contrast, for $\Phi_t(m,f_k)$ and $m > 0$, we observe similar correlation results across the entire operational bandwidth (e.g. for $f_1 = -1.5$ kHz and $f_2 = 1.5$ kHz, $\Phi_t(155\text{ ms}, f_1) = 0.5$ and $\Phi_t(155\text{ ms}, f_2) = 0.4$, respectively). The frequency correlation illustrates prominent selectivity of the channel frequency response, since $\Phi_f(0,k) \gg \Phi_f(m,k)$ for $\forall m,k$. Specifically, frequencies $f_1 = -2.1$ kHz, $f_2 = -1.5$ kHz, $f_3 = -0.6$ kHz and $f_4 = 0.3$ kHz exhibit high correlation vales $\Phi_f(0,f) \approx 5$, while $\Phi_f(\Delta f, f) < 1$, for for $f = f_1, f_2, f_3, f_4$, and $\Delta f > 0$.

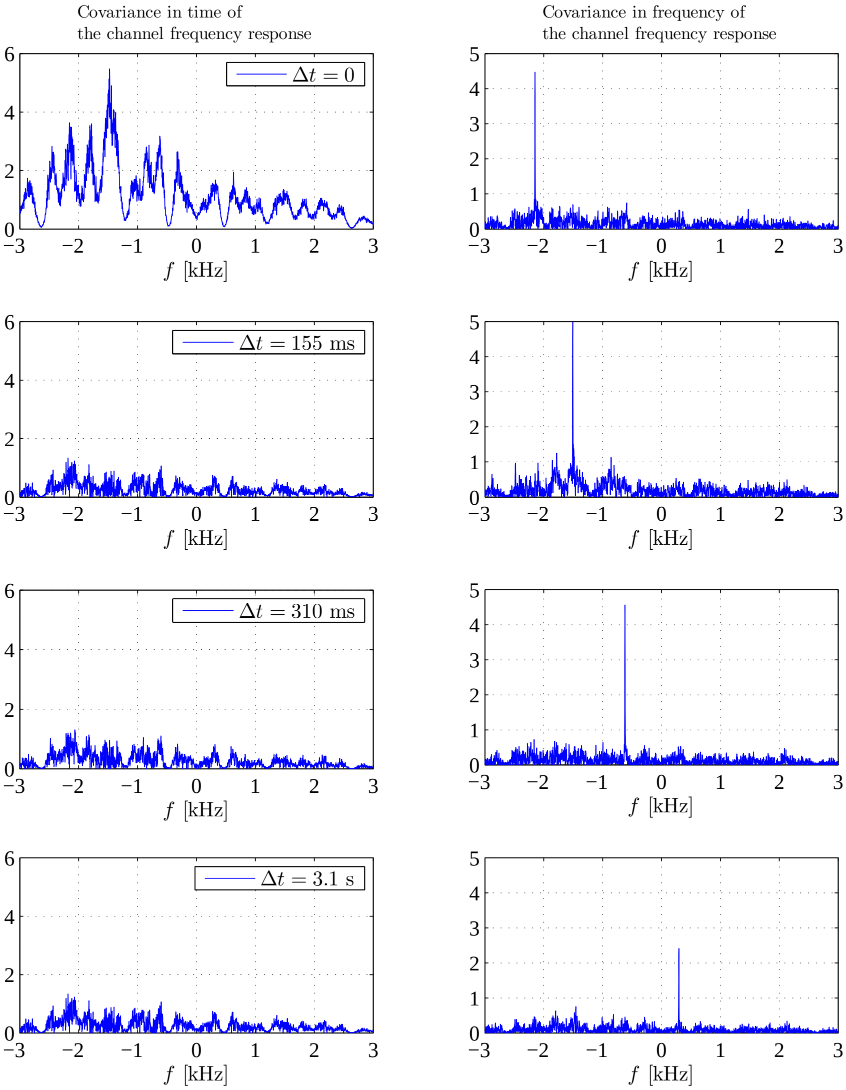

Figure 2.31: Time and frequency-correlation functions of the estimated channel frequency response.

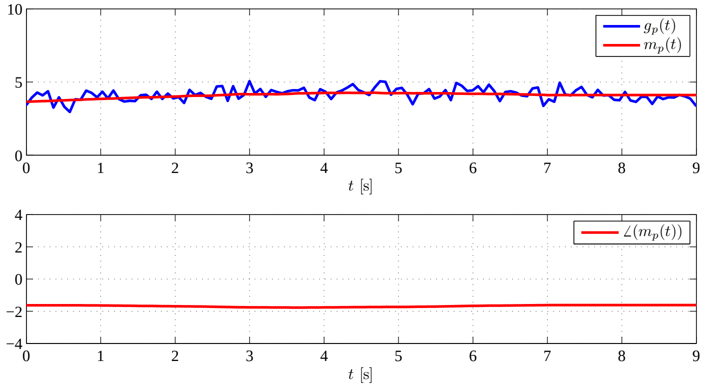

Figure 2.32: Time-varying mean.

2.4.4 Channel Impulse Response Correlation (KAM11)

As we have seen in the previous discussion, an UWA channel can be characterized by Rician fading with the slowly varying mean. Therefore, for the purpose of the channel characterization from the KAM11 experiment, we first extend the time-varying path model (2.15) such that

$$\begin{aligned} h'_p(t) &= (m_p(t) + h_p(t))e^{j2\pi f_c \int_{x=-\infty}^{t} a(x)dx} \\ &= (m_p(t) + h_p(t))e^{j\theta(t)}, \end{aligned} \tag{2.55}$$

where $m_p(t)$ is the slowly-varying mean, and $\theta_p(t)$ is the motion-induced phase offset driven by the Doppler scaling factor $a_p(t)$. In the following, we compensate for the mean and the motion-induced phase distortions prior to statistical channel characterization. In other words, we focus on correlation properties of the fast channel fluctuations modeled as $h_p(t)$ in (2.55).

In Figures 2.32 and 2.33, we present the estimate of the time-varying mean $m(t)$ and the Doppler-induced phase offset $\theta(t)$. After proper compensation of the mean and phase offset we proceed to statistical channel characterization. In particular, in Figures 2.34 and 2.35 we present experimental measurements of time-correlation function of the channel impulse response, where the blue curve gives the correlation of $h_p(t)$, and the red curve corresponds to the uncompensated model $h'_p(t)$.

In Figure 2.36, we compare the estimated time-correlation function to the

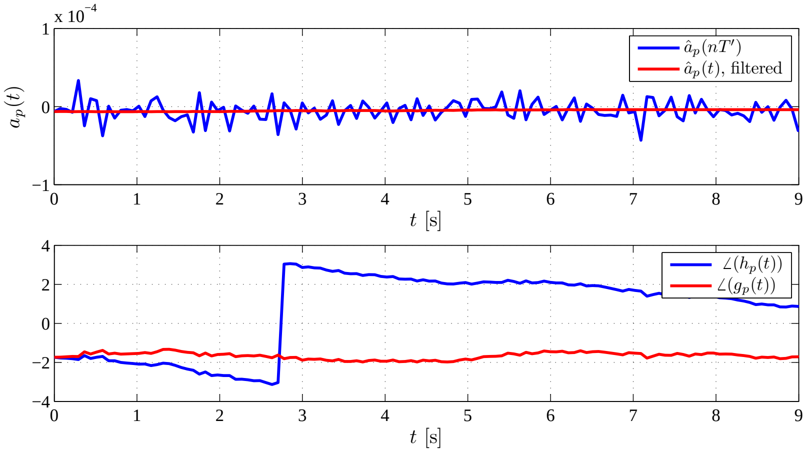

Figure 2.33: Estimate of the Doppler scaling factor and motion-induced phase offset.

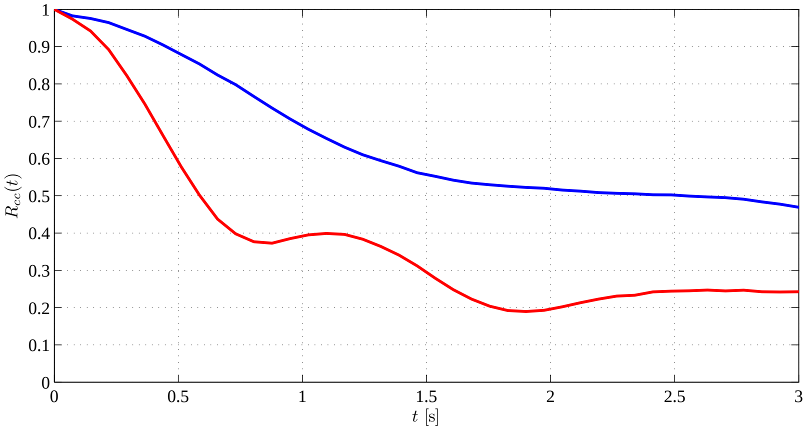

Figure 2.34: Time-correlation function.

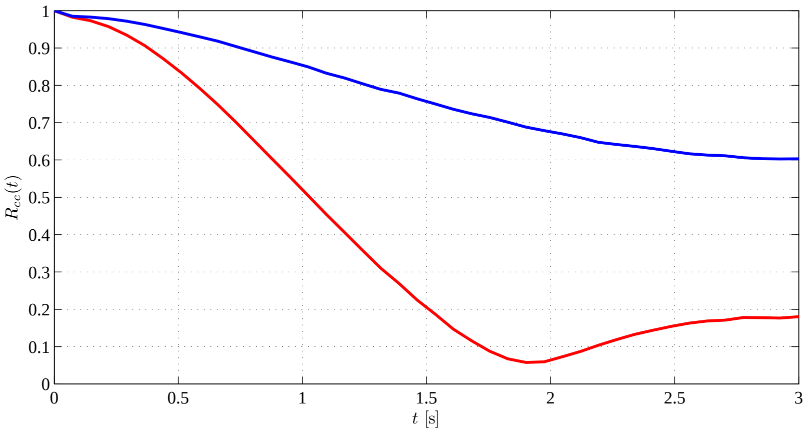

Figure 2.35: Time-correlation function.

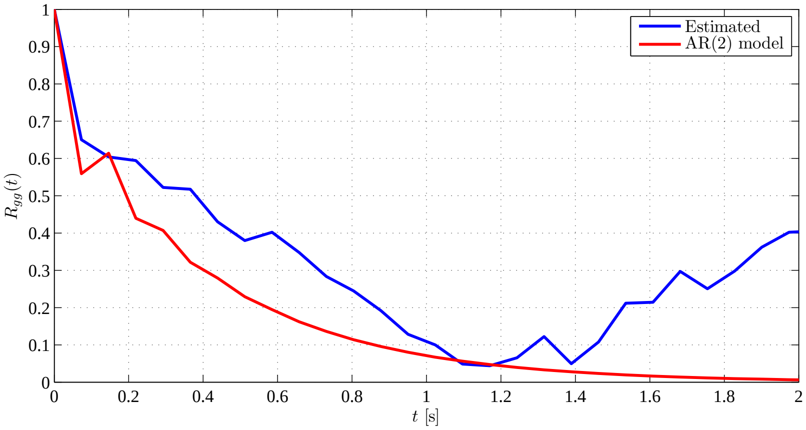

Figure 2.36: Auto-regressive model of the estimated time-correlation function.

one which corresponds to the second-order auto-regressive fading model with the optimized coefficients AR(2):$\{a_1 = 0.43, a_2 = 0.31\}$. This result indicate that the auto-regressive fading model may be considered as a reliable model for the underlying fading of the UWA channel.

2.4.5 Channel Frequency Response Time and Frequency Correlation (KAM11)

Examples of the time and frequency-correlation functions of the channel frequency response are illustrated in Figures 2.37 and 2.38. We observe from

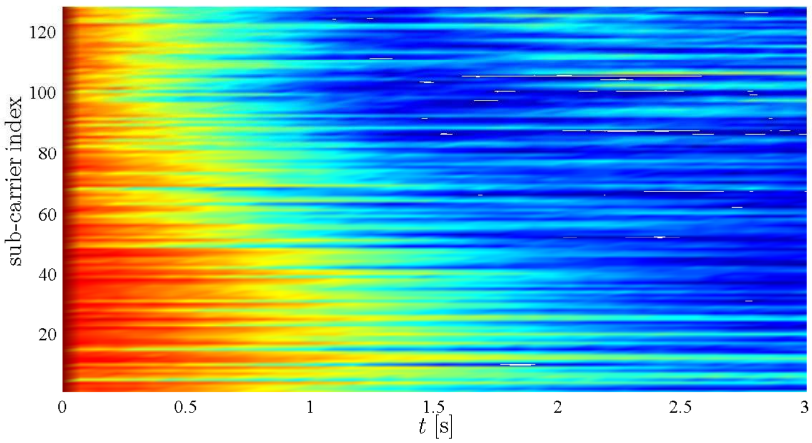

Figure 2.37: Time-correlation function of the channel frequency response.

Figure 2.37 that the channel shows more correlation at the lower parts of the operational bandwidth, while Figure 2.38 shows a relatively stable estimate of the channel coherence bandwidth $B_c \approx 150$ Hz, which corresponds to $T_m \approx 6$ ms. This observation is in agreement with the estimates of the channel impulse response from Figures 2.23 and 2.24.

2.5 Summary

In this chapter, we first reviewed the major properties of UWA channels, and derived continuous and discrete-time baseband channel models. Design and simulation of UWA communication systems requires accurate channel modeling due to the extreme channel complexity. Second, we considered short-term statistical characterization of the shallow water acoustic communication channel, based on a set of measured channel responses, obtained from signals recorded during the KAM08 and KAM11 experiments. Wideband single-carrier and multi-carrier probe signals are employed to measure the time-varying channel response, and to estimate its statistical properties that play an important role in the design of bandwidth-efficient and power-efficient communication systems. Specifically, we conducted a comprehensive study of the time and frequency-domain correlation properties of the UWA channel. Channel measurements were also used to examine

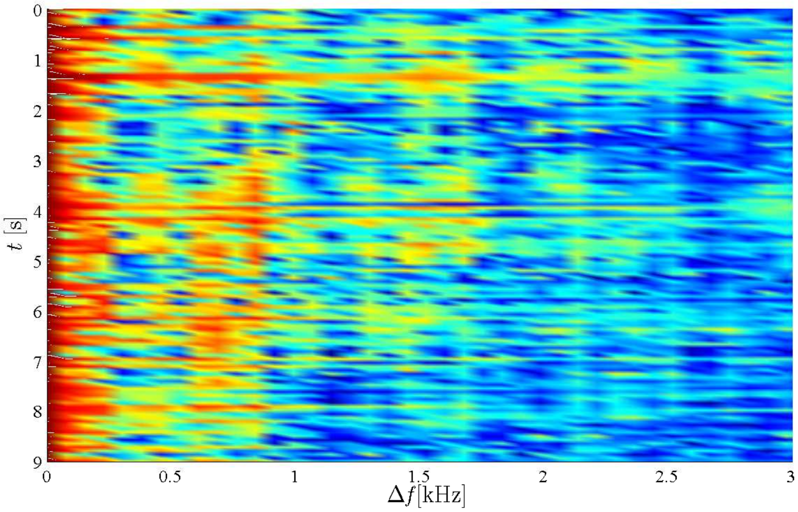

Figure 2.38: Frequency-correlation function of the channel frequency response.

several candidate fading models, indicating a good match with the Rician distribution. These measurements will be used in the following chapter to compute the average channel capacity assuming a quasi-stationary fading and nonwhite Gaussian noise.

Chapter 2, in part, is a reprint of the material as it appears in “Statistical characterization and capacity of shallow water acoustic channels,” by A. Radosevic, J. G. Proakis, and M. Stojanovic, IEEE Oceans’09 Conference, Bremen, Germany, May 2009. The dissertation author was the primary investigator and author of this paper.

Chapter 3

Capacity of Shallow Water Acoustic Channels

In this chapter we consider the evaluation of the capacity of shallow water acoustic channels. There are few available analyses regarding the capacity of the UWA channel. In [16], a time-invariant channel model is considered with additive Gaussian noise (possibly not white). Ray theory has been used to provide a deterministic (average) description of the multipath propagation. However, in order to explore the communication limits of this complex medium, it is necessary to have a statistical description of the random time variations of the channel; in [17], a ray-theory-based model is proposed where the individual multipath arrivals are modeled as Rayleigh random processes with non-Gaussian ambient noise [18].

Recent works [19, 20] and the work described in the previous chapter provide a short-term statistical characterization of the fading process, showing that a Rician model with a slowly time-varying parameterization satisfactorily matches the experimental data collected at some sites.

In wireless RF communication systems, the use of MIMO antenna systems with space-time coding has been shown [21, 22] to result in a linear increase in the ergodic capacity of a Rayleigh fading channel with the number of transmit or receive elements, whichever is smaller. The increase in the information rate, i.e. the spatial multiplexing gain, depends primarily on the fading distribution. This is an important observation for systems that do not exhibit Rayleigh fading, such as mobile-terrestrial radio systems where a line-of-sight component results in Rician fading, or, as we shall see, in acoustic channels. Ergodic capacity results can also be extended to frequency-selective fading channels [23–25], and any fading distribution under AWGN. These information-theoretical results are of great interest for the analysis of MIMO capacity and information rate limitations of UWA channels which remains an open area for research.

In this chapter, we will adopt the Rician model with time-varying k-factor and time-varying mean as the basis for an information-theoretical analysis of the UWA channels. We use the Rician fading model to assess the capacity of an underwater acoustic channels, and to evaluate the ergodic channel capacity and the related bandwidth efficiency for both SISO and MIMO systems. In particular, we first analyze the ergodic capacity of the UWA channel with rank-1 channel matrix and no individual path dispersion. We then extend these results to more realistic channel models with full-rank matrix and individual path dispersion. We consider two different scenarios: in one the transmitter has partial CSI and knows the statistics of the channel, while in the other it has no CSI at all. In both scenarios, perfect CSI at the receiver is assumed.

Besides the capacity analysis for unconstrained inputs, a more realistic scenario is to investigate the achievable information rate for Gaussian channels with ISI and input symbols drawn from finite-order modulation alphabets. For this case, analytical results are available and provide upper and lower bounds on the achievable information rate [26] (see [27] for the extension of the bounds in [26] to MIMO systems). None of the existing bounds seem to be suitable for ISI channels with long delay spreads and a sparse multipath structure. Another approach was introduced in [28], according to which we can obtain an unbiased estimate of the information rate by running long simulations of the channel and of the optimal maximum-a-posteriori detector, i.e. the BCJR algorithm. Unfortunately, this approach is infeasible for an UWA environment since the complexity of the BCJR algorithm grows exponentially with the delay spread of the channel, which is very large in UWA channels.

In this chapter, we also develop new bounds on the achievable rates for sparse channels with long memory. We obtain a lower bound which can be achieved by practical receivers, based on minimum-mean squared error (MMSE) channel shortening and suboptimal symbol detection for a reduced-state channel. An upper bound is given in the form of a semi-analytical solution derived using basic information theoretic inequalities, by a grouping of the channel taps into several clusters resulting in a newly defined SIMO channel. We show that the so obtained time-dispersive SIMO channel can be represented by an equivalent SISO channel with a significantly shorter channel memory. The reduced computational complexity allows the use of the BCJR algorithm for the newly defined channel. Exploiting the *sparseness* of the channel impulse response allows us to compute bounds on the achievable information rate that improve those in [26] and [27]. The proposed bounds are illustrated through several sparse channel examples and i.u.d. input symbols, showing that the upper bound significantly outperforms existing bounds. Performance of our lower bound strongly depends on the channel structure, showing best results for minimum-phase and maximum-phase systems.

This chapter is organized as follows. In Section 3.1 we assess the channel spectral efficiency based on the channel measurements from the previous chapter; in Section 3.2 we discuss the ergodic capacity of channels for the multiple-input single-output (MISO) and the MIMO setting with a rank-1 and full-rank channel matrix. In particular, the capacity analysis of flat and frequency-selective fading systems is based on distinguishing two scenarios with different amount of CSI at the transmitter: (1) no CSI, and (2) partial CSI, where only the statistical properties of the channel, but not the actual channel realizations, are known to the transmitter. Due to the long propagation delay, only the second scenario is deemed realistic in a general UWA channel; In Section 3.3, we describe the general framework under which new bounds on the achievable information rate of ISI channels with constrained inputs are derived, and present the performance results of the proposed bounds based on different channel examples; Finally, in the Summary section we give our concluding remarks.

3.1 Spectral Efficiency of UWA Channels using Channel Measurements

In this section, we evaluate the spectral efficiency of an UWA channel using the KAM08 channel measurements. From [20], we use the approximate model for the ambient noise power spectral density

$$10 \log N(f) = n_0 - 18 \log f \ [\text{dB}], \tag{3.1}$$

where the level n_0 is subject to adjustment for a particular UWA channel of interest. For comparison purposes, we show in Figure 3.1.(a) (along with the model (3.1)), the Welch PSD estimate [29] of the ambient noise, obtained from the experimental recordings during the silence periods. The PSD estimate from the environmental data shows a good match to the approximate model in 3.1.

The part (b) of the figure illustrates the histogram of the recorded ambient noise, indicating that this noise can be modeled as Gaussian. Given this noise model, the short-term channel capacity can be computed as

$$C(t_k^*) = \sum_i \Delta f \log_2 \left(1 + \frac{S(f_i)|H(f_i, t_k^*)|^2}{N(f_i)}\right), \tag{3.2}$$

where t_k^* denotes the k-th measurement interval of 12 consecutive transmissions of the single-carrier probe signal (i.e., t_k^* is discrete-time interval from $12(k-1)\Delta L$ to $12k\Delta L - 1$). Δf is a narrow band of frequencies centered at frequency f_i, the index i ranges across the given signal bandwidth, and $|H(f, t_k^*))|$ is the short-term estimate of the channel transfer function magnitude for the time interval t_k^*. $S(f)$ is the spectrum of the transmitted signal which maximizes the channel capacity subject to the constraint on finite transmission power. The optimal spectrum allocation is determined by the water-filling algorithm [30].

By averaging over all short-term estimates of the channel capacity, we obtain an estimate of the ergodic capacity

$$C = \frac{1}{Q} \sum_{q=1}^{Q} C(t_q^*), \tag{3.3}$$

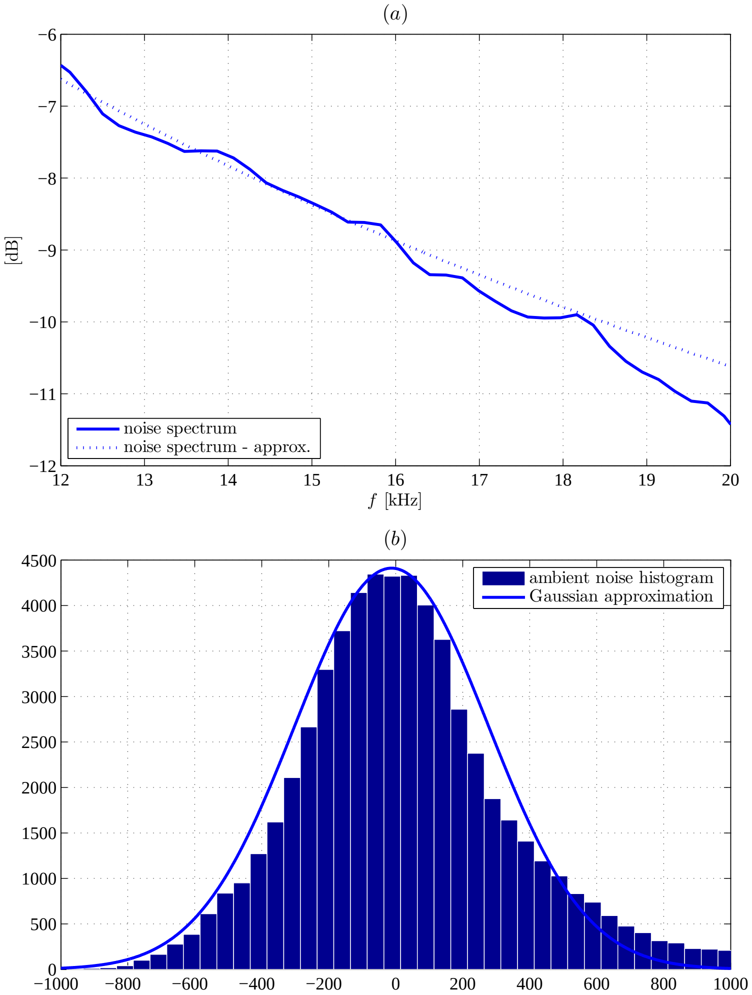

Figure 3.1: Ambient noise spectrum (a) and histogram (b).

where Q is the number of measurement intervals. The spectral efficiency is now obtained by normalizing the ergodic capacity by the bandwidth. Figure 3.2 illustrates the result of averaging the spectral efficiency over $K = 30$ realizations of $|H(f, t_k^*)|$ obtained from measurements of the channel impulse responses in a 57 s time interval from the KAM08 experiment.

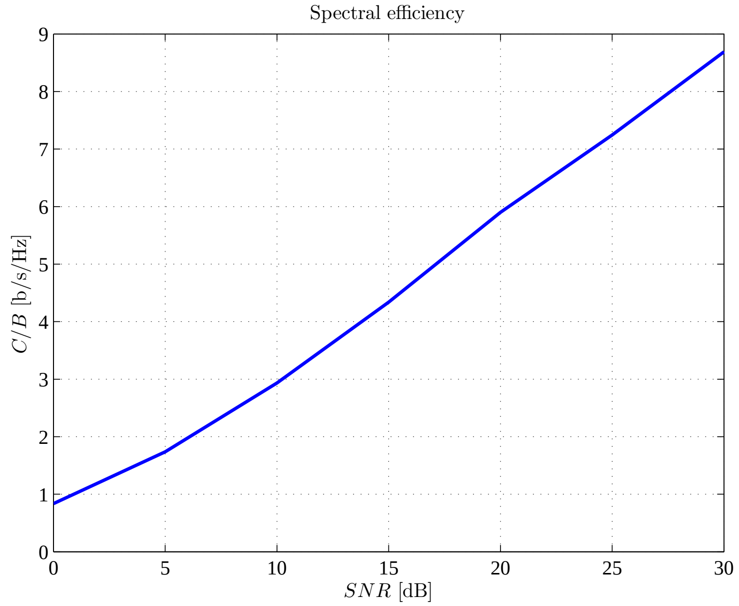

Figure 3.2: Average spectral efficiency.

3.2 Ergodic Capacity

In this section we assess the ergodic capacity of MISO and MIMO UWA channels by exploiting their statistical modeling from the previous chapter. Our focus is on use of the set of measured channel responses, obtained from the signals recorded during the Kauai acoustic communications (KAM08) experiment. We will discuss several cases: flat-fading and frequency-selective fading, various fading distributions, and various levels of the transmitter CSI. Since the complete CSI knowledge at the transmitter is not a realistic scenario, our focus will be on the following two cases: no knowledge, and only statistical knowledge of the channel at the transmitter side.

3.2.1 MIMO Channels with Rank-1 Matrix

For the MIMO system configuration, we assume a spatially correlated channel with N_t transmit and N_r receive elements. The channel matrix of size $N_t \times N_r$

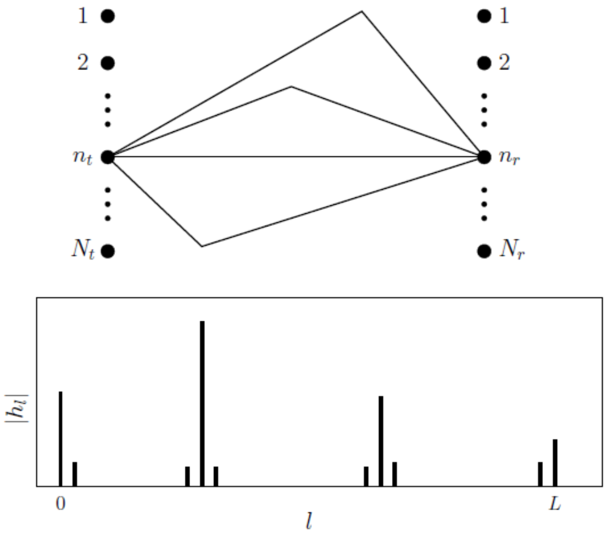

Figure 3.3: Pictorial example of a sparse MIMO channel.

is given by

$$\mathbf{H}_{m,n} = \sum_{l=0}^{L} \mathbf{H}_{l,n}\delta_{m-l}, \tag{3.4}$$

where $\mathbf{H}_l$ is the l-th tap gain matrix, containing $N_t \times N_r$ identically distributed elements which are defined similarly as the 1×1 coefficients h_l in the expression (2.21). Note that in the expression (3.4) we have assumed a uniform tap spacing as in the SISO case (2.20). More insights into the channel model are provided in Figure 3.3. We remark that typically very few channel taps contain energy as a consequence of the sparseness in UWA channel. Therefore, we have that

$$\mathbf{H}_{l,n} = \sqrt{\frac{\Omega_l k_l}{k_l + 1}}\overline{\mathbf{H}}_l + \sqrt{\frac{\Omega_l}{k_l + 1}}\widetilde{\mathbf{H}}_{l,n}, \tag{3.5}$$

where $\{\Omega_l\}$ represents the power of the multipath delay profile of the channel, $\overline{\mathbf{H}}_l$ is a rank-1 matrix of mean values with all elements equal to $(1+i)/\sqrt{2}$, and $\widetilde{\mathbf{H}}_{l,n} = \mathbf{\Theta}_{R,l}^{1/2}\widetilde{\mathbf{H}}_{\omega,l}\mathbf{\Theta}_{T,l}^{1/2}$. Here, $\widetilde{\mathbf{H}}_{\omega,l,n}$ is $N_t \times N_r$ matrix with independent and identically distributed (i.i.d.) complex Gaussian random variables with independent real and imaginary parts, each distributed as $\mathcal{N}(0, 1/2)$, and $\mathbf{\Theta}_{R,l}$ and $\mathbf{\Theta}_{T,l}$ are the receive and the transmit correlation matrices of the l-th tap. We assume that different taps are uncorrelated, i.e. the only correlation in the channel is among elements of the l-th tap, which is defined by $\boldsymbol{\Theta}_{R,l}$ and $\boldsymbol{\Theta}_{T,l}$. This assumption is justified for wideband acoustic systems in which the uniformly-spaced taps of the discrete-time model (3.4) can be associated with the *physical* propagation paths. We also assume that all the elements of the tap with index l have the same distribution, characterized by Ω_l and k_l.

According to (3.4), we will denote by L the total extent of ISI in our channel model. We will also denote by L' the number of significant channel taps, i.e., those taps whose energy is above a pre-specified threshold (typically, $L' \ll L$). In the following analysis we assume that the channel is effected by AWGN modeled as a $N_r \times 1$ circularly symmetric complex Gaussian vector with independent and identically distributed (i.i.d.) elements, with mean zero and variance per component equal to one.

Flat-fading

From the expression (13), a flat-fading channel model is obtained when only a single tap is taken. Omitting the tap's index, the system model is given by

$$\mathbf{y}_n = \mathbf{H}_n \mathbf{x}_n + \mathbf{w}_n, \tag{3.6}$$

where $\mathbf{x}_n$ is an $N_t \times 1$ input vector, $\mathbf{y}_n$ is an $N_r \times 1$ receive vector, and $\mathbf{w}_n$ is an $N_r \times 1$ vector of the circularly symmetric complex Gaussian noise. The ergodic capacity of the channel can be computed as the maximum of the mutual information,

$$C_{N_t,N_r} = \max_{p(\mathbf{x}),E\{\mathbf{x}^H\mathbf{x}\}\leq P} I(\mathbf{x};\mathbf{y}), \tag{3.7}$$

where $p\left(\mathbf{x}\right)$ is the pdf of the input signal vector $\mathbf{x}$ that satisfies a power constraint $E\left\{\mathbf{x}^H\mathbf{x}\right\} \leq P$. For the Gaussian noise channel, regardless of the channel fading distribution, the capacity-achieving distribution for the input signal, under the average power constraint, is circularly symmetric, zero-mean complex Gaussian, as long as there is complete CSI at the receiver and statistical CSI at the transmitter [21,22]. The covariance matrix $\mathbf{R}_{xx} = E\{\mathbf{x}\mathbf{x}^H\}$ of the capacity-achieving input signal depends on the fading distribution, which determines the flat-fading MIMO channel capacity as

$$C_{N_t,N_r} = \max_{tr\mathbf{R}_{xx}\leq P} E_{\mathbf{H}} \left\{ \text{logdet} \left(\mathbf{I}_{N_r} + \mathbf{H}\mathbf{R}_{xx}\mathbf{H}^H \right) \right\}, \tag{3.8}$$

where $\mathbf{I}_{N_r}$ is the identity matrix of size $N_r \times N_r$ and $tr(\cdot)$ denotes the trace of a matrix. If there is no CSI at the transmitter side, the capacity-achieving solution is $tr\mathbf{R}_{xx} = \sum_{i=1}^{N_t} | [\mathbf{R}_{xx}]_{i,i} |$, which is also the optimal solution for the Rayleigh fading case with statistical CSI at the transmitter [21]. In this case, equal power is allocated to all transmitters due to the lack of channel knowledge. For the case of Rician fading with limited (statistical) CSI, the capacity-achieving signal covariance remains unknown.

In Ref. [31], the authors proposed a sub-optimal heuristic solution in the form

$$\mathbf{R}_{xx} = \frac{P}{MN_t(1+k)}(\mathbf{I}_{N_t} + k\mathbf{\Psi}_{N_t}), \tag{3.9}$$

where $\mathbf{\Psi}_{N_t}$ is an $N_t \times N_t$ all-ones matrix. The idea behind this proposition is to exploit the knowledge of the Rician k-factor. If k is zero, we have a Rayleigh fading channel and the optimal solution for the covariance matrix is an identity matrix, while if k tends to infinity, we have a deterministic channel with AWGN, for which the optimal solution obtained by water-filling is the normalized matrix of all ones.

This suboptimal scheme is primarily designed to exploit the specular component in the Rican fading channel. For the Nakagami and log-normal models, the same scheme could cause severe performance degradation, and, hence, we do not consider it.

Frequency-selective Fading

An underwater acoustic channel that is characterized by frequency-selective fading, requires dealing with the memory in the channel as it was given in (3.4). Therefore, the analysis of the ergodic capacity of the MIMO system is given based on the observation of a large block of the input/output signal vectors. We will assume the channel to be constant over each block, so that the choice of the block length M is driven by the coherence time of the channel. Also, we will assume that the only constraint on the signal at the input of the channel is that the average transmission power cannot exceed P.

To assess the ergodic capacity of the Rician frequency selective channel, it is advantageous to represent a MIMO system by an input-output relationship

$$\mathbb{Y} = \mathbb{H}\mathbb{X} + \mathbb{W} \tag{3.10}$$

where $\mathbb{X}$ is an $MN_t \times 1$ space-time block vector of the input block stream, $\mathbb{Y}$ and $\mathbb{W}$ are $MN_r \times 1$ space-time block vectors of the output block stream and noise, respectively, and $\mathbb{H}$ is an $MN_t \times MN_r$ block-diagonal channel matrix. Because of the block-circulant property of the space-time channel matrix $\mathbb{H}$, a Rician frequency-selective MIMO channel can be represented as a set of M parallel independent MIMO channels [23]. One can alternatively think of an OFDM system with M sub-carriers, where each sub-band is affected by flat-fading. Therefore, the ergodic capacity of an equivalent OFDM system is equal to the sum of the ergodic capacities for each sub-band, i.e.,

$$C_{N_t,N_r} = \max_{tr\mathbf{R}_{xx,k} \le P} E\left\{ \frac{1}{M} \sum_{k=0}^{M-1} I_k \right\}, \tag{3.11}$$

where

$$I_k = \log\det\left|\mathbf{I}_{N_r} + \mathbf{H}_{E,k}\mathbf{R}_{xx,k}\mathbf{H}_{E,k}^H\right|,$$

and $\mathbf{H}_{E,k}$ denotes the channel matrix corresponding to the k-th subband. Depending on the amount of CSI at the transmitter, $\mathbf{R}_{xx,k}$ can be determined as optimal (capacity-achieving) or sub-optimal (resulting in information rates below the capacity) as discussed earlier.

Figures 3.4 and 3.5 illustrate the ergodic capacity for two cases: an $N_t \times 1$ MISO system and a 2×2 MIMO system. In each case, the experimental channel with four significant taps (see Figure 3.3) is used to obtain the rank-1 matrix of the mean values in the expression (3.5). Since for each significant tap, the Rician k-factor is on the order of 10, we present flat-fading results for $k = 10$ as a reference. We assume negligible correlation between different transmitter-receiver pairs ($\mathbf{\Theta}_{R,l} = \mathbf{I}_{N_r}$and $\mathbf{\Theta}_{T,l} = \mathbf{I}_{N_t}$). Therefore, numerical integration results should be regarded as idealized, since a realistic UWA system could have non-negligible

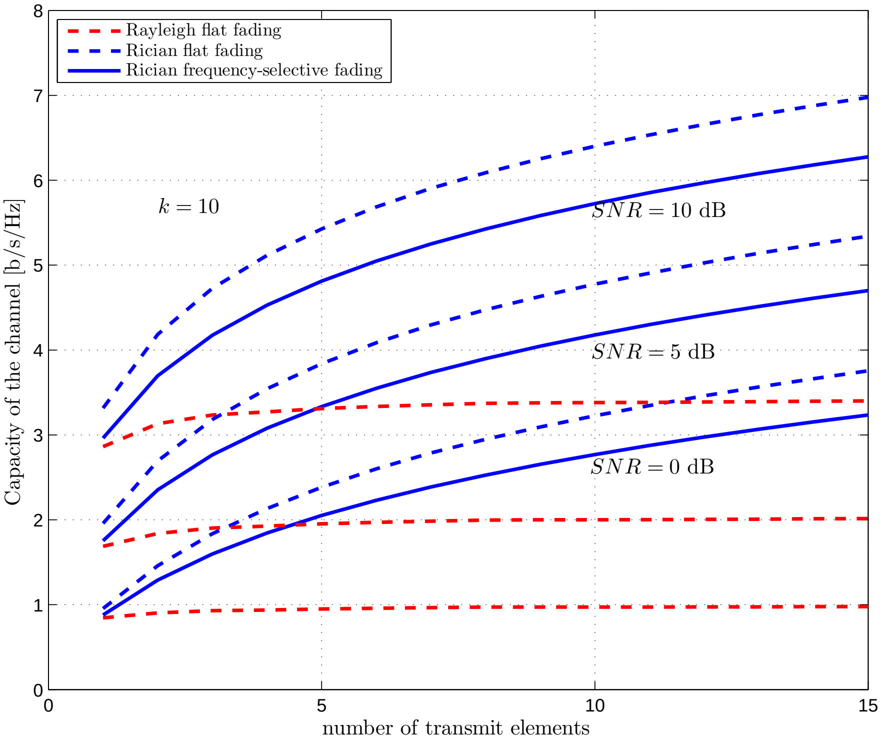

Figure 3.4: Ergodic capacity of an $N_t \times 1$ system for the sub-optimal signaling scheme defined by the expression (3.9).

spatial correlation at both the transmitter and receiver [32], which will degrade the system capacity.

Figure 3.4 illustrates the ergodic capacity for an $N_t \times 1$ system using the sub-optimal signaling scheme given by the expression (3.9). The information rates obtained by the sub-optimal signaling scheme are close to the capacity bound [31], especially for values of k on the order of 10 or more. Results for Rayleigh fading are provided as a reference, and we observe that the ergodic capacity is clearly greater in the Rician case.

Figure 3.5 illustrates the achievable information rates for different fading distributions under normalized second and fourth moments of the underlying distributions. Note that the Rician frequency-selective channel given in (3.10) shows poorer performance than the idealized flat-fading scenarios as well as Rayleigh

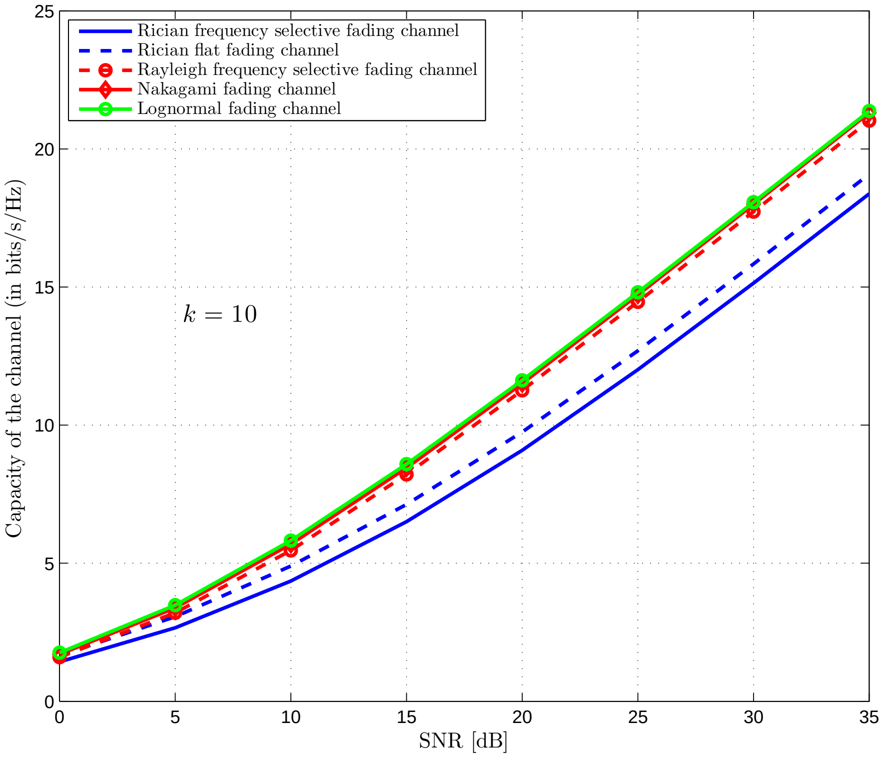

Figure 3.5: Ergodic capacity of a 2 × 2 system with no CSI at the transmitter.

frequency-selective channel. Performance will be degraded since the presence of the specular components in the rank-1 matrix of the mean values is not exploited optimally. This is especially emphasized for large Rician k-factors when the channel matrix in (3.4) becomes ill-conditioned. Therefore, even though a Rician channel can potentially provide greater capacities, we are not able to exploit this advantage due to the lack of the channel knowledge at the transmitter side. At the same time, Nakagami and log-normal fading will provide well-conditioned channel matrices, resulting in similar capacities due to matching of the higher moments. We should also note that the frequency-selectivity of the channel will not degrade system performance in the case of Rayleigh fading. This is true even for the Nakagami and log-normal channel because of the well-conditioned channel matrices, and matching of the higher moments will lead to the performance close to the Rayleigh fading scenario (both flat-fading and frequency-selective). Therefore, assuming the Rician model for an UWA channel, a system designer can exploit advantageous statistical knowledge of the channel at the transmitter side by implementing a receiver-transmitter feedback, and conveying information about slowly-varying statistical parameters of the underlying Rician fading distribution (e.g., the distribution mean, the variance and/or Rician k-factor). By designing adaptive space-time coding techniques which utilize these fading parameters the performance of a MIMO UWA system can be significantly improved.

3.2.2 MIMO Channels with the Full-rank Matrix

Let us define the discrete-time channel model as in (3.4) and (3.5). In contrast to the previous subsection, here $\bar{\mathbf{H}}_l$ is a deterministic matrix (i.e., the mean-value matrix of the Rician process) whose Frobenius norm is normalized to $\left\|\bar{\mathbf{H}}_l\right\|_F^2 = N_t N_r$ for all values of l, while $\tilde{\mathbf{H}}_l$ contains the random channel components, and can be written as

$$\tilde{\mathbf{H}}_l = \mathbf{\Theta}_{R,l}^{1/2} \tilde{\mathbf{H}}_{\omega,l} \mathbf{\Theta}_{T,l}^{1/2} \; , \tag{3.12}$$

where $\tilde{\mathbf{H}}_{\omega,l}$ is an $N_r \times N_t$ matrix of independent zero-mean complex Gaussian random variables whose Frobenius norm is $\left\|\tilde{\mathbf{H}}_{\omega,l}\right\|_F^2 = N_t N_r$ for all values of l, and

$\mathbf{\Theta}_{R,l}$ and $\mathbf{\Theta}_{T,l}$ are the receive and the transmit correlation matrices of the l-th tap. As in the previous subsection, we assume that different taps are uncorrelated, i.e., the only correlation in the channel is among the elements of the l-th tap, which is defined by $\mathbf{\Theta}_{R,l}$ and $\mathbf{\Theta}_{T,l}$.

Frequency-selective Fading

Similarly as in the previous subsection, the problem of the ergodic capacity evaluation can be conveniently approached in the frequency domain.

For the full-rank matrix of the channel mean values in (3.4), the sub-optimal covariance matrix for the i-th sub-band is given by

$$\mathbf{R}_{xx,i} = \frac{P}{MN_t(1+k_i)}(\mathbf{I}_{N_t} + k_i \mathbf{\Psi}_{N_t,i}), \tag{3.13}$$

where k_i is the Rician k-factor for the i-th sub-band, and $\mathbf{\Psi}_{N_t,i}$ is the $N_t \times N_t$ matrix that provides the exact water-filling solution in the case of a deterministic channel with AWGN when $k_i \to \infty$. The rationale behind this idea is to exploit the knowledge of the Rician k-factor in order to weight optimal solutions for the covariance matrix in two limiting scenarios: Rayleigh fading and deterministic channel.

In Figure 3.6 and Figure 3.7 we illustrate the ergodic capacities for two different 2×2 MIMO systems. The channel parameters have been set according to the data collected in the KAM08 experiment, which was conducted in shallow water off the western coast of Kauai, Hawaii, in June 2008. In both cases, the channel has length $L = 52$ and $L' = 4$ significant taps, with $\Omega_0 = 0.25$, $\Omega_{21} = 0.5$, $\Omega_{34} = 0.15$ and $\Omega_{52} = 0.1$. The values of k_l are all equal to 10, and the correlation between different transmit-receive pairs is neglected ($\mathbf{\Theta}_{R,l} = \mathbf{I}_{N_r}$ and $\mathbf{\Theta}_{T,l} = \mathbf{I}_{N_t}$). The results in Figure 3.6 refer to a channel where all $\bar{\mathbf{H}}_l$'s in (3.5) are different full-rank matrices. In this case the eigenvalue distribution of the matrix of the channel mean values for each sub-band tends to a uniform distribution. We note that the channel capacity is slightly greater than the capacity of the Rayleigh fading channel which is presented as a reference. Despite the sub-optimality of the heuristic solution, we observe a degradation in the performance of this signaling scheme with respect

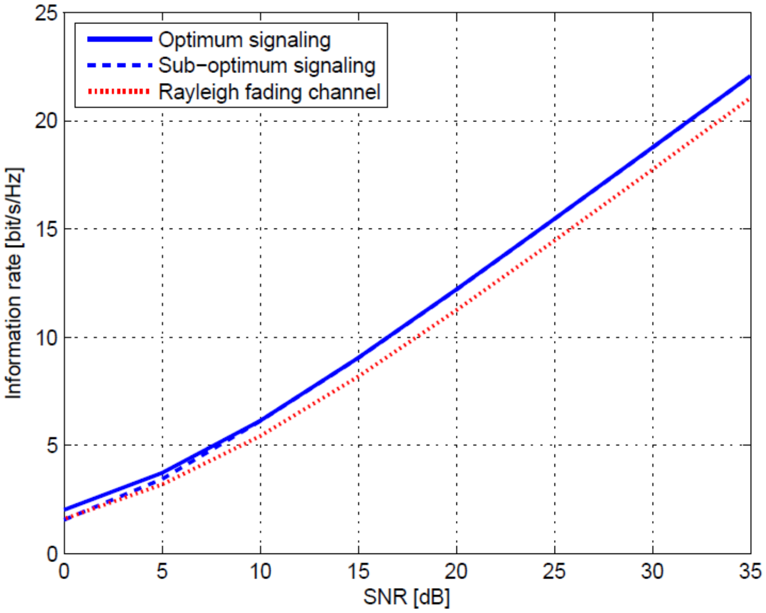

Figure 3.6: Ergodic capacity of a 2 × 2 system for uniform-like eigenvalue distribution of matrices of the channel mean values.

to the optimal one only at low SNR. Even though it is a sub-optimal solution, due to the low complexity implementation, it seems to be a convenient choice for system design. The results in Figure 3.7 refer to a channel where we intentionally assumed that all full-rank matrices of the channel mean values are identical, which will result in a non-zero eigenvalue distribution as opposed to the previous scenario. Clearly, the channel capacity is degraded in comparison to the results presented in Figure 3.6. We also note that the sub-optimal solution causes a more significant degradation than in the former case, which suggests that the heuristic solution is more effective when the eigenvalue distribution of the matrix of the channel mean values tends to a uniform distribution.

3.3 Information Rate for Standard Modulations

In this section, we consider the evaluation of the achievable information rate of ISI channels when the input symbols are constrained to take on values from

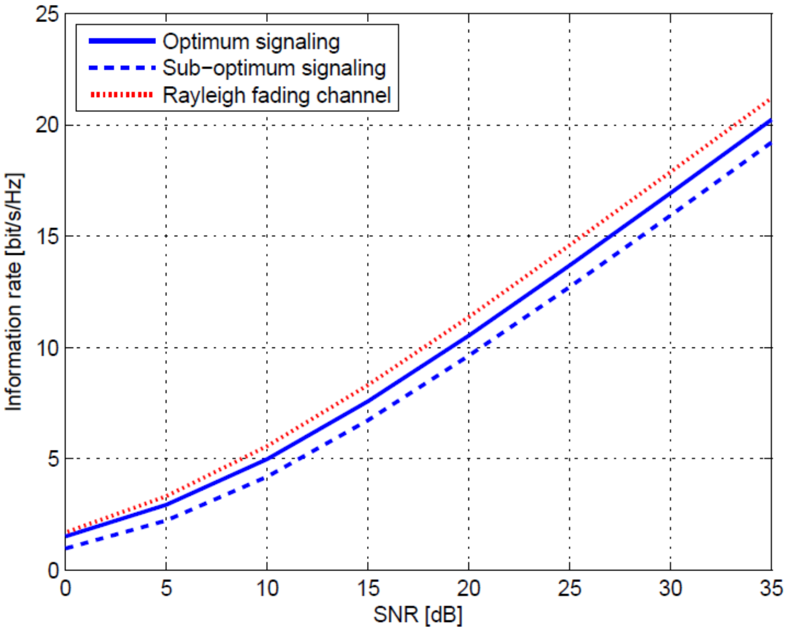

Figure 3.7: Ergodic capacity of a 2 × 2 system for non-uniform-like eigenvalue distribution of matrices of the channel mean values.

a finite signal constellation. As we have observed, shallow water acoustic channels typically exhibit extensive multipath spreads, resulting in ISI spans of tens or even hundreds of symbols for single-carrier systems. However, very few propagation paths carry significant energy even though severe multipath propagation spans a large number of symbol intervals, resulting in sparse ISI channels. For discrete-time ISI channel models with additive white Gaussian noise there is no single-letter expression for the achievable information rate that can be supported with a particular modulation alphabet [26]. Under independent and uniformly distributed (i.u.d.) or Markov input constraints, the achievable information rate can be estimated as accurately as desired by means of a simulation-based algorithm described in [33] [34]. This approach requires simulation of forward recursion of the full-complexity BCJR algorithm [33] with a trellis whose complexity increases exponentially with channel memory in order to estimate the joint probability of the output sequence. The so obtained probability is used to compute an estimate of the mutual information between the input and output sequences. Analytical simplifications are not available, and due to the long channel memory, this simulation-based analysis is basically infeasible for practical UWA channels.

The only tools for the characterization of the information rate of channels with long memory are upper and lower bounds on the achievable information rates. Shamai *et al.* [26] [35] investigated bounds on the capacity and the achievable information rate of the channel with memory excited by identically distributed (not necessary independent) inputs. They provided lower and upper bounds which can be interpreted as the average mutual information that corresponds to the output of an ideal decision feedback equalizer (DFE) with errorless past decisions (power degradation argument),[1] and a memoryless channel with independent and identically distributed (i.i.d.) inputs that collect the overall energy content of the channel impulse response (power enhancement argument),[2] respectively. While these bounds are obtained in the form of an integral, Arnold *et al.* [36] presented a simulation-based upper bound computed by means of a reduced-state recursion of the BCJR algorithm. Even though this bound is very tight for high SNR, it is very loose for low SNR, due to the fact that the probability mass of the output sequence is spread over all states. In [36] and [37], lower bounds are obtained under mismatched decoding, that is, when the BCJR algorithm assumes that the channel is governed by a transition law that differs from the actual channel law. Unfortunately, these bounds are loose, since minimum-phase representation of a sparse channel with a long memory doesn't collect a significant portion of the energy in the first few channel taps. The same observation holds for the matched-filter representation of the ISI channel, considered in [37]. A more advanced method is developed in [38], where the auxiliary channel for mismatched decoding is constrained to be an arbitrary finite-state machine, and the conditional probabilities between states are optimized at each stage of the algorithm. In a recent work [39], a proposed method for the computation of a lower bound requires evaluation of the

---

[1] In [26] a lower bound on the achievable information rate is obtained based on the ideal post-cursor cancellation where power degradation results from the channel memory introduced by ISI.

[2] In [26] an upper bound on the achievable information rate corresponds to single symbol transmission. For uncoded communications this leads to matched filter lower bound on the error probability as a result of power enhancement.

magnitude sum of the precursor ISI terms as well as identification of the dominant terms as seen at the output of the MMSE-DFE. The computational load required to obtain a tight bound is high, since the number of dominant terms of the precursor ISI for the sparse channels with large delay spreads is potentially very large. These bounds can be easily extended to MIMO systems based on the results given in [27] and [28]. None of the existing bounds seem to be suitable for ISI channels with long delay spreads and a sparse multipath structure.

In this section, we investigate bounds on the information rate of a deterministic channel with long memory and sparse multipath structure, assuming i.u.d. inputs drawn from a finite-order modulation alphabet. We propose a lower bound achievable by practical receivers, extending the initial analysis in [40] where a particular reduced-complexity soft-output detection scheme is employed based on the application of the sum-product algorithm to the factor graphs [41]. We analyze the performance of the receiver composed of a finite length impulse response (FIR) filter designed to reduce the number of channel states by applying a channel shortening that does not completely eliminate the ISI. We apply the modified BCJR algorithm of the trellis size matched to the memory of the reduced-state channel.

We propose a simulation-based approach for the computation of an upper bound. We group channel taps into several clusters resulting in a newly defined SIMO channel with a reduced channel memory. From the so obtained SIMO channel we derive an equivalent single-input single-output channel based on maximal ratio combining (MRC) using the maximum likelihood (ML) criterion. Using the BCJR algorithm we estimate the achievable information rate for the derived SISO channel and use it to obtain an upper bound on the achievable information rate of the sparse channel of interest. Therefore, we develop our lower and upper bounds by utilizing the modified and the classical BCJR algorithm, respectively, and operating on a trellis of reduced computational complexity.

3.3.1 System Model

We consider the transmission scheme depicted in Figure 3.8, where it is assumed that the channel input is a sequence of i.u.d. complex-valued symbols drawn from finite-order modulation alphabet of cardinality M, and transmission is from time index $n = 0$ to $n = N - 1$. This symbol sequence $\boldsymbol{x} = \{x_n\}_{n=0}^{N-1}$ is obtained by a direct mapping of information bits to symbols of the modulation alphabet. Assuming observation intervals that are shorter than the coherence time of the channel, and ideal synchronization, the physical propagation environment can be modeled as a fixed discrete-time channel, so that the received sample at time index n is given as [5]

$$y_n = \sum_{l=0}^{L} h_l x_{n-l} + w_n, \tag{3.14}$$

where $\{w_n\}_{n=0}^{N-1}$ are i.i.d. complex Gaussian random variables with zero-mean and variance σ^2 per dimension, $\boldsymbol{h} = \{h_n\}_{n=0}^{n=L}$ represents the discrete-time equivalent channel impulse response, and L is the channel memory. We focus on channels with long memory L , and very few non-zero channel taps h_l in order to emphasize the channel *sparseness*. We assume that $\boldsymbol{h}$ and σ^2 are known at the receiver.

The achievable information rate supported by the system (3.14) can be expressed as [42]

$$I(X;Y) = \lim_{N\to\infty} \frac{1}{N} I(\boldsymbol{x};\boldsymbol{y}), \tag{3.15}$$

which can be estimated as accurately as desired by using the simulation-based BCJR algorithm. Note that $\boldsymbol{x}$ is not defined for negative indices, for which we assume that $x_n = 0$. This fact will lead to an "edge effect" with a diminishing effect on the term from (3.15), as N tends to infinity. This approach requires simulation of a full-complexity forward recursion of the BCJR algorithm that processes a trellis with M^L states in order to estimate the joint probability of the output sequence. Due to the large values of L, this simulation-based analysis is practically infeasible. Therefore, upper and lower bounds on $I(X;Y)$ are required to characterize the achievable information rate for channels with long memory.

3.3.2 Lower Bound on $I(X;Y)$ – Preliminaries

A lower bound can be obtained based on the data-processing inequality [42], by considering an arbitrary receiver that processes the received samples $\boldsymbol{y}$, and

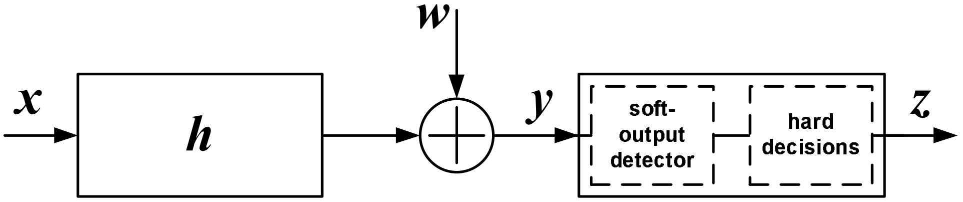

Figure 3.8: System model.

produces the decisions $\boldsymbol{z} = \{z_n\}_{n=0}^{N-1}$. In the case of hard-output detection, z_n is the estimate of the symbol x_n, and thus belongs to the signal constellation. For both hard and soft-output detection, the data-processing inequality guarantees that

$$\lim_{N\to\infty} \frac{1}{N} I\left(\boldsymbol{x};\boldsymbol{z}\right) = I\left(X;Z\right) \leq I\left(X;Y\right) \tag{3.16}$$

The mutual information in (3.16) still involves infinite-length sequences, which makes it impractical to compute when the channel and the receiver have memory. However, the chain rule for the mutual information guarantees that $I(X;Z)$ is lower bounded by

$$I_{LB} = I\left(x_n; z_n\right) \tag{3.17}$$

for each n at which the system is not affected by transient effects. Note that the evaluation of I_{LB} requires computation of the mutual information between elements of the sequences, and not between the entire sequences as in (3.16). Hence, similar to [40] where a different soft-output detector is employed, we can evaluate I_{LB} by first estimating the joint statistics of x_n and z_n through long simulations of the channel and the receiver, and then employing numerical methods. The specific receiver adopted for the computation of the lower bound in (3.17) does not affect its validity, but does affect the tightness of the inequality. In fact, the value of I_{LB} gives the ultimate information rate supported by a system adopting that specific receiver, when concatenated with a fully-interleaved outer code [43]. Hence, the better the receiver, the tighter the lower bound. Note that iterating between the outer channel decoder and the soft-output detector will increase the information rate at the output of the iterative receiver. Unfortunately, there is no information theoretic support that this side information will not violate the lower bound condition, since the data processing inequality is no longer applicable.

Optimal detection is based on the computation of the maximum *a posteriori* probability (APP) $P(x_n|\, \boldsymbol{y})$ of each detected modulation symbol x_n for each time instance n, given the received sequence $\boldsymbol{y} = \{y_n\}_{n=0}^{N-1}$. Unfortunately, providing APP as soft-output information is infeasible, since the optimal soft-output BCJR detector is impractical for implementation due to the long memory L of the channel. Therefore, suboptimal soft-output detection schemes are employed. This topic will be addressed later in this section.

3.3.3 Upper Bound on $I\,(X;Y)$ – Preliminaries

The upper bound in [26] is obtained based on the information rate computation of a memoryless channel with i.i.d. inputs that collects the overall energy content of the channel impulse response (power enhancement argument). The framework under which this bound is derived motivate us to propose a new class of upper bounds with the tightness governed by the multipath structure of the channel.

In general, we can re-write the mutual information $I(\boldsymbol{x};\boldsymbol{y})$, by applying the chain rule [26]:

$$\begin{aligned} I(\boldsymbol{x};\boldsymbol{y}) &= I(\boldsymbol{x}_0^{N-1};\boldsymbol{y}_0^{N-1}) \\ &= \sum_{n=0}^{N-1} I(x_n;\boldsymbol{y}_0^{N-1}|\, \boldsymbol{x}_0^{n-1}) \\ &\le \sum_{n=0}^{N-1} I(x_n;\boldsymbol{y}_0^{N-1}|\, \boldsymbol{x}_0^{n-1}, x_{n+1}, x_{n+2}, ..., x_{N-1}), \end{aligned} \tag{3.18}$$

where the inequality follows from the fact that we consider i.u.d. channel inputs $\boldsymbol{x}$. An abbreviated form $\boldsymbol{x}_i^j$ is used to denote the sequence $\{x_n\}_{n=i}^{j}$. This argument, following the derivation in [26], will lead to the well known upper bound on the achievable information rate for i.i.d. inputs based on MRC (power enhancement argument):

$$I\,(X;Y) = \lim_{N\to\infty} \frac{1}{N} I\,(\boldsymbol{x};\boldsymbol{y}) \le I(x_n;\rho x_n + w_n), \tag{3.19}$$

where

$$\rho = \sqrt{\sum_{l=0}^{L} |h_l|^2}. \tag{3.20}$$

Generally, this bound is not tight for channels with large delay spreads and strong ISI, meaning that the channel energy ρ is more or less evenly distributed among all channel taps. The reason is that collecting of the channel energy ρ into a single channel tap maximizes the achievable information rate among all ISI channels with the same energy constraint. This fact indicates that different channels with the same energy constraint support rates that are between the rates of the original channel (3.14) and the single-tap channel (3.19). In fact, we will see later in the section that a tighter bound on the achievable information rate can be obtained by grouping the channel taps into clusters as in (3.19), and exploiting the similar method as MRC. This will transform our channel into the newly defined SIMO channel with a reduced size memory, which leads to a less demanding computation of the achievable information rate of the modified channel, i.e., an upper bound on the information rate of the original one.

3.3.4 Lower Bound on Information Rate with i.u.d. Inputs

In order to compute the lower bound on the achievable information rate as in (3.17) suboptimal detectors are required that exploit the knowledge of the channel sparseness.

We have considered several receivers in the literature and found that the best performance/ complexity trade-off is provided by that proposed in [41], a reduced-complexity soft-output detector based on the application of the sum-product algorithms to factor graphs representing the joint APP of the transmitted symbols. The most attractive features of this receiver are its computational complexity, which increases exponentially not with the channel memory L (as in the BCJR algorithm), but with the number of non-zero taps. The advantage of this algorithm is very clear in the case of UWA channels characterized by long delay spreads and a sparse multipath structure. It was verified that the sum-product algorithm approaches the performance to the optimal BCJR algorithm [41] that

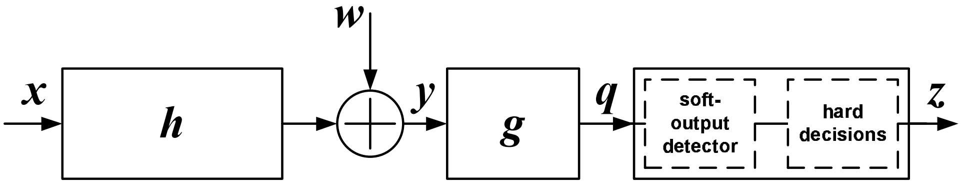

Figure 3.9: Reduced-complexity receiver structure.

computes exact marginal APPs of the transmitted symbols when the factor graph does not have cycles of length less than 6. The proposed lower bound significantly improves the lower bound from [35] as demonstrated by numerical examples previously reported in [40]. However, the receiver used in [40] requires multiple iterations that are critical for the proper functionality of the detector, and calibration of various parameters, which is very challenging for typical UWA channels with large delay spreads. There are also other suboptimal detectors that exploit knowledge of the channel sparseness [44] [45].

We consider an alternative receiver structure consisting of a channel shortening filter, and a modified soft-output BCJR detector employed with the objective of obtaining a suboptimal soft-output detector with a reasonable performance/complexity trade-off, and computational complexity that is lower than the receiver proposed in [41]. Essentially, bounds from this section and [40] originate from the same idea – to exploit the detector which is suitable for a sparse multipath structure and long channel delays. The receiver shown in Figure 3.9 is discussed in the rest of this section.

Prefiltering

Suboptimal detectors can be derived by reducing the memory of the channel at the input of the detector. For this purpose we consider linear channel shortening filters. Prefiltering will usually result in loss of the sparse structure of the channel, which makes our approach applicable even to general (non-sparse) ISI channels. The channel shortening filter in conjunction with the classical BCJR algorithm is no longer the optimal detector for soft-output detection and modifications to the classical BCJR are required in order to improve its performance. Nevertheless, the filter coefficients can be computed efficiently based on various design methods available in the literature, leading to significant complexity reduction.

In this section, the MMSE method similar to the one described in [46] [47] is used to design linear channel shortening filters. Let us define a target channel impulse response $\boldsymbol{f} = \{f_n\}_{n=0}^{n=L'}$ where L' is the memory of the target channel impulse response, and a MMSE equalizer filter $\boldsymbol{g} = \{g_n\}_{n=0}^{n=\bar{L}}$ with finite memory $\bar{L}$. The objective of the MMSE-based approach is to find the target function $\boldsymbol{f}$ and the equalizer filter $\boldsymbol{g}$ simultaneously by minimizing the mean-squared error between the equalizer output and the desired target. By defining the error sequence $\epsilon_n = \boldsymbol{f}^H \boldsymbol{x}_{n-L'}^n - \boldsymbol{g}^H \boldsymbol{y}_{n-\bar{L}}^n$, and under the assumption of independent inputs and independent noise samples, the MSE can be written as [47]

$$E\{|\epsilon_n|^2\} = \epsilon^2 = \boldsymbol{f}^H R_{xx} \boldsymbol{f} + \boldsymbol{g}^H R_{yy} \boldsymbol{g} - \boldsymbol{f}^H R_{xy} \boldsymbol{g} - \boldsymbol{g}^H R_{yx} \boldsymbol{f}, \tag{3.21}$$

where $R_{xx} = E\{\boldsymbol{x}_{n-L'}^n (\boldsymbol{x}_{n-L'}^n)^H\}$, $R_{yy} = E\{\boldsymbol{y}_{n-\bar{L}}^n (\boldsymbol{y}_{n-\bar{L}}^n)^H\}$ and $R_{xy} = E\{\boldsymbol{x}_{n-L'}^n (\boldsymbol{y}_{n-\bar{L}}^n)^H\}$ are $(L'+1) \times (L'+1)$ correlation, $(\bar{L}+1) \times (\bar{L}+1)$ correlation and $(L'+1) \times (\bar{L}+1)$ cross-correlation matrices, respectively.

Minimization of the MSE given by (3.21) with respect to both $\boldsymbol{f}$ and $\boldsymbol{g}$, is done under the constraint that $g_0 = 1$ to avoid the trivial solution $\boldsymbol{f} = 0$ and $\boldsymbol{g} = 0$. This constraint corresponds to the minimum-phase solution in the decision feedback equalizer design problem for large L'. In [46] it is shown that this constraint introduces less correlation in the noise at the output of the equalizer filter than other constraints such as fixed energy or partial response targets. In order to minimize the MSE subject to $g_0 = 1$, we write the Lagrangian in the following form:

$$\epsilon^2 = \boldsymbol{f}^H R_{xx} \boldsymbol{f} + \boldsymbol{g}^H R_{yy} \boldsymbol{g} - \boldsymbol{f}^H R_{xy} \boldsymbol{g} - \boldsymbol{g}^H R_{yx} \boldsymbol{f} - 2\lambda(\boldsymbol{e}_0^H \boldsymbol{f} - 1), \tag{3.22}$$

where $\boldsymbol{e}_0$ is a unit vector with first element having value 1 and all other elements set to 0. Taking the derivative of MSE with respect to $\boldsymbol{f}$, we obtain the following solution for the optimal target response at the output of the equalizer filter:

$$\boldsymbol{f}_{opt} = \frac{(R_{xx} - R_{xy} R_{yy}^{-1} R_{yx})^{-1} \boldsymbol{e}_0}{\boldsymbol{e}_0^H (R_{xx} - R_{xy} R_{yy}^{-1} R_{yx})^{-1} \boldsymbol{e}_0}. \tag{3.23}$$

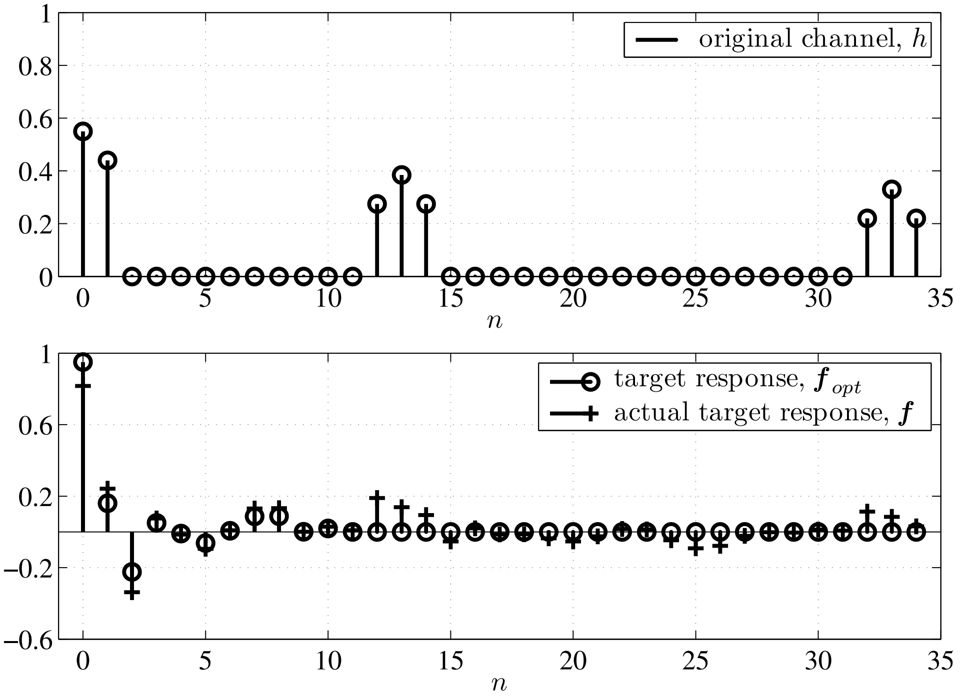

Figure 3.10: Example of the optimal and actual target response with $L' = 9$ for an underwater channel impulse response with $L = 34$.

Consequently, the optimal solution for the equalizer filter is obtained as

$$\boldsymbol{g}_{opt}^{H} = \boldsymbol{f}_{opt}^{H} R_{xy} R_{yy}^{-1}. \tag{3.24}$$

We note that other constraints may result in a lower MSE in (3.21), but at the expense of increased correlation among noise samples at the output of the equalizer filter $\boldsymbol{g}$.

In Figure 3.10, we provide an example of the channel shortening filter applied to a shallow water acoustic channel impulse response (measured in KAM08 experiment [19]). The optimal target channel impulse response $\boldsymbol{f}_{opt}$ is assumed to be of length $L' = 9$. We observe that the actual target channel impulse response $\boldsymbol{f}$ (obtained by convolving $\boldsymbol{h}$ and $\boldsymbol{g}_{opt}$) is close to $\boldsymbol{f}_{opt}$ (i.e. for $n \geq L' + 1$, the channel taps f_n are sufficiently small).

We assume that the channel output (3.14) is filtered by the linear equalizer $\boldsymbol{g}_{opt}$ from (3.24) and produces the output sequence $\boldsymbol{q} = \{q_n\}_{n=0}^{N-1}$. We consider equalizer filters which are nonsingular (this is guaranteed from the MMSE design [48]), or filter approximations [49], for which there exists a stable invertible filter. Under this condition, we can write

$$I\left(X;Y\right)=I\left(X;Q\right)=\lim_{N\to\infty}\frac{1}{N}I\left(\boldsymbol{x};\boldsymbol{q}\right), \tag{3.25}$$

where the sequence $\boldsymbol{q}$ preserves the information rate supported by the original channel output sequence $\boldsymbol{y}$. The achievable information rate $I\left(X;Q\right)$ is bounded as in (3.16) by employing a soft-output detector to the prefiltered sequence. Therefore, following the channel shortening filter $\boldsymbol{g}_{opt}$ given by (3.24), the classical BCJR algorithm with a $M^{L'}$ state trellis can be applied to the prefiltered sequence $\boldsymbol{q}$. Note that the classical BCJR is mismatched by coloring of the noise at the output of the equalizer, and a difference between the actual and the optimal target impulse responses as illustrated in Figure 3.10.

Modified BCJR

The noise correlation induced by $\boldsymbol{g}_{opt}$ degrades the performance of the classical BCJR algorithm significantly, and modifications of the classical algorithm are required. Therefore, we propose a modified BCJR detector based on noise prediction. For this trellis-based algorithm, let us define, at each time instance n, the state s_n as

$$s_n=(x_{n-L'},x_{n-L'+1},...,x_{n-2},x_{n-1}). \tag{3.26}$$

The branch metric of the classical BCJR algorithm is given as [50] [51]

$$\gamma_n(x_n,s_n)=\frac{1}{M}\exp\left(-\frac{1}{2\sigma^2}\left|y_n-\sum_{l=0}^{L}h_l x_{n-l}\right|^2\right). \tag{3.27}$$

Ideally, the branch metrics (3.27) can be modified by whitening the noise with infinite length impulse response filters. Because the linear filter design based on the MMSE criterion presented in the previous subsection introduces less noise correlation than other similar methods, we observed that an ideal infinite-length invertible filter can be approximated reliably by an FIR filter $\boldsymbol{g}_{inv}=\{g_{inv,n}\}_{n=0}^{\hat{L}}$, where $\hat{L}$ is the memory of the finite length approximation. Therefore, following similar arguments as in [52], the branch metric in (3.27) can be modified as

$$\gamma_n^*(x_n, \boldsymbol{s}_{n-\hat{L}}^n) = \frac{1}{M}\exp\left(-\frac{\left|\boldsymbol{g}_{inv}^H\left(\boldsymbol{q}_{n-\hat{L}}^n - \boldsymbol{p}(x_n, \boldsymbol{s}_{n-\hat{L}}^n)\right)\right|^2}{2\sigma^2}\right), \tag{3.28}$$

where $\boldsymbol{p}(x_n, \boldsymbol{s}_{n-\hat{L}}^n) = \{p_k\}_{k=n-\hat{L}}^{k=n}$ is a sequence of noiseless outputs of the target channel impulse response, $p_k = \sum_{l=0}^{L'} f_l x_{k-l}$. Since our modified BCJR algorithm has a trellis of size $M^{L'}$, the channel inputs x_{n-i}, for $L' + 1 \leq i \leq L' + \hat{L}$, are not available at time instant n, forcing us to use tentative decisions $\hat{x}_{n-i}$. These decisions can be obtained during a modified forward recursion of the BCJR algorithm as described in the remainder of this section.

Besides the branch metric formulation, an important part of the classical BCJR algorithm is given by two recursive equations [51]:

$$\alpha_{n+1}(s_{n+1}) = \sum_{x_n, s_n} I(x_n, s_n, s_{n+1})\gamma_n(x_n, s_n)\alpha_n(s_n), \tag{3.29}$$

$$\beta_n(s_n) = \sum_{x_n, s_{n+1}} I(x_n, s_n, s_{n+1})\gamma_n(x_n, s_n)\beta_{n+1}(s_{n+1}), \tag{3.30}$$

where $\alpha_n(s_n)$ and $\beta_n(s_n)$ are the state metrics of *forward recursion* (3.29) and *backward recursion* (3.30), respectively. $I(x_n, s_n, s_{n+1})$ is the indicator function equal to 1 if x_n, s_n and s_{n+1} satisfy the trellis constraints, and 0 otherwise. We will assume that the first state $\bar{s}_0$ and the last state $\bar{s}_{N+1}$ of the BCJR algorithm are known. Therefore, recursions (3.29) and (3.30) are initialized by $\alpha_0(\bar{s}_0) = 1$ and 0 for other state metrics, and $\beta_{N+1}(\bar{s}_{N+1}) = 1$ and 0 for other state metrics, respectively. The modification of the forward recursion given in equation (3.29) is based on the concept of survivor paths from the classical Viterbi algorithm [53] and it is given by

$$\alpha_{n+1}^*(s_{n+1}) = \max_{x_n, s_n} I(x_n, s_n, s_{n+1})\gamma_n^*(x_n, s_n)\alpha_n^*(s_n). \tag{3.31}$$

Once the tentative decisions $\hat{x}_{n-i}$ for $L' + 1 \leq i \leq L' + \hat{L}$ are obtained, we can compute the modified backward recursion in the following form:

$$\beta_n^*(s_n) = \sum_{x_n, s_{n+1}} I(x_n, s_n, s_{n+1})\gamma_n^*(x_n, s_n)\beta_{n+1}^*(s_{n+1}). \tag{3.32}$$

Note that the concept of survivor paths is not needed for backward recursion since tentative decisions are already available. We should point out that determining tentative decisions from the forward recursion (3.31) is more reliable in the case of a minimum-phase channel, suggesting that without any loss in the achievable information rate, every channel of interest should be transformed to a minimum-phase representation before the modified BCJR detector is employed. For maximum-phase systems, the alternative is to use the backward recursion to determine tentative decisions on transmitted symbols. The lower bound (3.17) is computed numerically by estimating the first order joint statistics of the channel input x_n and the soft-output z_n of the modified BCJR algorithm, as done in [43].

Note that the proposed receiver structure is applicable to non-sparse ISI patterns as well, but the effectiveness of the proposed approach is strictly limited by the design of the channel shortening filter. The equalizer filter from (3.24) would have to suppress most of the ISI which is outside the scope of the memory length L' of the target channel impulse response (3.24). We conducted extensive simulations which indicate that channel shortening is not effective for the channel with long memory and non-sparse structure, if the memory of the target channel impulse response is reasonably short. The reason is a high correlation among the noise samples at the output of the equalizer, which seriously limits the performance of the modified BCJR algorithm.

3.3.5 Upper Bound on Information Rate with i.u.d. Inputs

Let us consider a SIMO ISI channel with the channel outputs given by

$$y_{k,n} = h_{k(L'+1)}x_n + h_{k(L'+1)+1}x_{n-1} + ... + h_{k(L'+1)+L'}x_{n-L'} + w_{k,n}, \tag{3.33}$$

where $k = 0, 1, ..., K-1$, $K = \lceil (L+1)/(L'+1) \rceil$, $n = 0, 1, ..., N-1$ and $w_{k,n}$ is i.i.d. complex Gaussian random variable in both indices k and n, with zero-mean and variance σ^2 per dimension. The number of outputs (clusters) of the SIMO ISI channel is bounded by $K \leq L$, and depends on the sparse structure of the original channel (3.14). The achievable information rate of the SIMO channel from (3.33) can be expressed as

$$I(X;Y_1,Y_2,...,Y_K) = \lim_{N\to\infty}\frac{1}{N}I(\boldsymbol{x};\boldsymbol{y}_1,\boldsymbol{y}_2,...,\boldsymbol{y}_K), \tag{3.34}$$

where $\boldsymbol{y}_k = \{y_{k,n}\}_{n=0}^{N-1}$. Note from the expression (3.33) that the computational complexity of the achievable information rate of the derived SIMO channel is driven by the cluster with the longest memory $L_{eq} = \max_k L_k \leq L'$, where L_k is the memory of k-th cluster, and $k = 1,2,...,K$. The SIMO ISI channel of interest is illustrated in Figure 3.11. We note that noise in each cluster is i.i.d. with the variance equal to σ^2.

Instead of the inequality in (3.19), we can provide a tighter bound on the information rate by noting that we can group channel inputs (for simplicity) into blocks:

$$\begin{aligned} I(\boldsymbol{x};\boldsymbol{y}) &= I(\boldsymbol{x}_0^{N-1};\boldsymbol{y}_0^{N-1}) \qquad (3.35)\\ &= I(\boldsymbol{a}_0^{N-1};\boldsymbol{y}_0^{N-1})\\ &= \sum_{n=0}^{N-1} I(\boldsymbol{a}_n;\boldsymbol{y}_0^{N-1}|\,\boldsymbol{a}_0^{n-1})\\ &\leq \sum_{n=0}^{N-1} I(\boldsymbol{a}_n;\boldsymbol{y}_{1,0}^{N-1},\boldsymbol{y}_{2,0}^{N-1},...,\boldsymbol{y}_{K,0}^{N-1}|\,\boldsymbol{a}_0^{n-1}), \end{aligned}$$

where $\boldsymbol{a}_n = \{x_i\}_{i=n-L'}^{n}$. The inequality follows from the fact that we consider i.u.d. channel inputs $\boldsymbol{x}$ and multiple channel observations. This bound is strictly tighter than the one given by the inequality in (3.19) since we have excluded from the conditioning in (3.19) the future blocks $\boldsymbol{a}_{n+L'+1}^{N-1}$. Hence, we can bound the achievable information rate by that of the SIMO channel obtained by grouping the channel taps into no more than L clusters (by setting $K = L+1$ and conditioning on the future blocks we obtain the bound in (3.19)). At this point, we should indicate that grouping the channel inputs into blocks $\boldsymbol{a}_n$ of different size in (3.35), will organize the channel taps differently in order to exploit the knowledge of the sparse structure.

Since this approach for deriving an upper bound is motivated by the desire to avoid the long channel memory, we prefer to group the channel inputs such that the channel taps in all the clusters are either equally spaced, so that the

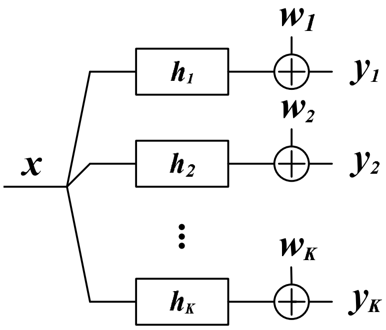

Figure 3.11: The derived SIMO ISI channel with K clusters of memory L_k, $k = 1, 2, ..., K$.

channel is potentially compressible, or all L_k's (and consequently L_{eq}) are relatively small. From an information theoretical viewpoint we emphasize that relative delays among clusters in the derived SIMO ISI channel in (3.33) are irrelevant. Therefore, for simplicity, we assume that the first tap in each cluster has zero delay and the last tap is at delay L_k, i.e. the taps in each cluster in the expression (3.33) are advanced by n time instances. Now, the k-th received element at time instant n can be written as

$$y_{k,n} = \sum_{l=0}^{L_k} h_{k,l} x_{n-l} + w_{k,n}, \tag{3.36}$$

where $h_{k,l}$ are determined from (3.33). It is useful to re-write the model in the following matrix notation:

$$\boldsymbol{y}_k = \mathbf{H}_k \boldsymbol{x} + \boldsymbol{w}_k, \tag{3.37}$$

where $\boldsymbol{y}_k$, $\boldsymbol{x}$, and $\boldsymbol{w}_k$ are column vectors collecting $\{y_{k,n}\}$, $\{x_n\}$, and $\{w_{k,n}\}$, respectively, while $\mathbf{H}_k$ is a matrix constructed from the ISI vector $\{h_{k,n}\}$. In the matrix model (3.37), the dimension of the column vectors is $N \times 1$, while the dimension of the matrix $\mathbf{H}_k$ is $N \times N$. The information rate of the system is completely defined by the conditional probability density function of the received vector $(\boldsymbol{y}_1, \boldsymbol{y}_2, \ldots, \boldsymbol{y}_K)$ given $\boldsymbol{x} = \boldsymbol{a}$, denoted by $p(\boldsymbol{y}_1, \boldsymbol{y}_2, \ldots, \boldsymbol{y}_K | \, \boldsymbol{a})$, and can be written as

$$\begin{aligned} p(\boldsymbol{y}_1, \boldsymbol{y}_2, \ldots, \boldsymbol{y}_K |\, \boldsymbol{a}) &= \prod_{k=1}^{K} p(\boldsymbol{y}_k |\, \boldsymbol{a}) \\ &= \prod_{k=1}^{K} \left(2\pi\sigma^2\right)^{-\frac{K}{2}} \exp\left\{ -\frac{\left\|\boldsymbol{y}_k - \mathbf{H}_k \boldsymbol{a}\right\|^2}{2\sigma^2} \right\} \end{aligned} \tag{3.38}$$

By expanding the expression on the right-hand side of (3.38) and neglecting factors which do not depend on $\boldsymbol{a}$, we can write

$$\begin{aligned} p(\boldsymbol{y}_1, \boldsymbol{y}_2, \ldots, \boldsymbol{y}_K |\, \boldsymbol{a}) &\propto \prod_{k=1}^{K} \exp\left\{ \frac{2\boldsymbol{y}_k^H \mathbf{H} \boldsymbol{a} - \boldsymbol{a}^H \mathbf{H}_k^H \mathbf{H}_k \boldsymbol{a}}{2\sigma^2} \right\} \\ &= \prod_{k=1}^{K} \exp\left\{ \left(\boldsymbol{x}^H - \frac{1}{2}\boldsymbol{a}^H\right) \mathbf{G}_k \boldsymbol{a} + \mathbf{N}_k \boldsymbol{a} \right\}, \end{aligned} \tag{3.39}$$

where we defined

$$\mathbf{G}_k = \frac{\mathbf{H}_k^H \mathbf{H}_k}{\sigma^2}, \tag{3.40}$$

$$\mathbf{N}_k = \frac{\boldsymbol{w}_k^H \mathbf{H}_k}{\sigma^2}. \tag{3.41}$$

Finally, we can re-write (3.39) as

$$p(\boldsymbol{y}_1, \boldsymbol{y}_2, \ldots, \mathbf{y}_K |\, \boldsymbol{a}) \propto \exp\left\{ \left(\boldsymbol{x}^H - \frac{1}{2}\boldsymbol{a}^H\right) \mathbf{G}_e \boldsymbol{a} + \mathbf{N}_e \boldsymbol{a} \right\}, \tag{3.42}$$

where we defined

$$\mathbf{G}_e = \sum_{k=1}^{K} \mathbf{G}_k, \tag{3.43}$$

$$\mathbf{N}_e = \sum_{k=1}^{K} \mathbf{N}_k. \tag{3.44}$$

It can be easily shown that $\mathbf{G}_e$ is a valid autocorrelation matrix and that

$$E\left\{\mathbf{N}_e^H \mathbf{N}_e\right\} = \mathbf{G}_e. \tag{3.45}$$

In practice, the relationship in (3.42) indicates that the information rate of the system is completely defined by the matched-filter representation of the ISI channel, scaled by the noise variance. Particularly, different noise-whitened representations are equivalent when their matched-filter representations are equal, which is well known. Hence, the SIMO channel is equivalent to a SISO channel with matched-filter representation $\mathbf{G}_e$. Practically, the outputs $\boldsymbol{z}_e = \{z_e\}_{n=0}^{N-1}$ of the equivalent SISO channel in a matched-filter representation can be obtained by matched-filtering and scaling (by the noise variance) of the cluster outputs, $\boldsymbol{y}_k$'s, followed by the summing operator. Therefore, the relationship in (3.42) implies identical achievable information rates of the SIMO channel in (3.36) and the equivalent SISO channel in (3.42). From the inequality (3.35), it follows that

$$\begin{aligned} I\left(X;Y\right) &= \lim_{N\to\infty}\frac{1}{N}I\left(\boldsymbol{x};\boldsymbol{y}\right) \\ &\leq \lim_{N\to\infty}\frac{1}{N}I\left(\boldsymbol{x};\boldsymbol{y}_1,\boldsymbol{y}_2,...,\boldsymbol{y}_K\right) \\ &= \lim_{N\to\infty}\frac{1}{N}I\left(\boldsymbol{x};\boldsymbol{z}_e\right) \\ &= I_{UB}, \end{aligned} \tag{3.46}$$

where we denote the output sequence of the equivalent SISO channel as $\boldsymbol{z}_e = \{z_e\}_{n=0}^{N-1}$. The upper bound I_{UB} is thus obtained on the achievable information rate for channels with memory. Our first observation is that unlike the bound derived in [26], which depends only on the overall power contained in the channel impulse response, the upper bound (3.47) depends on the channel structure as well. Note that the computational complexity of this bound depends exponentially on $L_{eq} \leq L'$. It is feasible to optimize I_{UB}, and it can be accomplished through two degrees of freedom inherently present in our approach: the number of clusters K in (3.36) and the distribution of the channel taps among the K clusters. Considering the number of clusters K, our preliminary results indicate that by choosing fewer clusters, better performance is obtained. Intuitively, this is expected, because in this way we minimize the number of observation sequences ($\boldsymbol{y}_k$'s) at the receiver. With regard to the distribution of the channel taps among clusters, we rely on our observations which suggest that we should not keep the strongest path alone in the ISI-free cluster (if such a cluster exists), but combine it with other taps. Another observation is that the bound is tighter if clusters have a power ratio that tends to a small value, i.e. we should place the weakest tap into a separate cluster, if feasible.

For non-sparse ISI channels, the idea of clustering the channel taps is also

Table 3.1: The channel impulse response examples.

Channel	L	$\boldsymbol{f}$
C_1	7	$\frac{1}{\sqrt{1.45}}[1\ \ 0\ \ 0\ \ 0\ \ .6\ \ 0\ \ 0\ \ .3]$
C_2	5	$\frac{1}{\sqrt{1.45}}[1\ \ 0\ \ 0\ \ .6\ \ 0\ \ .3]$
C_3	7	$\frac{1}{\sqrt{1.45}}[.3\ \ 0\ \ 0\ \ .6\ \ 0\ \ 0\ \ 0\ \ 1]$
C_4	7	$\frac{1}{\sqrt{1.49}}[.7\ \ 0\ \ 0\ \ 0\ \ .8\ \ 0\ \ 0\ \ .6]$
C_5	50	$\frac{1}{\sqrt{3.31}}[1\ \ .8\ \ 0\,(25)\ \ .5\ \ .7\ \ .5\ \ 0\,(18)\ \ .4\ \ .6\ \ .4]$

applicable. However, computational complexity of the corresponding upper bound is very high if we are aiming at obtaining a tight bound, i.e. if we split the channel taps into two clusters only, the memory of the SIMO channel will be half of the memory of the original channel, and it cannot be further compressed due to the channel non-sparseness. Increasing the number of clusters will degrade the tightness of the bound for a general ISI channel.

3.3.6 Examples

In this section, the performance of the simulation-based bounds that were developed earlier in this section are presented. For each of the channel examples, we will compare the performance of the proposed bounds with those reported in [26], [35] and [36]. The channel impulse responses considered in the computer simulation are shown in Table 3.1.

In Figure 3.12 we consider the achievable information rates with BPSK ($M = 2$) transmission over the minimum-phase channel C_1. Note that the channel is sparse with just three non-zero taps, and its delay spread is $L = 7$. All the zeros of channel C_1 in the Z-domain are inside the unit circle, making it a minimum-phase system. Consequently, the simulation-based upper bound [36] is very loose as it can be seen from Figure 3.12. In order to obtain the proposed upper bound, we group the channel taps $C_1(0) = 1.0$ and $C_1(4) = 0.6$ into one cluster, and the weak tap $C_1(7) = 0.3$ into the second cluster. The proposed upper bound now outperforms the simulation-based bound [36], and as it was shown earlier in this section, performs better than the power enhancement bound [26] over the entire SNR region. The former approach is illustrated in Figure 3.12 as bound $I_{UB}new, sub$ where we keep the first channel tap $C_1(0)$ alone. This is clearly a poor choice of channel clustering and the bound is very close to the power enhancement bound. The latter approach is trivial for the case of the channel with only three non-zero taps, since the memory of our equivalent SISO channel $\boldsymbol{z}_e$ reduces to $L' = 1$. We also note that our lower bound is tighter than bounds [35] achievable by practical receivers, where we assumed that the memory of the target channel response is $L' = 3$. This also indicates that tentative channel decisions obtained through the modified forward recursion of the BCJR algorithm in (3.31) are reliable, since the filter $\boldsymbol{g}_{opt}$ induces noise correlation that is mainly suppressed through the perfectly known channel inputs from the state definition in (3.26). We also compare our bound with the lower bound we presented previously in [40], which utilizes a detector based on the application of the sum-product algorithm to the factor graph of the channel impulse response. The performance of this detector converges to that of the optimal BCJR detector, since C_1 does not have cycles of length less than 6. We observe that our bound, based on a channel shortening filter and the modified BCJR detector, converges to the optimal detector performance for high SNR, while slight degradation is observed for low SNR, where tentative decisions are less reliable.

In Figure 3.13 we consider a minimum-phase channel C_2 with a channel structure similar to C_1. The span of the ISI is shorter, and for $L' = 3$ the simulation-based upper bound [36], based on the reduced-search on the full-complexity trellis, is tighter than the one for C_1. The reason for such behavior is that more channel states carrying a significant portion of the estimated probability mass of the channel output sequence are included into reduced-search. Since we use the same strategy of grouping channel taps into clusters, our upper bound is the same as in the case of the previous channel C_1. We also observe that the tightness of our lower bound is slightly improved, since prefiltering will introduce less correlation in the noise by canceling out only the weak ISI components for tap indices strictly greater than $L' = 3$. We note that our bound performs almost as well as the one previously proposed [40] for a factor graph-based detector.

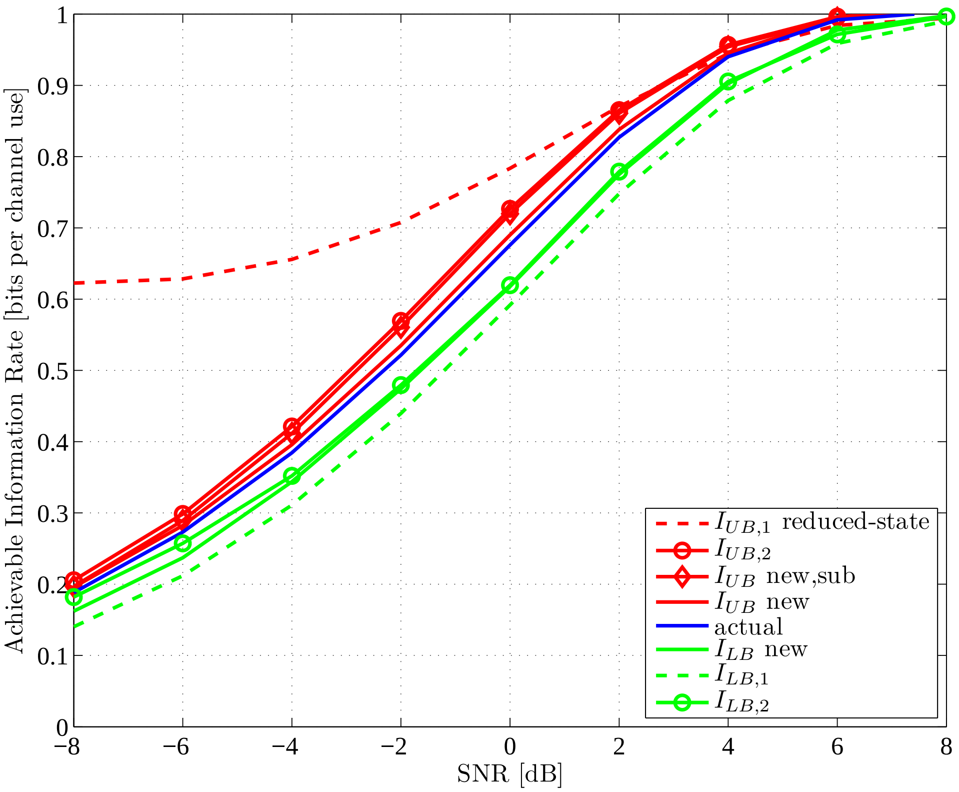

Figure 3.12: Bounds on the achievable information rate for minimum-phase channel C_1. Target memory $L' = 3$ is assumed for the computation of both, $I_{UB}new$ and $I_{LB}new$. $I_{UB,1}$ is the reduced-state upper bound from [36]. $I_{UB,2}$ is the upper bound from [26]; $I_{LB,1}$ is the lower from [35]; $I_{LB,2}$ is the lower bound from [40].

In Figure 3.14 we consider a maximum-phase representation of C_1. The tightness of our upper bound is similar to the one for the minimum-phase channel, since the power ratio among channel taps is the same as in the previous examples. The simulation-based upper bound [36] is significantly looser for the entire SNR region, and therefore, it is omitted from the figure. As for the lower bound, the performance is seriously degraded unless we redefine our approach to increase the reliability of tentative decisions. This can be accomplished by running the modified backward recursion in (3.32) as in (3.31), and then the modified forward recursions with these decisions. With this approach, we observe significant improvement in the receiver performance as shown in Figure 3.14 by comparing $I_{LB}new, backward$ with $I_{LB}new, forward$. We note that the lower bound based on the power degra-

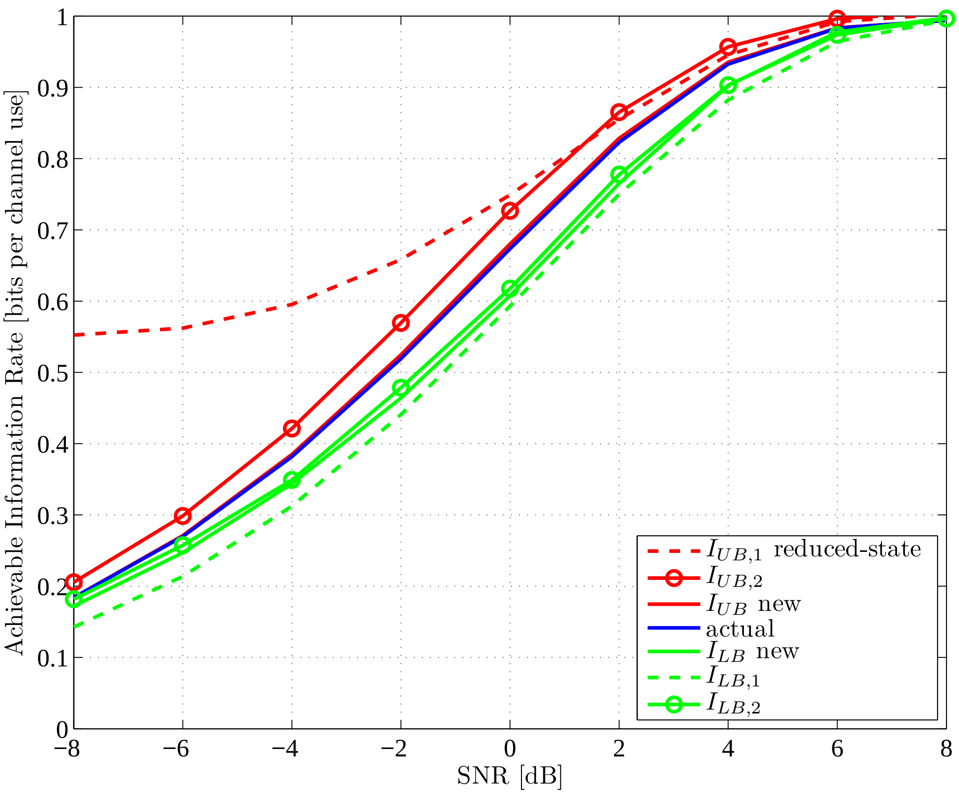

Figure 3.13: Bounds on the achievable information rate for minimum-phase channel C_2. Target memory $L' = 3$ is assumed for the computation of both, $I_{UB}new$ and $I_{LB}new$. $I_{UB,1}$ is the reduced-state upper bound from [36]. $I_{UB,2}$ is the upper bound from [26]; $I_{LB,1}$ is the lower from [35]; $I_{LB,2}$ is the lower bound from [40].

dation argument is sensitive to the phase of the channel. Since C_3 and C_1 are equivalent channels, identical performance comparison as in Figure 3.12 between our bound and the one previously proposed [40] is observed.

In Figure 3.15 we consider a mixed-phase channel C_4. For this channel the upper bound is similar to those from the previous examples, and obtained by grouping $C_4(0)$ and $C_4(4)$ into one cluster and $C_4(7)$ into a second one, whereas the lower bound shows a degradation due to unreliable tentative decisions, obtained either by means of forward or backward recursion. We also observe that the bound based on factor graphs [40] outperforms our bound I_{LB} significantly. This result suggests that a mixed-phase type of channel may be transformed either to a minimum-phase or a maximum-phase representation $(I_{LB}new, min - phase)$

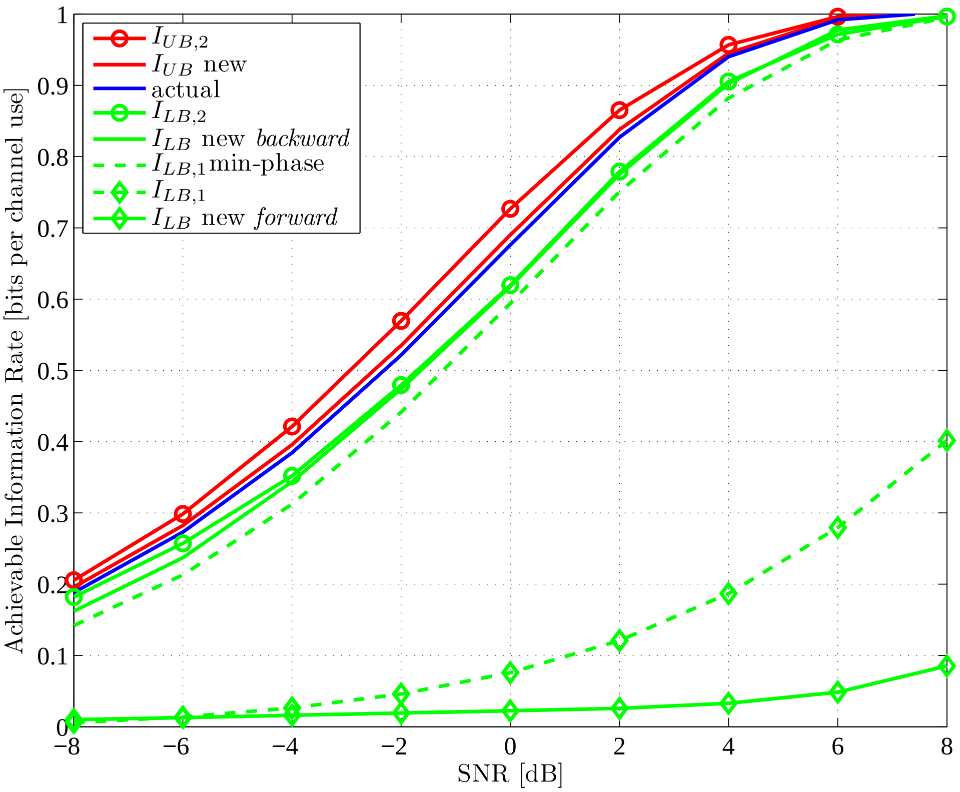

Figure 3.14: Bounds on the achievable information rate for maximum-phase channel C_3. Target memory $L' = 3$ is assumed for the computation of $I_{UB}new$, $I_{LB}new, forward$ and $I_{LB}new, backward$. $I_{UB,2}$ is the upper bound from [26]; $I_{LB,1}$ is the lower from [35]; $I_{LB,2}$ is the lower bound from [40].

prior to the application of the reduced-state modified BCJR. However, this method will certainly provide a looser lower bound than the one treated in our approach, because the modified BCJR shows the best performance for the minimum-phase channel representation. The validity of the bound obtained from the minimum-phase representation, follows from the fact that the achievable information rate of the channel is insensitive to the channel phase.

In Figure 3.16 we illustrate the proposed bounds for the channel C_5 (with long memory of $L = 50$), and clustered non-zero tap pattern, where few consecutive channel taps carry significant energy. The simulation-based upper bound [36] is omitted since it is loose for the entire SNR region. We derive the proposed upper bound by assigning each of the channel clusters to the clusters of the SIMO

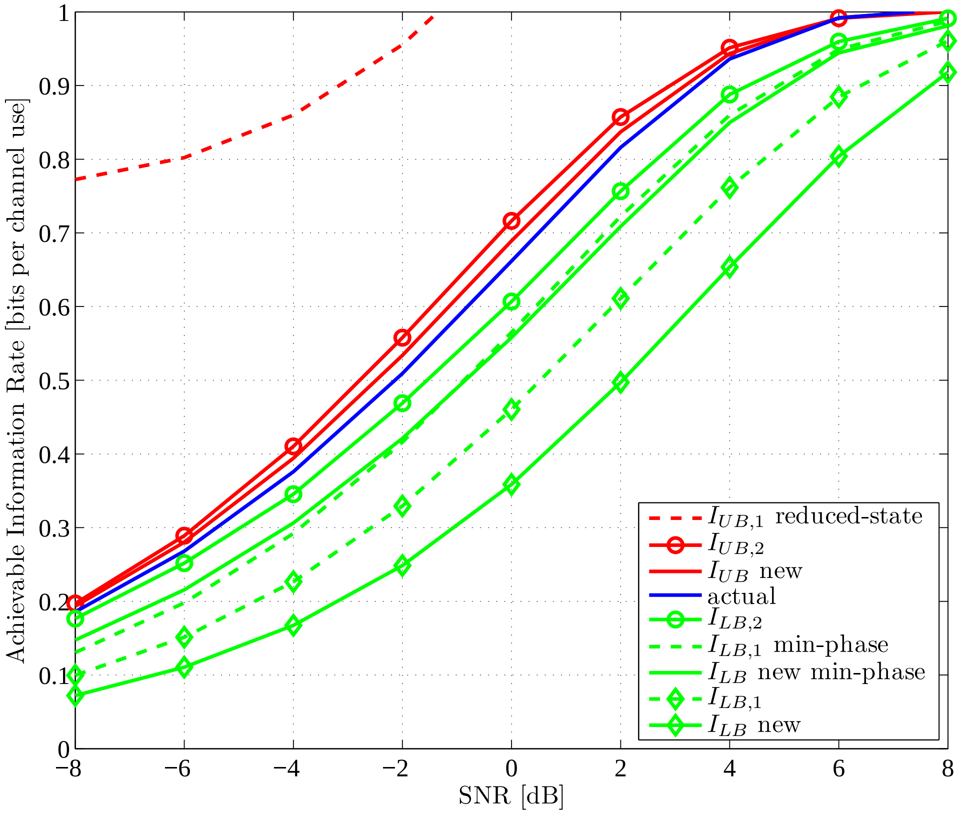

Figure 3.15: Bounds on the achievable information rate for mixed-phase channel C_4. Target memory $L' = 3$ is assumed for the computation of $I_{UB}new$, $I_{LB}new$ and $I_{LB}new, min - phase$. $I_{UB,1}$ is the reduced-state upper bound from [36]. $I_{UB,2}$ is the upper bound from [26]; $I_{LB,1}$ is the lower from [35]; $I_{LB,2}$ is the lower bound from [40].

channel (3.33). As we observe, the proposed upper bound shows a significant improvement with respect to the bound [26] based on the power enhancement argument. The new lower bound on the channel impulse response shows significant improvement with respect to the one based on the power degradation argument due to strong ISI components present in the large delay spread of the channel C_5. We emphasize that $L' = 9$ is considered to be sufficiently large in order for the actual target channel impulse response $\boldsymbol{f}$ to be relatively close to the optimal one $\boldsymbol{f}_{opt}$ for this example. Since the receiver used in [40] requires calibration of various parameters that are critical for the proper functionality of the detector, this bound was not considered in the case of the realistic UWA channel with the large delay

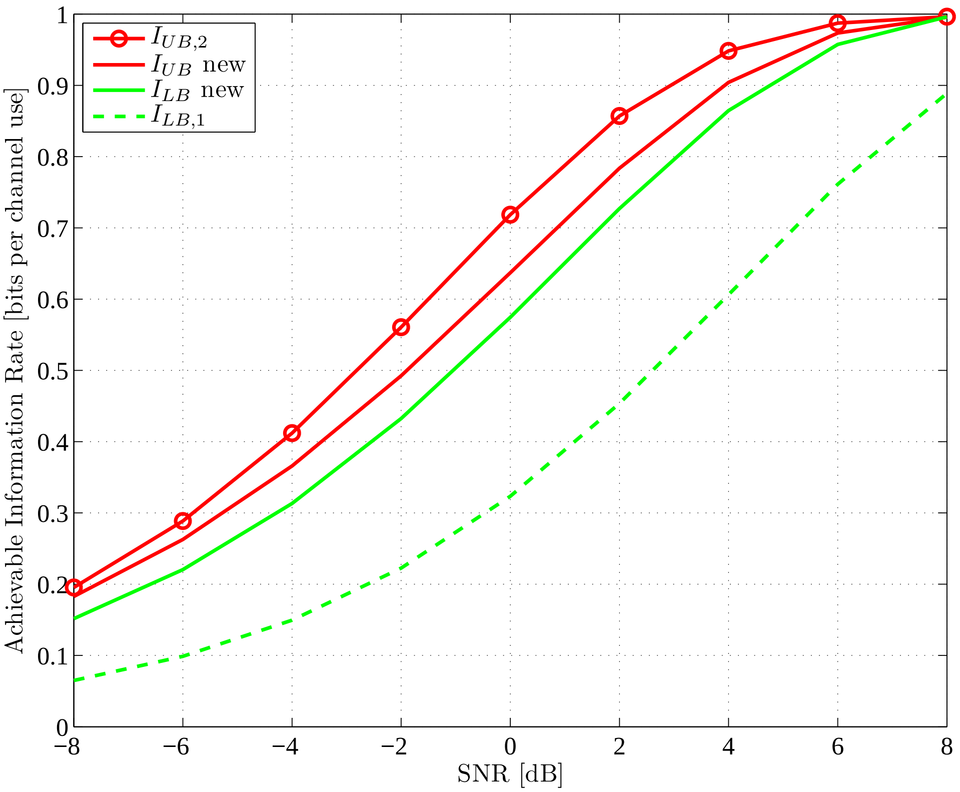

Figure 3.16: Bounds on the achievable information rate for minimum-phase channel C_5. Target memory $L' = 9$ is assumed for the computation of both, $I_{UB}new$ and $I_{LB}new$. $I_{UB,2}$ is the upper bound from [26]; $I_{LB,1}$ is the lower from [35];

spread, as in the case of C_5. The newly proposed detector has slight performance degradation, and significantly lower implementation complexity, which is the main reason why we favor it.

3.4 Summary

In these chapter we used the experimentally recorded measurements to compute the average channel capacity assuming a quasi-stationary fading and nonwhite Gaussian noise. We then evaluated the MIMO ergodic channel capacity under different fading models, assuming either no channel information at the transmitter, or limited knowledge of the channel statistics. Statistical knowledge about the channel fading at the transmitter side could be a useful parameter in system design. By implementing receiver-transmitter feedback in the system, the information about slowly-varying mean, variance and/or Rician k-factor can be conveyed. Utilizing these parameters through adaptive space-time coding techniques, the system capacity can be improved significantly.

We have also examined upper and lower bounds on the achievable information rate of the discrete-time additive white Gaussian channel with long memory and sparse structure. The proposed lower bound is attainable by practical receivers, with varying degrees of tightness depending upon the specific receiver used. Particularly we consider a receiver structure consisting of a channel shortening filter and a modified BCJR detector with the objective of obtaining a suboptimal soft-output detector with reasonable performance/complexity trade-off. The lower bound improves upon usefulness of the existing bounds for minimum-phase and maximum-phase channels, and indicates the utility of the considered reduced-complexity receiver. For mixed-phase systems, the lower bound shows poor performance due to the unreliable tentative decisions made by the modified BCJR algorithm.

The proposed upper bound is based on grouping of the channel taps into clusters. Performance of the upper bound depends on the strategy for channel clustering, and it can be optimized further by computer search. For sparse channels with a long memory, this approach leads to a significant complexity reduction in the simulation of the newly defined SISO channel, which also yields the upper bound on the achievable information rate of the actual channel. As illustrated by examples, the upper bound significantly outperforms the bounds previously published in the literature.

Sections 3.1 and 3.2, in part, are a reprint of the material as it appears in “Statistical characterization and capacity of shallow water acoustic channels,” by A. Radosevic, J. G. Proakis, and M. Stojanovic, IEEE Oceans’09 Conference, Bremen, Germany, May 2009. The dissertation author was the primary investigator and author of this paper.

Section 3.2, in part, is a reprint of the material as it appears in “Capacity of MIMO systems in shallow water acoustic channels,” by A. Radosevic, D. Fertonani,

T. M. Duman, J. G. Proakis, and M. Stojanovic, IEEE 43rd Asilomar Conference on Signals, Systems and Computers, Nov. 2009. The dissertation author was the primary investigator and author of this paper.

Section 3.3, in part, is a reprint of the material as it appears in “Bounds on the information rate for sparse channels with long memory and i.u.d. inputs,” by A. Radosevic, D. Fertonani, T. M. Duman, J. G. Proakis, and M. Stojanovic, IEEE Transactions on Communications, vol. 59, no. 12, pp. 3343 – 3352, December 2011. The dissertation author was the primary investigator and author of this paper.

Chapter 4

Adaptive OFDM Modulation

OFDM has recently emerged as a promising alternative to single-carrier systems for UWA communications because of its robustness to channels that exhibit long delay spreads and frequency selectivity [54, 55]. However, applying OFDM to UWA channels is a challenging task because of its sensitivity to frequency offset that arises due to motion. In particular, because of the low speed of sound and the fact that acoustic communication signals occupy a bandwidth that is not negligible with respect to the center frequency, motion-induced Doppler effects result in major problems such as non-uniform frequency shift across the signal bandwidth and inter-carrier interference [10, 56].

Time-varying multipath propagation and limited bandwidth place significant constraints on the achievable throughput of UWA communication systems. In order to support high spectral efficiencies, we consider communication systems employing adaptive modulation schemes. While adaptive signaling techniques have been extensively studied for radio channels [57–60], only preliminary results for UWA channels are reported in [61] and [62], where simulations and recorded data are used to demonstrate the effectiveness of the proposed adaptation metrics.

The performance of an adaptive system depends on the transmitter's knowledge of the channel which is provided via feedback from the receiver. Since sound propagates at a very low speed, the design and implementation of an adaptive system essentially relies on the ability to predict the channel at least one travel time ahead. This is a very challenging task for communications in the range of several kilometers which imposes significant limitations on the use of feedback. However, our work has shown that channel prediction is possible over such intervals of time using a low-order predictor [63]. Crucial to successful channel prediction is motion compensation that stabilizes the non-uniform Doppler shift and enables (sparse) channel estimation. The so-obtained channel estimates contain only a few significant coefficients that are shown to be stable enough to support prediction several seconds into the future.

In this chapter we discuss techniques for spectrally-efficient UWA OFDM communications. In particular, we explore design aspects of adaptive OFDM modulation, and study its performance using real-time at-sea experiments. Our design criterion is to maximize the system throughput under a target average BER. Our approach and major contributions are the following:

- We estimate small Doppler rates (less than 10^{-4}) that correspond either to drifting of the instruments, or residuals after initial resampling in mobile systems (e.g. systems using autonomous underwater vehicles). Proper Doppler compensation ensures stability over intervals of time that are long enough to support channel prediction several seconds ahead.

- We exploit the sparse multipath structure of the channel impulse response to estimate the most significant channel paths and simplify the prediction problem. Specifically, we estimate only a few significant paths of the channel within a possibly large overall delay spread. We treat the statistical properties of the underlying random process of the channel fading as unknown, and compute the parameters of a linear predictor adaptively, by applying a recursive least squares (RLS) algorithm.

- We develop two modulation schemes, distinguished by the level of adaptivity: Scheme 1 adjusts only the modulation level and assumes a uniform power allocation, while Scheme 2 adjusts both the modulation level and the power allotted to each sub-carrier.

- We propose a new design criterion for an adaptive OFDM system based on the information that is fed back to the transmitter. Specifically, we consider two cases. In the first case, the information about the modulation alphabet and the quantized power level for each sub-carrier is computed at the receiver and fed back to the transmitter. In the second case, the quantized channel estimates are fed back, and the adaptive algorithm for bit-loading and power allocation is implemented at the transmitter.

- We demonstrate the effectiveness of the proposed adaptive schemes using computer simulations, test channels recorded during the Kauai Acoustic Communications MURI 2008 (KAM08) experiment in shallow water off the western coast of Kauai, Hawaii, in June 2008, and real-time at-sea experiments conducted during the Kauai Acoustic Communications MURI 2011 (KAM11) experiment at the same location in July 2011. The numerical and experimental results show that the adaptive modulation scheme can provide significant throughput improvements as compared to conventional, nonadaptive modulation for the same power and target BER.

The system design assumes a feedback link from the receiver that is exploited in two forms: one that conveys the modulation alphabet and quantized power levels to be used for each sub-carrier, and the other that conveys a quantized estimate of the sparse channel impulse response. The second approach is shown to be advantageous, as it requires significantly fewer feedback bits for the same system throughput. The effectiveness of the proposed adaptive schemes is demonstrated using computer simulations, real channel measurements recorded in shallow water off the western coast of Kauai, Hawaii, in June 2008, and real-time at-sea experiments conducted at the same location in July 2011.

This chapter is organized as follows. In Section 4.1 we describe the system and channel model for adaptive OFDM modulation; in Section 4.2, we introduce a linear RLS predictor for the channel tap coefficients; in Section 4.3, we propose the rules for selection of the modulation levels, the information that is fed back to the transmitter, and the adaptive OFDM schemes; in Section 4.4 we demonstrate the performance of the proposed adaptive schemes using numerical and experimental results that are based on recorded test channels and real-time at-sea trials, respectively; Finally, we provide our concluding remarks in the summary of the chapter.

4.1 System and Channel Model

Let us consider an OFDM system with K sub-carriers, where the n-th block of the input data symbols $X_{k,n}$, $k = 0, 1, \ldots, K-1$, is modulated using the inverse fast Fourier transform (IFFT). The block of input data consists of information-bearing symbols and pilots, with corresponding sets denoted as S_d and S_p, respectively. We assume that the information symbols are independent, while candidate modulations are BPSK, QPSK, 8PSK and 16QAM with two-dimensional Gray mapping. In other words, for the k-th sub-carrier, where $k \in S_d$, and the n-th block, the modulation schemes $\mathcal{M}_{k,n} \in \{2, 4, 8, 16\}$, and if no data is transmitted $\mathcal{M}_{k,n} = 1$. It is assumed that the pilot symbols ($k \in S_p$) take values from the QPSK modulation alphabet. For each modulation alphabet, we assume a uniform distribution of the constellation points with a normalized average power. The transmitter sends frames of OFDM blocks, such that one OFDM block occupies an interval $T' = T + T_g$, where T and T_g are the symbol duration and the guard time interval, respectively. We denote by $B = K/T$ the total bandwidth of the system, by f_0 the frequency of the first sub-carrier, by $f_c = f_0 + B/2$ the central frequency, and by $\Delta f = 1/T$ the sub-carrier separation.

4.1.1 Modeling of the Time-varying Path Delay $\tau_p(t)$

In Section 2.1, we defined the baseband impulse response of the overall channel as (2.15)

$$h(\tau, t) = \sum_{p=0}^{P-1} h_p(t)\delta(\tau - \tau_p(t)). \tag{4.1}$$

If we follow the approach from our work [63], we model the time-varying path delays as

$$\tau_p(t) = \tau_{p0} - \int_{x=0}^{t} a_p(x)dx, \tag{4.2}$$

where $a_p(t)$ is the Doppler scaling factor which is some function of time. This model includes the fixed term τ_{p0} which describes the nominal propagation delay corresponding to the system geometry at the time of transmission, and an additional term $\int_{x=0}^{t} a_p(x)dx$ that describes the effect of motion at the time of observation either due to drifting of the instruments (Doppler rates less than 10^{-4}) in stationary systems, or residuals after initial resampling in mobile systems (e.g. systems using autonomous underwater vehicles). The system motion during a period of time corresponding to a few seconds (or several data packets) is modeled by velocity and acceleration terms which lead to a linear Doppler rate $a_p(t)$. A more accurate model could include higher-order terms; however, experimental results confirm that this is not necessary. Specifically, we model $a_p(t)$ as a piecewise linear function

$$a_p(t) = a_p(n-1) + (a_p(n) - a_p(n-1))\left(\frac{t}{T} - n + 1\right), \tag{4.3}$$

where $(n-1)T \leq t \leq nT$, and $a_p(n)$ are the Doppler scaling factors evaluated at time instances nT.

This channel model is deemed suitable for the time scales of interest to an adaptive UWA communication system, since providing a reliable predicted CSI depends on the availability of a stable signal reference that can be obtained through accurate motion compensation. For example, for a 2 km link and the center frequency $f_c = 20$ kHz, a small Doppler rate $a_p(t) \sim 10^{-5}$ can cause the phase of $c_p(t)$ in Eq. (2.14) to change up to π radians during a time interval of 1.33 seconds that corresponds to the propagation delay of one travel time.[1] Such a phase shift can considerably degrade the performance of channel prediction and the reliability of the corresponding CSI. In other words, proper Doppler compensation ensures stability over intervals of time that are long enough to support channel prediction several seconds ahead.

The model (4.2) allows one to decouple the phase $2\pi f_c \tau_p(t)$ into two terms, one that is not related to motion, and another that is related to motion. While the first term may not be predictable with sufficient accuracy because the frequency f_c may be several orders of magnitude larger than the inverse of the path

---

[1] Here we should make a distinction between making the prediction for one travel time ahead, and for the round-trip time (two travel times ahead), since the two cases correspond to different feedback implementation strategies, i.e. different functions performed by the two ends of a link.

delay, the second term can be predicted using the estimates of the Doppler scaling factors $a_p(n)$. With this fact in mind, we proceed to develop a channel prediction method that focuses on two general terms: a complex-valued coefficient $g_p(t) = h_p(t)e^{-j2\pi f_c \tau_{p0}}$, and a motion-induced phase $\theta_p(t) = 2\pi f_c \int_{x=0}^{t} a_p(x)dx$. In other words, we model the baseband channel response as

$$g(\tau, t) \;=\; \sum_{p=0}^{P-1} g_p(t)e^{j\theta_p(t)}\delta(\tau - \tau_p(t)) \tag{4.4}$$

where we treat each $g_p(t)$ as an unknown complex-valued channel coefficient, which is assumed to be stable over a prolonged period of time (tens of seconds), and $\theta_p(t)$ as an unknown motion-induced phase, which is modeled as a second-order polynomial based on the expressions (4.2) and (4.3). We emphasize that this model is valid for some interval of time, but its parameters may change from one such interval to another.

Our goal is to develop a two-step procedure in which we first estimate the channel coefficients at the receiver from a probe signal, and then use the so-obtained estimates to form predictions, which are finally fed back to the transmitter. This CSI will be used at the receiver (or the transmitter) to perform adaptive allocation of the modulation levels and power for each sub-carrier in the current OFDM block transmission.

4.2 Channel Estimation and Channel Prediction

In this section we present the method for estimating the sparse channel coefficients, and the method for predicting their future values.

4.2.1 Channel Estimation

Channel estimation consists of two steps. In the first step, initial phase compensation is performed to produce a stable reference signal. This step includes resampling by a nominal (average) Doppler factor and removal of the phase offset $\theta_p(t)$. Here, we should emphasize that the process relies on the estimates of the

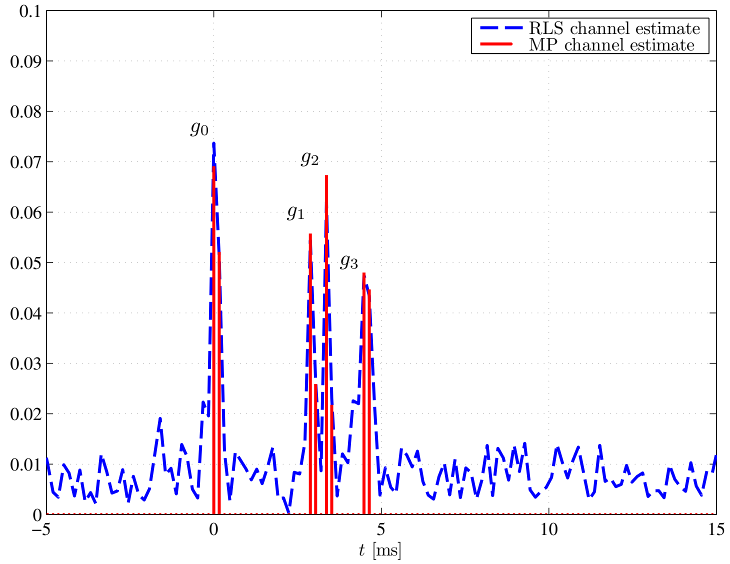

Figure 4.1: Channel estimates obtained by the RLS and the MP algorithm.

Doppler scaling factors $a_p(n)$, which are assumed to be available with a certain precision (e.g. from a dedicated synchronization preamble). In the second step, the so-obtained signal is used to estimate the path coefficients $g_p(t)$. The Doppler factors are not needed thereafter, as we conjecture that the channel coefficients after motion-compensation exhibit sufficient stability to allow prediction several seconds into the future.

Figure 4.1 illustrates the channel estimates obtained from real data collected during the KAM08 experiment. After the initial phase compensation, we perform channel estimation from the received signal using the matching pursuit (MP) algorithm [64]. Note from Figure 4.1 that the MP algorithm produces 8 coefficients, where neighboring coefficients belong to the same propagation path due to the path dispersion [1]. For further analysis we merge adjacent coefficients so as to represent the channel via four propagation paths g_0, g_1, g_2 and g_3. Therefore, the MP algorithm provides estimates of the channel coefficients $g_p(t)$, assuming that $P = 4$ channel coefficients are sufficient for the description of the sparse multipath structure. These estimates are denoted by $\tilde{g}_p(n)$, and computed at time instances nT separated by $T = 155$ ms. For comparison purposes, we also provide the channel estimate obtained using the RLS algorithm. Different peaks in the channel estimates can be associated with multiple surface and bottom reflections calculated from the geometry of the experiment. As it can be seen from the figure, the MP algorithm successfully estimates the significant channel coefficients, and reduces the estimation error with respect to that incurred by the RLS algorithm.

We emphasize that positions of the significant paths may drift on a larger time scale (tens of seconds), and therefore have to be updated accordingly. In Figure 4.2, we show the magnitudes and phases of the significant paths over a time period of 8 s. As we initially conjectured, the phases of $g_p(t)$ remain relatively stable for more than a few seconds (a propagation delay over several kilometers).

4.2.2 Channel Prediction

As we previously reported in [63], the future values of $g_p(t)$ are predicted from the estimates $\tilde{g}_p(t)$. In particular, if the OFDM blocks are periodically transmitted at time instances $t = nT'$, we use M observations made at times $n, n-1, ..., n-M+1$ to predict the channel at time $n+1$. To account for possible correlation between the path coefficients, we allow for their joint prediction. In other words, we use all P channel coefficients to predict each new coefficient. The prediction is thus made as

$$\hat{\mathbf{g}}(n+1) = \mathbf{W}^H(n)\tilde{\mathbf{g}}_M(n), \tag{4.5}$$

where

$$\hat{\mathbf{g}}(n+1) = [\tilde{g}_0(n+1)\ \tilde{g}_1(n+1)\ \dots\ \tilde{g}_{P-1}(n+1)]^T, \tag{4.6}$$

$$\begin{aligned}\tilde{\mathbf{g}}_M(n) \ =\ & [\tilde{g}_0(n)\dots\tilde{g}_0(n-M+1)\tilde{g}_1(n)\dots\tilde{g}_1(n-M+1)\tilde{g}_{P-1}(n)\dots \\ & \dots\tilde{g}_{P-1}(n-M+1)]^T. \end{aligned} \tag{4.7}$$

The matrix $\mathbf{W}(n)$ contains $MP \times P$ prediction coefficients that are to be determined.

Because the second-order statistics are not available for the random process $\mathbf{g}\,(n+1)$, we compute $\mathbf{W}(n)$ adaptively, by applying the RLS algorithm [29] as

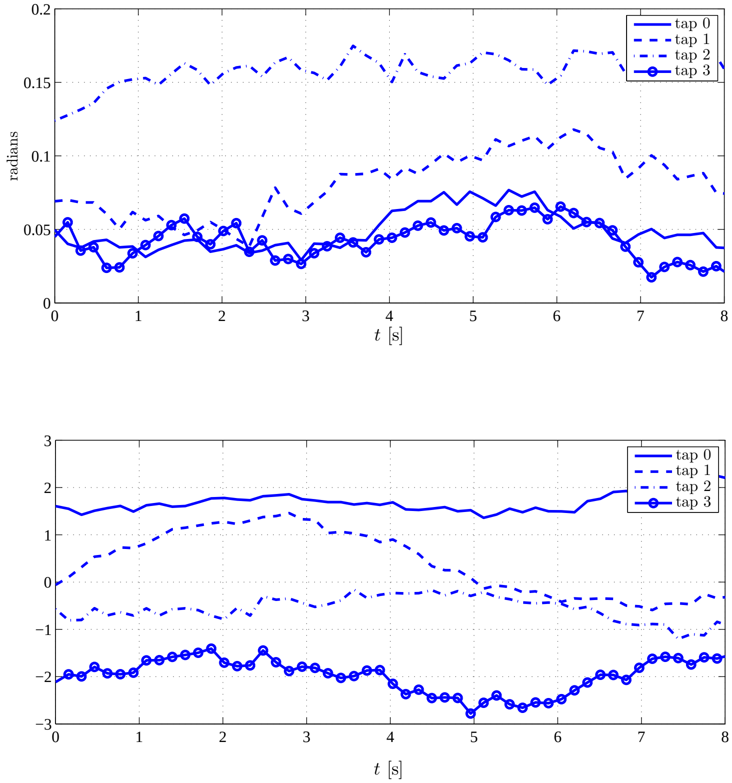

Figure 4.2: Magnitudes (top) and phases (bottom) of the channel path coefficients.

Table 4.1: Prediction RLS algorithm

The algorithm initialization:

$$\mathbf{W}[0] = \mathbf{0} \tag{4.8}$$

$$\mathbf{R}[0] = \delta^{-1}\mathbf{I} \text{ (δ is a small positive constant)} \tag{4.9}$$

The joint RLS algorithm (for $n = 1, 2, \ldots$):

$$\mathbf{k}(n) = \frac{\lambda^{-1}\mathbf{R}(n-1)\tilde{\mathbf{g}}_M(n-1)}{1+\lambda^{-1}\tilde{\mathbf{g}}_M^H(n-1)\mathbf{R}(n-1)\tilde{\mathbf{g}}_M(n-1)} \tag{4.10}$$

$$\hat{\mathbf{g}}(n) = \mathbf{W}(n-1)\tilde{\mathbf{g}}_M(n-1) \tag{4.11}$$

$$\mathbf{e}(n) = \tilde{\mathbf{g}}(n) - \hat{\mathbf{g}}(n) \tag{4.12}$$

$$\mathbf{W}(n) = \mathbf{W}(n-1) + \mathbf{k}^H(n)\mathbf{e}(n) \tag{4.13}$$

$$\mathbf{R}(n) = \lambda^{-1}(1 - \mathbf{k}(n)\tilde{\mathbf{g}}_M^H(n-1))\mathbf{R}(n-1) \tag{4.14}$$

specified in Table 4.1. In Eq. (4.9), $\mathbf{R}$ is an $MP \times MP$ matrix which represents an estimate of the inverse joint auto-correlation matrix $E\left\{\tilde{\mathbf{g}}_M(n)\tilde{\mathbf{g}}_M^H(n)\right\}$ and δ is a small constant, typically a fraction of the minimum among variances of the channel coefficients jointly predicted by the RLS algorithm.

As discussed earlier, UWA systems suffer from inherently long propagation delays, which pose additional challenges in the design of a predictor. To counteract this problem, channel prediction one travel time ahead is achieved by using an RLS predictor of a low order M (e.g. $M = 1$ or $M = 2$) and a small forgetting factor λ (e.g. $\lambda = 0.5 - 0.75$, which corresponds to an effective window of length $L_{eff} = 1/(1-\lambda) = 2$). Note that the forgetting factor λ is uniquely specified for all P channel coefficients. With a small order M and only a few significant paths, i.e. a small P, computational complexity of joint channel prediction is sufficiently low to allow for a practical implementation.

The structure of the matrix $\mathbf{W}(n)$ is primarily driven by the geometry of the propagation environment, i.e. not all of the propagation paths are mutually correlated. In the present data set, the strongest arrival often exhibits more stability, and the contribution from the other, weaker paths in its prediction appears to be negligible. Therefore, the strongest path can be predicted independently, without loss in performance. In other words, if the channel coefficient k corresponds to the strongest path, Eq. (4.13) can be modified as follows: the k-th column of $\mathbf{W}(n)$ is recursively updated only for those elements that correspond to the prior observations of the k-th coefficient $(\tilde{g}_k(n), \tilde{g}_k(n-1), \ldots, \tilde{g}_k(n-M+1))$. In addition, exploiting the correlation among the remaining paths may lead to a performance improvement, whose exact amount is determined by the environmental profile, and accuracy of the channel and Doppler estimates.

After performing channel prediction at the receiver, the so-obtained CSI is used to initialize adaptive allocation of the modulation levels and power across the OFDM sub-carriers. As we will discuss later, depending on which end of the communication link performs adaptive allocation, different types of information are fed back over a low-rate feedback channel. In the following, we describe the design framework, initially proposed in [62], under which we developed two practical adaptive modulation schemes, and we also discuss the design of band-limited feedback.

4.3 Adaptive OFDM Modulation and Power Allocation

The system model assumes that residual Doppler effects are negligible after proper initial motion compensation (resampling by a nominal Doppler factor and removal of the phase offset $\theta_p(t)$). After this initial step, it is also assumed that the channel is constant at least over the transmission interval T of one OFDM block. Therefore, the received signal can be expressed as

$$Y_{k,n} = G_{k,n}\sqrt{C_{k,n}}X_{k,n} + N_{k,n}, \tag{4.15}$$

where

$$G_{k,n} = \sum_{p=0}^{P-1} g_p(n) e^{-j2\pi(k\Delta f - B/2)\tau_{p0}}, \tag{4.16}$$

and $Y_{k,n}$, $C_{k,n}$, and $N_{k,n}$ are, respectively, the received signal after fast Fourier transform (FFT) demodulation, the transmitted power, and zero-mean circularly symmetric complex AWGN with variance $\sigma_N^2/2$ per dimension. The noise term includes the effects of ambient noise and residual ICI on the k-th sub-carrier and the n-th OFDM block, which is approximated as a Gaussian random variable.

For the transmission of each OFDM block we adaptively compute the size of the modulation alphabet $\mathcal{M}_{k,n}$ and the transmission power $C_{k,n}$. The objective of our adaptive OFDM system is to maximize the throughput by maintaining a target average BER. In order to maintain the BER at a fixed value, we propose the following optimization criterion:

$$\begin{aligned} \underset{\mathcal{M}_{0,n},\ldots,\mathcal{M}_{K-1,n}}{\text{maximize}} \quad & \sum_{k=0}^{K-1} \log_2 \mathcal{M}_{k,n} \\ \text{subject to} \quad & \sum_{k=0}^{K-1} C_{k,n} \leq C_n, \\ & \frac{1}{K}\sum_{k=0}^{K-1} P_{e,k} = P_b, \end{aligned} \tag{4.17}$$

where C_n is the overall average power allocated to the n-th OFDM block, $P_{e,k}$ is the average BER for the k-th sub-carrier, and P_b is the target average BER. The average power can be expressed as $C_n = C + C_{n-1,r}$ where C is a constant and $C_{n-1,r}$ is the residual power from the previous block which was not allocated (i.e., $C_{r,n-1}$ is less than the minimum power increment required by the algorithm for a one-bit increase of the overall throughput). Here, we should emphasize the difference between total power allocation and distribution of this total power among the sub-carriers. In the former case, one can design an adaptive scheme where the total power C is adaptively allocated (and uniformly distributed among the sub-carriers) in order to achieve the prespecified performance (e.g. the target average BER or SNR at the receiver) for the *fixed* system throughput, whereas in the latter case, the fixed total power C is non-uniformly distributed among the sub-carriers to achieve the prespecified performance, and to *maximize* the system throughput.

In order to reduce the computational complexity of the adaptive algorithm, the sub-carriers of the n-th OFDM block can be grouped into clusters. If we assume $K = 2^d$, we group consecutive sub-carriers into $Q = 2^{d_Q}$ clusters, where $K/Q = 2^{d-d_Q}$ is the size of each cluster. We denote by $C^Q_{q,n}$ and $\mathcal{M}^Q_{q,n}$, respectively, the allocated power and the modulation level corresponding to the q-th cluster, $q = 0, 1, \ldots, Q-1$. The optimal power level for each cluster q depends on the transfer function of the channel. If the channel does not change much within a cluster, computation of $C^Q_{q,n}$ and $\mathcal{M}^Q_{q,n}$ is performed based on the average channel gain in cluster q. Note that if a cluster is affected by a deep fade, it will be dominated by the sub-carrier with the lowest channel gain. Clustering reduces the computational load, but implies a decrease in throughput as compared to the full computation of modulation levels and powers for all sub-carriers.

4.3.1 Thresholds for Modulation Levels $\mathcal{M}_{k,n}$

Due to the large propagation delays, the proposed adaptive OFDM transmission relies on channel prediction. We obtain predictions of the channel gains $G_{k,n}$ one travel time ahead based on the time-domain predictions of the most significant channel coefficients (4.5). We model the prediction error on the p-th channel path as a complex zero-mean circularly symmetric Gaussian random variable with variance $\sigma^2_{e,p}/2$ per dimension. Furthermore, based on the *a priori* knowledge obtained from the channel prediction, we model $G_{k,n}$ as a complex Gaussian random variable with mean

$$\widehat{G}_{k,n} = \sum_{p=0}^{P-1} \hat{g}_p(n) e^{-j2\pi(k\Delta f - B/2)\tau_{p0}}, \tag{4.18}$$

and variance $\sigma^2_e = \sum_{p=0}^{P-1} \sigma^2_{e,p}$, where P is the number of significant time-domain channel coefficients. Assuming that the current channel gain $G_{k,n}$ is perfectly known, we apply maximum likelihood symbol detection for the AWGN channel at the output of the matched filter. Thus, the probability of bit error for the k-th sub-carrier for MPSK/MQAM is well approximated by [58]

$$P_k(G_{k,n}, C_{k,n}, \mathcal{M}_{k,n}) \approx 0.2 e^{-\frac{m(\mathcal{M}_{k,n})}{2(\mathcal{M}_{k,n}-1)} \frac{C_{k,n}}{\sigma^2_W} |G_{k,n}|^2}, \tag{4.19}$$

where the coefficients $m(\mathcal{M}_{k,n})$ are determined numerically for each modulation alphabet, as accurately as desired for the BER approximation and take values $2.2, 3.3, 3.5$ and 3.6 for $\mathcal{M}_{k,n} = 2, 4, 8$ and 16, respectively.

For transmission of the n-th OFDM block, the adaptive system has knowledge of the predicted values $\widehat{G}_{k,n}$, but not of the full channel $G_{k,n}$. Therefore, from Eq. (4.19), the average BER on the k-th sub-carrier is obtained as [58]

$$\begin{aligned} P_{e,k} &\approx E\left[P_k(G_{k,n}, C_{k,n}, \mathcal{M}_{k,n}) \,|\, \widehat{G}_{k,n}\right] \\ &\approx 0.2 \frac{\exp\left(-\frac{|\widehat{G}_{k,n}|^2}{\sigma_e^2}\left(1 - \frac{1}{1+\frac{m(\mathcal{M}_{k,n})}{2(\mathcal{M}_{k,n}-1)}\frac{C_{k,n}}{\sigma_N^2}\sigma_e^2}\right)\right)}{1 + \frac{m(\mathcal{M}_{k,n})}{2(\mathcal{M}_{k,n}-1)}\frac{C_{k,n}}{\sigma_N^2}\sigma_e^2}. \end{aligned} \tag{4.20}$$

For a given target $P_{e,k}$, we now compute the thresholds $C^*_{k,n}(\mathcal{M}_{k,n})$ for the available modulation levels. The solution for $C^*_{k,n}(\mathcal{M}_{k,n})$ (see Appendix A for more details) is given by

$$\begin{aligned} C^*_{k,n}(\mathcal{M}_{k,n}) &= \frac{2(\mathcal{M}_{k,n}-1)\sigma_N^2}{m(\mathcal{M}_{k,n})\sigma_e^2}\left\{\frac{|\widehat{G}_{k,n}|^2}{\sigma_e^2}\left[\mathcal{W}_0\left(\frac{|\widehat{G}_{k,n}|^2}{\sigma_e^2} e^{\left(\frac{|\widehat{G}_{k,n}|^2}{\sigma_e^2} + \ln\frac{P_{e,k}}{0.2}\right)}\right)\right]^{-1} - \right. \\ &\qquad \left. - 1 \right\}, \end{aligned} \tag{4.21}$$

where $\mathcal{W}_0(x)$ $(x > -1/e)$ is the principal branch of the Lambert $\mathcal{W}$-function, the inverse function of $x = W\exp(W)$. Note that, if $|\widehat{G}_{k,n}|^2/\sigma_e^2 \gg \ln(P_{e,k}/0.2)$, the threshold goes to zero, i.e $C^*_{k,n}(\mathcal{M}_{k,n}) \to 0$. This case corresponds either to high SNR regimes with reliable CSI, or to very high target BERs of the system. Reasonably accurate approximations for $\mathcal{W}_0(x)$, which can be computed efficiently, are provided in [65]. We should emphasize that different thresholds correspond to different average values of $\widehat{C}_{k,n}$, since all of the sub-carriers are affected by the prediction error of the same variance σ_e^2. On the OFDM block level, further simplifications are possible by dividing the available bandwidth into Q clusters, leading to a 2^{d-d_Q} fold reduction in the number of computations in (4.21).

The optimization problem (4.17) is hard to solve from the standpoint of a practical implementation, because it is computationally too intensive to be run at the receiver (or the transmitter) for every OFDM block. Therefore, we pursue sub-optimal solutions which are obtained by relaxing one of the problem constraints. Specifically, we focus on two adaptive schemes in the rest of this section.

4.3.2 Adaptive Scheme 1

The optimal solution for (4.17) includes a non-uniform power allocation for a maximum attainable throughput, such that the target average BER is P_b. Consequently, each sub-carrier contributes to the average BER differently, due to the frequency selectivity of the channel. However, the problem can be simplified if we consider adaptive allocation of the modulation levels while distributing the power uniformly among the sub-carriers. Since we adaptively allocate only the modulation levels, the so-obtained solution for (4.17) will be sub-optimal. Specifically, we apply a greedy algorithm that computes the modulation levels in a given block n using the allocations from the previous block $n-1$ for initialization. The proposed algorithm is given in Table 4.2. Similar algorithms have already been considered in [66] and [67].

After initialization of the algorithm for each sub-carrier, as given by Eqs. (4.22)–(4.25), we successively increase the modulation levels for those sub-carriers that require the smallest power increment (4.26)–(4.38), while maintaining the average BER below the target P_b. If the set of modulation levels from the previous transmission interval is not a greedy-based solution for the currently available CSI $\{\widehat{G}_{k,n}\}$, the algorithm greedily searches for the closest solution which is used as a new initialization point of the algorithm. Also, if the algorithm does not support the throughput from the previous transmission interval (i.e., it fails during the initialization step), it searches for the sub-carrier k^* with the largest power decrement that is required in order to decrease the modulation level $\mathcal{M}_{k^*,n}$. The algorithm is terminated when the pre-specified P_b is achieved. The algorithm complexity is significantly reduced by clustering the available bandwidth as discussed in the previous section. The thresholds are determined for each cluster, and the algorithm is initialized for $q = 0, 1, \dots, Q-1$. The computation of $C^Q_{q,n}$ and $\mathcal{M}^Q_{q,n}$ follows the same steps (4.26)–(4.38).

Table 4.2: Modulation level allocation

```
**Initialization** (**for** $k = 0, \dots, K-1$):
    $C_{k,0} = \frac{C_n}{K};\ \mathcal{M}_{k,0} = 1;$                                   (4.22)
**Iterative algorithm** (**for** $n = 1, 2, \dots$):
**Step 1** (**for** $k = 0, \dots, K-1$):
    $\mathcal{M}_{k,n} = \mathcal{M}_{k,n-1}; C_{k,n} = \frac{C_n}{K};$                   (4.23)
$P_e = \frac{1}{K} \sum_{k=0}^{K-1} P_{e,k}(\mathcal{M}_{k,n});$                          (4.24)
$s_0 = \mathrm{sign}(P_b - P_e); s = s_0; s_1 = 0;$                                        (4.25)
**Step 2** (**for** $k = 0, \dots, K-1$):
    **if** $(s = -1\ \&\ \mathcal{M}_{k,n} = 1)\quad \Delta P_{e,k} = 1;$                   (4.26)
    **elseif** $(s = 1\ \&\ \mathcal{M}_{k,n} = 16)\quad \Delta P_{e,k} = 1;$               (4.27)
    **else** $\Delta P_{e,k} = P_{e,k}(2^s \mathcal{M}_{k,n}) - P_{e,k}(\mathcal{M}_{k,n});$ (4.28)
**Step 3**:
$k_s^* = \min_k \arg \{\Delta P_{e,k}\};$                                                  (4.29)
**if** $(s_1 = 1\ \&\ \Delta P_{e,k_s^*} = 1)$ **end**;                                      (4.30)
**elseif** $(\Delta P_{e,k_s^*} = 1)$ **go to Step 4**;                                       (4.31)
$P_e = P_e + \frac{1}{K} \Delta P_{e,k_s^*};\ \mathcal{M}_{k_s^*,n} = 2^s \mathcal{M}_{k_s^*,n};$ (4.32)
**if** $(s_1 = 0)\quad s = -s;$                                                             (4.33)
**if** $(s_1 = 0\ \&\ s \neq s_0)$ **go to Step 2**;                                         (4.34)
**if** $(s_1 = 0\ \&\ k_s^* \neq k_{-s}^*)$ **go to Step 2**;                                (4.35)
**Step 4**:
**if** $(s_1 = 0)$                                                                          (4.36)
    $s_0 = \mathrm{sign}(P_b - P_e); s = s_0; s_1 = 1;$
**if** $(\mathrm{sign}(P_e - P_b) = s_0)$ **end**;                                           (4.37)
**go to Step 2**;                                                                           (4.38)
```

4.3.3 Adaptive Scheme 2

In the second scheme we consider adaptive allocation of the modulation levels and the sub-carrier powers such that $P_{e,k} = P_b$ for each sub-carrier.

Once the thresholds are computed from (4.21), we apply the adaptive algorithm of Table 4.3 to generate the signal of the n-th OFDM block. Similarly as in the previous case, we use a greedy algorithm for the modulation level allocation.

The algorithm is initialized according to expressions (4.39)–(4.42) for all sub-carriers $k = 0, \ldots \ldots, K-1$ at time n. For each iteration of the algorithm (4.43)–(4.56) we search for the sub-carrier k^* with the smallest power increment that is required in order to increase the modulation level $\mathcal{M}_{k^*,n}$. As in Scheme 1, if the algorithm fails during the initialization step, it searches for the sub-carrier k^* with the largest power decrement that is required in order to decrease the modulation level $\mathcal{M}_{k^*,n}$. For those sub-carriers that are in a deep fade, no data is transmitted (zero power is allocated). The algorithm is terminated when the available power C_n is exhausted, or when all sub-carriers achieve the maximum modulation level (16QAM). Because of the additional freedom to adjust the power, this scheme will achieve a higher overall throughput as compared to Scheme 1. As before, the complexity can be reduced by introducing sub-carrier clustering.

4.3.4 Limited Feedback for Adaptive UWA Systems

We assume that a limited-feedback channel is available for conveying information from the receiver back to the transmitter. Two types of feedback information are considered: the modulation alphabet and the quantized power levels for each sub-carrier/cluster, or the quantized estimate of the sparse channel impulse response.

If the channel changes slowly across frequencies, neighboring sub-carriers are allocated the same modulation and power levels. In such a case, it is not necessary to feed back the channel information for each sub-carrier, i.e., the total number of bits that are fed back can be reduced. Moreover, the power levels can be quantized, such that L_c bits are used to represent each quantization level. Also, L_m bits are used to represent the available modulation levels. For example, in

Table 4.3: Modulation and power level allocation

```
Initialization (for $k = 0, \ldots, K-1$):
    $C_{k,0} = 0; \mathcal{M}_{k,0} = 1;$                                                  (4.39)
Iterative algorithm (for $n = 1, 2, \ldots$):
Step 1 (for $k = 0, \ldots, K-1$):
    $\mathcal{M}_{k,n} = \mathcal{M}_{k,n-1}; C_{k,n} = C^{*}_{k,n}(\mathcal{M}_{k,n});$                 (4.40)
$C_{all,n} = \sum_{k} C_{k,n};$                                                        (4.41)
$s_0 = \mathrm{sign}(C_n - C_{all,n}); s = s_0; s_1 = 0;$                                     (4.42)
Step 2 (for $k = 0, \ldots, K-1$):
    if $(s = -1 \;\&\; \mathcal{M}_{k,n} = 1)$   $\Delta C_k = \infty;$                               (4.43)
    elseif $(s = 1 \;\&\; \mathcal{M}_{k,n} = 16)$   $\Delta C_k = \infty;$                           (4.44)
    else $\Delta C_k = C^{*}_{k,n}(2^{s}\mathcal{M}_{k,n}) - C_{k,n};$                             (4.45)
Step 3:
$k^{*}_{s} = \min_{k} \arg \left\{ \Delta G_k \right\};$                                          (4.46)
if $(s_1 = 1 \;\&\; \Delta C_{k^{*}_{s}} = \infty)$   end;                                        (4.47)
elseif $(\Delta C_{k^{*}_{s}} = \infty)$   go to Step 4;                                       (4.48)
$C_{all,n} = C_{all,n} + \Delta C_{k^{*}_{s}};$                                                (4.49)
$C_{k^{*}_{s},n} = C_{k^{*}_{s},n} + \Delta C_{k^{*}_{s}}; \mathcal{M}_{k^{*}_{s},n} = 2^{s}\mathcal{M}_{k^{*}_{s},n};$                  (4.50)
if $(s_1 = 0)$   $s = -s;$                                                           (4.51)
if $(s_1 = 0 \;\&\; s \neq s_0)$   go to Step 2;                                           (4.52)
if $(s_1 = 0 \;\&\; k^{*}_{s} \neq k^{*}_{-s})$   go to Step 2;                                   (4.53)
Step 4:
if $(s_1 = 0)$                                                                    (4.54)
    $s_0 = \mathrm{sign}(C_n - C_{all,n}); s = s_0; s_1 = 1;$
if $(\mathrm{sign}(C_{all,n} - C_n) = s_0)$   end;                                            (4.55)
go to Step 2;                                                                   (4.56)
```

our case we describe four modulation levels using $2^{L_m} = 8$ indices, which is more than the needed minimum. In contrast, $P(2L_g + L_t)$ bits are required to convey the information about P significant coefficients in the channel impulse response, assuming that $2L_g$ bits and L_t bits are required to represent the quantized complex gain and the delay of each dominant channel coefficient, respectively.

Due to the long propagation delay and time-division duplexing, we assume a feedback channel which imposes a limit on the maximum number of bits that can be conveyed to the transmitter. Therefore, lossless data compression techniques can be used at the receiver to reduce the number of bits that are conveyed back to the transmitter. For example, Run–Length–Encoding (RLE) [68] is a simple coding scheme that provides good compression of data that contains many runs of zeros or ones. It can be applied together with the well-known Lempel-Ziv-Welch (LZW) code [69] (used as an inner code), to efficiently compress the feedback information. As we will see in the following section, assuming perfect CSI at the receiver, feeding back the channel state information about the sparse multipath structure and making the decision on the transmitter side is shown to be advantageous since it requires significantly fewer bits.

4.4 Numerical and Experimental Results

In this section we present the performance of the proposed prediction method using real data collected during the KAM08 experiment, and numerical and experimental results from the KAM08 and KAM11 experiments on the performance of the proposed adaptive schemes from the previous section.

4.4.1 Channel Prediction - Numerical Results

Results in this section are given for the transmissions from the fourth transducer from the bottom (49.5 m depth). Our wideband channel probe signal is a Turyn sequence [14] of length 28, BPSK modulated onto a carrier of frequency $f_c = 16$ kHz at a rate of 6250 bps. The probe signal is transmitted every $T = 155$ ms for a 60 s transmission interval. The sampling rate is 50 kHz.

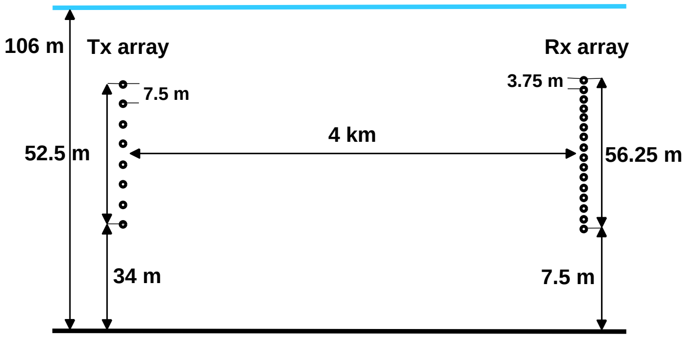

Figure 4.3: The geometry of the KAM08 experiment.

Since propagation delay for one travel time is 2.67 s, and the channel probe is transmitted every 155 ms, our goal is to predict the channel at least $N = 17$ steps ahead. The geometry of the experiment is illustrated in Figure 4.3.

Our first task is to clearly indicate that an RLS algorithm of a small order M and a small forgetting factor λ is the right choice for the design of adaptive prediction (4.5). To do so, we analyze the behavior of the RLS algorithm for different values of M and λ. In Fig 4.4, we compare the mean squared error in the prediction for different M and λ for path 0 (see Figure 4.1 for path numbering), with single-channel processing at the receive element Rx 7. The advantage of using channel prediction is apparent for $M = 1$ and $\lambda = 0.5$, for which a 5 dB improvement is obtained at the prediction lag of 2.67 s (propagation delay of the actual system geometry in the experiment). In Fig 4.5, we compare the MSE achieved by the prediction $\hat{g}_0(n + N)$ with that achieved by an outdated estimate $\tilde{g}_0(n)$. Channel prediction is performed independently for each coefficient in this example, i.e. the matrix $\mathbf{W}(n)$ is constrained to be diagonal.

In Figure 4.6, we illustrate the benefits of multi-channel processing. The MSE result indicates an obvious advantage when two receive elements are combined to predict desired channel coefficient. Increasing the number of the receive elements for multi-channel processing further improves the performance of channel prediction.

In Table 4.4, we provide the MSE achieved by joint channel path prediction relative to individual prediction. We assume single-channel processing ($L = 1$).

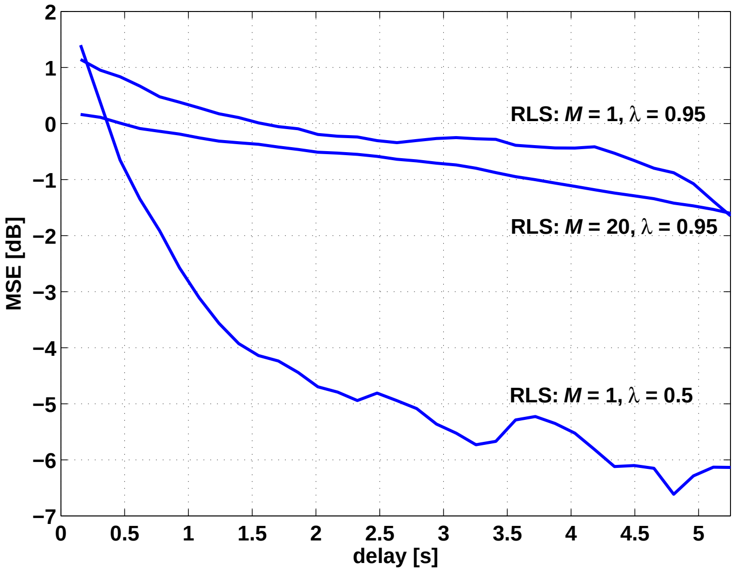

Figure 4.4: Performance of the RLS algorithm: Mean squared error (MSE) of the predicted coefficient $\hat{g}_0(n+N)$ relative to its outdated estimate $\tilde{g}_0(n)$, as a function of prediction lag NT. Results are shown for $L = 1$ (Rx 7) and different combinations of the filter size M and the forgetting factor λ.

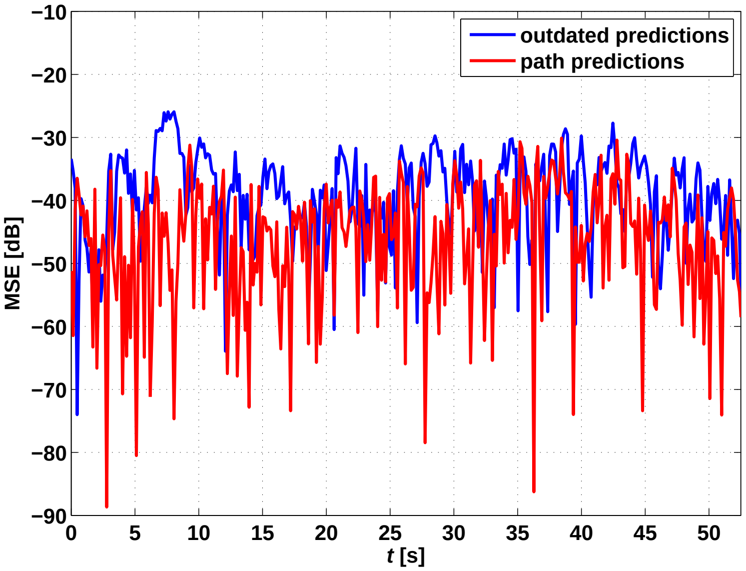

Figure 4.5: Performance of the RLS algorithm for path 0, with $M = 1$, $\lambda = 0.5$, $N = 17$ and $L = 1$ (Rx 7).

Table 4.4: Relative MSE (in decibels) for $N = 17$. Boldface numbers correspond to cases in which joint prediction yields an improvement.

Rx 9			Rx 10		
g_0	g_1	g_2	g_0	g_1	g_2
1.94	0.14	0.15	2.99	0.35	**-5.09**
1.48	**-1.10**		1.61	**-1.88**	
0.44		−0.13	1.48		**-7.34**
	-1.19	0.54		−0.15	**-1.55**

Rx 8				Rx 13	
g_0	g_1	g_2	g_3	g_0	g_1
1.76	0.28	0.69	0.96	1.08	**-2.08**
−0.64	−0.24				
	−0.81	**-1.21**			
	−0.37		**-1.57**		

Rx 7				Rx 16	
g_0	g_1	g_2	g_3	g_0	g_1
0.03	1.29	2.68	**-3.16**	1.42	**-2.11**
-2.47		1.07			
	-1.34	0.26			
		1.07	**-4.94**		

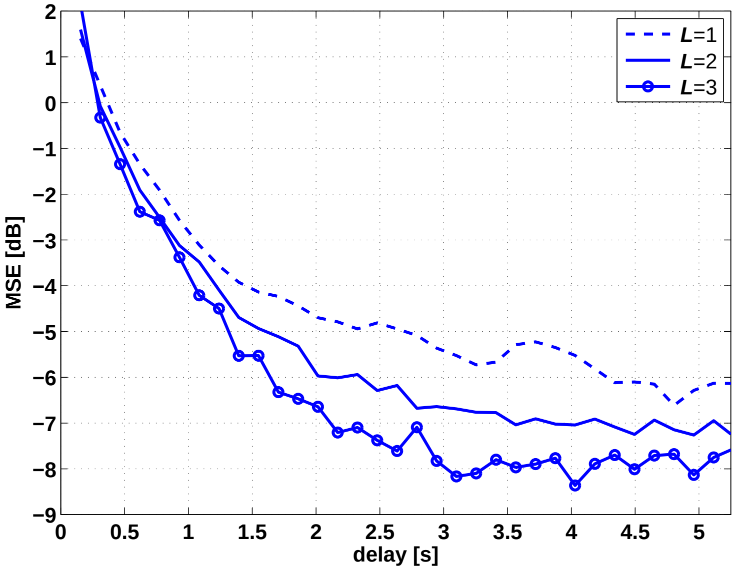

Figure 4.6: Performance of the RLS algorithm for path 0 as a function of prediction lag NT, with $M = 1$ and $\lambda = 0.5$. Single-channel processing (L=1) uses Rx 7; two-channel processing uses Rx 7 and Rx 16; three-channel processing uses Rx 7, Rx 10 and Rx 16.

We present results for 6 different elements from the receiver array – Rx 7, 8, 9, 10, 13 and 16 (Rx 16 is the closest element to the ocean surface). With Rx 7 and Rx 8, $P = 4$ significant paths are identified; with Rx 9 and Rx 10, $P = 3$, and with Rx 13 and Rx 16, $P = 2$. For example, with Rx 7, the second row represents the case in which $g_0(t)$ and $g_2(t)$ are predicted jointly, while $g_1(t)$ and $g_3(t)$ are predicted independently. Results are given for four channel paths identified as significant. Blank cells in the table indicate that the corresponding paths are not combined for joint prediction. This combination yields a 2.47 dB improvement in the prediction of $g_0(t)$, but 1.07 dB degradation in the prediction of $g_2(t)$. Joint prediction of all four paths does not result in any improvement, except for $g_3(t)$, indicating that not all of the propagation paths are mutually correlated. Joint estimation of paths 0 and 3, which are the weak ones (see Figure 4.1), yields a good improvement when these paths are combined with path 2, with the corresponding reductions in the MSE of 2.47 dB and 4.98 dB, respectively. Path 1 appears to be fairly independent from the rest of the channel impulse response.

These results indicate that there is a certain advantage to joint path prediction. More importantly, our results show that channel prediction, whether conducted individually or jointly for the significant paths, is possible even in the presence of long acoustic delays, and that it offers an improvement over an ignorant approach that uses outdated channel estimates. This fact offers a motivation to pursue adaptive modulation as a means of achieving improved performance over time-varying UWA channels.

4.4.2 Adaptive OFDM Modulation

The numerical results on adaptive OFDM modulation are based on channel measurements recorded during the KAM08 experiment, and experimental results from the real-time at-sea trials that were conducted during the KAM11 experiment. Both experiments were conducted at the same location with operational areas marked in Figure 1.1.

4.4.3 Numerical Results from the KAM08 Experiment

The KAM08 experiment took place in 100 m deep water, with a communication distance of 4 km. The transmitter was deployed at the location Sta00 (see Figure 1.6) as a 52.5 m aperture vertical array of 8 ITC-1001 transducers (7.5 m spacing), with a sampling rate of $f_{s,Tx} = 100$ kHz. The receiver was deployed at the location Sta08 as a 56.25 m aperture vertical line array (VLA) of 16 elements (3.75 m spacing), with a sampling rate of $f_{s,Rx} = 50$ kHz. The performance results are based on the channel estimates for transmissions between the fourth transducer from the bottom (49.5 m deep) and the tenth hydrophone from the bottom (65.25 m deep). We assume an OFDM transmission with $K = 512$ sub-carriers and a frequency separation of 15.25 Hz. The target average BER is $P_b = 10^{-3}$. We estimate the channel using the MP algorithm, and predict the five significant channel coefficients 2.67 s ahead.

In Figure 4.7 we provide an example of the estimated channel frequency response and the channel prediction for the error variance $\sigma_e^2 = -24$ dB, which

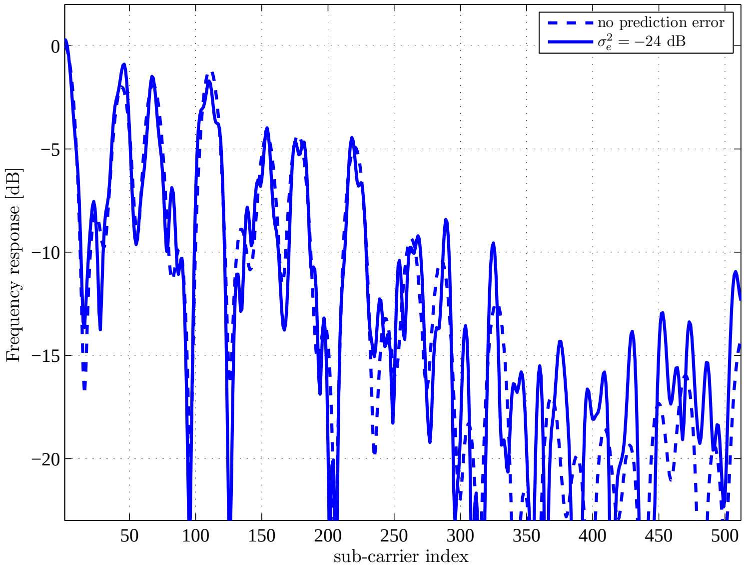

Figure 4.7: Channel frequency response and its prediction for $\sigma_e^2 = -24$ dB.

is measured relative to the overall channel power. Figure 4.8 presents achievable throughput results for the OFDM systems that employ Scheme 1 and Scheme 2 without clustering for $\sigma_e^2 = -24$ dB, which is measured relative to the overall channel power. We also provide performance results for the non-adaptive scheme (with uniform power and modulation levels) and the optimal solution, which is evaluated using the interior-point method [70] to solve the nonlinear convex optimization problem (4.17). Interestingly, Scheme 2 shows a slight performance loss only for the high SNR regime as compared to the optimal solution, while Scheme 1 exhibits a performance degradation for the entire SNR region. Both schemes significantly outperform the non-adaptive solution.

In Figure 4.9 we present the throughput achievable by Scheme 1 and Scheme 2 without clustering, and with clusters of size $K/Q = 4, 8$ and 16. We observe a difference in the performance of Scheme 1 and Scheme 2 since the channel exhibits a severe frequency selectivity. We also note that bandwidth partitioning reduces the overall throughput (especially when clusters of size 16 are chosen), because the size of the modulation alphabet for each cluster is driven by the sub-carrier with the lowest channel gain.

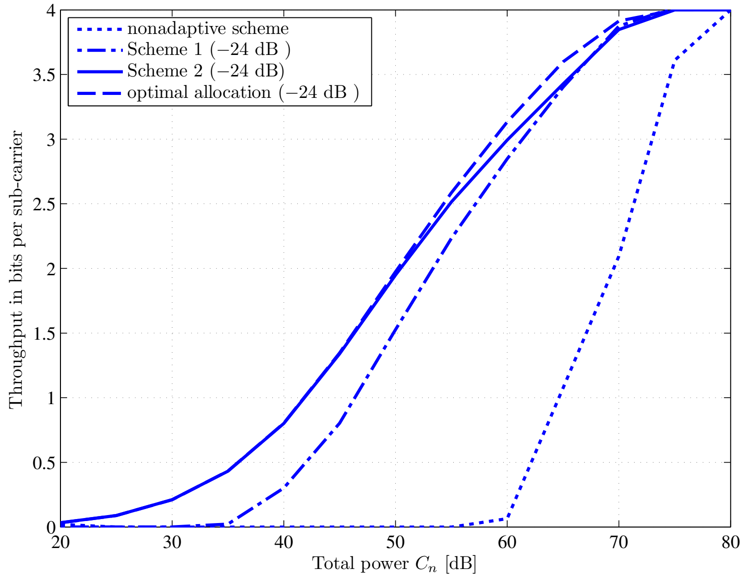

Figure 4.8: Throughput performance of the various schemes considered.

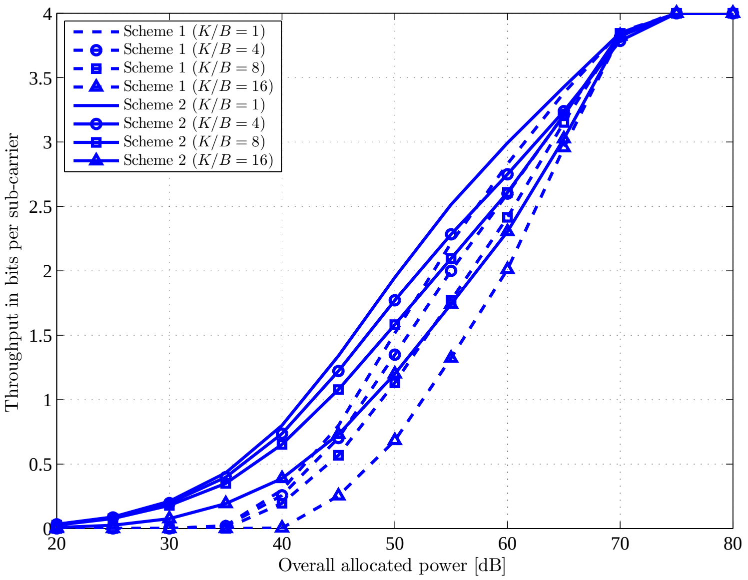

Figure 4.9: Throughput per sub-carrier for Schemes 1 and 2 with target $P_b = 10^{-3}$.

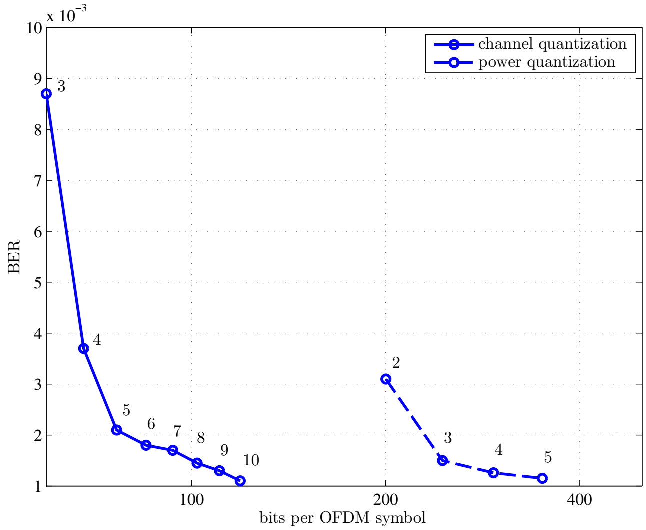

Figure 4.10: Performance of limited feedback for Scheme 2 with $Q = 1$, overall power C_n of 60 dB and average throughput of 3 bits per sub-carrier. Numbers on the graph indicate the number of bits that are used to represent the quantized power levels (dashed line), and the real and the imaginary parts of each quantized channel coefficient (solid line).

In Figure 4.10 we summarize the feedback requirements of Scheme 2 without clustering ($Q = 1$). Feeding back the power and modulation level computed at the receiver clearly requires more bits than feeding back the (sparse) channel response. $L_c = 2, 3, 4$ and 5 bits are used to represent the quantized power levels, and $L_m = 3$ bits are used to represent the five modulation levels (no transmission, BPSK, QPSK, 8PSK and 16QAM), resulting in a total of $2560, 3072, 3584$ and 4096 bits with $K = 512$ and $Q = 1$. The feedback information is then compressed as discussed in Section 4.4, resulting in 201, 245, 294 and 350 bits (the values indicated on the x-axis). If the channel response is fed back, $L_g = 3, 4, \ldots, 10$ bits are used to represent the real and the imaginary parts of each quantized channel coefficient, and $L_t = 8$ bits are used to represent the corresponding delays. The feedback information is then compressed similarly as in the previous strategy. We note that the minimum number of bits required to maintain the target average BER at 10^{-3} is 350 and 120 for the two cases, i.e. that feeding back the channel response reduces the feedback requirements approximately three fold. When clustering is

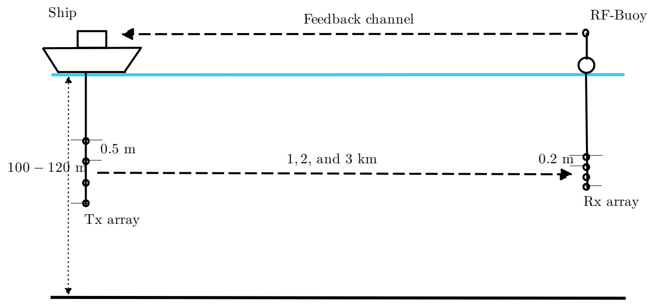

Figure 4.11: The geometry and the setup of the adaptive system.

applied, the two feedback strategies require a similar number of bits to feed back; however, clustering is performed at the expense of reducing the overall throughput of Scheme 2.

4.4.4 Experimental Results from the KAM11 Experiment

The KAM11 experiment took place in $100 - 120$ m deep water, with communication distances of 1, 2 and 3 km. The transmitter was deployed from the ship as a 1.5 m aperture vertical array of 4 ITC-1032 transducers (0.5 m spacing) at different locations within the operational area while the ship was stationary. The sampling rate was $f_{s,Tx} = 100$ kHz. The RF-coupled receiver was deployed at the location Sta05 and Sta10 (see Figure 1.8) as a 0.6 m aperture VLA of 4 elements (0.2 m spacing), with a sampling rate of $f_{s,Rx} = 100$ kHz. Both the transmitter and the receiver were deployed in the middle of the water column. A feedback from the recorder buoy was provided using an RF link. The geometry of the experiment and the setup of the system are given in Figure 4.11. The OFDM frame contains 4 blocks with $K = 1024$ sub-carriers per block, at a central frequency of $f_c = 30$ kHz. The receiver operates coherently where 50% of sub-carriers are used as pilots. The total bandwidth and the guard time are $B = 10$ kHz and $T_g = 100$ ms, respectively. Frame synchronization is performed using a PN-sequence of duration 25 ms and the symbol rate 10 ksymb/s. The presented performance results are generated by employing maximal ratio combining (MRC) of signals received at four elements. However, we should emphasize that even though MRC is used for data detection, we use only one receive element to perform channel estimation and adaptive allocation in order to minimize the processing time at the receiver.

The adaptive system is initialized at the transmitter-end (a terminal at the ship) by sending activation commands to the receiver-end (a terminal at the RF-coupled buoy) through the wireless link. Once a confirmation message is received from the receiver terminal, the transmitter-end executes a sequence of operations such as acquiring the ship position from GPS, gathering various environmental data, etc. This is followed by the first OFDM frame transmission with a uniform power allocation and QPSK modulation alphabet for all data sub-carriers. Once the frame is detected at the receiver, it is stored at the local drive for further processing. In particular, we perform initial synchronization using the PN-preamble, which is followed by Doppler estimation and compensation as suggested in [56]; we then conduct channel estimation using the orthogonal matching pursuit (OMP) algorithm [64], and perform coherent detection for each OFDM block of the received frame; finally, using the channel estimates, we execute Scheme 2 at the receiver to compute the power and modulation levels, which are then fed back to the transmitter and used for the next OFDM frame transmission. During each real-time trial, we transmitted between 30 and 50 consecutive OFDM frames in order to demonstrate the performance of the proposed adaptive scheme, and the functionality of the implemented system.

Among various constraints on the real-time implementation of the system (e.g. out-of-band interference from the other systems simultaneously tested, a weak RF link for certain positions of the ship, weather conditions, etc.), the most important limitation is determined to be the total round-trip-time of the system that was on the order of $10 - 20$ s. This significant delay was mainly caused by all-level processing of the system at both sides of the link (acquiring GPS and environmental data before each transmission, and after each reception, data detection and recording, etc.), while physical propagation contributed with delays

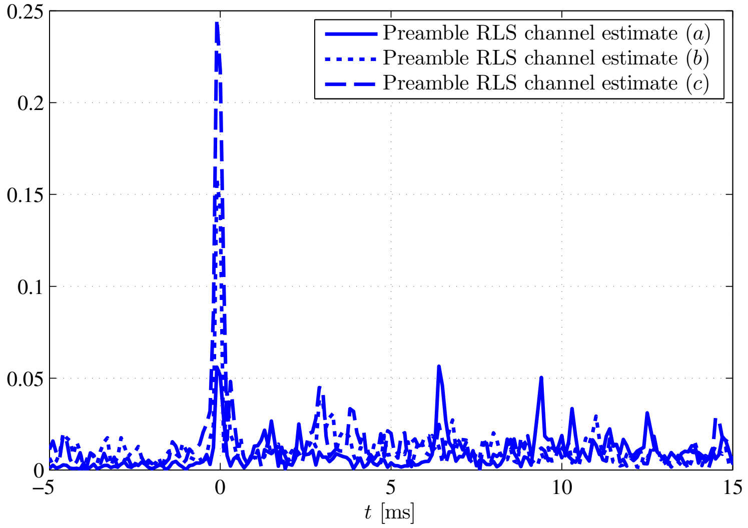

Figure 4.12: Channel estimates from initial frame synchronization preamble for three consecutive non-adaptive OFDM frame transmissions. The average time interval between two consecutive frame transmissions is (roughly) 20 s.

of $0.67 - 2$ s and delays in the RF feedback link.

In Figure 4.12 we show the channel estimates obtained from the frame synchronization preamble of a 2 km link for three consecutive non-adaptive QPSK-modulated OFDM frame transmissions, labeled as a, b and c. As mentioned earlier, the average time interval between two consecutive frame transmissions is (roughly) 20 s. Note the significant variations of the channel impulse response within a one-minute time interval. For the given consecutive OFDM frame transmissions, in Figure 4.13 we provide the performance results for the receiver with four elements. Note that poor performance is achieved for transmissions a and b, while a fair performance is obtained for transmission c, corresponding to very high SNR observed at the receiver (see Figure 4.12). If the target average BER for OFDM systems is set to $10^{-2} - 10^{-3}$, the non-adaptive scheme should use either more power, or reduce the overall throughput by employing the BPSK modulation alphabet which is preferable for the power limited systems.

In Figure 4.14 we illustrate channel estimates of a 2 km link for three consecutive adaptive OFDM frame transmissions, labeled as a, b and c. The available

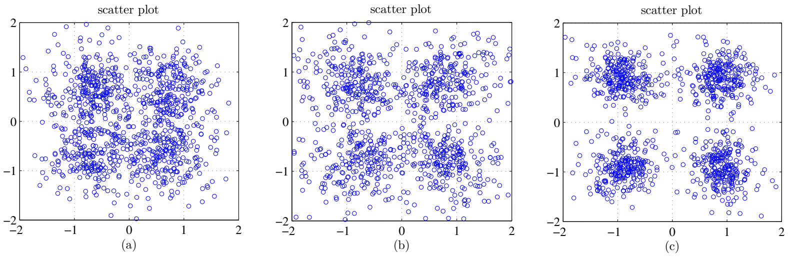

Figure 4.13: Scatter plots for three consecutive non-adaptive OFDM frame transmissions, each containing 4 OFDM blocks. The average time interval between two consecutive frame transmissions is (roughly) 20 s. The corresponding channel impulse response estimates are given in Figure 4.12.

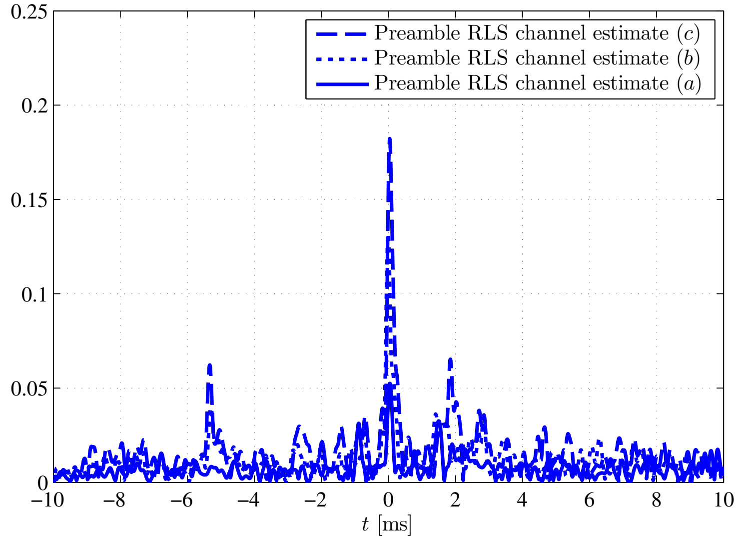

Figure 4.14: Channel estimates from initial frame synchronization preamble for three consecutive adaptive OFDM frame transmissions. The average time interval between two consecutive frame transmissions is (roughly) 20 s.

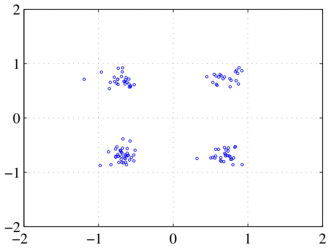

(*a*) QPSK

Figure 4.15: Scatter plot (*a*) for the first adaptive OFDM frame transmission, each containing 4 OFDM blocks. The adaptive Scheme 2 allocates only QPSK modulation alphabet to the data-sub-carriers.

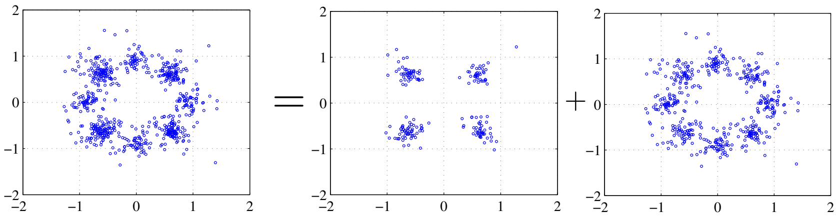

(*b*) QPSK and 8PSK QPSK 8PSK

Figure 4.16: Scatter plot (*b*) for the second adaptive OFDM frame transmission, each containing 4 OFDM blocks. The adaptive Scheme 2 allocates QPSK and 8PSK modulation alphabets to the data-sub-carriers.

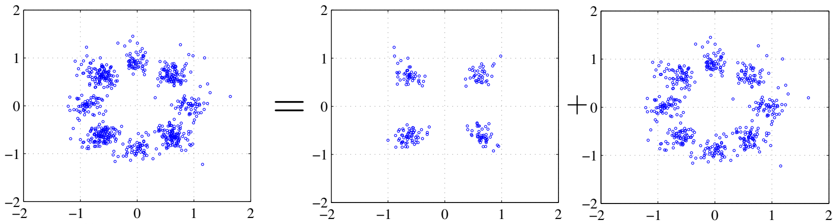

(*c*) QPSK and 8PSK QPSK 8PSK

Figure 4.17: Scatter plot (*c*) for the third adaptive OFDM frame transmission, each containing 4 OFDM blocks. The adaptive Scheme 2 allocates QPSK and 8PSK modulation alphabets to the data-sub-carriers.

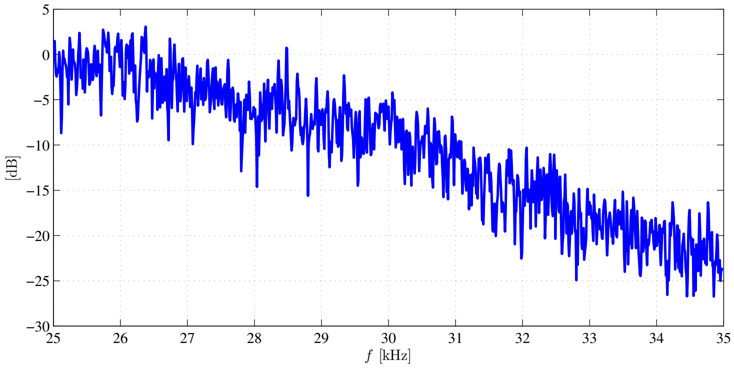

Figure 4.18: A sample estimate of the channel frequency response for the OFDM system with $K = 1024$ sub-carriers.

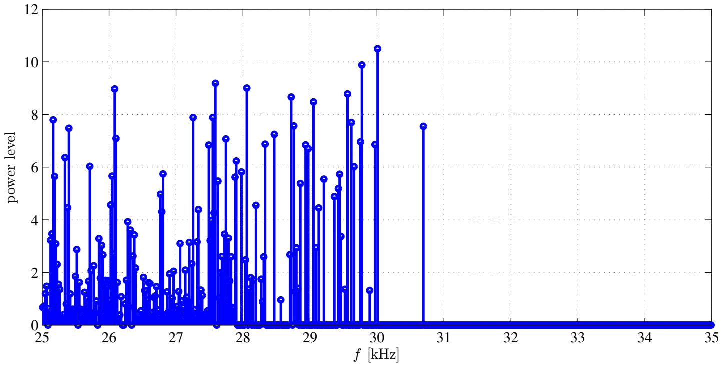

Figure 4.19: A sample power allocation for data sub-carriers based on Scheme 2 and the channel response from Figure 4.18.

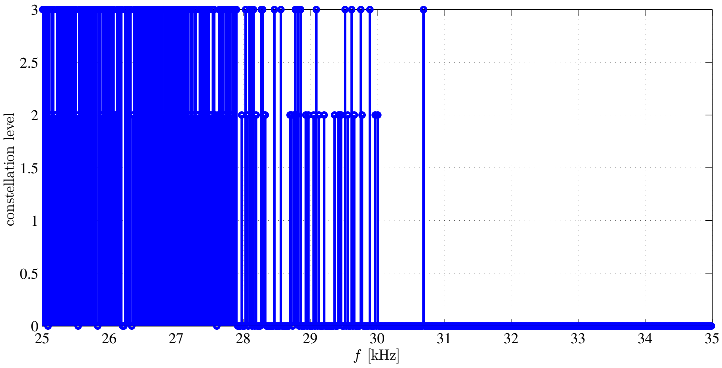

Figure 4.20: A sample constellation level allocation for data sub-carriers based on Scheme 2 and the channel response from Figure 4.18.

adaptive modulation alphabets are BPSK, QPSK and 8PSK. As in the previous set of non-adaptive OFDM block transmissions, we note significant variations in the channel impulse response within an one-minute time interval. For the given consecutive OFDM frame transmissions, in Figs. 4.15, 4.16 and 4.17 we provide the performance results for the receiver with four elements. For the target average BER set to $10^{-2} - 10^{-3}$, we note that a good performance is achieved for all three transmissions (a, b, and c in Figs. 4.15, 4.16 and 4.17, respectively), since Scheme 2 successfully tracks the underlying channel variations. Due to large propagation delays and significant channel variations that impose severe limitations on channel prediction, the adaptive scheme tends to oscillate in performance around the target BER. In Figs. 4.18, 4.19 and 4.20, we illustrate the channel frequency response, the allocated power and modulation levels across the data sub-carriers, respectively. A high attenuation in the frequency region $30 - 35$ kHz is mainly due to the cutoff frequency of the hydrophones which is located around 30 kHz, resulting in a severe roll-off across the upper part of the operational bandwidth. We emphasize that this system limitation was not known *a priori*, and the whole operational bandwidth ($25 - 35$ kHz) was used for OFDM transmissions. However, Scheme 2 has successfully demonstrated the ability to adapt to the system limitations by allocating the power and modulation levels to the lower part of the frequency region as illustrated in Figs. 4.19 and 4.20.

4.5 Summary

In this chapter we explored design aspects for adaptive OFDM modulation over time-varying UWA channels. First, we investigated the possibility of predicting an UWA channel at least one travel time ahead. The key step in providing a stable reference for channel prediction is compensation of the motion-induced phase offset. Matching pursuit algorithms are used to identify the significant path coefficients, which are then processed by a low-order adaptive RLS predictor to account for large prediction lags (long feedback delays). Second, assuming that the channel is predicted one travel time ahead with a given accuracy, approximate expressions for the BER of each sub-carrier (or a cluster of adjacent sub-carriers) are obtained. From these expressions, a set of thresholds is obtained that determine the modulation level and the power needed on each sub-carrier in order to maximize the throughput while keeping the average BER at the target level. Third, spectrally-efficient adaptive schemes (Scheme 1 and Scheme 2) are applied to allocate the modulation and the power across the OFDM sub-carriers. Finally, assuming a limited feedback channel, two competitive strategies were analyzed: one that feeds back the quantized power level for each sub-carrier/cluster, and another that feeds back the quantized estimate of the significant channel coefficients in the time domain. The second strategy is found to offer better performance, as it requires significantly fewer feedback bits. Numerical and experimental results that are obtained with recorded channels and real-time at-sea experiments, respectively, show that the adaptive modulation scheme provides significant throughput improvements as compared to conventional, nonadaptive modulation at the same power and target BER. This work leads us to conclude that adaptive modulation methods may be viable for reliable, high-rate UWA communications. To our knowledge, this is the first work that presents adaptive modulation results for UWA links with real-time at-sea experiments.

Sections 4.1, 4.2 and 4.4, in part, are a reprint of the material as it appears in "Channel prediction for adaptive modulation in underwater acoustic communications," by A. Radosevic, T. M. Duman, J. G. Proakis, and M. Stojanovic, IEEE Oceans'11 Conference, Santander, Spain, June 2011. The dissertation author was the primary investigator and author of this paper.

Sections 4.3 and 4.4, in part, are a reprint of the material as it appears in "Adaptive OFDM for underwater acoustic channels with limited feedback," by A. Radosevic, T. M. Duman, J. G. Proakis, and M. Stojanovic, 45rd Asilomar Conference on Signals, Systems and Computers, Nov. 2011. The dissertation author was the primary investigator and author of this paper.

Sections 4.1 through 4.4, in part, are also a reprint of the material as it appears in "Adaptive OFDM modulation for underwater acoustic communications: design considerations and experimental study," by A. Radosevic, R. Ahmed,

T. M. Duman, J. G. Proakis, and M. Stojanovic, submitted for publication in IEEE Journal of Oceanic Engineering.

Chapter 5

Selective Decision Directed Channel Estimation for UWA OFDM Systems

As we have discussed in Chapter 2, UWA channels are characterized by time-varying multipath that results in frequency selective fading. Delay spreading in a UWA channel can occur over tens of milliseconds; however, a typical channel impulse response is characterized by a sparse multipath structure, i.e., a few propagation paths carry most of the channel energy [1]. Moreover, acoustic propagation is best supported at low frequencies making the UWA communications inherently wideband. All of these properties of UWA channels make coherent signal detection challenging. Particularly, a receiver operating in the coherent mode relies on its ability to track the motion-induced phase variations and to estimate the channel as accurately as needed in order to achieve satisfactory system performance. For wideband UWA OFDM systems, this practically means that for each transmitted OFDM block one needs to estimate the nonuniform Doppler effects across the operational bandwidth and the channel impulse response for equalization and coherent detection [54].

Pilot-assisted channel estimation (CE) is used as a standard method to obtain necessary CSI for reliable coherent communications. For OFDM systems a uniformly spaced pilot grid is shown to be a robust pilot allocation strategy for CE under various conditions if the channel is time-invariant, i.e. without ICI [71], while allocation of uniformly spaced blocks of pilots is effective for channels with ICI [72]. There are several studies in the existing literature regarding coherent UWA OFDM communications that propose various CE methods for obtaining the reliable CSI on a block-by-block basis [73]– [74]. While uniform pilot allocation is effective for block-by-block processing of OFDM words at the receiver, an improved CE method can be derived by exploiting the channel correlation in time to obtain tentative decisions on the data sub-carriers and thus obtain additional channel information at the corresponding frequency locations [10]. In other words, for the currently received OFDM block, the CSI from data sub-carriers is delivered in a *decision directed* (DD) manner based on channel estimates which are already available at the receiver from the previously received OFDM block. In the context of UWA communications, in [10] and [11], a fully decision directed method is exploited for CE and high system throughputs are achieved. This method assumes a large channel coherence time, spanning over several transmitted blocks and tracking of a common Doppler factor after initial resampling.

In this chapter we explore the performance of a *selective* DD CE method for OFDM based communications. We combine the CSI from the pilot sub-carriers, and the reliable *a priori* CSI from previous OFDM blocks that is used to selectively choose data sub-carriers for DD CE. The method is based on either *hard* selection of data sub-carriers where we choose those sub-carriers that have high SNRs, or *soft* selection where we weight *all* data sub-carriers for reliable DD CE. Particularly, in the process of hard selection we choose those sub-carriers that have high SNR, while in the process of soft selection we weight the data sub-carriers for reliable channel estimation. The latter approach is shown to be advantageous since the CSI from *all* data sub-carriers is exploited. We couple selective decision directed CE with different channel reconstruction methods such as least-squares (LS) with thresholding [11], OMP [64], and basis pursuit denoising (BPD) [75].

Later in this chapter, we study the performance of the selective DD CE method over multipath Rician fading channels, where fading is modeled as an auto-regressive (AR) random process. For uncoded and low density parity check

(LDPC)-coded OFDM systems, we explore the trade-offs resulting from using a varying number of pilots and/or DD data sub-carriers, the effect of the receiver-end diversity, and the impact of channel properties (such as the Rician k-factor and the Doppler spread) in terms of the overall system throughput and BER. Using experimental data and numerical results, we demonstrate performance improvements of the proposed selective DD CE scheme as compared to the block-by-block pilot-assisted CE scheme with a uniform pilot grid and the full DD CE scheme.

The chapter is organized as follows. In Section 5.1 we describe the system model for selective DD CE. In particular, we introduce the selection strategies for data sub-carriers, present the selective phase tracking scheme, and propose the selective DD CE in the context of different channel reconstruction methods; in Section 5.2, we present experimental results that demonstrate the performance of the proposed channel estimation method; in Section 5.3, we study the performance of the proposed CE method over multipath Rician fading channels; in Section 5.4, we present corresponding numerical results for uncoded and LDPC-coded systems; Finally, we provide our concluding remarks in the summary of the chapter.

5.1 System and Channel Model

Let us consider similarly as in Chapter 4 an OFDM system with K sub-carriers and a total bandwidth B. We denote by f_0, $f_c = f_0 + B/2$ and $\Delta f = B/K$, the frequency of the first sub-carrier, the central frequency, and the sub-carrier separation, respectively. The set of information bearing sub-carriers and pilots are denoted as $\mathcal{S}_d$ and $\mathcal{S}_p$, respectively, while $\mathcal{S}_d \cup \mathcal{S}_p = 0, 1, ..., K-1$. The same modulation alphabet QPSK is used for both information and pilot symbols, and the power of the modulated symbols is normalized to unity. The corresponding continuous-time passband zero-padded (ZP) OFDM signal can be represented as

$$s(t) = \begin{cases} \mathrm{Re}\left\{ \sum\limits_{k=0}^{K-1} X_k e^{j2\pi(f_0 + k\Delta f)t} \right\} & , 0 \le t < T \\ 0 & , T \le t < T', \end{cases} \tag{5.1}$$

where X_k is the modulated symbol on the k-th sub-carrier, $T' = T + T_g$, $T = K/B$ is the symbol duration, and T_g is the guard time interval. Let us define the impulse response of the overall channel that includes the initial resampling operation at the receiver by a common Doppler factor as

$$h(\tau, t) = \sum_{p=0}^{P-1} h_p(t)\delta(\tau - \tau_p(t)), \tag{5.2}$$

where P is the number of distinct propagation paths, τ is the delay variable and t is the time at which the channel is observed. The coefficient $h_p(t)$ is the real-valued gain of the path p, and $\tau_p(t)$ is the corresponding delay. The received signal at the output of the channel is given as

$$r(t) \;=\; \sum_{p=0}^{P-1} h_p(t)s(t - \tau_p(t)) + n(t), \tag{5.3}$$

where $n(t)$ represents the AWGN[1] process with zero-mean and power spectral density normalized to unity. From Eq.(5.3) we further define the equivalent baseband received signal $y(t)$ with respect to the frequency f_c as

$$y(t) \;=\; \sum_{k=0}^{K-1}\sum_{p=0}^{P-1} h_p(t)e^{-j2\pi(f_0+k\Delta f)\tau_p(t)}X_k e^{j2\pi(k\Delta f-B/2)t} + w(t), \tag{5.4}$$

where $w(t)$ is the baseband representation of the noise process $n(t)$. If we model the time-varying path delays as in Chapter 4

$$\tau_p(t) = \tau_{p0} - \int_{x=0}^{t} a_p(x)dx, \tag{5.5}$$

we obtain the following representation of the baseband received signal

$$y(t) = \sum_{k=0}^{K-1}\sum_{p=0}^{P-1} g_p(t)e^{-j2\pi(k\Delta f-B/2)\tau_{p0}+j\theta_{p,k}(t)}X_k e^{j2\pi(k\Delta f-B/2)t} + w(t), \tag{5.6}$$

where $g_p(t) = h_p(t)e^{-j2\pi f_c\tau_{p0}}$ is a complex-valued channel coefficient, and $\theta_{p,k}(t) = 2\pi(f_0+k\Delta f)\int_{x=0}^{t} a_p(x)dx$ is the path-specific motion-induced phase offset observed on the k-th sub-carrier.

If the OFDM blocks are periodically transmitted at time instances $t = nT'$, the demodulator output corresponding to the k-th sub-carrier at time n is written

---

[1] The AWGN assumption incurs no loss of generality even though acoustic noise is not white.

as

$$\begin{aligned} Y_k(n) &= \frac{1}{T}\int_{t=(n-1)T'}^{nT'} y(t)e^{-j2\pi(k\Delta f-B/2)t}dt \\ &= \sum_{p=0}^{P-1} g_p(n)e^{-j2\pi(k\Delta f-B/2)\tau_{p0}}\Bigg\{\rho_{k,k}^{(p,n)}X_k(n)+ \\ &\qquad +\sum_{\substack{m=0\\m\neq k}}^{K-1}\rho_{k,m}^{(p,n)}X_m(n)\Bigg\}+W_k(n), \end{aligned} \tag{5.7}$$

where $\rho_{k,m}^{(p,n)}$ is the ICI term from the m-th sub-carrier and p-th path, and $W_k(n)$ is noise. From this point on, we assume that initial resampling by a common (dominant) Doppler factor removes a major portion of the ICI, such that $\rho_{k,k}^{(p,n)} \approx 1$, for every p, k, and n. We assume that channel coefficients $g_p(n)$ and Doppler factors $a_p(n)$ are constant at least for the duration of one OFDM block [10] [11]. Therefore, we have

$$Y_k(n) \approx \sum_{p=0}^{P-1} g_p(n)e^{j\theta_{p,k}(n)}e^{-j2\pi(k\Delta f-B/2)\tau_{p0}}X_k(n)+W'_k(n), \tag{5.8}$$

where $W'_k(n)$ is a modified noise term of the variance $\sigma_{w,k}^2$ that includes residual ICI on the k-th sub-carrier. In the simplest case when $a_p(n)=0, \forall p$, the model in (5.8) corresponds to a time-invariant channel; if $a_p(n)=a(n), \forall p$, we have a channel where all the paths experience the same Doppler effect. For this particular case, a single tracking mechanism is needed in order to track the phase offset correctly, as previously reported in [11], and the received signal from Eq.(5.8) is simplified as

$$\begin{aligned} Y_k(n) &\approx e^{j\theta_k(n)}\sum_{p=0}^{P-1} g_p(n)e^{-j2\pi(k\Delta f-B/2)\tau_{p0}}X_k(n)+W'_k(n) \\ &= e^{j\theta_k(n)}G_k(n)X_k(n)+W'_k(n) \end{aligned} \tag{5.9}$$

where

$$\theta_k(t) = 2\pi(f_0+k\Delta f)\int_{x=0}^{t} a(x)dx, \tag{5.10}$$

is the common motion-induced phase offset, and $G_k(n)$ is the channel frequency response at the k-th sub-carrier at time n. In this chapter, we will consider a modified version of the tracking mechanism in [11] that conforms to the proposed selection process for the data sub-carriers. In general, the signal replicas from different propagation paths may not experience the same Doppler, and multiple Doppler factors may need to be tracked.

5.1.1 Selection of Data Sub-carriers

Regardless of the phase tracking method, the quality of Doppler estimates depends on the quality of tentative decisions, which in turn depends on the signal quality, i.e. the SNR on their respective sub-carriers, and the reliability of the CSI that is already available at the receiver. For example, if we track the common Doppler factor $a(n)$ as in (5.9), we measure the motion-induced phase offsets $\theta_k(n)$ at different sub-carriers and provide the average value $\tilde{a}(n)$ as the Doppler estimate. Doppler estimates are more reliable at sub-carriers with high SNR than at those with low SNR. Therefore, for frequency-selective UWA channels, *weighting* the contribution of the sub-carriers with respect to their SNRs for Doppler estimation provides more reliable estimates than the case when all sub-carriers are weighted equally to produce an average. Similarly, if decision directed data sub-carriers are to be used in channel estimation, more reliable tentative decisions are obtained at the sub-carriers with high SNRs and a good channel estimate from the previously received OFDM block. Errors in the tentative decisions are more likely to occur at low SNR regions, resulting in a degraded performance of CE. Therefore, it is beneficial to introduce a *selective* strategy for choosing data sub-carriers that will be used in a decision directed CE. In the following we describe the *hard* and *soft* selection strategies employed in the section.

5.1.2 Hard Selection

In this case, we choose a *portion* of the data sub-carriers for Doppler and channel estimation. Specifically, we select those sub-carriers that satisfy a minimum SNR requirement at the receiver. We denote the set of selected data sub-carriers as $\mathcal{S}_{dd} = \{k : SNR_k \geq SNR_{Th}\}$, where $k \in \mathcal{S}_d$ and $SNR_{Th} =$

$\alpha \max_k SNR_k$ $(0 \leq \alpha \leq 1)$ is the minimum required SNR at the receiver. The pilots and the selected data sub-carriers are weighted with unity, i.e., the weight vector $\boldsymbol{\gamma}(n) = [\gamma_0(n)\gamma_1(n) \cdots \gamma_{K-1}(n)]^T$ is defined as

$$\gamma_k(n) = \begin{cases} 1, & k \in \mathcal{S}_{dd} \cup \mathcal{S}_p, \\ 0, & \text{otherwise.} \end{cases} \tag{5.11}$$

5.1.3 Soft Selection

In contrast to the strategy of hard selection, in this case we weight *all* data sub-carriers for reliable Doppler and channel estimation according to the SNR of the sub-carriers. In order to obtain the weight vector for soft selection, let us first assume that the motion-induced phase offset from Eq.(5.9) is perfectly compensated at the receiver. Thus, the received signal at the k-th sub-carrier is given as

$$Y'_k(n) = G_k(n)X_k(n) + W''_k(n). \tag{5.12}$$

Due to imperfect CSI and the presence of noise, tentative decisions on the data symbols are subject to errors. This can be expressed in the following form:

$$Y'_k(n) = G_k(n)\tilde{X}_k(n) + G_k(n)(X_k(n) - \tilde{X}_k(n)) + W''_k(n), \tag{5.13}$$

where $\tilde{X}_k(n)$ is the hard-decision on the data symbol. Assuming a unit-amplitude modulation alphabet (e.g. QPSK), multiplying both sides of (5.13) by the conjugate of the tentative decision $\tilde{X}^*_k(n)$ at the k-th sub-carrier, we obtain

$$Z_k(n) = G_k(n) + \underbrace{G_k(n)(\tilde{X}^*_k(n)X_k(n) - 1) + W'''_k(n)}_{W_{e,k}(n)}, \tag{5.14}$$

where $W_{e,k}(n)$ is an equivalent noise term that includes the effect of errors in the tentative decisions. Note from Eq. (5.14) that the data sub-carriers experience different noise levels, since the variance of $W_{e,k}(n)$ directly depends on the reliability of the symbol decision and the channel gain. This implies that the received signals across the data sub-carriers are not equally reliable when used as the additional observations for Doppler and channel estimation. If we assume $E\{W_{e,k_1}(n)W^*_{e,k_2}(n)\} = 0$ $(k_1 \neq k_2)$, the best *linear* unbiased estimator is obtained by weighting of the received signals, such that the resulting observations experience equal noise levels, which is followed by LS estimation [76]. In other words, the vector of the received signals is subject to *noise whitening* prior to CE. Therefore, if we define the variance of the equivalent noise as $\sigma^2_{e,k}(n) = E\{|W_{e,k}(n)|^2\}$, the weight vector $\boldsymbol{\gamma}(n)$ is set to

$$\gamma_k(n) = \begin{cases} \sigma_{w,k}\sigma^{-1}_{e,k}(n), & k \in \mathcal{S}_{dd} \\ 1, & k \in \mathcal{S}_p. \end{cases} \tag{5.15}$$

Note from Eq.(5.14) that the equivalent noise has non-Gaussian distribution. In order to provide a simple (albeit sub-optimal) solution for the weight vector, we introduce a Gaussian approximation for the noise term with the variance $\sigma^2_{e,k}(n)$. From Eq.(5.14), this variance is written as

$$\sigma^2_{e,k}(n) = \sigma^2_{w,k}\left(1 + 2\left(1 - \mathrm{Re}\left\{E\{\tilde{X}^*_k(n)X_k(n)\}\right\}\right)\frac{|G_k(n)|^2}{\sigma^2_{w,k}}\right). \tag{5.16}$$

Since the channel gain $G_k(n)$ is unknown, the channel estimate $\hat{G}_k(n-1)$ from the previously received OFDM block is used instead. The estimation error caused by the imperfect (outdated) CSI is modeled as a Gaussian random variable with the variance σ^2_e. Under these assumptions, it can be shown (see Appendix B) that an upper bound on the variance term from Eq.(5.16) is given by

$$\begin{aligned} \sigma^2_{e,k}(n) &\leq \sigma^2_{UB,k}(n) \\ &\triangleq \sigma^2_{w,k}\left(1 + \frac{\sqrt{\frac{8}{\pi}}\max_l\left\{|\hat{G}_k(n-1)|\right\}}{\frac{\sigma^2_{w,k}}{\left(\sigma^2_{w,k}+\sigma^2_e\right)^{\frac{1}{2}}}e^{\frac{|\hat{G}_k(n-1)|^2}{2(\sigma^2_{w,k}+\sigma^2_e)}}}\right). \end{aligned} \tag{5.17}$$

Finally, by substituting $\sigma^2_{e,k}(n) = \sigma^2_{UB,k}(n)$ into Eq.(5.15), we obtain a simple closed-form solution for the weight vector $\boldsymbol{\gamma}(n)$. Since the CSI from all data subcarriers is exploited, the strategy of soft selection is expected to result in a better performance compared to the one based on hard selection.

5.1.4 Selective Phase Tracking

In this section we briefly describe data sub-carrier selection in the context of Doppler estimation. Doppler estimation is based on the method [11] which is extended here to use not only the pilots but the selected data sub-carriers as well. Based on the model (5.9) of the received signal in the frequency domain, the update equation for phase tracking is given as the weighted average of the Doppler estimates across the sub-carriers

$$\hat{a}(n) = \frac{1}{|\mathcal{S}_{dd} \cup \mathcal{S}_p|} \sum_{k \in \mathcal{S}_{dd} \cup \mathcal{S}_p} \boldsymbol{\gamma}(l) \left(\frac{\angle \hat{X}_k(n) X_k^*(n)}{\pi (f_0 + k\Delta f) T'} \right) - \hat{a}(n-1), \tag{5.18}$$

where $|\cdot|$ denotes the cardinality of a set, and $\hat{X}_k(n)$ is the soft-decision on the k-th data symbol at the output of the detector at time n. $\mathcal{S}_{dd} \subseteq \mathcal{S}_d$ corresponds to the set of decision directed data sub-carriers used as an additional set of observations in generating a reliable CSI. In (5.18) we assume a linear Doppler behavior, where the phase $\theta_k(n)$ changes as a second-order polynomial in time. If $S_{dd} = \emptyset$, the summation in (5.18) is carried out over S_p only, and the approach reduces to that of [11].

5.1.5 Selective Decision Directed Channel Estimation

For rapidly varying channels, a robust strategy for obtaining reliable CSI is block-by-block pilot-assisted CE. In contrast, for slowly (or moderately) time varying channels with a coherence time that spans over a few consecutive OFDM blocks, CE can benefit from additional *a priori* channel knowledge obtained during the previous block transmissions. In other words, channel correlation in time can be exploited to improve the quality of tentative decisions. Those symbol decisions that correspond to sub-carriers with a good SNR can be selected to assist in the decision directed CE. They can be used as additional pilots to improve the quality of CE beyond that afforded by the original pilots only. Furthermore, one can benefit from the decision directed CSI by making multiple iterative passes through each OFDM block.

5.1.6 Selective Channel Reconstruction

At time instant (block) n the estimate of the impulse response is represented by L coefficients

$$\mathbf{g}(n) = [g_0(n), g_1(n), \ldots, g_{L-1}(n)]^T, \tag{5.19}$$

which are equally spaced at $1/B$. Assuming a high bandwidth (sufficient resolution) these coefficients offer a good representation of the actual propagation paths. Under the assumption of *sparse* multipath structure of the UWA channels, only $P \ll L$ coefficients of the vector $\mathbf{g}(n)$ are significant, while the rest can be neglected.

Among numerous reconstruction methods found in the literature, we focus on coupling selective decision directed CE with three reconstruction methods, suitable for sparse channel estimation:

1. Least-Squares estimator with thresholding [11]. This is a two step estimation method in which we first minimize the cost function:

   $$\hat{\mathbf{g}}(n) = \min_{\mathbf{g}(n)} \|\mathbf{W}(n)\mathbf{y}(n) - \mathbf{W}(n)\mathbf{X}(n)\mathbf{F}\mathbf{g}(n)\|^2, \tag{5.20}$$

   where $\mathbf{W}(n) = diag(\boldsymbol{\gamma}(n))$, and $\mathbf{X}(n)$ is the $K \times K$ diagonal matrix of the pilot symbols and the selected tentative decisions on data symbols; $\mathbf{y}(n)$ is the vector of the received signals from (5.8) on the corresponding pilot sub-carriers and decision directed data sub-carriers; $\mathbf{F}$ is the Discrete Time Fourier Transform matrix whose rows correspond to the pilot and the decision directed data frequencies. It can be observed from Eq.(5.20) that the decision directed sub-carriers provide additional observations.

   In the second step, the elements of the channel estimate $\hat{\mathbf{g}}(n)$ that are below some prespecified threshold g_{Th} are set to zero [11]. Obviously, this method improves upon a widely used LS channel estimator which minimizes the energy of the residual error without having the knowledge about the sparse multipath structure of the channel. The drawback of this method is that the variance of the estimation noise depends on the ratio of the number of unknown channel coefficients to the number of observations.

2. Orthogonal Matching Pursuit [64] is an iterative LS-based estimator, where the number of iterations is defined by the number of unknown channel coefficients that are to be estimated. In the available literature, different stopping criteria are utilized to specify the number of iterations, since the number of dominant channel coefficients is not known in advance; here, we use stopping criteria that measure the channel coefficient energy in the current iteration relative to the previous one.

3. Basis Pursuit Denoising [75], commonly used in the compressive sensing theory, can be formulated as:

$$\begin{aligned}\hat{\mathbf{g}}(n) &= \min_{\mathbf{g}(n)} \frac{1}{2}\|\mathbf{W}(n)\mathbf{y}(n) - \mathbf{W}(n)\mathbf{X}(n)\mathbf{F}\mathbf{g}(n)\|^2 + \\ &\qquad + \lambda\|\mathbf{g}(n)\|_1, \end{aligned} \tag{5.21}$$

   where $||\cdot||_1$ denotes the l_1 norm, and λ is a regularization factor that puts weight on channel sparsing, enforced by l_1 reconstruction. There are several algorithms in the literature that solve the combined l_1/l_2 problem efficiently. This estimation method is expected to provide a better quality of the CSI when the channel is sparse, and a reduced estimation error as compared to the regular LS estimator.

Our goal is to analyze the performance of these channel reconstruction methods when coupled with Doppler tracking and selective decision directed operation, and compare them with the existing counterparts that are strictly pilot-based. We also explore the effect of varying the number of pilots and/or decision directed data sub-carriers.

5.2 Experimental Results

We present results based on real data measurements from the Mobile Acoustic Communication Experiment 2010 (MACE'10) experiment. The OFDM frame contains $N_{bl} = 16$ blocks with $K = 512$ sub-carriers per block at a central frequency of $f_c = 13$ kHz. The first block is used for initialization of the coherent receiver.

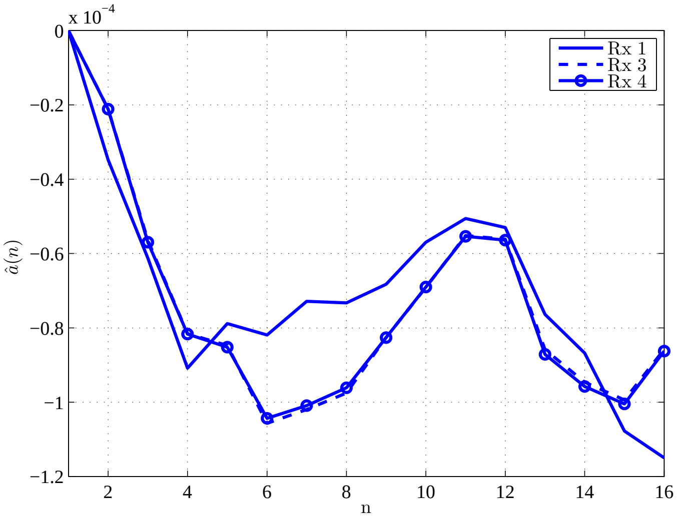

Figure 5.1: Performance of the phase tracking mechanism (5.18) across 16 OFDM blocks. Each receive element has a separate PLL.

The total bandwidth and the guard time are $B = 4.8$ kHz and $T_g = 100$ ms, respectively. The sampling rate is 40 kHz. The presented performance results are generated by employing maximal ratio combining of signals received at three elements.

Figure 5.1 shows the estimated Doppler rate as a function of time. Results are shown for the three receiver elements. Even though the receive elements are co-located they experience different Dopplers, the fact that motivates us to utilize separate tracking mechanisms (5.18) for each element. In Figure 5.2, we illustrate the performance of the full pilot-assisted CE based on LS and OMP channel reconstruction. The quality of the channel estimates justifies the usage of the threshold $h_{Th} = -26$ dB (with respect to the strongest channel tap) and the number of unknown channel taps $P = 30$ for the LS and the OMP, respectively.

Figs. 5.3–5.5 illustrate the performance for varying number of pilots and the LS with thresholding, the OMP, and the BPD as the channel reconstruction methods, respectively. From Figure 5.3, we note that the advantage of exploiting the channel correlation in time and soft selection of the CSI from the data subcarriers is apparent for $|\mathcal{S}_p| = 32, 64$ and 128, since the performance is significantly improved as compared to the case when only the pilots ($|S_{dd}| = 0$) are used.

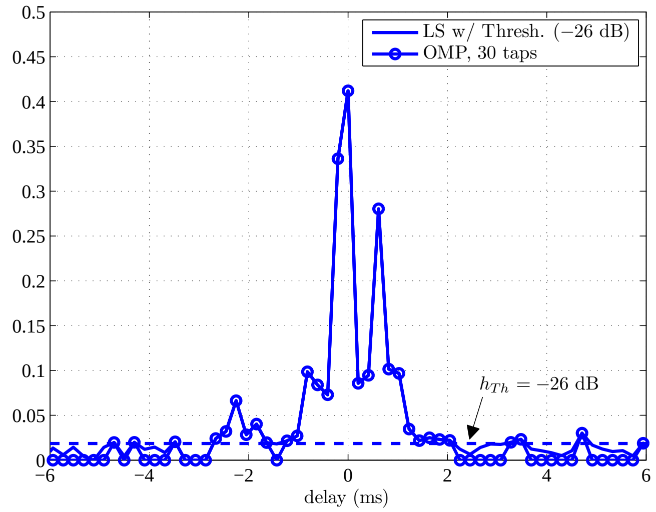

Figure 5.2: Performance of the pilot-assisted CE based on LS and OMP channel reconstruction with $|\mathcal{S}_p| = 512$. The threshold $g_{Th} = -26$ dB (with respect to the strongest channel tap) and the number of unknown channel taps $P = 30$ are used for LS and OMP, respectively.

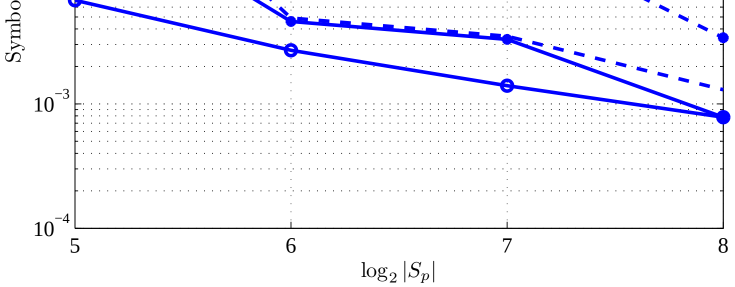

Figure 5.3: Performance of selective decision directed CE with $|\mathcal{S}_p| = 32, 64, 128$ and 256 pilots, and $K = 512$ carriers. LS channel reconstruction is used with the threshold $g_{Th} = -26$ dB (with respect to the strongest channel tap). The performance of the pilot-assisted and the non-weighted decision directed CE is provided as reference.

Moreover, note that the strategy of soft selection with 64 pilots results in the same performance as the conventional pilot-assisted CE with 128 pilots. This demonstrates the strength of selective decision feedback by allowing for fewer pilots to achieve a target system performance, which in turn results in an increase of the spectral efficiency. The strategy of hard selection for $\alpha = 0.25$ shows a good improvement as compared to the pilot-assisted CE for $|\mathcal{S}_p| = 32$, while the non-weighted decision directed CE (specified in the figures with full DD) results in a performance degradation for most of the pilot allocations, since not all of the data sub-carriers have reliable CSI. For $|\mathcal{S}_p| = 32$, note also that the strategy of hard selection performs worse than the corresponding non-weighted approach, since a large portion of data sub-carriers is ignored by introducing zero weights, and, therefore, no CSI is exploited. For low spectral efficiencies, i.e. $|\mathcal{S}_p| = 256$, we note a minor improvement of selection-based strategies, since a very accurate CSI is derived from the pilot sub-carriers.

In Figure 5.4, we observe a two-fold decrease of the error rate attained by the decision directed CE with soft selection and $|\mathcal{S}_p| = 32, 64$ and 128, with respect to the block-by-block pilot-assisted CE. This is a significant gain in performance, which confirms the utility of selective decision feedback. Similarly as for the LS-based CE, the strategy of soft selection with 32 and 64 pilots results in the same performance as the pilot-assisted CE with 64 and 128 pilots, respectively. The strategy of hard selection shows the same performance as the pilot-assisted CE, except for $|\mathcal{S}_p| = 32$. In Figure 5.5, we observe a similar performance of the pilot-assisted and the considered decision directed strategies. This similarity in the results is explained by the fact that the l_1 norm term dominates in the combined cost function (5.21), which in turn results in a minor impact of the selection strategies on CE. Note from the previous results that the OMP-based CE offers the best performance.

Figure 5.6 shows the distribution of errors in the time domain, for the $|S_p| = 32$ and the OMP channel reconstruction. We observe that all decision directed CE methods perform better than their pilot-based counterparts. Specifically, decision directed CE with hard selection shows an improvement as compared to the pilot-

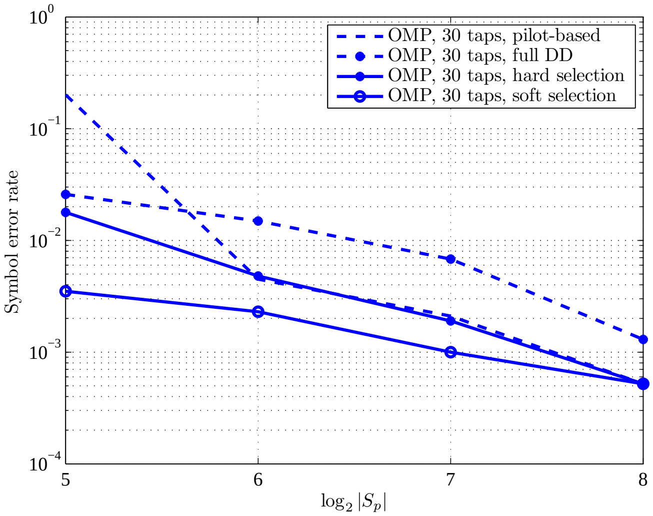

Figure 5.4: Performance of selective decision directed CE with $|\mathcal{S}_p| = 32, 64, 128$ and 256 pilots, and $K = 512$ carriers. OMP channel reconstruction is used with the number of unknown channel taps $P = 30$. The performance of the pilot-assisted and the non-weighted decision directed CE is provided as reference.

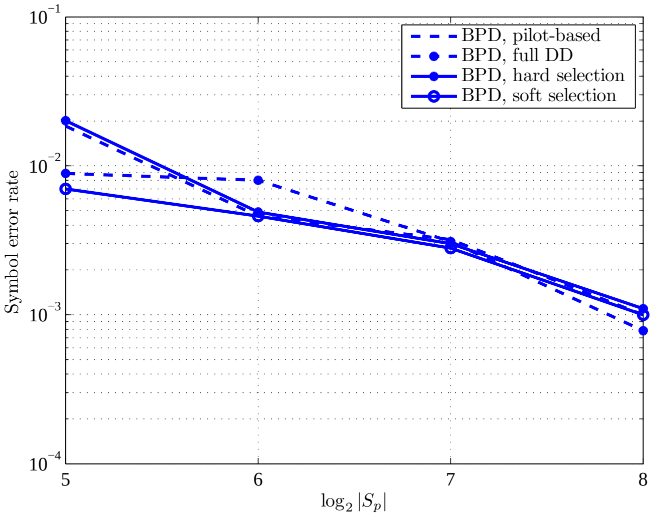

Figure 5.5: Performance of selective decision directed CE with $|\mathcal{S}_p| = 32, 64, 128$ and 256 pilots, and $K = 512$ carriers. BPD channel reconstruction is used. The performance of the pilot-assisted and the non-weighted decision directed CE is provided as reference.

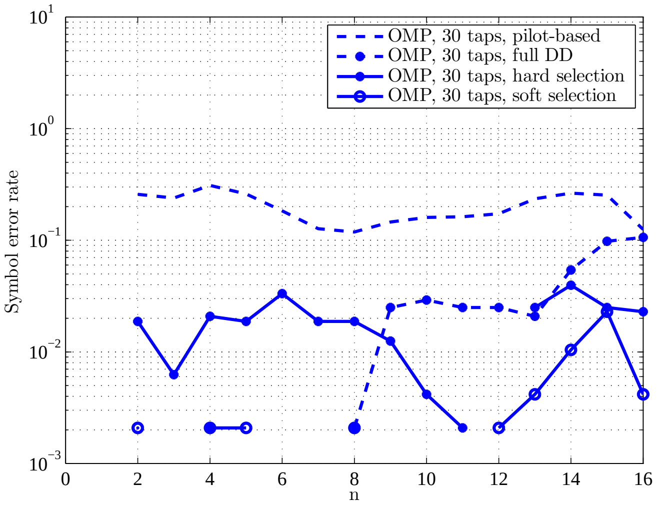

Figure 5.6: Performance of selective decision directed CE across OFDM blocks for $|\mathcal{S}_p| = 32$, $K = 512$ carriers, and OMP channel reconstruction.

based CE, while the best performance is achieved using the soft selection strategy. For the given $K = 512$ and $|S_p| = 32$, note that only 6.25% of the sub-carriers are allocated as pilots, and, therefore, a high spectral efficiency of the system is achieved.

5.3 Selective Decision Directed Channel Estimation over Multipath Rician Fading Channels

In this section we study the performance of the selective DD CE method from the previous section over multipath Rician fading channels, where fading is modeled as an AR random process. In particular, we explore the impact of channel properties such as the Rician k-factor and the Doppler spread on the performance of the selective DD CE scheme. Our focus on Rician fading is motivated by our results on statistical characterization of underwater acoustic (UWA) channels [19]. The selective DD CE method is based on combining the CSI derived from the pilot sub-carriers, and the predicted CSI from the data sub-carriers, which is *a priori* available at the receiver and obtained as a linear combination of the CSIs from the previously received OFDM blocks; therefore, this approach further improves the performance of the scheme from the previous section, where outdated CSI from the data sub-carriers is used instead. Using numerical simulations of uncoded and LDPC-coded OFDM, we demonstrate performance improvements as compared to the full (non-weighted) DD CE and the block-by-block pilot-assisted CE with a uniform pilot grid.

5.3.1 Channel Model

We consider an OFDM system with N sub-carriers, where the n-th block of input data symbols $x_l(n)$, $l = 0, \ldots, N-1$, is modulated using the inverse fast Fourier transform (IFFT). The block of input data consists of information bearing symbols and pilots, with corresponding sets denoted as S_d and S_p, respectively. It is assumed that the data symbols $x_l(n)$ take values from a QPSK modulation alphabet with unit power. One OFDM block occupies an interval of duration $T' = T+T_g$, where T and T_g are the symbol duration and the guard interval, respectively. The total bandwidth of the system is B, and the sub-carrier separation is $\Delta f = 1/T = B/N$.

We assume a single-input-multiple-output (SIMO) system configuration with D elements at the receiver. If the OFDM blocks are periodically transmitted at time instances nT', we define the discrete-time equivalent baseband impulse response of the channel between the transmitter and the r-th receiver as

$$g_r(m,n) = \sum_{p=0}^{P-1} g_{r,p}(n)\delta(m - m_{r,p}), \tag{5.22}$$

where P is the number of distinct propagation paths, m is the delay variable with resolution $1/B$, and n is the observation time interval. The coefficient $g_{r,p}(n)$ is the complex-valued gain of the path p, and $m_{r,p}$ is the corresponding delay.

5.3.2 Channel Fading

The system model assumes that the channel is constant over the transmission interval of one OFDM block, and changes from one block to the next. The fading process of the p-th channel tap at time n is modeled as an AR random process [77]

$$g_{r,p}(n) = \mu_{r,p} + \sum_{m=1}^{I_{r,p}} \alpha_{r,p,m}(g_{r,p}(n-m) - \mu_{r,p}) + w_{r,p}(n), \tag{5.23}$$

where $I_{r,p}$, $\alpha_{r,p,m}$ and $\mu_{r,p}$ are, respectively, the order, the complex-valued parameters and the complex mean of the discrete-time process AR($I_{r,p}$), and $w_{r,p}(n)$ is the complex (circularly symmetric) AWGN process with zero-mean and variance $\sigma^2_{w,p}$. In general, the random process (5.23) is stable if the roots of the polynomial $z^{I_{r,p}} - \sum_{m=1}^{I_{r,p}} \alpha_{r,p,m} z^{I_{r,p}-m}$ lie within the unit circle.

Since $g_{r,p}(n)$ is a complex Gaussian random process with a non-zero mean it corresponds to a *Rician* fading model with mean $\mu_{r,p} = E\{g_{r,p}(n)\}$, and variance [29]

$$\sigma^2_{r,p} = E\{|g_{r,p}(n) - \mu_{r,p}|^2\} = \sum_{m=1}^{I_{r,p}} \alpha_{r,p,m}\gamma_{r,p,-m} + \sigma^2_{w,p}, \tag{5.24}$$

where $\gamma_{r,p,m} = E\{g_{r,p}(n) g^*_{r,p}(n-m)\} - |\mu_{r,p}|^2$ is the auto-covariance of the wide-sense stationary process (5.23). If the parameters $\alpha_{r,p,m}$ of the process are known, the auto-covariance $\gamma_{r,p,m}$ can be computed by applying the reverse Levinson-Durbin algorithm to the Yule-Walker equations of the AR($I_{r,p}$) process (5.23) [29]. If the parameters of the AR processes (5.23) are unknown, a RLS algorithm [29] can be employed to estimate them.

Since each propagation path in (5.22) has potentially a different value of the Rician k-factor, we define the *overall*

$$k_r = \frac{\sum_{p=0}^{P-1} |\mu_{r,p}|^2}{\sum_{p=0}^{P-1} \sigma^2_{r,p}} = \frac{\sum_{p=0}^{P-1} \Omega_{r,p} \frac{k_{r,p}}{k_{r,p}+1}}{\sum_{p=0}^{P-1} \Omega_{r,p} \frac{1}{k_{r,p}+1}}, \tag{5.25}$$

where $k_{r,p} = |\mu_{r,p}|^2 / \sigma^2_{r,p}$, and $\Omega_{r,p} = E\{|G_{r,p}(n)|^2\}$. The total power of the channel is normalized to one, i.e. $\sum_{p=0}^{P-1} \Omega_{r,p} = 1$. Limiting cases of $k \to \infty$ and $k = 0$ correspond to the AWGN and the Rayleigh fading channel models, respectively.

5.3.3 Channel Correlation in Time

In order to characterize the channel time-variations, we define the time covariance function of the channel as [5]

$$\gamma_{r,m} = \sum_{p=0}^{P-1} \gamma_{r,p,m}, \tag{5.26}$$

where it is assumed that distinct propagation paths are mutually uncorrelated. Therefore, the Doppler power spectrum of the channel becomes [5]

$$S_r(\nu) = \sum_{m} \gamma_{r,m} e^{-j2\pi\nu m T'}. \tag{5.27}$$

We define the Doppler spread $B_{d,r}$ of the channel as the 3-dB bandwidth of the Doppler power spectrum $S_r(\nu)$.

Since the channel is constant over the interval of one OFDM block, the received signal at the r-th receive element and l-th sub-carrier after FFT demodulation is modeled as

$$y_{r,l}(n) = G_{r,l}(n) x_l(n) + z_{r,l}(n), \tag{5.28}$$

where

$$G_{r,l}(n) = \sum_{p=0}^{P-1} G_{r,p}(n) e^{-j2\pi l m_{r,p}/N}, \tag{5.29}$$

and $z_{r,l}(n)$ is circularly symmetric complex AWGN with zero-mean and variance σ_z^2, $\forall r, l$.

5.3.4 Tentative Decisions on Data Sub-carriers

Let us first define the vectors

$$\boldsymbol{x}(n) = [x_0(n), \ldots, x_{N-1}(n)]^T \tag{5.30}$$

$$\boldsymbol{y}_r(n) = [y_{r,0}(n), \ldots, y_{r,N-1}(n)]^T \tag{5.31}$$

$$\boldsymbol{z}_r(n) = [z_{r,0}(n), \ldots, z_{r,N-1}(n)]^T, \tag{5.32}$$

where r is the index of the receive element, and the matrix

$$\mathbf{G}_r(n) = \mathrm{diag}[G_{r,0}(n), \ldots, G_{r,N-1}(n)]. \tag{5.33}$$

Following this notation, we can write

$$\boldsymbol{y}_r(n) = \mathbf{G}_r(n)\boldsymbol{x}(n) + \boldsymbol{z}_r(n). \tag{5.34}$$

Due to imperfect CSI and the presence of noise, tentative decisions on the data symbols are subject to errors. Tentative decisions are obtained from the LS estimates

$$\hat{\boldsymbol{x}}(n) = \left(\sum_{r=1}^{M_r} \widehat{\mathbf{G}}_r^{\prime}(n)\widehat{\mathbf{G}}_r(n)\right)^{-1} \left(\sum_{r=1}^{M_r} \widehat{\mathbf{G}}_r^{\prime}(n)\boldsymbol{y}_r(n)\right), \tag{5.35}$$

were the prime denotes conjugate transpose. Note that the channel is not known at the receiver, and that the data symbol estimates $\hat{\boldsymbol{x}}(n)$ at time n are obtained by using the predicted CSI $\widehat{\mathbf{G}}_r(n)$, $r = 1, \ldots, M_r$. This channel knowledge is *a priori* available at the receiver and obtained as a linear combination of the CSIs from the previously transmitted OFDM blocks [29]. If the input data block $\boldsymbol{x}(n)$ contains pilots, we replace the corresponding data estimates with the transmitted data symbols, i.e. $\hat{x}_l(n) = x_l(n)$, where $l \in S_p$.

5.3.5 Selection of Data Sub-carriers

Since the channel gain $G_{r,l}(n)$ is unknown, the channel prediction $\widehat{G}_{r,l}(n)$ is used instead. If we assume that the outdated CSI $G_{r,l}(n-i)$, $i > 0$, and the mean of the AR process (5.23) are perfectly known at the receiver, the prediction error caused by the predicted CSI follows from the expression in (5.29), and it is given as

$$\begin{aligned} e_{r,l}^{(\beta)}(n) &= G_{r,l}(n) - \widehat{G}_{r,l}(n) \\ &= \sum_{p=0}^{P-1} \left(g_{r,p}(n) - \hat{g}_{r,p}(n)\right) e^{-j2\pi l m_{r,p}/N} \\ &= \sum_{p=0}^{P-1}\left(\sum_{i=1}^{I'_{r,p}} \frac{(g_{r,p}(n-i) - \mu_{r,p})}{(\alpha_{r,p,i} - \beta_{r,p,i})^{-1}} + w_{r,p}(n)\right) e^{-j2\pi l m_{r,p}/N}, \end{aligned} \tag{5.36}$$

where $\hat{g}_{r,p}(n) = \mu_{r,p} + \sum_{i=1}^{J_{r,p}} \beta_{r,p,i}(g_{r,p}(n-i) - \mu_{r,p})$ is the channel tap prediction, $\{\beta_{r,p,i}\}$ is the receiver's estimate of the parameters $\{\alpha_{r,p,i}\}$ of the fading process (5.23), and $I'_{r,p} = \max\{I_{r,p}, J_{r,p}\}$, where $J_{r,p}$ is the estimate of the order $I_{r,p}$.

If the parameters of the fading process are perfectly known at the receiver (i.e. $J_{r,p} = I_{r,p}$ and $\beta_{r,p,i} = \alpha_{r,p,i}$), the prediction error is minimized (in the MSE sense), and depends on the noise $w_{r,p}(n)$ only. The mean of the error process $e^{(\beta)}_{r,l}(n)$ is zero, while the variance is given by

$$\begin{aligned}\sigma^{(\beta)2}_{e,r,l} =& E\left\{|e^{(\beta)}_{r,l}(n)|^2\right\}\\ =& \sum_{p=0}^{P-1}\left(\sum_{i,j=1}^{I'_{r,p}} \frac{(\alpha_{r,p,i}-\beta_{r,p,i})}{(\alpha_{r,p,j}-\beta_{r,p,j})^{-1}}\gamma_{r,p,i-j} + \sigma^2_{w,p}\right). \end{aligned} \tag{5.37}$$

Since the prediction error $e^{(\beta)}_{r,l}(n)$ has approximately a Gaussian distribution (due to the errors in the tentative decisions), we can follow the approach from the previous section to show that the variance of the equivalent noise (5.16) is given as

$$\sigma^2_{r,l}(n) \;=\; \sigma^2_z + 4|\widehat{G}_{r,l}(n)|^2 Q\left(\sqrt{\frac{|\widehat{G}_{r,l}(n)|^2}{\sigma^{(\beta)2}_{e,r,l}+\sigma^2_z}}\right). \tag{5.38}$$

Finally, by substituting $\sigma^2_{r,l}(n)$ into (5.15), we obtain a simple closed-form solution for the weight vector $\mathbf{w}_r(n)$.

5.4 Numerical Results for Rician Fading Channels

In this section we present numerical results on the performance of the selective DD CE over a simulated channel which follows the model in (5.22), (5.23) and (5.19). The normalized delay spread $L = \lceil T_m B \rceil$ of the simulated channel is set to 8, while the number of distinct propagation paths is $P = 4$, and the corresponding non-zero channel coefficients from (5.19) are $h_{r,0}, h_{r,1}, h_{r,3}$ and $h_{r,7}$, $\forall r$. Assuming that the positions of the non-zero channel taps are fixed (i.e. $m_{r,p}(n) = m_{r,p}, \forall r, p$), time-variation of the channel taps follows the model (5.23). The channel power is normalized to unity (5.25), and the channel has an exponential delay profile such that $E\{|h_{r,0}|^2\} = 0.33$, $E\{|h_{r,1}|^2\} = 0.29$, $E\{|h_{r,3}|^2\} = 0.23$ and $E\{|h_{r,7}|^2\} = 0.15$, $\forall r$. We assume that the overall Rician factor $k_r = k$, $\forall r$.

We study the performance of DD CE for uncoded and LDPC-coded OFDM, where in the case of channel coding we use a regular LDPC code $(1064, 133, 3)$ with code rate $R = 7/8$, that is constructed using a pseudo-random method from [78]. For the i-th OFDM frame, the coded symbols are combined with uniformly-spaced pilot symbols to form the input data blocks $\boldsymbol{x}(j + (i-1)N_{bl})$, $j = 0, \dots, N_{bl} - 1$. In simulations, we transmit 3240 OFDM frames with $N_{bl} = 20$ blocks per frame and $N = 32$.

Figure 5.7 shows the results for the uncoded OFDM system. The four channel taps are generated with the following α-parameters: $\mathrm{AR}_1 = [0.95]$, $\mathrm{AR}_2 = [0.9 \quad -0.7]$, $\mathrm{AR}_3 = [0.5 \quad 0.3]$, $\mathrm{AR}_4 = [0.4 \quad -0.1]$, while the resulting normalized Doppler spreads (5.27) of the corresponding channel taps are: $B_{d,1}T' = 0.0125$, $B_{d,2}T' = 0.18$, $B_{d,3}T' = 0.0325$ and $B_{d,4}T' = 0.2$. Figs. 5.7.a and 5.7.b correspond to Rician factors $10\log_{10} k = 5$ dB and 10 dB, respectively. For $10\log_{10} k = 5$ dB, the receiver with the weighted DD CE and 25% of sub-carriers used as pilots shows a better performance than the non-weighted DD CE, and a slight improvement when compared to the conventional pilot-assisted CE with the same number of pilots. For $10\log_{10} k = 10$ dB, the weighted DD CE (with 12.5% pilots) shows a better performance than the pilot-based CE (with 25% pilots). In other words, the proposed method outperforms the pilot-based scheme while offering a two-fold reduction in the number of pilots. This significant performance gain is observed for high values of k since they imply slow time-variations in the channel, which in turn lead to an increased reliability of the predicted CSI and the tentative decisions on data sub-carriers that are used as additional pilots for CE.

Figure 5.8 illustrates the performance variation for different values of the Rician k-factor at an SNR of 10 dB. Note that for higher values of k the proposed weighted DD scheme offers noticeable performance improvements. In particular, for $10\log_{10} k = 8$ dB the performance of the selective DD scheme (12.5%) matches the performance of the traditional pilot-assisted scheme (25%). These observations are of particular interest for spectrally efficient OFDM schemes with a reduced number of pilot sub-carriers. When 12.5% of sub-carriers are used as pilots, note that Rayleigh fading ($k = 0$) results in a poor performance of all the considered

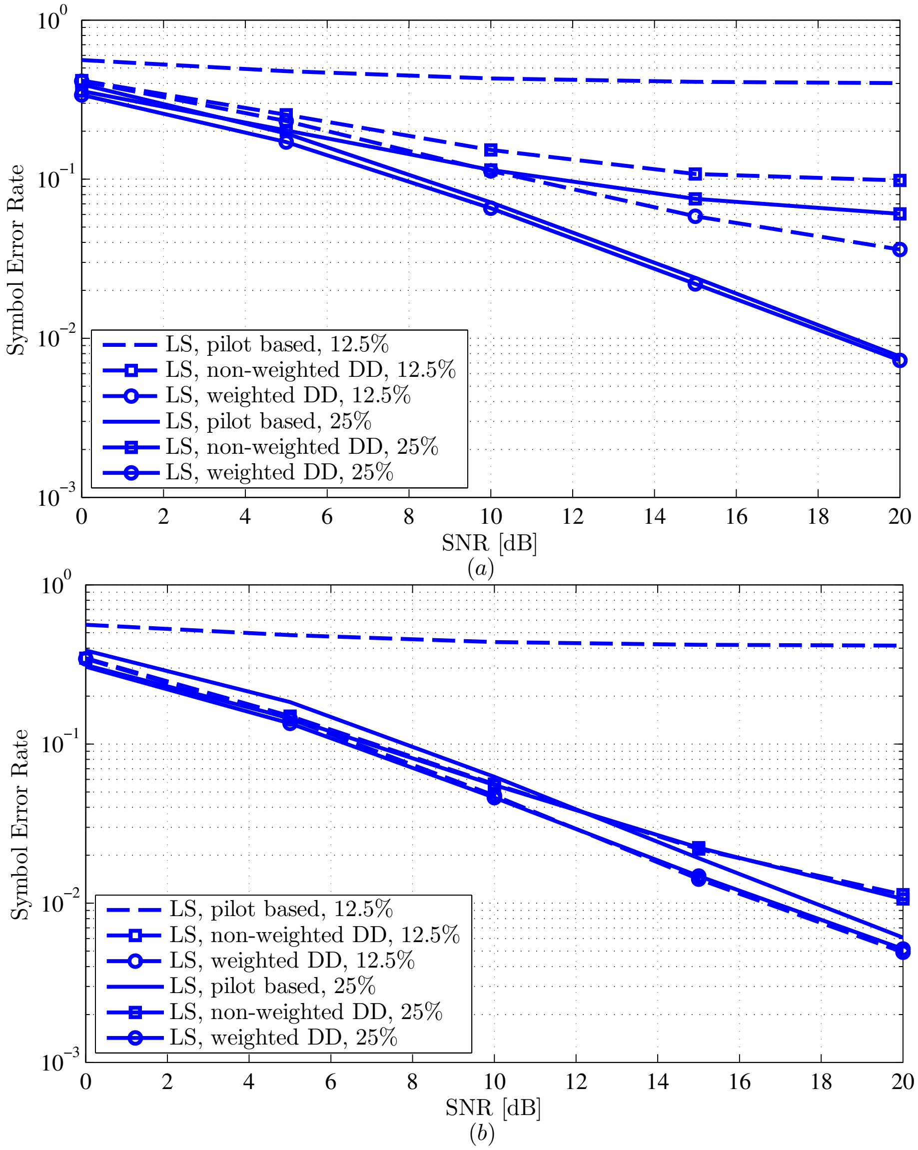

Figure 5.7: Performance of selective DD CE with $|\mathcal{S}_p| = 4$ and 8 pilots, and $N = 32$ carriers. The total Rician k-factor is set to 5 and 10 dB for the figures (a) and (b), respectively. The performance of the pilot-assisted and the non-weighted DD CE is provided as reference.

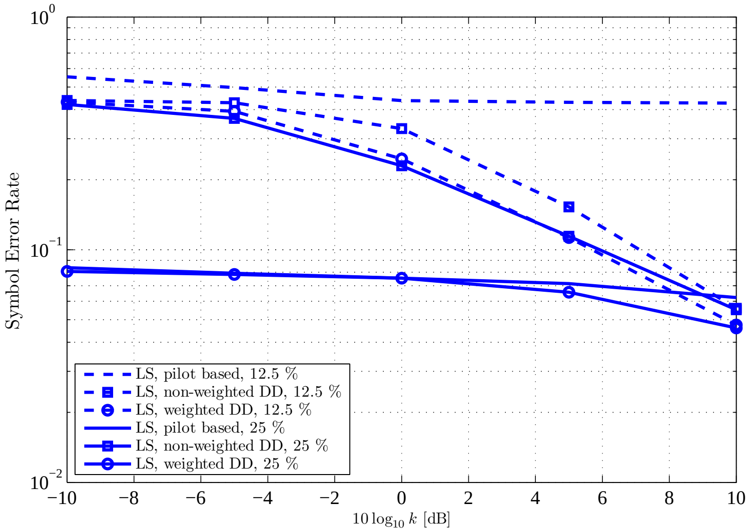

Figure 5.8: Performance of selective DD CE with $|\mathcal{S}_p| = 4$ and 8 pilots, and $N = 32$ carriers, and $SNR = 10$ dB. The performance of the pilot-assisted and the non-weighted DD CE is provided as reference.

schemes. In Figure 5.9 we present performance results when the receiver-end diversity is employed. Note that the weighted DD CE offers a higher performance improvement as the diversity order increases over the entire range of examined SNRs.

In Figure 5.10 we illustrate performance results for the LDPC-coded OFDM system with $R = 9/10$. Similar to the uncoded system, the weighted DD CE shows a significant performance improvement when compared to the non-weighted DD CE. In particular, for $SNR = 10$ dB, we observe a four-fold reduction in the achievable BER. Note that the performance saturates for high SNR regions due to channel prediction error. Further performance improvements are possible by reducing the code rate R, which in turn reduces the spectral efficiency of the system. In Figure 5.11 we illustrate the performance of the LDPC-coded OFDM system with $R = 7/8$ as a function of SNR for different values of the normalized Doppler spread $B_d T'$ which is now assumed to be equal for all paths, each of them obeying the same AR process of order 1. Similar to the uncoded system, the weighted DD CE outperforms the non-weighted DD CE over the entire range of examined Doppler spreads and SNRs. We also note that rapid time-variations of the channel

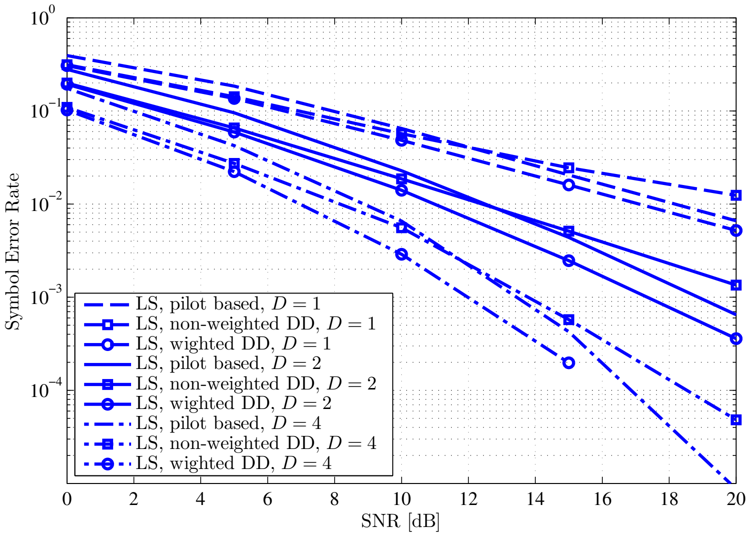

Figure 5.9: Performance of selective DD CE with $|\mathcal{S}_p| = 8$, and $N = 32$ carriers, when the receiver-end diversity of order D is employed. The total Rician k-factor is set to 10 dB. The performance of the pilot-assisted and the non-weighted DD CE is provided as reference.

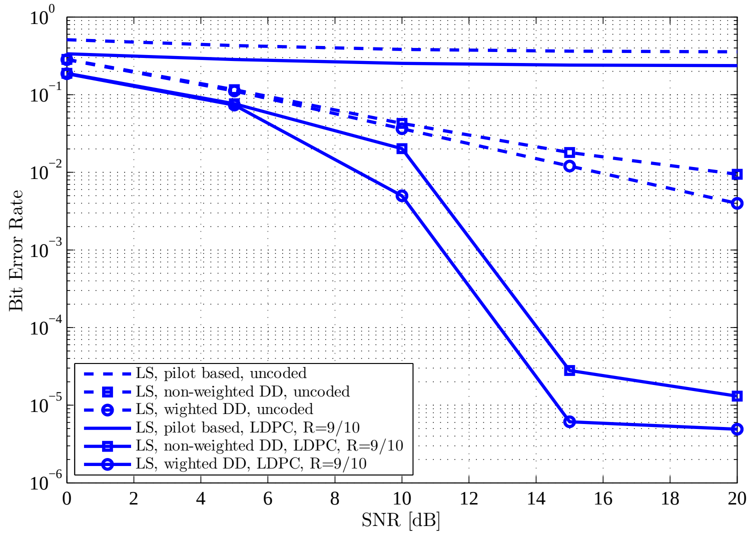

Figure 5.10: Performance of selective DD CE with $|\mathcal{S}_p| = 4$, and $N = 32$ carriers, when the LDPC code of rate $R = 9/10$ is employed. The total Rician k-factor is set to 10 dB. The performance of the pilot-assisted and the non-weighted DD CE is provided as reference.

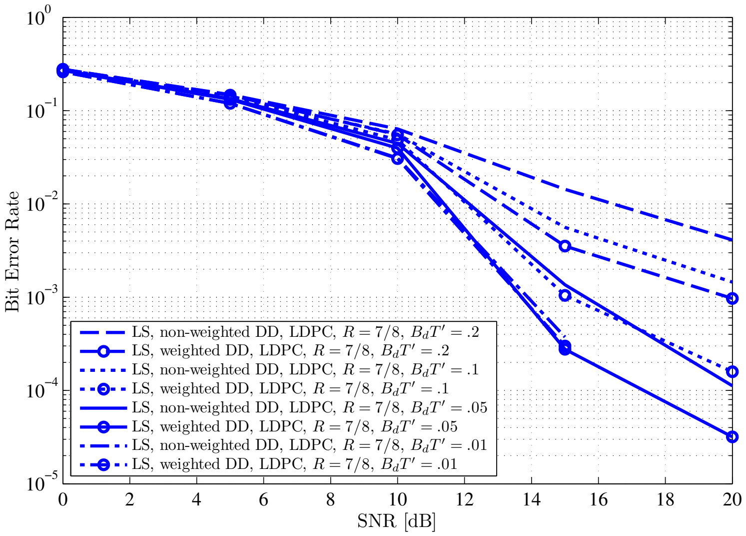

Figure 5.11: Performance of selective DD CE with $|\mathcal{S}_p| = 4$, and $N = 32$ carriers, when the LDPC code of rate $R = 7/8$ is employed for different levels of the normalized Doppler spread B_dT'. The performance of the non-weighted DD CE is provided as a reference.

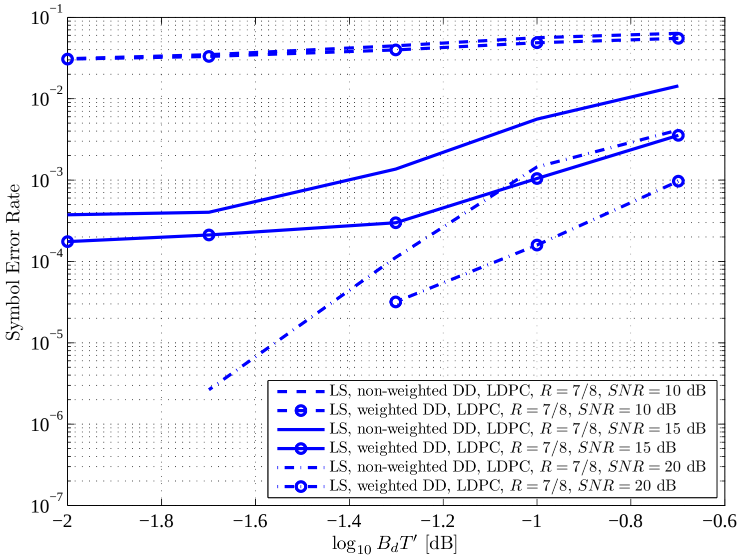

Figure 5.12: Performance of selective DD CE with $|\mathcal{S}_p| = 4$, and $N = 32$ carriers, as a function of the normalized Doppler spread B_dT'. The LDPC code of rate $R = 7/8$ is employed. The performance of the non-weighted DD CE is provided as a reference.

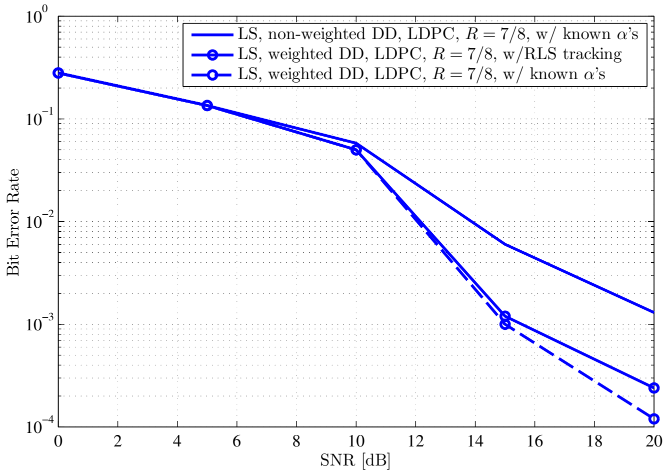

Figure 5.13: Performance of selective DD CE with $|\mathcal{S}_p| = 4$, and $N = 32$ carriers, when the LDPC code of rate $R = 7/8$ is employed. The normalized Doppler spread is $B_d T' = 0.1$. The RLS forgetting factor is set to 0.95. The performance of the non-weighted DD CE is provided as a reference.

saturate the performance of the coded OFDM system. However, if the channel variations are small (e.g. $B_d T' = .01$), the non-weighted DD CE approaches the performance of the selective DD CE due to a considerable increase in reliability of the data sub-carriers, and the fact that the channel becomes deterministic as $k \to \infty$ (i.e. AWGN). Similarly, in Figure 5.12 we show the performance of the LDPC coded system with $R = 7/8$ as a function of the Doppler spread of the channel. For $SNR = 20$ dB, the weighted DD CE results in a superior performance, while for $SNR = 10$ dB it performs similarly with the non-weighted DD CE.

In Figure 5.13 we illustrate the performance of selective DD CE when the parameters $\alpha_{r,p}$ of the fading process are unknown and estimated using an RLS algorithm at the receiver. The order of the process is assumed to be known. We note a small loss in performance due to unknown channel parameters.

5.5 Summary

In this chapter we investigated the performance of selective decision directed channel estimation over slowly (and moderately) time-varying UWA channels. Particulary, we proposed hard and soft selection of the data sub-carriers that are used to aid channel estimation. Three forms of channel estimation were considered: LS with thresholding, orthogonal matching pursuit, and basis pursuit denoising, each coupled with a Doppler rate estimation for phase tracking. The channel estimates obtained in one OFDM block are used to detect the data in that block, and also to generate selected tentative decision for the next block. Selective decision directed channel and Doppler estimation were compared to the full decision directed operation, and to the conventional pilot-only operation using experimental data. The strategy of soft selection was shown to be superior, since it exploits the channel knowledge from all the data sub-carriers. It outperforms the fully decision directed receiver as well as all the other strategies considered with the same number of pilots.

Based on the simulation results utilizing both uncoded and LDPC-coded OFDM systems, selective DD CE was compared to the non-weighted DD and the pilot-only CE over time-varying Rician fading channels. In particular, we explored the effect of varying the number of pilots and/or decision directed data sub-carriers, the effect of the receiver-end diversity, and the impact of channel properties, such as the Rician k-factor and the Doppler spread of the channel. The selective DD CE approach was found to outperform all the other strategies considered with the same number of pilots, and shows the greatest performance improvement for channels with high Doppler rates and receiver-end diversity. More importantly, selective decision directed operation matches the performance of a conventional receiver using fewer pilots. It can thus be regarded as a method for increasing the spectral efficiency of OFDM.

Sections 5.1 and 5.2, in part, are a reprint of the material as it appears in "Selective decision directed channel estimation for UWA OFDM systems," by A. Radosevic, T. M. Duman, J. G. Proakis, and M. Stojanovic, 49th Allerton Conference on Communication, Control, and Computing, Sept. 2011. The dissertation author was the primary investigator and author of this paper.

Sections 5.3 and 5.4, in part, are a reprint of the material as it appears in "Selective decision directed channel estimation for OFDM communications over multipath Rician fading channels," by A. Radosevic, T. M. Duman, J. G. Proakis, and M. Stojanovic, International Workshop on Signal Processing Advances in Wireless Communications (SPAWC), accepted. The dissertation author was the primary investigator and author of this paper.

Chapter 6

Conclusions and Future Work

In this dissertation we provided a comprehensive study of the statistical properties and the information-theoretical performance limits of the UWA channel. We also considered design aspects for UWA systems with adaptive OFDM modulation, and introduced a decision directed channel estimation method for high-rate UWA OFDM-based communications.

In particular, in Chapter 2 we considered short-term statistical characterization of the UWA channel based on a set of measured channel responses, obtained from signals recorded during the KAM08 and KAM11 experiments. Wideband single-carrier probes were found to offer satisfactory channel estimates. Channel measurements were used to examine several candidate fading models, indicating a good match with the Rician distribution. We also studied the correlation properties of the UWA channel in both the time and the frequency domain. In the case of a stationary UWA system, the time correlation properties of the channel indicate fast variations of the channel phase as the result of inherently present motion in the system. Moreover, the estimated time correlation function shows a good match with the auto-regressive fading model of a small order. The time correlation function of the channel frequency response indicates that the lower part of the operational bandwidth (the high SNR region), exhibits more stability in time than the higher part (the low SNR region).

Due to time constraints in my research, only a limited amount of data collected during the KAM11 experiment was used in constructing our UWA channel model. Future work should focus on a large amount of unprocessed data from the KAM11 experiment, and examine (in the similar manner as for the data recorded during the KAM08 experiment) how candidate fading models match the underlying channel distribution.

The statistical properties of the UWA channel can play an important role in the design of bandwidth-efficient and power-efficient communication systems. For example, statistical knowledge about the channel fading could be a useful parameter in the design of adaptive systems. In particular, implementing receiver-transmitter feedback in the system, information about a slowly-varying mean, variance and/or Rician k factor can be conveyed. These parameters can be utilized through adaptive modulation and coding techniques, which can further improve the system performance. This research topic, in part, was addressed in our work, by applying the concept of adaptive modulation to the design of UWA communication systems. Furthermore, one can think of a coding scheme that utilizes the statistical properties of the UWA channel (in both the time and the frequency domain) to cope with the time-varying frequency-selective nature of the UWA channel. Besides relying on the channel coherence time and bandwidth, an ingenious scheme can also exploit non-uniform correlation properties of the channel (frequency response) across the operational bandwidth of the system.

In Chapter 3 we used the experimentally recorded channel measurements from Chapter 2 to assess the average and the ergodic channel capacity under different fading models, assuming either no channel information at the transmitter, or limited knowledge of the channel statistics. We showed that utilizing the channel state information at the transmitter can improve the channel capacity significantly. We have also examined upper and lower bounds on the achievable information rate of the discrete-time additive white Gaussian channel with long memory and sparse structure. This channel model was motivated by the multipath properties of the UWA channel examined in Chapter 2. The proposed lower bound is attainable by any practical receiver, with varying degrees of tightness depending upon the specific receiver used. Particularly, we considered a receiver structure consisting of a channel shortening filter and a modified BCJR detector with the objective of obtaining a suboptimal soft-output detector with reasonable performance/complexity trade-off. The lower bound improves upon usefulness of the existing bounds for minimum-phase and maximum-phase channels, and indicates the utility of the considered reduced-complexity receiver. For mixed-phase systems, the lower bound shows poor performance due to the unreliable tentative decisions made by the modified BCJR algorithm. The proposed upper bound is based on grouping of the channel taps into clusters. Performance of the upper bound depends on the strategy for channel clustering, and it can be optimized further by computer search. For sparse channels with a long memory, this approach leads to a significant complexity reduction in the simulation of the newly defined SISO channel, which also yields the upper bound on the achievable information rate of the actual channel. As illustrated by examples, the upper bound significantly outperforms the bounds previously published in the literature.

Future work on the channel capacity should take into account local dispersion of the physical propagation paths, and incorporate it into evaluation of the ergodic capacity. In particular, one can exploit the clustered structure of the channel impulse response and high correlation among the channel taps within a cluster, to provide more accurate estimates of the channel capacity. Furthermore, this approach could be exploited to develop capacity-achieving coding techniques, particularly efficient for a class of multipath fading channels with local (path) dispersion. With regard to the bounds on the achievable information rate, a comprehensive study on the performance of the proposed bounds is needed for MIMO system configurations. Moreover, one can think of efficient space-time coding techniques that exploit the effects of the time, frequency and spatial diversity in UWA channels, and use the proposed bounds as a performance benchmark.

In Chapter 4 we explored design aspects of adaptive modulation based on OFDM for UWA communications, and investigated its performance using real-time at-sea experiments. In particular, we first investigated the possibility of predicting an UWA channel, where the key step in providing a stable reference for channel prediction is compensation of the motion-induced phase offset. Second, approximate expressions for the BER of each sub-carrier (or a cluster of adjacent sub-carriers) were obtained. From these expressions, a set of thresholds is obtained that determine the modulation level and the power needed on each sub-carrier in order to maximize the throughput while keeping the average BER at the target level. Third, spectrally-efficient adaptive schemes are applied to allocate the modulation and the power across the OFDM sub-carriers. Numerical and experimental results that are obtained with recorded channels and real-time at-sea experiments, respectively, show that the adaptive modulation scheme provides significant throughput improvements as compared to conventional, nonadaptive modulation at the same power and target BER. This work leads us to conclude that adaptive modulation methods may be viable for reliable, high-rate UWA communications. To our knowledge, this is the first work that presents adaptive modulation results for UWA links with real-time at-sea experiments.

Due to time constraints of the KAM11 experiment, we have not tested the performance of our adaptive scheme as a function of different system parameters such as the communication distance, the operational bandwidth, the central frequency, the number of sub-carriers, the number of pilots, the total power available at the transmitter, etc. These additional tests could give us more insight about the major limitations in the design of adaptive UWA communication systems. Future work should extend the work from this dissertation by introducing novel coding strategies for UWA communications, and couple them with the proposed adaptive modulation methods. To that extent, one should consider a possibility of rate control that introduces an additional level of adaptivity in the system design. As mentioned earlier, the time correlation of the channel frequency response can be a useful parameter in future work on adaptive UWA OFDM-based communications.

In Chapter 5 we investigated the performance of selective decision directed channel estimation over slowly (and moderately) time-varying UWA channels. Particulary, we proposed hard and soft selection of the data sub-carriers that are used to aid channel estimation. The channel estimates obtained in one OFDM block are used to detect the data in that block, and also to generate selected tentative decision for the next block. Selective decision directed channel estimation was compared to the full decision directed operation, and to the conventional pilot-only operation using experimental data. The strategy of soft selection was shown to be superior, since it exploits the channel knowledge from all the data sub-carriers. It outperforms the fully decision directed receiver as well as all the other strategies considered with the same number of pilots. Based on the simulation results utilizing both uncoded and LDPC-coded OFDM systems, selective DD CE was compared to the non-weighted DD and the pilot-only CE over time-varying Rician fading channels. The selective DD CE approach was found to outperform all the other strategies considered with the same number of pilots, and shows the greatest performance improvement for channels with high Doppler rates and receiver-end diversity. More importantly, selective decision directed operation matches the performance of a conventional receiver using fewer pilots. Thus, it can be regarded as a method for increasing the spectral efficiency of OFDM.

Future work regarding this topic should include analytical work for determining the performance limits of the proposed channel estimation method under different channel fading models. In particular, derivation of a Cramer-Rao bound for such estimator could be a potential research problem of interest. Our work should be generalized for MIMO system configurations, and the performance of the proposed scheme should be studied for different coding techniques (e.g. space-time block coding). Also, it would be interesting to explore the performance improvements of communication systems with iterative receiver structures (and corresponding turbo equalization) when coupled with the proposed decision directed channel estimation method.

Appendix A

Derivation of the thresholds $C^*_{k,n}(\mathcal{M}_{k,n})$

Let us multiply both sides of the Eq. (4.20) by $|\widehat{G}_{k,n}|^2/(0.2\sigma_e^2)\exp(|\widehat{G}_{k,n}|^2/\sigma_e^2)$

$$\underbrace{\frac{|\widehat{G}_{k,n}|^2}{\sigma_e^2} e^{\frac{|\widehat{G}_{k,n}|^2}{\sigma_e^2} + \ln\left(\frac{P_{e,k}}{0.2}\right)}}_{x} = \underbrace{\frac{\frac{|\widehat{G}_{k,n}|^2}{\sigma_e^2}}{1 + \frac{m(\mathcal{M}_{k,n})}{2(\mathcal{M}_{k,n}-1)} \frac{C_{k,n}}{\sigma_N^2} \sigma_e^2}}_{W} \underbrace{e^{\frac{\frac{|\widehat{G}_{k,n}|^2}{\sigma_e^2}}{1 + \frac{m(\mathcal{M}_{k,n})}{2(\mathcal{M}_{k,n}-1)} \frac{C_{k,n}}{\sigma_N^2} \sigma_e^2}}}_{e^W}. \qquad (A.1)$$

For $x > -1/e$, the inverse function of $x = W\exp(W)$ is given as the principal branch of the Lambert $\mathcal{W}$-function, $\mathcal{W}_0(x)$. Therefore, the Eq. (A.1) can be re-written as

$$\mathcal{W}_0\left(\frac{|\widehat{G}_{k,n}|^2}{\sigma_e^2} e^{\frac{|\widehat{G}_{k,n}|^2}{\sigma_e^2} + \ln\left(\frac{P_{e,k}}{0.2}\right)}\right) = \frac{\frac{|\widehat{G}_{k,n}|^2}{\sigma_e^2}}{1 + \frac{m(\mathcal{M}_{k,n})}{2(\mathcal{M}_{k,n}-1)} \frac{C_{k,n}}{\sigma_N^2} \sigma_e^2}. \qquad (A.2)$$

From here, depending on the target modulation level $\mathcal{M}_{k,n}$ at the sub-carrier k at time n, the power level threshold $C^*_{k,n}(\mathcal{M}_{k,n})$ is given as

$$\begin{aligned} C^*_{k,n}(\mathcal{M}_{k,n}) = \frac{2(\mathcal{M}_{k,n}-1)\sigma_N^2}{m(\mathcal{M}_{k,n})\sigma_e^2} \Bigg\{ \frac{|\widehat{G}_{k,n}|^2}{\sigma_e^2} \left[\mathcal{W}_0\left(\frac{|\widehat{G}_{k,n}|^2}{\sigma_e^2} e^{\left(\frac{|\widehat{G}_{k,n}|^2}{\sigma_e^2} + \ln\frac{P_{e,k}}{0.2}\right)}\right)\right]^{-1} - \\ -1 \Bigg\}, \qquad (A.3) \end{aligned}$$

which completes the derivation of (4.21).

Appendix B

Derivation of the upper bound (5.17) on the variance term $\sigma_{e,k}^2(n)$

In the presence of the imperfect (outdated) CSI, the received signal (5.12) at the k-th sub-carrier can be expressed in the following form:

$$\begin{aligned} Y_k'(n) &= (\hat{G}_k(n-1) + E_k)X_k(n) + W_k''(n) \\ &= \hat{G}_k(n-1)X_k(n) + E_k' + W_k''(n), \end{aligned} \tag{B.1}$$

where $\hat{G}_k(n-1)$ is the CSI from the previous block transmission, and E_k is the estimation error modeled as a Gaussian random variable with the variance σ_e^2. Based on the assumption of a unit-amplitude QPSK modulation with constellation points $\mp 1, \mp j$ (5.14), the probability of bit error for the k-th sub-carrier at time n is given as [5]

$$P_b(n) = Q\left(\sqrt{\frac{|\hat{G}_k(n-1)|^2}{\sigma_e^2 + \sigma_{w,k}^2}}\right). \tag{B.2}$$

If we exploit the symmetry of the modulation alphabet, and assume that the transmitted symbols are equally probable *a priori* and the bit errors are independent, the term $E\{\tilde{X}_k^*(n)X_k(n)\}$ from Eq.(5.16) can be expressed in the following form:

$$\begin{aligned} E\{\tilde{X}_k^*(n)X_k(n)\} &= E\{\tilde{X}_k^*(n)X_k(n)|X_k(n)=1\} \\ &= 1\cdot(1-P_b(n))^2+j\cdot(1-P_b(n))P_b(n)- \\ &\quad -j\cdot P_b(n)(1-P_b(n))-1\cdot P_b^2(n) \\ &= 1-2P_b(n) \\ &= 1-2Q\left(\sqrt{\frac{|\hat{G}_k(n-1)|^2}{\sigma_e^2+\sigma_{w,k}^2}}\right). \end{aligned} \tag{B.3}$$

By substituting (B.3) into Eq.(5.16), the variance $\sigma_{e,k}^2(n)$ is written as

$$\sigma_{e,k}^2(n) = \sigma_{w,k}^2\left(1+4Q\left(\sqrt{\frac{|\hat{G}_k(n-1)|^2}{\sigma_e^2+\sigma_{w,k}^2}}\right)\frac{|\hat{G}_k(n-1)|^2}{\sigma_{w,k}^2}\right). \tag{B.4}$$

Now, by using the bound on the Q-function [5]

$$Q(x) < \frac{1}{x}\frac{1}{\sqrt{2\pi}}e^{-x^2/2}, \tag{B.5}$$

we obtain the upper bound (5.17) on the variance term $\sigma_{e,k}^2(n)$

$$\begin{aligned} \sigma_{e,k}^2(n) &< \sigma_{w,k}^2\left(1+\frac{\sqrt{\frac{8}{\pi}}|\hat{G}_l(n-1)|}{\frac{\sigma_{w,k}^2}{\left(\sigma_{w,k}^2+\sigma_e^2\right)^{\frac{1}{2}}}e^{\frac{|\hat{G}_l(n-1)|^2}{2(\sigma_{w,k}^2+\sigma_e^2)}}}\right) \\ &\le \sigma_{w,k}^2\left(1+\frac{\sqrt{\frac{8}{\pi}}\max_l\left\{|\hat{G}_l(n-1)|\right\}}{\frac{\sigma_{w,k}^2}{\left(\sigma_{w,k}^2+\sigma_e^2\right)^{\frac{1}{2}}}e^{\frac{|\hat{G}_l(n-1)|^2}{2(\sigma_{w,k}^2+\sigma_e^2)}}}\right) \\ &= \sigma_{UB,k}^2(n). \end{aligned} \tag{B.6}$$

Bibliography

[1] M. Stojanovic, "Underwater acoustic communications: Design considerations on the physical layer," in *Proceedings of IEEE/IFIP Fifth Annual Conference on Wireless On demand Network Systems and Services* (WONS 2008), (Garmisch-Partenkirchen, Germany), January 2008.

[2] F. B. Jensen, W. A. Kuperman, M. B. Porter, and H. Schmidt, *Computational Ocean Acoustics.* Springer, 2011.

[3] W. S. Hodgkiss, H. C. Song, M. Badiey, A. Song, and M. Siderius, "Kauai acomms muri 2008 (kam08) experiment trip report," *Technical Report*, 2008.

[4] W. S. Hodgkiss, H. C. Song, G. Deane, M. Badiey, A. Song, and J. Preisig, "Kauai acomms muri 2008 (kam11) experiment trip report," *Technical Report*, 2011.

[5] J. G. Proakis, *Digital Communications.* New York: McGraw-Hil, 4th ed., 2001.

[6] L. M. Brekhovskikh and Y. P. Lysanov, *Fundamentals of Ocean Acoustics.* New York: Springer, 3rd ed., 2003.

[7] M. Stojanovic, "On the relationship between capacity and distance in an underwater acoustic communication channel," *ACM SIGMOBILE Mobile Computing and Communications Review* (MC2R), vol. 11, pp. 34–43, October 2007.

[8] R. Coates, *Underwater Acoustic Systems.* New York: Wiley, 1989.

[9] M. Stojanovic, J. Catipovic, and J. Proakis, "Reduced-complexity spatial and temporal processing of underwater acoustic communication signals," *Journal of the Acoustical Society of America*, vol. 98, pp. 961–972, August 1995.

[10] M. Stojanovic, "OFDM for underwater acoustic communications: Adaptive synchronization and sparse channel estimation," in *Proceedings of International Conference on Acoustics, Speech, and Signal Processing* (ICASSP'08), April 2008.

[11] M. Stojanovic, “MIMO OFDM over underwater acoustic channels,” in *Proceedings of 43rd Asilomar Conference on Signals, Systems and Computers*, November 2009.

[12] M. Stojanovic, J. Catipovic, and J. Proakis, “”adaptive multichannel combining and equalization for underwater acoustic communications,” *Journal of the Acoustical Society of America*, vol. 94, pp. 1621–1631, September 1993.

[13] D. Tse and P. Viswanath, *Fundamentals of Wireless Communicatio*. Cambridge University Press, 2005.

[14] R. J. Turyn, “Sequences with small correlation,” in *Error Correcting Codes: Proceedings of a Symposium (*H. B. Mann, ed.), pp. 195–228, New York: Wiley, 1968.

[15] M. Stojanovic, J. Catipovic, and J. Proakis, “Phase coherent digital communications for underwater acoustic channels,” *IEEE Journal of Oceanic Engineering*, vol. 19, pp. 100–111, January 1994.

[16] H. M. Kwon and T. Birdsall, “Channel capacity in bits per joule,” *IEEE Journal of Oceanic Engineering*, vol. 11, pp. 97–99, January 1986.

[17] M. Chitre, “A high-frequency warm shallow water acoustic communications channel model and measurements,” *JASA*, vol. 122(5), pp. 2580–2586, November 2007.

[18] H. Leinhos, “Capacity calculations for rapidly fading communications channels,” *IEEE Journal of Oceanic Engineering*, vol. 21, pp. 137–142, April 1996.

[19] A. Radosevic, J. G. Proakis, and M. Stojanovic, “Statistical characterization and capacity of shallow water acoustic channels,” in *Proceedings IEEE Oceans’09 Conference*, (Bremen, Germany), May 2009.

[20] P. Qarabaqi and M. Stojanovic, “Statistical modeling of a shallow water acoustic communication channel,” in *Proceedings of Underwater Acoustic Measurements Conference*, (Nafplion, Greece), June 2009.

[21] I. E. Telatar, “Capacity of multi-antenna gaussian channels,” *European Transactions on Telecommunications*, vol. 10, pp. 585–595, November 1999.

[22] G. J. Foschini and M. J. Gans, “On limits of wireless communications in a fading environment when using multiple antennas,” *Wireless Personal Communications*, vol. 6, pp. 311–335, 1998.

[23] L. Pillutla and S. K. Jayaweera, “Mimo capacity of an ofdm-based system under ricean fading,” in *Proceedings of IEEE Vehicular Technology Conference* (VTC), (Milan, Italy), May 2004.

[24] H. Bolcskei, D. Gesbert, and A. Paulraj, "On the capacity of ofdm-based spatial multiplexing systems," *IEEE Transactions on Communications*, vol. 50, pp. 225–234, February 2002.

[25] X. G. S. Jin and X. You, "On the ergodic capacity of rank-1 ricean-fading mimo channels," *IEEE Transactions on Information Theory*, vol. 53, pp. 502–517, February 2007.

[26] S. Shamai, L. H. Ozarow, and A. D. Wyner, "Information rates for a discrete-time gaussian channel with intersymbol interference and stationary inputs," *IEEE Transactions on Information Theory*, vol. 37, pp. 1527–1539, November 1991.

[27] W. J. Higley, "Self-adaptive processes for the mitigation of coherent multipath in ocean acoustics," in *Ph.D. dissertation*, (University of California at San Diego), 2007.

[28] Z. Zhang, T. M. Duman, and E. M. Kurtas, "Achievable information rates and coding for mimo systems over isi channels and frequency-selective fading channels," *IEEE Transactions on Communications*, vol. 52, pp. 1698 – 1710, October 2004.

[29] D. G. Manolakis, V. K. Ingle, and S. M. Kogon, *Statistical and Adaptive Signal Processing*. New York: McGraw-Hil, 2000.

[30] C. E. Shannon, "A mathematical theory of communication," *Bell System Technical Journal*, October 1948.

[31] S. K. Jayaweera and V. H. Poor, "On the capacity of multiple-antenna systems in rician fading," *IEEE Transactions on Wireless Communications*, vol. 4, pp. 1102–1111, May 2005.

[32] L. A. Pflug, G. E. Ioup, J. W. Ioup, and P. Jackson, "Variability in higher order statistics of measured shallow-water shipping noise," in *Proceedings of IEEE Signal Processing Workshop on Higher-Order Statistics*, pp. 400–404, July 1997.

[33] D. Arnold and H.-A. Loeliger, "On the information rate of binary-input channels with memory," in *Proceedings of IEEE International Conference on Communications*, vol. 9, pp. 2692–2695, June 2001.

[34] H. D. Pfister, J. B. Soriaga, and P. H. Siegel, "On the achievable information rates of finite state isi channels," in *Proceedings of IEEE GLOBECOM'01*, vol. 9, (San Antonio, TX), pp. 2992–2996, November 2001.

[35] S. S. (Shitz) and R. Laroia, “The intersymbol interference channel: Lower bounds on capacity and channel precoding loss,” *IEEE Transactions on Information Theory*, vol. 42, pp. 1388–1404, September 1996.

[36] D. M. Arnold, H. Loeliger, P. O. Vontobel, A. Kavcic, and W. Zeng, “Simulation-based computation of information rates for channels with memory,” *IEEE Transactions on Information Theory*, vol. 52, pp. 3498–3508, August 2006.

[37] F. Rusek and D. Fertonani, “Lower bounds on the information rate of intersymbol interference channels based on the ungerboeck observation model,” in *Proceedings of IEEE International Symposium on Information Theory (ISIT 2009)*, (Seoul, Korea), pp. 2992–2996, July 2009.

[38] P. Sadeghi, P. O. Vontobel, and R. Shams, “Optimization of information rate upper and lower bounds for channels with memory,” *IEEE Transactions on Information Theory*, vol. 55, pp. 663–688, February 2009.

[39] S. Jeong and J. Moon, “Computing lower bounds on the information rate of the intersymbol interference channels,” *arXiv:1001.3911v1 [cs.IT]*, vol. 55, pp. 663–688, January 2010.

[40] A. Radosevic, D. Fertonani, T. M. Duman, J. G. Proakis, and M. Stojanovic, “Capacity of mimo systems in shallow water acoustic channels,” in *Proc. 43rd Asilomar Conference on Signals, Systems and Computers*, November 2009.

[41] G. Colavolpe and G. Germi, “On the application of factor graphs and the sum-product algorithm to ISI channels,” *IEEE Transactions on Communications*, vol. 53, pp. 818–825, May 2005.

[42] T. M. Cover and J. A. Thomas, *Elements of Information Theory.* New York: ohn Wiley & Sons, 1991.

[43] S. ten Brink, G. Kramer, and A. Ashikhmin, “Design of low-density parity-check codes for modulation and detection,” *IEEE Transactions on Communications*, vol. 52, pp. 670–678, April 2004.

[44] N. Benvenuto and R. Marchesani, “The viterbi algorithm for sparse channels,” *IEEE Transactions on Communications*, vol. 44, pp. 287–289, March 1996.

[45] N. C. McGinty, R. A. Kennedy, and P. Hoeher, “Parallel trellis viterbi algorithm for sparse channels,” *IEEE Transactions on Communications*, vol. 2, pp. 143–145, May 1998.

[46] J. Moon and W. Zeng, “Equalization for maximum likelihood detectors,” *IEEE Transactions on Magnetics*, vol. 31, pp. 1083–1087, March 1995.

[47] N. Al-Dhahir and J. M. Cioffi, "Efficiently computed reduced-parameter input-aided mmse equalizers for ml detection: A unified approach," *IEEE Transactions on Information Theory*, vol. 42, pp. 903–915, May 1996.

[48] J. Chow and J. M. Cioffi, "A cost-effective maximum likelihood receiver for multicarrier systems," in *Proceedings of IEEE International Conference on Communications*, (Chicago, IL), pp. 948–952, June 1992.

[49] N. AI-Dhahir, A. H. Sayed, and J. M. Cioffi, "A high-performance cost-effective pole-zero mmse-dfe," in *Proceedings of Allerton Conference on Communication, Control, and Computing*, (Chicago, IL), pp. 1166–1175, September 1993.

[50] L. R. Bahl, J. Cocke, F. Jelinek, and J. Raviv, "Optimal decoding of linear codes for minimizing symbol error rate," *IEEE Transactions on Information Theory*, vol. 20, pp. 284–287, March 1974.

[51] D. Fertonani, A. Barbieri, and G. Colavolpe, "Reduced-complexity bcjr algorithm for turbo equalization," *IEEE Transactions on Communications*, vol. 55, pp. 2279–2287, December 2007.

[52] A. Kavcic and J. M. F. Moura, "The viterbi algorithm and markov noise memory," *IEEE Transactions on Communications*, vol. 46, pp. 291–301, January 2000.

[53] A. J. Viterbi, "Error bounds for convolutional codes and an asymptotically optimum decoding algorithm," *IEEE Transactions on Information Theory*, vol. IT-13, pp. 260–269, April 1967.

[54] B. Li, S. Zhou, M. Stojanovic, L. Freitag, and P. Willet, "Multicarrier communications over underwater acoustic channels with nonuniform doppler shifts," *IEEE Journal of Oceanic Engineering*, vol. 33, pp. 198–209, April 2008.

[55] B. Li, J. Huang, S. Zhou, K. Ball, M. Stojanovic, L. Freitag, and P. Willett, "Mimo-ofdm for high rate underwater acoustic communications," *IEEE Journal of Oceanic Engineering*, vol. 34, pp. 634–645, October 2009.

[56] M. Stojanovic, "Low complexity ofdm detector for underwater acoustic channels," in *Proc. IEEE Oceans'06 Conference*, (Boston, MA), September 2006.

[57] A. J. Goldsmith and S.-G. Chua, "Variable-rate variable-power mqam for fading channels," *IEEE Transactions on Communications*, vol. 45, pp. 1218–1230, October 1997.

[58] D. L. Goeckel, "Adaptive coding for time-varying channels using outdated fading estimates," *IEEE Transactions on Communications*, vol. 47, pp. 844–855, June 1999.

[59] T. Keller and L. Hanzo, "Adaptive multicarrier modulation: a convenient framework for time-frequency processing in wireless communications," *Proceedings IEEE*, vol. 88, pp. 611–640, May 2000.

[60] B. Krongold, K. Ramchandran, and D. Jones, "Computationally efficient optimal power allocation algorithms for multicarrier communication systems," *IEEE Transactions on Communications*, vol. 48, pp. 23–27, January 2000.

[61] S. Mani, T. M. Duman, and P. Hursky, "Adaptive coding/modulation for shallow-water uwa communications," in *Proc. of Acoustic 2008*, (Paris, France), July 2008.

[62] A. Radosevic, T. M. Duman, J. G. Proakis, and M. Stojanovic, "Adaptive ofdm for underwater acoustic channels with limited feedback," in *Proc. 45th Asilomar Conference on Signals, Systems and Computers*, November 2011.

[63] A. Radosevic, T. M. Duman, J. G. Proakis, and M. Stojanovic, "Channel prediction for adaptive modulation in underwater acoustic communications," in *Proceedings IEEE Oceans'11 Conference*, (Santander, Spain), June 2011.

[64] W. Li and J. Preisig, "Estimation of rapidly time-varying sparse channelss," *IEEE Journal of Oceanic Engineering*, vol. 32, pp. 927–939, October 2007.

[65] R. M. Corless, G. H. Gonnet, D. E. G. Hare, D. J. Jeffrey, and D. E. Knuth, "On the lambert w function," *Adv. Comput. Math. 5*, pp. 329–359, 1996.

[66] R. F. H. Fisher and J. B. Huber, "A new loading algorithm for discrete multitone transmission," in *Proceedings Globecom '96*, (London, U.K.), pp. 724–728, November 1996.

[67] J. Campello, "Practical bit loading for dmt," in *Proceedings of International Conference Communications* (ICC99), vol. 2, (Vancouver, BC, Canada), pp. 801–805, Jun 1999.

[68] S. Golomb, "Run-length encodings," *IEEE Transactions on Information Theory*, vol. 24, pp. 399–401, May 1966.

[69] J. Ziv and A. Lempel, "A universal algorithm for sequential data compression," *IEEE Transactions on Information Theory*, vol. 24, pp. 337–343, May 1977.

[70] S. Mehrotra, "On the implementation of a primal-dual interior point method," *SIAM Journal on Optimization*, vol. 2, no. 4, pp. 575–601, 1992.

[71] L. Tong, B. M. Sadler, and M. Dong, "Pilot-assisted wireless transmissions: General model, design criteria, and signal processing," *IEEE Signal Processing Magazine*, vol. 21, pp. 12–26, November 2004.

[72] X. Ma, G. B. Giannakis, and S. Ohno, "Optimal training for block transmissions over doubly-selective wireless fading channels," *IEEE Transactions on Signal Processing*, vol. 51, pp. 1351–1366, May 2003.

[73] T. Kang and R. A. Iltis, "Iterative carrier frequency offset and channel estimation for underwater acoustic ofdm systems," *IEEE Journal on Selected Areas in Communications*, vol. 26, pp. 1650–1661, December 2008.

[74] C. R. Berger, J. Gomes, and J. Moura, "Study of pilot designs for cyclic-prefix ofdm on time-varying and sparse underwater acoustic channels," in *Proceedings IEEE Oceans'11 Conference*, (Santander, Spain), June 2011.

[75] S. S. Chen, D. L. Donoho, and M. A. Saunders, "Atomic decomposition by basis pursuit," *SIAM Rev.*, vol. 43, no. 1, pp. 129–159, 2001.

[76] T. Kariya and H. Kurata, *Generalized Least Squares.* Wiley, 2004.

[77] K. E. Baddour and N. C. Beaulieu, "Autoregressive modeling for fading channel simulation," *IEEE Transactions on Wireless Communications*, vol. 4, pp. 1650–1661, July 2005.

[78] D. J. C. MacKay and R. M. Neal, "Near shannon limit performance of low density parity check codes," *Electron. Lett.*, vol. 33, pp. 457–458, March 1997.